

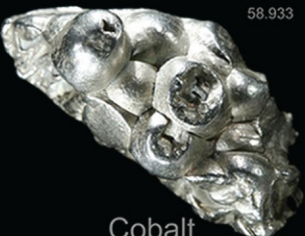






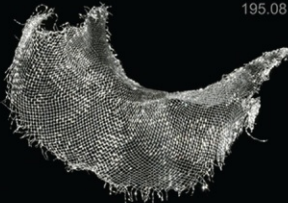

Конденсированные среды и межфазные границы

РЕЦЕНЗИРУЕМЫЙ НАУЧНЫЙ ЖУРНАЛ

Condensed Matter and Interphases

Kondensirovannyye Sredy i Mezhfaznye Granitsy
PEER-REVIEWED SCIENTIFIC JOURNAL

Том
Vol. 23, No. 2
2021

<p>Co 27 58.933</p>  <p>Cobalt</p>	<p>Ni 28 58.693</p>  <p>Nickel</p>	<p>Cu 29 63.546</p>  <p>Copper</p>
<p>Rh 45 102.91</p>  <p>Rhodium</p>	<p>Pd 46 106.42</p>  <p>Palladium</p>	<p>Ag 47 107.87</p>  <p>Silver</p>
<p>Ir 77 192.22</p>  <p>Iridium</p>	<p>Pt 78 195.08</p>  <p>Platinum</p>	<p>Au 79 196.97</p>  <p>Gold</p>

Condensed Matter and Interphases

Kondensirovannye sredy i mezhfaznye granitsy

Peer-reviewed scientific journal

Published since January 1999

Periodicity: Quarterly

Volume 23, No. 2, 2021

Full-text version is available in the Russian language on the website: <https://journals.vsu.ru/kcmf>

Condensed Matter and Interphases (Kondensirovannye Sredy i Mezhfaznye Granitsy) publishes articles in Russian and English dedicated to key issues of condensed matter and physicochemical processes at interfaces and in volumes.

The mission of the journal is to provide open access to the results of original research (theoretical and experimental) at the intersection of contemporary condensed matter physics and chemistry, material science and nanoindustry, solid state chemistry, inorganic chemistry, and physical chemistry, and to share scientific data in the **following sections**: atomic, electron, and cluster structure of solids, liquids, and interphase boundaries; phase equilibria and defect formation processes; structure and physical and chemical properties of interphases; laser thermochemistry and photostimulated processes on solid surfaces; physics and chemistry of surface, thin films and heterostructures; kinetics and mechanism of formation of film structures; electrophysical processes in interphase boundaries; chemistry of surface phenomena in sorbents; devices and new research methods.

The journal accepts for publication: reviews, original articles, short communications by leading Russian scientists, foreign researchers, lecturers, postgraduate and undergraduate students.

FOUNDER AND PUBLISHER:

Voronezh State University

The journal is registered by the Russian Federal Service for Supervision of Communications, Information Technology and Mass Media, Certificate of Registration ПИ № ФС77-78771 date 20.07.2020

The journal is included in the List of peer reviewed scientific journals published by the Higher Attestation Commission in which major research results from the dissertations of Candidates of Sciences (PhD) and Doctor of Science (DSc) degrees are to be published.

Scientific specialties of dissertations and their respective branches of science are as follows: 02.00.01 – Inorganic Chemistry, 02.00.04 – Physical Chemistry, 02.00.05 – Electrochemistry, 02.00.21 – Solid State Chemistry (Chemical sciences); 01.04.07 – Condensed Matter Physics (Physical Sciences)

The journal is indexed and archived in: Russian Scientific Index Citations, Scopus, Chemical Abstract, EBSCO, DOAJ, CrossRef

Editorial Board and Publisher Office:

1 Universitetskaya pl., Voronezh 394018

Phone: +7 (432) 2208445

<https://journals.vsu.ru/kcmf/about>

E-mail: kcmf@main.vsu.ru

Signed for printing 30.06.2021

Price – not fixed

Subscription is available using the unified catalogue “Russian Press”, subscription index 80568

When reprinting the materials, a reference to the Condensed Matter and Interphases must be cited

The journal’s materials are available under the Creative Commons “Attribution” 4.0 Global License



© Voronezh State University, 2021

EDITOR-IN-CHIEF:

V. N. Semenov, DSc in Chemistry, Professor (Voronezh)

VICE EDITORS-IN-CHIEF:

E. P. Domashevskaya, DSc in Physics and Mathematics, Professor (Voronezh)

P. Volovitch, DSc, Professor (Paris, France)

EDITORIAL BOARD:

N. N. Afonin, DSc in Chemistry, Professor (Voronezh)

V. I. Vasil'eva, DSc in Chemistry, Associate Professor (Voronezh)

A. V. Vvedenskii, DSc in Chemistry, Professor (Voronezh)

V. V. Gusarov, DSc in Chemistry, Associate Member of the RAS (St. Petersburg)

V. E. Guterman, DSc in Chemistry, Professor (Rostov-on-Don)

B. M. Darinskii, DSc in Physics and Mathematics, Professor (Voronezh)

V. P. Zlomanov, DSc in Chemistry, Professor (Moscow)

V. M. Ievlev, DSc in Physics and Mathematics, Full Member of the RAS (Moscow)

A. D. Izotov, DSc in Chemistry, Associate Member of the RAS (Moscow)

O. A. Kozaderov, DSc in Chemistry, Associate Professor (Voronezh)

A. I. Marchakov, DSc in Chemistry, Professor (Moscow)

I. Ya. Mittova, DSc in Chemistry, Professor (Voronezh)

V. V. Nikonenko, DSc in Chemistry, Professor (Krasnodar)

O. V. Ovchinnikov, DSc in Physics and Mathematics, Professor (Voronezh)

S. N. Saltykov, DSc in Chemistry, Associate Professor (Lipetsk)

V. F. Selemenev, DSc in Chemistry, Professor (Voronezh)

V. A. Terekhov, DSc in Physics and Mathematics, Professor (Voronezh)

E. A. Tutov, DSc in Chemistry, Associate Professor (Voronezh)

P. P. Fedorov, DSc in Chemistry, Professor (Moscow)

V. A. Khonik, DSc in Physics and Mathematics, Professor (Voronezh)

V. A. Shaposhnik, DSc in Chemistry, Professor (Voronezh)

A. B. Yaroslavtsev, DSc in Chemistry, Associate Member of the RAS (Moscow)

INTERNATIONAL MEMBERS OF THE EDITORIAL BOARD:

M. B. Babanly, DSc in Chemistry, Associate Member of the ANAS (Baku, Azerbaijan)

T. Bellezze, DSc (Ancona, Italy)

R. M. Mane, DSc (Kolhapur, India)

Nguyen Anh Tien, PhD in Chemistry, Associate Professor (Ho Chi Minh City, Vietnam)

V. V. Pan'kov, DSc in Chemistry, Professor (Minsk, Belarus)

F. Scholz, DSc, Professor (Greifswald, Germany)

M. S. Wickleder, DSc, Professor (Cologne, Germany)

V. Sivakov, DSc (Jena, Germany)

EXECUTIVE SECRETARY:

V. A. Logacheva, PhD in Chemistry (Voronezh)

CONTENTS

REVIEW

Fedorov P. P., Yarotskaya E. G.
Zirconium dioxide. Review

169

ORIGINAL ARTICLES

*Akhmetkhanov R. M., Chernova V. V.,
Shurshina A. S., Lazdina M. Yu., Kulish E. I.*
Study of the formation of structures in solutions
of chitosan – polyvinyl alcohol polymer blends

188

Bui Xuan Vuong, Nguyen Anh Tien
Sol-gel synthesis, crystal structure and magnetic
properties of nanocrystalline praseodymium
orthoferrite

196

*Vasil'ev M. G., Vasil'ev A. M., Izotov A. D.,
Kostin Yu. O., Shelyakin A. A.*
Growing epitaxial layers of InP/InGaAsP
heterostructures on the profiled InP surfaces
by liquid-phase epitaxy

204

Grigoryan G. S., Solodukha A. M.
Anomalous behaviour of dynamic electrical
conductivity in semiconductor ferroelectric
ceramics near the phase transition temperature

212

Dokhov M. P.
On the limitations of the applicability
of Young's equations temperature

218

*Kozlov G. V., Magomedov Gas. M.,
Magomedov Gus. M., Dolbin I. V.*
The structure of carbon nanotubes
in a polymer matrix

223

Kolesnikov A. V., Ageenko E. I.
Features of the discharge of zinc in the
background solution of sodium sulphate
under stirring conditions

229

*Mammadli P. R., Gasymov V. A., Dashdiyeva G. B.,
Babanly D. M.*
Phase relations in the CuI-SbSI-SbI₃
composition range of the Cu-Sb-S-I
quaternary system

236

*Mittova V. O., Khoroshikh A. O., Zemchenkova O. V.,
Ryazantsev S. V., Maslov O. V., Korzh E. V.,
Ryasnaya-Lokinskaya L. S., Alabovsky V. V.*
Gender differences in lipid metabolism

245

*Myslitskaya N. A., Tcibulnikova A. V., Samusev I. G.,
Slezhkin V. A., Bryukhanov V. V.*
Heat wave dynamics in frozen water droplets
with eosin molecules under the femtosecond
excitation of a supercontinuum

260

*Orujlu E. N., Aliev Z. S., Jafarov Y. I., Ahmadov E. I.,
Babanly M. B.*
Thermodynamic study of manganese tellurides
by the electromotive force method

273

*Syrkov A. G., Kabirov V. R., Pomogaybin A. P.,
Ngo Quoc Khanh*
Electrophilic-nucleophilic properties
as a factor in the formation of antifriction
and hydrophobic properties of surface-modified
metals with ammonium and organosilicon
compounds

282



Condensed Matter and Interphases

Kondensirovannye Sredy i Mezhfaznye Granitsy
<https://journals.vsu.ru/kcmf/>

Review

Review article

<https://doi.org/10.17308/kcmf.2021.23/3427>

Zirconium dioxide. Review

P. P. Fedorov✉, E. G. Yarotskaya

*Prokhorov General Physics Institute of the Russian Academy of Sciences,
38 Vavilova str., GSP-1, Moscow 119991, Russian Federation*

Abstract

A review of zirconium dioxide or zirconia ZrO_2 is presented. The finding of zirconium compounds in nature, the physical and chemical properties of ZrO_2 are given, the polymorphism of zirconium oxide, and the phase diagrams of systems with its participation are considered. The areas of application of zirconia compounds are highlighted: automotive industry, electronics industry, energy and industrial ecology, equipment manufacturing and mechanical engineering the production of zirconium-based refractories, ceramics, enamels, glass, superhard materials, applications in medicine, nuclear energetics, and many others areas of human activity. Cubic modification of zirconium dioxide, stabilized by oxides of rare earth elements, is a jewelry stone (fianite). Partially stabilized zirconium dioxide is a versatile structural material with very high resistance to crack propagation. Solid solutions of REE oxides, especially scandium, have a high oxygen conductivity, which is used in sensors for measuring the partial pressure of oxygen and in fuel cells. Attention is paid to heat-resistant oxide ceramic materials with low thermal conductivity used in the quality of heat-resistant coatings. Considerable attention was paid to the second most important mineral of zirconia - baddeleyite (ZrO_2). Baddeleyite is widely used in the production of refractory materials. It is mined for the production of metallic zirconium. The achievements of Soviet and Russian scientists in the development of technologies for the production of fianite and artificial baddeleyite are presented.

Keywords: Fianite, Baddeleyite, Zircon, Ceramics, Solid solutions, Oxides of rare earth elements, Phase diagrams, Inert matrix nuclear fuel

Acknowledgments: the authors are grateful to M. A. Borik, Yu. I. Golovin, V.V. Gusarov, O. V. Almyasheva, E. V. Polyansky for the discussion and E. V. Chernova for help in preparing the manuscript.

For citation: Fedorov P. P., Yarotskaya E. G. Zirconium dioxide. Review. *Kondensirovannye sredy i mezhfaznye granitsy = Condensed Matter and Interphases*. 2021;23(2): 169–187. <https://doi.org/10.17308/kcmf.2021.23/3427>

Для цитирования: Федоров П. П., Яроцкая Е. Г. Двоксид циркония. Обзор. *Конденсированные среды и межфазные границы*. 2021;23(2): 169–187. <https://doi.org/10.17308/kcmf.2021.23/3427>

✉ Pavel P. Fedorov e-mail: ppfedorov@yandex.ru

© Fedorov P. P., Yarotskaya E. G., 2021



The content is available under Creative Commons Attribution 4.0 License.

1. Introduction

Zirconia ZrO_2 was first synthesized in 1789. In 1892 in Sri Lanka and in Brazil the mineral baddeleyite was discovered. Since 1900 stabilized zirconia with high ionic conductivity was already widely in use as a glow bar for lighting (“Nernst caps”). Since the 1920s tons of zirconia were used as refractory ceramics [1–7]. Now, materials based on zirconia are widely used as single crystals, structural and functional ceramics, film coatings, microfibrils and nanopowders, and composite materials [8–35].

Large transparent crystals of cubic zirconia stabilized by rare earth (REE) oxides dopants are used in jewellery as an imitation diamonds due to their high refractive index and dispersion. In the USSR such crystals were called fianite, abbreviated from the Russian name Physical Institute of the Russian Academy of Sciences of the USSR where they were synthesised using the original cold crucible technique [9]. Partially stabilized two-phase zirconia (PSZ) with a small concentration of stabilizing additive is a material with a very high fracture toughness, as a result of which it is used, for example, for the manufacture of cutting tools [10, 11].

Ceramics based on zirconia (ZrO_2) are versatile construction materials for various purposes (<https://www.ceramtec.ru>), characterized by their refractoriness and high corrosion resistance [8, 12–18]. It should be noted that zirconia ceramics are significantly more expensive than alumina ceramics. Thus, zirconia ceramics are used for the manufacture of critical parts, for example, in the nuclear industry [36], in metallurgy for troughs, crucibles for the continuous casting of steels, crucibles for melting platinum and rare earth elements [19], pipes, in the manufacture of drawing tools for forming wire products, and in the automotive industry for the manufacture of brake discs for high-end cars.

In the aviation and space industry, it is irreplaceable, since due to its properties aircraft and spaceships can withstand very high temperatures [16–17, 20–21, 28–31]. It is also used in medicine, for example, for endoprosthetic as the heads of artificial hip joints. It exhibits its best qualities for dental prostheses in dentistry [22–23].

Solid solutions based on ZrO_2 with a fluorite structure are solid electrolytes. Under heating,

they exhibit high oxygen electrical conductivity, which makes these materials a suitable working medium for solid oxide fuel cells (SOFC) [10, 24–26]. They are also used in other electrochemical devices such as oxygen partial pressure sensors. High ionic conductivity correlates with low thermal conductivity [27], and films of solid solutions based on ZrO_2 are used for the production of heat-insulating (thermal barrier) coatings that combine heat resistance, very low thermal conductivity, and high strength [28–31].

A wide range of composite materials of various types with the participation of zirconia is being developed [8, 13, 32–35]. Ceramometal materials are used, for example, for joining ceramic and steel parts.

Recently, interest in heat-resistant fibres for thermal insulation purposes (<https://www.ceramtec.ru>), [20, 37, 38], as well as zirconia nanopowders, has increased [39–41]. Nanopowders are hydrophilic; their surface is covered with adsorbed water [42]. NanoFormula (Estonia) produces the nanopowders NZirconiumOxide-01 (pure ZrO_2 monoclinic structure, average particle size 20 nm, specific surface area 25 m^2/g) and NZirconiumOxide-02 (tetragonal crystal system, stabilized by 3–8 % Y_2O_3 , average particle size 40 nm, specific surface area 40 m^2/g). Their areas of application are extensive: functional ceramics, high-purity pigments, porcelain, glazes, pyro-optical elements, in high-capacity capacitors, optical carriers, in elements that reproduce images, in optical shutters, in glass for stereoscopic television, in memory devices, in abrasive materials, insulators, in fire-retardant materials, in X-ray technology, in high-temperature and corrosion-resistant components, in pipes, in crucibles, in piezoelectric elements, in ion exchange, filters, in transmitting elements, in heating elements, in artificial jewelry, as additives in fuel, in batteries (nanoformula.tiu.ru).

This review discusses zirconia, its minerals, occurrence in nature, applications, chemical properties, features of isomorphism, and materials based on it.

2. Distribution in nature

Zirconium compounds are widespread in the lithosphere. According to various Clarke numbers (numbers expressing the average

content of chemical elements in the earth's crust, hydrosphere, Earth, cosmic bodies, geochemical or cosmochemical systems, etc., in relation to the total mass of this system), zirconium content ranges from 170 to 250 g/t. Concentration in seawater is $5 \cdot 10^{-5}$ mg/l.

Zirconium is a lithophilic element. In nature, there are only its compounds with oxygen in the form of oxides and silicates. Despite the fact that zirconium is a trace element, there are about 40 zirconium minerals: zircon (ZrSiO_4) (67.1 % ZrO_2), baddeleyite (ZrO_2), eudialyte $(\text{Na, Ca})_5(\text{Zr, Fe, Mn})[\text{O, OH, Cl}][\text{Si}_6\text{O}_{17}]$, and etc. In all deposits, zirconium is accompanied by hafnium, which isomorphically substitutes zirconium [43].

Zircon is the most abundant zirconium mineral. It is found in all types of rocks, but mainly in granites and syenites. The largest zirconium deposits are located in the USA, Australia, Brazil, and India. In Russia, which accounts for 10 % of the world's zirconium reserves (3rd place in the world after Australia and South Africa), the main deposits are Kovdor bedrock baddeleyite-apatite-magnetite in Murmansk oblast, Tugan placer zircon-rutile-ilmenite in Tomsk oblast, Central placer zircon-rutile-ilmenite in Tambov oblast, Lukoyanovskoe placer zircon-rutile-ilmenite in the Nizhny Novgorod oblast, Katuginskoe bedrock zircon-pyrochlore-cryolite in the Chita region and Ulug-Tanzek primary zircon-pyrochlore-columbite deposit. Almost unlimited reserves of zirconium are concentrated in the alkaline syenites of the Khibiny Massif on the Kola Peninsula, where this metal is part of many minerals, in particular eudialyte. In industry, the raw materials for the production of zirconium are zirconium concentrates with a mass content of zirconia of at least 60-65%, obtained by the enrichment of zirconium ores [1–6].

3. Polymorphism

Zirconia (ZrO_2) with a melting point of about 2700 °C is one of the most refractory metal oxides. Its density is 5.68 g/cm³ at 20 °C. It exists in three crystalline forms: stable under standard conditions monoclinic (*m*) modifications (space group $P2_1/c$, $Z = 4$), occurring in nature in the form of the mineral baddeleyite [44, 45];

medium temperature tetragonal (*t*) modifications (space group $P4_2/nmc$, $Z = 4$), metastable under normal conditions, and high-temperature cubic polymorph (*c*) of fluorite type (space group $Fm\bar{3}m$, $Z = 4$) [46]. The data on the temperatures of phase transitions determined in different studies differ significantly (see the summary in [47]). Intervals of <1170; 1170–2370; 2370–2680 °C can be considered as the regions of thermodynamic stability of the phases [48]. However, the scheme of ZrO_2 polymorphism is still the subject of discussion [49].

Both monoclinic and tetragonal structures are distortions of the cubic structure of the fluorite type with coordination numbers 7, 8, and 8 for these structural types. The transition of the tetragonal phase to the monoclinic phase is reversible athermal (i.e., not characterised by any specific transition temperature) martensitic transformation associated with a large temperature hysteresis (~ 200 °C), a change in volume (~ 7 %), and a large shear deformation (~ 15 %). Upon cooling, the transformation may be explosive [1,50]. This has a very significant negative impact from the point of view of technologies for materials based on zirconia. Both high-temperature cubic and medium-temperature tetragonal modifications are easily stabilized by various impurities.

The regions of stability of various modifications of zirconia substantially depend not only on the purity of the reagents, but also on the partial pressure of oxygen. The reducing atmosphere leads to the formation of a wide range of ZrO_{2-x} solid solution and stabilizes the cubic modification both upward and downward in temperature (maximum on the melting curve at 2800 °C and eutectoid equilibrium at 1460 °C and the composition $\text{ZrO}_{1.86}$) [47]. Oxygen-deficient samples are black and have specific intrinsic luminescence [51].

Under high pressure, another cotunnite-type modification of ZrO_2 with the structural type PbCl_2 (orthorhombic crystal system, space group $Pnam$, $Z = 4$) occurs [48].

4. Preparation and chemical properties

Zirconia can be obtained by metal oxidation, oxidation of tetrachloride in an oxygen atmosphere, calcining thermally unstable

compounds (oxychloride, nitrate, oxalate, etc.), or the heat treatment of hydroxides. In the latter case, amorphous zirconia is first formed, which is converted into monoclinic phase at 450–480 °C. Moreover, cubic and tetragonal modifications that are metastable under these conditions can form as intermediate phases [4].

The gel $ZrO_2 \cdot nH_2O$ easily precipitates from aqueous solutions of zirconium salts, for example, zirconyl nitrate $ZrO(NO_3)_2 \cdot nH_2O$ [52]. However, the dehydration of the gel and its purification from adsorbed impurities is not an easy task. In addition to direct heat treatment, it can be achieved by hydrothermal treatment [53] and spray drying methods [54]. Zirconia with superacid properties is obtained by the heat treatment of a mixture of zirconium hydroxide with sulphuric acid. Fibres with a diameter of 100–200 nm were obtained by the electrospinning method from an aqueous solution of a mixture of zirconium oxychloride with polyvinyl alcohol, which, after annealing at temperatures above 800 °C, contained only zirconia [38]. Technology for obtaining ZrO_2 by processing zircon concentrate using ammonium fluorides was developed [55].

Complex compositions with the participation of zirconia were obtained by various methods: fusion in a cold crucible, sintering, co-precipitation [56, 57], hydrothermal synthesis [56, 58], plasma chemistry [25–33, 40], sol-gel method [59–60], chemical combustion [61–63], etc.

Zirconia during heating is not completely reduced by magnesium; it is reduced by calcium hydride to metallic zirconium at 800 °C. Heating with oxides of calcium, strontium, or barium as well as with alkalis or alkali metal carbonates provides metazirconates. It easily dissolves in boiling hydrofluoric acid, forming hexafluorozirconic acid. Zirconia practically is not decomposed by cold and hot hydrochloric and nitric acids. The reaction with hydrochloric acid takes place only if the zirconia is thoroughly ground. It reacts with hot concentrated sulphuric acid. It is partially soluble in 50 % KOH. It does not react with chlorine and bromine even at high temperatures. It does not react with halides of alkali and alkaline earth metals, metallic sodium, oxygen, sulphur, selenium, or tellurium. It does not react with hydrogen even at 2000 °C with a pressure of 150

atm. It does not react with beryllium at 1600 °C. It does not react with fluorine at 100 °C, but at 525 °C it completely fluorinated to zirconium tetrafluoride. Above 300 °C it reacts with either carbon tetrachloride or phosgene to form zirconium tetrachloride. Above 600 °C in the presence of carbon, it reacts with chlorine to form zirconium tetrachloride. Above 1400 °C it reacts with carbon to form zirconium carbide. When heated to 1800 °C it reacts with boron to form zirconium borides and boron oxides. At 550 °C it reacts with anhydrous hydrogen fluoride to form zirconium tetrafluoride. At 1000 °C it reacts with carbon disulphide to form zirconium sulphide. It reacts with silicon to form zirconium silicides in an electric furnace. It does not react with molten aluminium at its melting point (660 °C), but at high temperatures, the reaction proceeds to form aluminium oxide and an intermetallic compound of zirconium and aluminium. During heating with titanium tetrachloride, it forms zirconium tetrachloride. During heating it reacts with hexafluorosilicates, forming hexafluorozirconates [2–7]. The chemical activity of zirconia increases with the transition to the nano state.

5. Crystal structure stabilisation and phase diagrams

If monoclinic zirconia is heated to ~ 1170 °C, then it transforms into a tetragonal form, accompanied by a noticeable decrease in volume. During cooling a reverse transition occurs with great supercooling, and moulded parts such as fibres or ceramic parts are destroyed by thermal cycling. This causes the technical need for the stabilization of the crystal structure in order to exclude phase transitions, namely, for the transformation of the monoclinic lattice into tetragonal or cubic forms, stable over a wide temperature range. The stabilization was carried out by introducing dopants with the formation of solid solutions due to the isomorphic substitutions of cations. Such stabilization can be carried out with isovalent isomorphism, for example, in the ZrO_2 – CeO_2 system, see Fig. 1 (cerium dioxide crystallises in the cubic structure of fluorite and is isostructural to the high-temperature modification ZrO_2) [64]. However, heterovalent isomorphic substitutions are most effective [66–88]. In ZrO_2 –MO (M = Mg,

Ca) and $ZrO_2-R_2O_3$ (R – rare earth elements) systems, wide regions of cubic solid solutions of $Zr_{1-x}M_xO_{2-x}$ and $Zr_{1-x}R_xO_{2-0.5x}$ are formed based on the high-temperature modification of ZrO_2 . The area of their existence is in the zone of low temperatures, in a non-equilibrium state this is up to room temperature. In addition, in a number of systems, the formation of such solid solutions is accompanied by the formation of maxima on the melting curves, i.e., high-temperature stabilization. In phase diagrams, these solid solutions decompose upon cooling according to the eutectoid scheme (Fig. 2), and at low temperatures, they are thermodynamically unstable. However, these transformations (decomposition) are strongly inhibited. In addition, in ZrO_2-MO and $ZrO_2-R_2O_3$ systems ordered fluorite-like phases are formed, bounding the regions of fluorite solid solutions, such as $R_4Zr_3O_{12}$ (R is the REE of the yttrium subgroup), $R_2Zr_2O_7$ pyrochlore type (R – REE of the cerium subgroup) $Ca_6Zr_{19}O_{44}$, $CaZr_4O_9$. A number of ordered phases are formed in the $ZrO_2-Sc_2O_3$ system, the composition of which is the subject of discussion [77, 78, 81]. In the ZrO_2-CaO system a binary compound – calcium zirconate $CaZrO_3$, melting at 2300 °C is also formed [65].

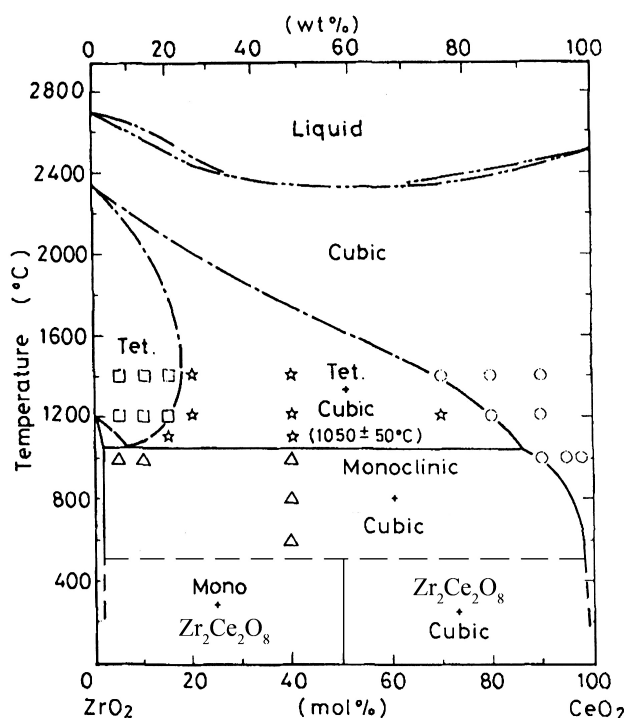


Fig. 1. Phase diagram of ZrO_2-CeO_2 system according to [64, 65]

Oxides CaO , MgO , Y_2O_3 are most widely used as stabilisers [13]. Joint industrial alloying with calcium and magnesium is possible using cheap dolomite raw materials [89]. Stabilisation of ZrO_2 at a annealing temperature of 1700–1750 °C is achieved with the addition of 10 mol. % CaO or MgO , or 8 mol. % Y_2O_3 . The degree of stabilisation of ZrO_2 depends on the type of stabiliser, its amount, the temperature of the stabilising annealing, the amount of impurities contained in zirconia, and other factors. A decrease in the size of crystallites leads to an expansion of the stability regions. Zirconia stabilised with CaO and Y_2O_3 is less prone to destabilisation than zirconia stabilised with magnesium oxide. In the presence of moisture, destabilisation is accelerated [88, 90].

The interest in zirconia systems with yttria (Fig. 2) and especially scandia is determined by the high anionic conductivity of fluorite solid solutions, which determines the choice of materials based on them as a working body for fuel cells [71–88, 91–93]. The problem of the stability of solid $Zr_{1-x}Sc_xO_{2-0.5x}$ solutions and their relatively rapid degradation (ageing) under operating conditions is important [85, 91–93]. For increased stability of the solid solution, co-doping is used, the introduction of additives, such as Y_2O_3

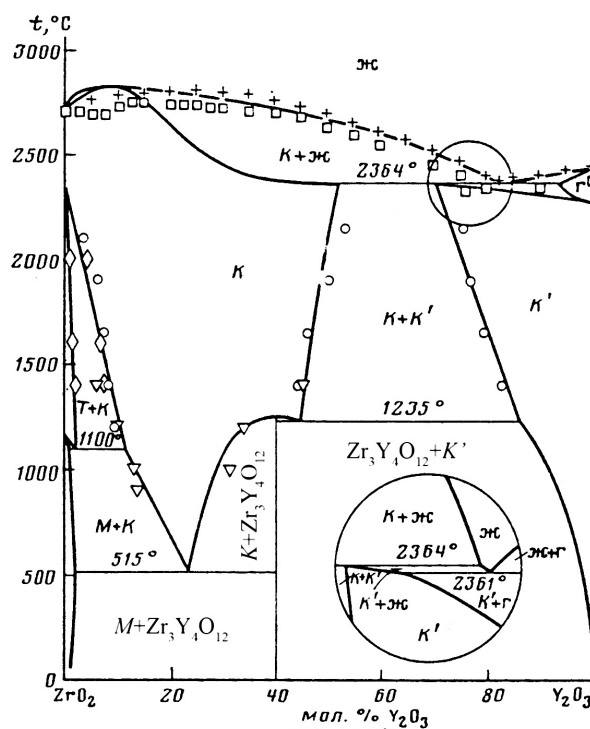


Fig. 2. Phase diagram of $ZrO_2-Y_2O_3$ system according to [68]

and other oxides together with scandia [72].

The study of phase diagrams with the participation of zirconia encountered great difficulties due to the refractoriness of the studied objects. A major achievement was the development of a method for thermal analysis using solar ovens, which allowed obtaining reliable information on liquidus curves [94, 95]. For plotting phase diagrams in reactive-active systems containing refractory oxides, an original method of melting in a cold crucible was used [36, 96].

In the published versions of the phase diagrams of systems with zirconia, there are serious contradictions, caused primarily by insufficient equilibration time. The activation energy of cationic diffusion in these systems is very high and amounts to about 400 kJ/mol [97, 98]. The fallacy of numerous studies devoted to the study of phase equilibria in the low-temperature region has been demonstrated by Japanese researchers from the Tokyo Institute of Technology [73,100], see fig. 3. On numerous published $(\text{Zr,Hf})\text{O}_2 - \text{R}_2\text{O}_3$ “phase diagrams” at temperatures below 1600 °C frozen states are

depicted instead of equilibrium phase regions (see, for example, [76, 99]). In particular, the results of numerous studies of $\text{ZrO}_2 - \text{Sc}_2\text{O}_3$ in the low-temperature region are extremely contradictory [71, 77–86]. The use of the liquid phase (hydrothermal synthesis) for acceleration of achieving equilibrium allowed obtaining the most reliable data on $\text{ZrO}_2 - \text{R}_2\text{O}_3$ ($\text{R} = \text{Er}, \text{Y}, \text{Sc}$), $\text{ZrO}_2 - \text{CeO}_2$ systems [64, 71, 100].

The actual behaviour of materials in systems based on zirconia upon cooling is determined mainly not by equilibrium phase transformations, but by diffusionless phase transitions. Accordingly, the so-called metastable phase diagrams, in which, instead of two-phase regions, there are martensitic phase transformation lines, are of great importance see Fig. 3b (line T_0^{t-m}). These transitions are accompanied by the mass twinning of the samples. In cooled samples of binary oxides, in addition to the phases m, t, c corresponding to zirconia polymorphs, the second tetragonal t' phase with a low degree of tetragonality (the ratio of the unit cell parameters $c/2a \sim 1.005$) is also systematically present, as well as the phase t'' for which the cubic lattice metric is preserved

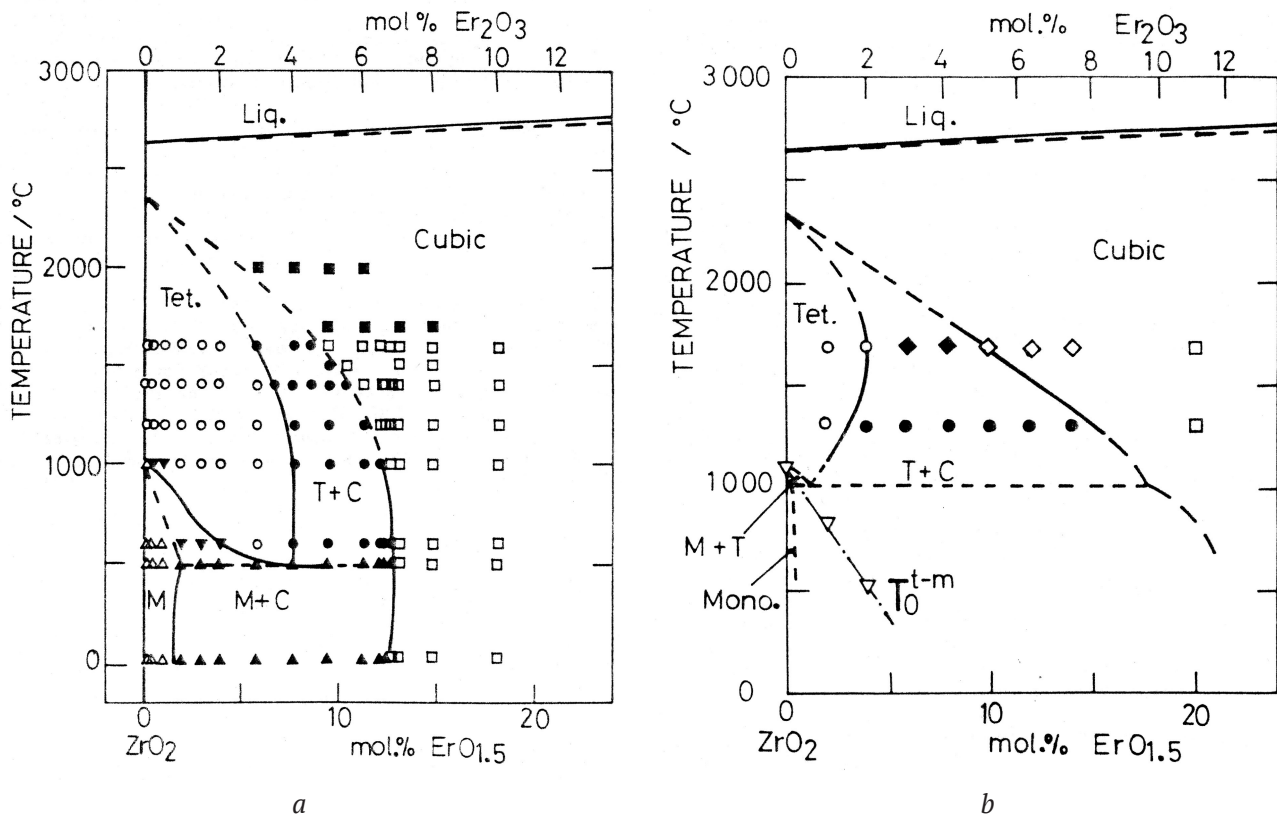


Fig. 3. Incorrect (a) and correct (b) versions of the phase diagram of $\text{ZrO}_2 - \text{Er}_2\text{O}_3$ system according to [99] and [100], respectively

($c/2a = 1.000$) [71]. Tetragonal distortions corresponding to space group $P4_2/nmc$, is caused by displacements in the anionic sublattice and, apparently, do not affect the cationic motif. These phases appear during quenching of a high-temperature cubic solid solution. Differences between the t' , t'' and c phases are clearly detected by the Raman scattering method [71, 73].

6. Fianites

The introduction of bivalent and trivalent cations into the fluorite lattice during the formation of wide regions of solid solutions based on the cubic high-temperature modification of ZrO_2 is accompanied by the formation of anionic vacancies, which are structural defects. With an increase in the concentration of solid solutions, there is an accumulation of vacancies associated with impurity cations with a lower charge. The short-range order transforms into the long-range one upon the formation of ordered fluorite-like phases. Features of structural changes can be traced by X-ray diffraction [73], Raman scattering [71, 73, 101–103], by the luminescent label methods [87], high-temperature neutron diffraction [75], EXAFS [75], transmission electron microscopy, and electron diffraction [72, 77]. Raman scattering is more sensitive to structural changes in the lattice of solid solutions than the X-ray diffraction method [104].

The high content of vacancies in doped samples leads to a sharp increase in the anionic conductivity of the corresponding solid solutions. Concentration dependences of electrical conductivity pass through a maximum at a content of about 10 mol. % R_2O_3 reaching values of $5 \cdot 10^{-2} \text{ Ohm}^{-1} \text{ cm}^{-1}$ at $800 \text{ }^\circ\text{C}$ [71]. The highest electrical conductivity is realised in the ZrO_2 – Sc_2O_3 system. Many options for a qualitative explanation of such dependences have been proposed, but there are no quantitative models. It should be noted that monocrystalline samples of solid solutions based on ZrO_2 have a higher ionic conductivity than ceramics of the same composition. This is true even for ceramics with negligible porosity, and this is an unexpected circumstance, since the surface conductivity is usually higher than the bulk conductivity due to the facilitated movement of ions through grain boundaries. This effect is associated with

the pushing back to the boundaries of ceramic grains impurities (in particular, silicon) with the formation of phases with low electrical conductivity [72].

The accumulation of both cationic substitutional defects and anionic vacancies in the structure causes the effective scattering of phonons in crystals. It leads to a dramatic drop in the thermal conductivity of solid solutions with an increase in the concentration of REE oxides. In this case, the temperature dependences of thermal conductivity acquire the form characteristic of glass, with a monotonic decrease with decreasing temperature, in contrast to the crystals, characterised by the presence of a maximum of thermal conductivity at low temperatures [103, 105–106]. High ionic conductivity correlates with low thermal conductivity [27]. Assessment of the thermal conductivity of samples is the simplest way to distinguish artificial fianites from diamonds, which have very high thermal conductivity.

Stabilisation of the high-temperature cubic modification of zirconia with a face-centred cell of the fluorite type by forming wide regions of solid solutions that do not undergo phase transformations down to low temperatures allows growing single crystals of the corresponding composition from the melt. The maxima on the melting curves of these solid solutions facilitate the preparation of single crystals of high optical quality. The old name for artificial cubic ZrO_2 stabilised by various impurities is arkelite [3].

In 1970–1972, at the Lebedev Physical Institute of the Academy of Sciences of the USSR (FIAN), a breakthrough in the synthesis of crystalline materials based on ZrO_2 and HfO_2 , which were called fianites, was made [9]. The breakthrough was achieved by a new technology for obtaining high-temperature dielectric crystals by Direct Radio Frequency Heating Technique using a cold container (skull melting) [9, 107].

In the working area of the crystal growth apparatus a “cold” container is located. This container is a water-cooled cylindrical crucible, consisting of several copper hollow segments (Fig. 4). A mixture of ZrO_2 and an oxide of the stabilising element is loaded into the crucible. For the initial melting, a small amount of metal (20–50 g) that will not contaminate the melt

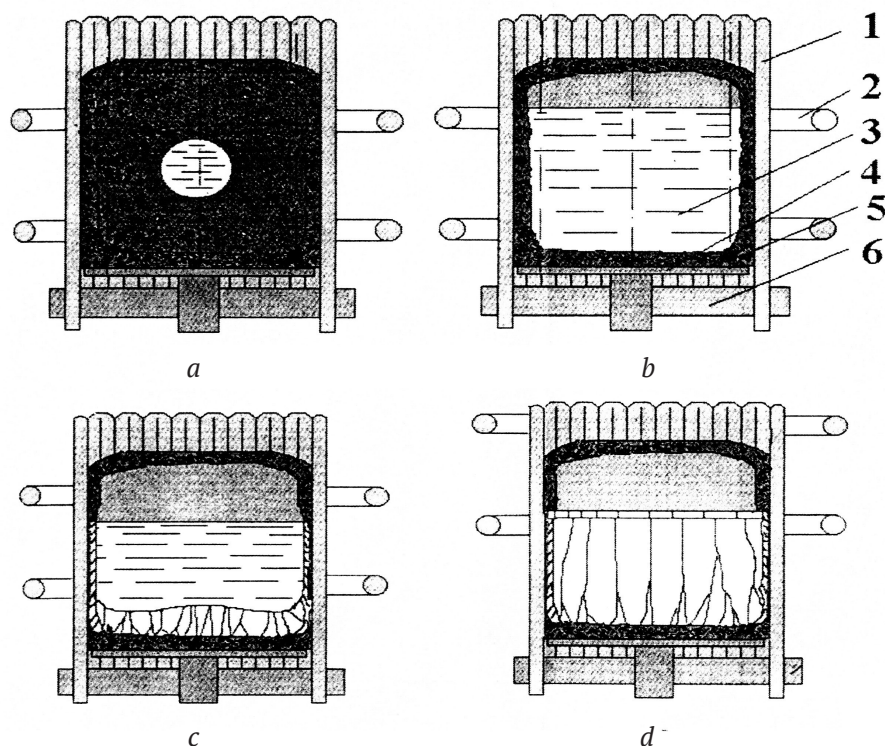


Fig. 4. Stages of crystal synthesis by directed crystallisation of the melt in a cold container using direct radio frequency heating technique. a – starting melting; b – homogenisation of the melt; c – crystal growth process; d – complete crystallisation of the volume of the melt. 1 – walls of the cold container; 2 – inductor; 3 – melt; 4 – cooled bottom; 5 – garnissage; 6 – insulating ring

is placed in the central part of the crucible, for example, Zr or Y. When the process is started, the metal heats up and melts with the formation of an electrically conductive liquid phase that initiates the melting of the batch mixture. In this case, the entire batch mixture is melted, except for the garnissage – a layer 3–5 mm thick near the walls and at the bottom of the water-cooled crucible. If necessary, a batch mixture is added to the melt using a special device. In order to stabilise the melt-garnissage boundary, the melt is usually kept for 0.1–1 hour before the onset of crystallisation. Then, the pulling mechanism is turned on, and the crucible with the melt is vertically lowered from the influential section of the electromagnetic field at a speed of 2–30 mm/h with such a simultaneous decrease in the generator power that the temperature of the residual melt remains within the specified limits. As a result of the synthesis, an ingot of crystals is formed, covered on the outside with a layer of unmelted batch mixture and on top with a glassy crust of the residual melt. Under

mechanical action, the ingot is easily split, with the formation of columnar-shaped fianite crystals. The quality and yield of colourless fianite largely depends on the purity of the batch mixture components. Out of the harmful impurities, SiO₂ should be mentioned. Sometimes in colourless fianite, a slight yellowish tint is observed, which can be removed by annealing the crystals in air at temperatures above 800 °C. Coloured crystals can be synthesised using substandard colourless fianite previously ground into powder, as a component of the batch mixture. This technique is especially effective when obtaining densely coloured crystals and allows reducing the cost of production.

Fianites of various compositions have high refractoriness and chemical resistance. The melting point of fianites is 2600 - 2750 °C. They do not oxidise or evaporate at temperatures above 2500 °C. Fianite is an insulator up to 300 °C, at temperatures above 300 °C it acquires noticeable ionic conductivity. Hardness according to the Mohs hardness scale is 8, microhardness is 14,000–

20,000 MN/m², density 5.5–6 g/cm³, refractive index dispersion 0.059–0.065 [107, 108]. The colour of fianites and their density are determined by the chemical composition. A black colour, close to the colour of morion, is obtained by annealing fianites in a vacuum or by processing with γ -radiation.

Optical lenses, providing a high degree of magnification are made from fianites. This material is promising in the chemical industry for the manufacture of high-temperature heaters operating in oxidising environments. The traditional use of fianites as a raw material for making jewellery is based on their high optical properties, hardness, and various colours of stones (Table 1). Fianite is processed in certain crystallographic directions, when faceted to enhance the “play” of the stone, the upper platform is made large, and the lower part of the stone is increased in height.

The industrial production of fianites for jewellery purposes was started in the USSR in 1972 [9]. A crystalline material similar to fianite, imitating precious stones, is produced abroad under the name cubic zirconia (CZ). The names “diamonesque” (USA), “djevalit” (Switzerland), “zirconia” (Austria) are outdated. The jewellery name “zircon”, which is used in Russia, is not correct. A large amount of fianite-like material

is produced in the countries of south-east Asia (China, Burma, Thailand, Hong Kong). Crystalline materials of emerald green and sapphire blue colour based on ZrO₂ are known on the world market under the trade name “siox”.

At VNIISIMS (the now closed All-Russian Institute for the Synthesis of Mineral Raw Materials) [109], technologies for the synthesis of fianites of various colours, including polychrome crystals, with differently coloured zones within a single crystal were developed. The melting of batch mixtures of various compositions was carried out sequentially in one container, and before the melting of each subsequent composition of the batch mixture, partial crystallisation of the melt of the batch mixture of the previous composition occurred.

7. Partially Stabilised Zirconia

A separate class of materials based on ZrO₂ is the so-called group of partially stabilised zirconia (PSZ) [10, 11]. When an amount of stabiliser, insufficient for the formation of the cubic phase, is introduced into zirconia, a material is formed containing a tetragonal phase, usually, together with a monoclinic or cubic phase. In the ZrO₂–Y₂O₃ system, partially stabilised zirconia is formed from the melt at a content of 2–5 mol. % of yttria [110].

Table 1. The colour range of coloured fianites depending on the introduced chromophore [109]

Chromophore	Content, %	Colour	Imitation of natural stone
Y ³⁺	14–44	Colourless	Diamond
Pr ³⁺	2–20	Dark cherry	Ruby
Ce ⁴⁺	2–20	Red-burgundy	Ruby
Ce ³⁺	0.1–2	Yellow-orange	Padparadscha
Er ³⁺	fifteen	Pink	Vorobyevite
Tb ³⁺	0.01–5	Yellow	Heliodor
Pr ³⁺	0.1–2	Amber	Amber
Cu ²⁺	0.5–2	Dark yellow	Citrine
Ti ⁴⁺	0.1–2	Yellow brown	Hyacinth
Ni ²⁺	0.1–2	Light brown	Topaz
Ho ³⁺	0.1–5	Green yellow	Demantoid
Fe ³⁺	0.01–0.8	Yellow green	Chrysolite
Tm ³⁺	1–5	Pale green	Beryl
Nd ³⁺	0.1–1	Gray green	Grossular
Dy ³⁺	3–5	Salad green	Chrysoprase
Cr ³⁺	0.1–1	Olive	Olivine
Cu ²⁺	0.1–0.5	Light blue	Aquamarine
Co ³⁺	0.01–0.5	Red-violet	Amethyst
Mn ⁴⁺	0.1–1	Brown violet	Sapphire

King and Yavorsky [111] were the first to note that during heating (cooling) in a two-phase sample stabilised with magnesium oxide a reversible $t \rightarrow m$ phase transition occurs, which is accompanied by a change in the stress pattern in grains or around grains and affects the microhardness. Garvey, Hannink, and Pascoe [10] proposed a stress-relief phase transition model, increasing the strength of such materials. Mechanical stresses at the tip of a growing microcrack initiate a phase transition, accompanied by a local increase in volume, and, accordingly, pressures of compressive stresses weaken tensile stresses at the tip of a microcrack, which stabilises the crack, slowing its growth.

The PSZ samples have a thin twinned domain structure, are opaque, characterized by high microhardness (13.5–15.0 GPa) and crack resistance (about 6–13 MPa m^{0.5}). The materials may contain other phases, for example, a mixture of phases t and t' with varying degree of tetragonality ($c/2a$), which is 1.014–1.015 and 1.004–1.005 for t - and t' -phases, respectively, in the ZrO_2 - Sc_2O_3 - Y_2O_3 system [112]. Phase t transforms under load.

By varying the amount of the added stabiliser, it is possible to achieve optical effects that mimic those of natural opal. In particular, opalescent translucent and opaque crystals were synthesised in the ZrO_2 - Y_2O_3 - Gd_2O_3 - Sm_2O_3 system [109]. A similar effect was obtained by E. Polyanskii using the introduction of carbon microimpurities into the melt [109]. These stones are usually polished as cabochons. Opalescent crystals of the corresponding colours can be synthesised by the introduction of different luminophores into ZrO_2 . It is possible to obtain banded opalescent stones, in which there is an alternation of transparent and opalescent layers, as in natural agates and onyx. The formation of such bands is associated with the formation of structurally different layers in the melt.

8. Baddeleyite

The second important mineral of zirconia is baddeleyite (ZrO_2). It was first discovered in 1892 in Sri Lanka and Brazil. It is named after Joseph Baddeley, who described the mineral in Sri Lanka. Baddeleyite is an accessory mineral in carbonatite deposits, where it occurs near

the contact between basic alkaline rocks with limestone. It is characteristic of carbonatites of the Kola Peninsula and Karelia.

It is an ore of zirconium. Also it is used as a raw material for the ceramic industry and in the production of refractories. In Russia it is mined in the Kovdor deposit in Murmansk oblast and it is also mined in Brazil and in South Africa where the largest baddeleyite deposits are located in Phalaborwa. Common impurities are HfO_2 – up to 3 %, Fe_2O_3 – up to 2 %, Sc_2O_3 – up to 1 %.

The baddeleyite crystal system is monoclinic: $C_{2h}^5 - P2_1/c$; lattice parameters: $a = 5.169$, $b = 5.341$, $c = 5.341$ Å; $\beta = 99^\circ 15'$. Crystals are usually twinned and have a lamellar habitus. The crystal structure represents the distorted structure of CaF_2 . Zr is in sevenfold coordination with respect to oxygen atoms, Zr–O distances varie from 2.04 to 2.26 Å. Parallel (100) layers of O atoms, located on the tops of slightly distorted square motifs, alternate with layers in which O atoms form a motif of squares and triangles; in this case, the Zr atoms are located in seven vertex polyhedra formed by the superposition of oxygen layers of both types. The arrangement of the O atoms is almost square in one of the layers is so insignificantly distorted that when rotated by 180° their relative position is almost the same; this explains the frequent twinning of baddeleyite crystals according to (100) [44]. Complex twins are often observed.

The baddeleyite forms oriented intergrowth with pyrochlore, crystals of which grow epitaxially on baddeleyite crystals. It is found in the form of aggregates. Crystals are partly radially fibrous. Baddeleyite has a different colour, it ranges from colourless to iron black. In thin fragments it is translucent. The hardness of baddeleyite is 6.5. Cleavage according to (001) is perfect, according to (010) and (110) it is imperfect.

When heated to 1100–1200 °C, it reversibly transforms into a tetragonal modification (ruffite); the reverse transition occurs at 950–850 °C; the tetragonal modification transition temperature increases in the presence of SnO_2 impurity. At 800 °C it can dissolve up to 10% SnO_2 .

For research purposes, single crystals of baddeleyite can be obtained at temperatures up to 1100 °C by various methods, including hydrothermal crystallisation [113]. When grown

from a solution in a melt, lead fluoride, $\text{Na}_2\text{B}_4\text{O}_7$, $\text{Li}_2\text{Mo}_2\text{O}_7$ [114], or mixtures of alkali metal fluorides with vanadium or boron oxides can be used as flux [109]. Crystals are recovered by dissolving the flux in acid.

ZrO_2 crystallises at a temperature of about 450 °C from an amorphous gel precipitated as a result of treatment of $\text{ZrOCl}_2 \cdot 8\text{H}_2\text{O}$ with ammonia. The exothermic effect of crystallisation corresponds to almost complete dehydration. However, in this case, a metastable tetragonal modification is formed, stabilised by residual water. The transformation into the monoclinic modification is associated with complete dehydration and occurs above 950 °C [115–116]. VNIISIMS [109] developed practically important methods for the synthesis of baddeleyite by the one-stage annealing of amorphous ZrO_2 with the addition of a mineraliser in the air. Depending on the amount of the mineraliser (fluorides of elements of groups II–III of the periodic system), end products with different amounts of impurities are obtained. An admixture of corundum is formed when aluminium fluoride is used as a mineraliser. Powdered baddeleyite is used as a filler in special-purpose rubbers and fluoroplastics for the manufacture of dielectric film materials.

Until recently, technological ceramics were obtained only from synthetic zirconia, and natural baddeleyite was considered unsuitable even for producing refractories due to the structural polymorphism of zirconia. Meanwhile, it is important for Russia to expand the range of products that can be made from baddeleyite. Golovin, Zhigachev et al. (Tambov State University) [8, 117–118] investigated the possibility of neutralising silicon inclusions in baddeleyite and showed the fundamental possibility of synthesising high-quality structural ceramics from the domestic natural zirconia – baddeleyite.

As a result of ultrafine grinding of the purified baddeleyite of the Kovdor mining and processing plant using planetary mill, powders with a characteristic crystallite size less than 20 nm were obtained. Ground baddeleyite contained up to 80 % tetragonal and cubic phases. Thus, the possibility of obtaining zirconia containing metastable tetragonal and cubic phases based on unconventional raw materials was demonstrated.

It is characteristic that the fine grinding of synthetic zirconia led to partial amorphisation of the monoclinic phase, but did not change the phase composition of the powder [119].

The effect of the addition of multilayer carbon nanotubes on the strength and plasticity of ceramics based on baddeleyite, partially stabilized by calcium oxide with the formation of a tetragonal phase, was investigated. It was shown that along with the transformation hardening in the synthesised composites, additional mechanisms of crack deceleration were effectively triggered due to the reinforcing effect of carbon nanotubes. Samples of baddeleyite ceramics modified with carbon nanotubes with high performance characteristics corresponding to the requirements for high-quality ceramics were obtained, synthesised from the traditional imported raw material, synthetic zirconia.

Baddeleyite ceramics are actively used for lining of a glass melting bath due to their chemical and fire resistance properties.

9. Nuclear energetics

Another area for the potential application of materials based on zirconia is inert matrix nuclear fuel (IMF), which is a ceramic nuclear fuel evenly distributed in an inert matrix [120–126]. The benefits of IMF over traditional uranium fuel include the possibility of a more complete use of plutonium, an increase in uranium burn up, the ability to transmute “minor” actinides (Np, Am, Cm), reducing the amount of highly toxic radioactive waste to be buried, and the possibility of burying waste without processing it.

Studies on the creation of IMF were started in the 50–60s in the USA on the basis of ZrO_2 – UO_2 and ZrO_2 – CaO – UO_2 systems. Subsequently, the phase composition of the IMF was adjusted taking into account the requirements imposed on the material of the inert matrix, namely: low neutron capture cross section; high melting temperature (2500–2800 °C); high thermal conductivity; compatibility with a fissile fuel composition and fuel cladding materials; absence of phase transformations and amorphisation in the range of operating temperatures of a nuclear installation; high radiation resistance; high mechanical strength, sufficient elasticity and hardness; low solubility in hot water or other

heat transfer fluids; stability under disposal conditions; acceptable cost.

Ceramics based on stabilised zirconia satisfies most requirements and allows obtaining products with a high density (more than 95 % of theoretical). However, it is characterised by low thermal conductivity. In addition, thermodynamically unstable cubic solid solutions are subjected to phase decomposition under severe operating conditions. A promising option is the use of $Zr_2R_2O_7$ phases with the pyrochlore structure, where R – rare earth elements of the cerium subgroup (see Fig. 5).

10. Conclusion

The manifestation of the main materials science triad: composition – structure – properties with subsequent application, and the important informational role of phase diagrams is revealed can be seen based on the example of ZrO_2 . The phases based on zirconia have such a combination of physicochemical characteristics that make them, in the full sense of the word, polyfunctional materials. The reversible transformation of deformation energy into phase transition energy in a partially stabilised ZrO_2 , providing the

amazing fracture resistance characteristic of this material is unique. The nano-sized domains penetrating these materials and facilitating the implementation of the stress-induced phase transition suggests the role of nanotechnology in materials science. From the point of view of methodology, this indicates the need to supplement the materials science triad with one more variable – dispersity, which was actually proposed by I. V. Tananaev [127].

Heterovalent fluorite solid solutions based on ZrO_2 with a variable number of ions in the unit cell fully combine the features of phases with grossly non-stoichiometry [128], such as the formation of maxima on the melting curves [129], high ionic conductivity combined with low thermal conductivity [27], and the formation of ordered low-temperature phases. By these properties they are similar to fluoride solid solutions formed in MF_2 - RF_3 systems [130].

The stabilisation method of high-temperature modifications by heterovalent isomorphic substitutions, which led to the creation of fianites, was used by us for the stabilisation of α - GdF_3 [131] and α - Na_2SO_4 [132] with the growth of laser single crystals.

Phase equilibria at low temperatures in systems with ZrO_2 are among the unsolved fundamental issues. Since the time of achieving equilibrium, controlled by cationic diffusion, increases exponentially with decreasing temperature [133], the study of low-temperature equilibria is a very difficult and often insoluble problem. Regions for which the time for establishing equilibrium by means of dry sintering is about 1 year can be considered as being low-temperature regions. For systems based on zirconium and hafnium oxides, this is about 1600 °C.

The use of solvents, in particular, the method of hydrothermal synthesis, allowed significantly advance towards the low-temperature region in ZrO_2 - R_2O_3 and ZrO_2 - CeO_2 systems [64, 65, 71]. However, in the ZrO_2 - CaO system such experiments [66] were not enough for the accurate determination of the temperature of the eutectoid [89, 134–135]. Thermodynamic modelling is not always reliable. In particular, the temperature of the eutectoid decomposition of the cubic phase in the ZrO_2 - Y_2O_3 system differs according to the data of different models by hundreds of

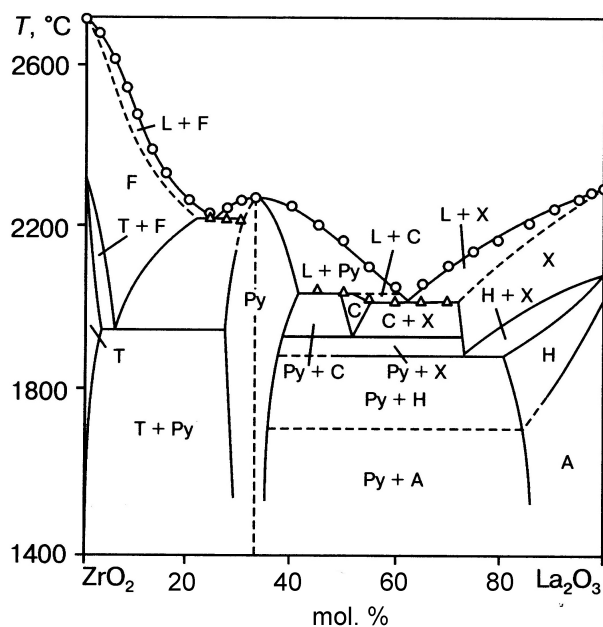


Fig. 5. Phase diagram of ZrO_2 - La_2O_3 system according to [94]. F and C are cubic phases with a fluorite structure, Py is a phase with a pyrochlore structure with an idealised composition $Zr_2La_2O_7$, T – solid solution based on the tetragonal modification of ZrO_2 , A, H, X – solid solutions based on various modifications of La_2O_3

degrees [68, 69, 136], and in [47] it was below absolute zero, which contradicts the third law of thermodynamics. It can be expected that the use of salt melts will allow making progress in this matter.

It can be stated that we have a very poor idea of the formation of ordered phases in systems with ZrO_2 , their compositions, structures, regions of stability, and their relationships with disordered solid solutions. This is clearly seen in the example of the results of studies of ZrO_2 –CaO, ZrO_2 – Sc_2O_3 systems. As Bevan rightly emphasised in 1970 [77], we do not know the true structure and compositions of the ordered phases, since the cation lattice in the studied samples shows no signs of ordering. While the anionic sublattice is in the process of ordering, the cationic sublattice is delayed due to the extremely slow cationic diffusion. Despite the active research and accumulated results over the past 50 years, this statement remains true. It can be assumed that the precursors of low-temperature orderly phases are non-equilibrium phases t' and t'' , systematically appearing in PSZ samples. It should be noted that in Ce_2O_3 – CeO_2 system, where ordering is determined only by anionic diffusion, a whole homologous series of ordered phases has been revealed [137]. Similar phenomena should be looked for in ZrO_2 – R_2O_3 systems. The ZrO_2 – In_2O_3 system is of interest from the point of view of searching for ordered phases [138–139], since indium oxide is a crystallochemical low-melting analogue of scandia.

The nature of phase transformations in low-temperature regions of systems with ZrO_2 is traditionally interpreted through the concept of metastable equilibria [71]. However, it is quite possible that the corresponding samples are not in a metastable state, but in a labile state, the escape from which is extremely slow. The practical possibility of using materials in a labile state violates one of the postulates of chemical thermodynamics [140].

According to the third law of thermodynamics, a decrease in temperature leads to a decrease in entropy, a decrease in the concentration of defects, and decomposition of solid solutions, thus the low-temperature region can be a source of new ordered phases, stoichiometric or close to them compositions, which can become the basis for new functional materials.

Author contributions

The authors made an equal contribution to the preparation of the review.

Conflict of interests

The authors declare that they have no known competing financial interests or personal relationships that could have influenced the work reported in this paper.

References

1. Sabbarao E. C. Zirconia - an overview. In: *Proc. First Int Conf.: Science and Technology of Zirconia*. Cleveland: Ohio; 1981. P. 1–24.
2. Atterer M., Balters H., Banse H., et. al. Zirconium. *Gmelin Handbook of Inorganic Chemistry*. Teil 42. Berlin: Springer; 1958.
3. Blumental W. B. *The chemical behavior of zirconium*. N.-Y.: Princeton, D. Van Nostrand Comp., Inc., N.J.; 1958.
4. Korovin S. S., Zimina G. V., Reznik A. M., Bukin V. I., Korniyushko V. F. / Ed. Korovin S. S. *Redkie i rasseyannyye elementy. Khimiya i tekhnologiya. T. 1*. [Rare and scattered elements. Chemistry and technology. Vol. 1]. Moscow: MISIS publ.; 1996. 376 p. (In Russ.)
5. Rakov E. G. *Tsirkonii. Khimicheskaya entsiklopediya v 5 t.* [Zirconium. Chemical encyclopedia in 5 volumes. Zefirov N. S. (ed.)]. Moscow: Bol'shaya Rossiiskaya entsiklopediya Publ.; 1998(5). p. 384–783. (In Russ.)
6. Nielsen R. *Zirconium and zirconium compounds*. Weinheim Germany: Wiley-VCH; 2000. https://doi.org/10.1002/14356007.a28_543.pub2
7. *Oksidy titana, tseriya, tsirkoniya, ittriya, alyuminiya. Svoystva, primeneniye i metody polucheniya* [Oxides of titanium, cerium, zirconium, yttrium, aluminum. Properties, application and methods of obtaining]. Novosibirsk: Izd-vo SO RAN Publ.; 2010. 246 p. (In Russ.)
8. Zhigachev A. O., Golovin Yu. I., Umrikhin A. V., Korenkov V. V., Tyurin A. I., Rodaev V. V., D'yachek T. A. *Keramicheskie materialy na osnove dioksida tsirkoniya* [Ceramic materials based on zirconium dioxide]. Golovin Yu. I. M. (ed.). Moscow: Tekhnosfera publ.; 2018. 357 p. (In Russ.)
9. Osiko V. V., Borik M. A., Lomonova E. E. Crucible-free methods of growing oxide crystals from the melt. *Annual Review of Materials Science*. 1987;17: 101–122. <https://doi.org/10.1146/annurev.ms.17.080187.000533>
10. Garvie R. C., Hannink R. H. J., Pascoe R. T. Ceramic Steel? *Nature*. 1975;258(5537): 703–704. <https://doi.org/10.1038/258703a0>
11. Osiko V. V., Borik M. A., Lomonova E. E. Synthesis of refractory materials by skull melting. In: *Springer Handbook of Crystal Growth*. N.Y.: Springer; 2010. p. 433–477. https://doi.org/10.1007/978-3-540-74761-1_14

12. Stevens R. Engineering properties of zirconia. In: *Engineered Materials. Handbook, ASM International, Ceramics and Glasses*. 1991;4: 775–786.
13. Bocanegra-Bernal M. H., de la Torre S. D. Phase transitions in zirconium dioxide and related materials for high performance engineering ceramics. *Journal of Materials Science*. 2002;37(23): 4947–4971. <https://doi.org/10.1023/a:1021099308957>
14. Boch P., Niepce J. C. *Ceramic materials: processes, properties and applications*. (eds.) ISTE Ltd; 2007. 573 p. <https://doi.org/10.1002/9780470612415>
15. Geodakyan D. A., Kostanyan A. K., Geokchyan O. K., Geodakyan K. D. Zirconium dioxide heat-resistant compositions. *Refractories and Technicals Ceramics*. 2010;6: 11–16. Available at: <https://www.elibrary.ru/item.asp?id=15483557> (In Russ., abstract in Eng.)
16. Kablov E. N., Grashchenkov D. V., Isaeva N. V., Solntsev S. S. Perspektivnye vysokotemperaturnye keramicheskie kompozitsionnye materialy [Promising high-temperature ceramic composite materials]. *Rossiiskii khimicheskii zhurnal*. 2010;54(1): 20–24. Available at: <https://www.elibrary.ru/item.asp?id=14307270> (In Russ.)
17. Kablov E. N. Strategic areas of developing materials and their processing for the period up to 2030. *Aviation Materials and Technologies*. 2012;S: 7–17. Available at: <https://elibrary.ru/item.asp?id=18084815> (In Russ., abstract in Eng.)
18. Golovin Yu. I., Korenkov V. V., Razlivalova S. S., Rodaev V. V. Physicomechanical properties of porous zirconia ceramics. *Russian Metallurgy (Metally)*. 2018;10: 961–967. <https://doi.org/10.1134/s0036029518100063>
19. Primachenko V. V., Martynenko V. V., Szulik I. G., Kushchenko I. A. Vysokoogneupornye tigly iz stabilizirovannogo dioksida tsirkoniya dlya induktsionnoi plavki metallov platinovoi gruppy, izgotovlennye metodom vibrolit'ya [Highly refractory crucibles made of stabilized zirconium dioxide for induction melting of platinum group metals, manufactured by vibrocasting] *Litiyo i Metallurgiya (Foundry Production and Metallurgy)* 2012;3(66): 166–168. Available at: <https://www.elibrary.ru/item.asp?id=21801425> (In Russ.)
20. Zimichev A. M., Solovjeva E. P. Zirconia fiber high temperature application (Review). *Aviation Materials and Technologies*. 2014;3: 55–61. Available at: <https://www.elibrary.ru/item.asp?id=21875161> (In Russ., abstract in Eng.)
21. Akishin A. I. *Effects of space conditions on materials*. N.-Y.: Nova Science Publ.; 2001. 199 p.
22. Kelly J. R., Denry I. Stabilized zirconia as a structural ceramics: An overview. *Dental Materials*. 2008;24(3): 289–298. <https://doi.org/10.1016/j.dental.2007.05.005>
23. Manicone P. F., Iommetti P. R., Raffaelli L. An overview of zirconia ceramics: Basic properties and clinical applications. *Journal of Dentistry*. 2007;35(11): 819–826. <https://doi.org/10.1016/j.jdent.2007.07.008>
24. Goodenough J. B. Oxide-ion electrolytes. *Annual Review of Materials Research*. 2003;33(1): 91–128. <https://doi.org/10.1146/annurev.matsci.33.022802.091651>
25. Kendall K. Progress in solid oxide fuel cell materials. *International Materials Reviews*. 2005;50(5): 257–264. <https://doi.org/10.1179/174328005x41131>
26. Fergus J. F. Electrolytes for solid oxide fuel cells. *Journal of Power Sources*. 2006;162(1): 30–40. <https://doi.org/10.1016/j.jpowsour.2006.06.062>
27. Fedorov P. P., Popov P. A. Printsip ekvivalentnosti istochnikov besporyadka i teploprovodnost' tverdykh tel [The principle of equivalence of sources of disorder and the thermal conductivity of solids]. *Nanosystems: Physics, Chemistry, Mathematics*. 2013;4(1):148–159. Available at: <https://www.elibrary.ru/item.asp?id=18964066> (In Russ.)
28. Wu J., Wei X., Pature N. P., Klemens P. G., Gell M., García E., Miranzo P., Osendi M. I. Low-thermal-conductivity rare-earth zirconates for potential thermal-barrier-coating applications. *Journal of the American Ceramic Society*. 2002;85(12): 3031–3035. <https://doi.org/10.1111/j.1151-2916.2002.tb00574.x>
29. Schulz U., Leyens C., Fritscher K., Peters M., Saruhan-Brings B., Lavigne O., Dorvaux J.-M., Poulain M., Mévrel R., Caliez M. Some recent trends in research and technology of advanced thermal barrier coatings. *Aerospace Science and Technology*. 2003;7(1): 73–80. [https://doi.org/10.1016/s1270-9638\(02\)00003-2](https://doi.org/10.1016/s1270-9638(02)00003-2)
30. Solntsev S. S. Erosion and moisture resistant thermoregulating coatings for thermal protection system of “Buran” reusable spaceship. *Aviation Materials and Technologies*. 2013;S1: 94–124. Available at: <https://www.elibrary.ru/item.asp?id=20423927>
31. Okovity V. A., Panteleenko F. I., Okovity V. V., Astashinsky V. M., Uglov V. V., Chimanskiy V. I., Cerenda N. N. Formation and investigation of plasma powder coatings made of oxide ceramics modified with high-energy effects. *Science & Technique*. 2018;17(5): 378–389. <https://doi.org/10.21122/2227-1031-2018-17-5-378-389> (In Russ.)
32. Al'myasheva O. V., Vlasov E. A., Khabenskii V. B., Gusarov V. V. Thermal stability and catalytic properties of the composite amorphous Al₂O₃-nanocrystals ZrO₂. *Russian Journal of Applied Chemistry*. 2009;82(2): 217–221. <https://doi.org/10.1134/s1070427209020104>
33. Artemov S. A., Borik M. A., Volkova T. V., Gerasimov M. V., Kulebyakin A. V., Lomonova E. E., Milovich F. O., Myzina V. A., Ryabochkina P. A., Tabachkova N. Y. Influence of growth and heat treatment conditions on lasing properties of ZrO₂-Y₂O₃-Ho₂O₃ crystals. *Optical Materials*. 2020;99: 109611. <https://doi.org/10.1016/j.optmat.2019.109611>
34. Dresvyannikov A. F., Petrova E. V., Khayrullina A. I. Production technology of binary aluminum and zirconium oxide systems. *Khimicheskaya Tekhnologiya*. 2017;18(8): 367–376. Available at:

<https://www.elibrary.ru/item.asp?id=29867439> (In Russ., abstract in Eng.)

35. Dzyaz'ko Y. S., Belyakov V. N., Stefanyak N. V., Vasilyuk S. L. Anion-exchange properties of composite ceramic membranes containing hydrated zirconium dioxide. *Russian Journal of Applied Chemistry*. 2006;79(5): 769–773. <https://doi.org/10.1134/s1070427206050132>

36. Almjashv V. I., Barrachin M., Bechta S.V., Bottomley D., Defoort F., Fischer M., Gusarov V. V., Hellmann S., Khabensky V. B., Krushinov E. V., Lopukh D. B., Mezentseva L. P., Miassoedov A., Petrov Yu. B., Vitol S. A. Eutectic crystallization in the $\text{FeO}_{1.5}\text{-UO}_{2+x}\text{-ZrO}_2$ system. *Journal of Nuclear Materials*. 2009;389(1): 52–56. <https://doi.org/10.1016/j.jnucmat.2009.01.006>

37. Shidenkenni T. Y. Formation of unstabilized and yttria stabilized ZrO_2 fibers from a suspension of monodispersed ZrO_2 . *Journal of the Ceramic Society of Japan*. 2006;114(1331): 590–593. <https://doi.org/10.2109/jcersj.114.590>

38. Korenkov V. V., Rodaev V. V., Shuklinov A. V., Stolyarov R. A., Zhigachev A. O., Tyurin A. I., Lovtsov A. R., Razlivalova S. S. Synthesis and properties of multifunctional ceramic nano-fibers using electro-spun. *Tambov University Reports. Series: Natural and Technical Sciences*. 2013;18(6-2): 3156–3159. Available at: <https://www.elibrary.ru/item.asp?id=21106136> (In Russ., abstract in Eng.)

39. Shabanova N. A., Popov V. V., Sarkisov P. D. *Khimiya i tekhnologiya nanodispersnykh oksidov* [Chemistry and technology of nanodispersed oxides]. Moscow: Akademkniga Publ.; 2006. 309 p. (In Russ.)

40. Ivanov Yu. F., Tumanov Yu. M., Dedov N. V., Khasanov O. L. Structure and phase composition of nanostructured powder on the base of zirconium dioxide synthesized by plasmachemical method. *Physics and Chemistry of Materials Treatment*. 2012;5: 37–45. Available at: <https://www.elibrary.ru/item.asp?id=18053701> (In Russ., abstract in Eng.)

41. Pozhidaeva O. V., Korytkova E. N., Romanov D. P., Gusarov V. V. Formation ZrO_2 nanocrystals in hydrothermal media of various chemical composition. *Russian Journal of General Chemistry*. 2002;72(6): 849–853. <https://doi.org/10.1023/A:1020409702215>

42. Al'myasheva O. V., Ugolkova V. L., Gusarov V. V. Thermochemical analysis of desorption and adsorption of water on the surface of zirconium dioxide nanoparticles. *Russian Journal of Applied Chemistry*. 2008;81(4): 609–613. <https://doi.org/10.1134/s1070427208040071>

43. *Geologicheskii slovar': v 2-kh tomakh* [Geological Dictionary: in 2 vol.]. K. N. Paffengol'ts, et al. (eds.). Moscow: Nedra Publ.; 1978. (In Russ.)

44. Belov N. V. Kristallicheskaya struktura baddeleyita (monoklinnoi ZrO_2). *Kristallografiya* [Crystal structure of baddeleyite (monoclinic ZrO_2). Crystallography]. 1960;5(3): 460–461. (In Russ.)

45. Smith D. K., Newkirk H. W. The crystal structure of baddeleyite (monoclinic ZrO_2) and its relation to the polymorphism of ZrO_2 . *Acta Crystallographica*. 1965;18(6): 983–991. <https://doi.org/10.1107/s0365110x65002402>

46. French R. H., Glass S. J., Ohuchi F. S., Xu Y.-N., Ching W. Y. Experimental and theoretical studies on the electronic structure and optical properties of three phases of ZrO_2 . *Physical Review B*. 1994;49(8): 5133–5142. <https://doi.org/10.1103/physrevb.49.5133>

47. Chen M., Hallstedt B., Gauckler L. J. Thermodynamic modeling of the $\text{ZrO}_2\text{-YO}_{1.5}$ system. *Solid State Ionics*. 2004;170(3-4): 255–274. <https://doi.org/10.1016/j.ssi.2004.02.017>

48. Haines J., Leger J.M., Atouf A. Crystal structure and equation of state of cotunnite-type zirconia. *Journal of the American Ceramic Society*. 1995;78(2): 445–448. <https://doi.org/10.1111/j.1151-2916.1995.tb08822.x>

49. Gorelov V. P. High-temperature phase transitions in ZrO_2 . *Physics of the Solid State*. 2019;61:1288–1293. <https://doi.org/10.1134/S1063783419070096>

50. Chevalier J., Gremillard L., Virkar A. V., Clarke D. R. The tetragonal monoclinic transformation in zirconia: lessons learned and future trends. *Journal of the American Ceramic Society*. 2009;92(9): 1901–1920. <https://doi.org/10.1111/j.1551-2916.2009.03278.x>

51. Ashraf S., Irfan M., Kim D., Jang J.-H., Han W.-T., Jho Y.-D. Optical influence of annealing in nano and submicron-scale ZrO_2 powders. *Ceramics International*. 2014;40(6): 8513–8518. <https://doi.org/10.1016/j.ceramint.2014.01.063>

52. Ivanov V. K., Kopitsa G. P., Baranchikov A. Ye., Sharp M., Pranzas K., Grigiriev S. V. Mesostructure, fractal properties and thermal decomposition of hydroxys zirconia and hafnia. *Russian Journal of Inorganic Chemistry*. 2009;54(15): 2091–2106. <https://doi.org/10.1134/s0036023609140022>

53. Al'myasheva O. V., Fedorov B. A., Smirnov A. V., Gusarov V. V. Razmer, morfologiya i struktura chastits nanoporoshka dioksida tsirkoniya, poluchennogo v gidrotermal'nykh usloviyakh [Size, morphology and structure of particles of zirconium dioxide nanopowder obtained under hydrothermal conditions]. *Nanosystems: Physics, Chemistry, Mathematics*. 2010;1(1): 26–36. Available at: <https://www.elibrary.ru/item.asp?id=15648758> (In Russ.)

54. Lyamina G. V., Ilela A. E., Kachaev A. A., Dalbanbai A., Kolosov P. V., Cheprasova M. Nanopowders of aluminum oxide and zirconium from solutions of their salts by spray drying. *Butlerov Communications*. 2013;33(2): 119–123. Available at: <https://www.elibrary.ru/item.asp?id=18938977> (In Russ., abstract in Eng.)

55. Smorokov A. A., Kraydenko R. I. Poluchenie dioksida tsirkoniya s ispol'zovaniem ftoridov ammoniya [Obtaining zirconium dioxide using

- ammonium fluorides. *Polzunovskiy Vestnik*. 2017;3: 126–130. Available at: <https://www.elibrary.ru/item.asp?id=30502289> (In Russ.)
56. Veselova V. O., Yurlov I. A., Ryabochkina P. A., Belova O. V., Dudkina T. D., Egorysheva A. V. Synthesis and luminescent properties of nanocrystalline $(1-x)$ $ZrO_{2-x}Er_2O_3$ ($x = 0.015-0.5$) solid solutions. *Russian Journal of Inorganic Chemistry*. 2020;65(9):1298–1303. <https://doi.org/10.1134/s0036023620090211>
57. Oliveira A. P., Torem M. L. Influence of some precipitant variables on thermal behavior of $ZrO_2-Y_2O_3$ and ZrO_2-CeO_2 precipitated gels. *Journal of Materials Science*. 2000;35: 667–672. <https://doi.org/10.1023/a:1004796931837>
58. Smirnov A. V., Fedorov B. A., Tomkovich M. V., Almyasheva O. V., Gusarov V. V. Nanochastitsy so stroeniem “yadro-obolochka”, formiruyushchiesya v sisteme $ZrO_2-Gd_2O_3-H_2O$ v gidrotermal'nykh usloviyakh [Nanoparticles with a “core-shell” structure formed in the $ZrO_2-Gd_2O_3-H_2O$ system in hydrothermal conditions]. *Doklady Akademii Nauk*. 2014; 456 (2): 171–173. <https://doi.org/10.7868/s0869565214140138> (In Russ.)
59. Asadi S., Abdizadeh H., Vahidshad Y. Effect of crystalline size on the structure of copper doped zirconia nanoparticles synthesized via sol-gel. *Journal of Nanostructures*. 2012;2(2): 205–212. <https://doi.org/10.7508/JNS.2012.02.008>
60. Kicio H., Komameni S., Roy R. Preparation of $La_2Zr_2O_7$ by sol-gel route. *Journal of the American Ceramic Society*. 1991;74(2): 422–424. <https://doi.org/10.1111/j.1151-2916.1991.tb06899.x>
61. Nandi C., Jain D., Grover V., Krishnan K., Banerjee J., Prakash A., Khan K. B., Tyagi A. K. $ZrO_2-NdO_{1.5}$ system: Investigations of phase relation and thermophysical properties. *Materials & Design*. 2017;121: 101–108. <https://doi.org/10.1016/j.matdes.2017.02.030>
62. Zhukov A. V., Min T., Chizhevskaya S. V., Merkushev A. O. The obtaining of zirconia nanopowders. *Advances in Chemistry and Chemical Technology*. 2013;27(6): 33–37. Available at: <https://www.elibrary.ru/item.asp?id=20382880> (In Russ., abstract in Eng.)
63. Abdala P. M., Craievich A. F., Fantini M. C. A., Temperini M. L. A., Lamas D. G. Metastable phase diagram of nanocrystalline $ZrO_2-Sc_2O_3$ solid solutions. *The Journal of Physical Chemistry C*. 2009;113(13): 18661–18666. <https://doi.org/10.1021/jp904584e>
64. Somiya Sh., Yashima M., Kakihana M., Yoshimura M. Revised phase diagram of the system ZrO_2-CeO_2 below 1400 C. *Journal of the American Ceramic Society*. 1983;66(7): 506–510. <https://doi.org/10.1111/j.1151-2916.1983.tb10591.x>
65. Thomson J. B., Armstrong A. R., Bruce P. G. An oxygen-rich pyrochlore with fluorite composition. *Journal of Solid State Chemistry*. 1999;148(1): 56–62. <https://doi.org/10.1006/jssc.1999.8347>
66. Stubican V. S., Ray S. P. Phase equilibria and ordering in the system ZrO_2-CaO . *Journal of the American Ceramic Society*. 1977;60(11-12): 534–537. <https://doi.org/10.1111/j.1151-2916.1977.tb14100.x>
67. Stubican V. S., Hink R. C., Ray S. P. Phase equilibria and ordering in the system $ZrO_2-Y_2O_3$. *Journal of the American Ceramic Society*. 1978;61(1-2): 17–21. <https://doi.org/10.1111/j.1151-2916.1978.tb09220.x>
68. Degtyarev S. A., Voronin G. F. Raschet fazovoi diagrammy v sisteme $ZrO_2-Y_2O_3$ [Calculation of the phase diagram in the $ZrO_2-Y_2O_3$ system]. *Russian Journal of Physical Chemistry A*. 1987; 61(3): 617–622. 9 (In Russ.)
69. Du Y., Jin Z., Huang P. Thermodynamic assessment of the $ZrO_2-YO_{1.5}$ system. *Journal of the American Ceramic Society*. 1991;74(7): 1569–1577. <https://doi.org/10.1111/j.1151-2916.1991.tb07142.x>
70. Andrievskaya E. R. Fazovye ravnovesiya v sistemakh oksidov gafniya, tsirkoniya, itriya s oksidami redkozemel'nykh elementov [Phase equilibria in systems of oxides of hafnium, zirconium, yttrium with oxides of rare earth elements]. Kiev: Naukova Dumka Publ.; 2010. 471 p.
71. Yashima M., Kakihana M., Yoshimura M. Metastable-stable phase diagrams in the zirconia-containing systems utilized in solid-oxide fuel cell application. *Solid State Ionics*. 1996;86-88: 1131–1149. [https://doi.org/10.1016/0167-2738\(96\)00386-4](https://doi.org/10.1016/0167-2738(96)00386-4)
72. Borik M. A., Bredikhin S. I., Bublik V.T., et al. Structure and conductivity of yttria and scandia-doped zirconia crystals grown by skull melting. *Journal of the American Ceramic Society*. 2017;100(1-12): 5536–5547. <https://doi.org/10.1111/jace.15074>
73. Fujimori H., Yashima M., Kakihana M., Yoshimura M. Structural changes of scandia-doped zirconia solid solutions: Rietveld analysis and Raman scattering. *Journal of the American Ceramic Society*. 1998;81(110): 2885–2893. <https://doi.org/10.1111/j.1151-2916.1998.tb02710.x>
74. Arachi Y. High-temperature structure of Sc_2O_3 -doped ZrO_2 . *Solid State Ionics*. 2004;175(1-4): 119–121. <https://doi.org/10.1016/j.ssi.2004.09.025>
75. Liu Z.-G., Ouyang J.-H., Wang B.-H., Zhou Y., Li J. Preparation and thermophysical properties of $Nd_xZr_{1-x}O_{2-x/2}$ ($x = 0.1, 0.2, 0.3, 0.4, 0.5$) ceramics. *Journal of Alloys and Compounds*. 2008;466: 39–44. <https://doi.org/10.1016/j.jallcom.2007.11.147>
76. Pascual C., Duran P. Subsolvus Phase Equilibria and ordering in the system $ZrO_2-Y_2O_3$. *Journal of the American Ceramic Society*. 1983;66(1): 23–28. <https://doi.org/10.1111/j.1151-2916.1983.tb09961.x>
77. Thornber M. R., Bevan D. J. M., Summerville E. Mixed oxides of the type MO_2 fluorite- M_2O_3 . V. Phase studies in the systems $ZrO_2-M_2O_3$ ($M = Sc, Yb, Er, Dy$). *Journal of Solid State Chemistry*. 1970;1(3-4): 545–553. [https://doi.org/10.1016/0022-4596\(70\)90140-4](https://doi.org/10.1016/0022-4596(70)90140-4)
78. Spiridonov F. M., Popova L. N., Popilskii R. Ya. On the phase relations and the electrical conductivity in the

system ZrO_2 - Sc_2O_3 . *Solid State Ionics*. 1970;2(3): 430–438. [https://doi.org/10.1016/0022-4596\(70\)90102-7](https://doi.org/10.1016/0022-4596(70)90102-7)

79. Ruh R., Garrett H. J., Domagala R. F., Patel V. A. The system zirconia-scandia. *Journal of the American Ceramic Society*. 1977;60(9-10): 399–403. <https://doi.org/10.1111/j.1151-2916.1977.tb15521.x>

80. Shevchenko A. V., Maister I. M., Lopato L. M. Vzaimodeistvie v sistemakh HfO_2 - Sc_2O_3 and ZrO_2 - Sc_2O_3 pri vysokikh temperaturakh [Interaction in the systems HfO_2 - Sc_2O_3 and ZrO_2 - Sc_2O_3 at high temperatures]. *Izvestiya Akademii nauk SSSR. Neorganicheskie materialy (Inorganic Materials)*. 1987;23: 1320–1324. (In Russ.)

81. Zyryn A. V., Red'ko V. P., Lopato L. M., Shevchenko A. V., Maister I. M., Zaitseva Z. A. Uporyadochennyye fazy v sistemakh ZrO_2 - Sc_2O_3 i HfO_2 - Sc_2O_3 [Ordered phases in ZrO_2 - Sc_2O_3 and HfO_2 - Sc_2O_3 systems]. *Izvestiya Akademii nauk SSSR. Neorganicheskie Mmaterialy (Inorganic Materials)*. 1987;23: 1325–1329. (In Russ.)

82. Sheu T.-S., Xu J., Tien T.-Y. Phase relationships in the ZrO_2 - Sc_2O_3 and ZrO_2 - In_2O_3 systems. *Journal of the American Ceramic Society*. 1993;76(8): 2027–2032. <https://doi.org/10.1111/j.1151-2916.1993.tb08328.x>

83. Hirano M., Kato E. Transformation of Sc_2O_3 -doped tetragonal zirconia polycrystals by aging under hydrothermal conditions. *Journal of Materials Science*. 1999;34(6): 1399–1405. <https://doi.org/10.1023/A:1004583023044>

84. Fujimori H., Yashima M., Kakihana M., Yoshimura M. β -cubic phase transition of scandia-doped zirconia solid solution: Calorimetry, x-ray diffraction, and Raman scattering. *Journal of Applied Physics*. 2002;91(10): 6493–6498. <https://doi.org/10.1063/1.1471576>

85. Du K., Kim C.-H., Heuer A. H., Goettler R., Liu Zh. Structural evolution and electrical properties of Sc_2O_3 -stabilized ZrO_2 -aged at 850 C in air and wet-forming gas ambient. *Journal of the American Ceramic Society*. 2008;91(5): 1626–1633. <https://doi.org/10.1111/j.1551-2916.2007.02138.x>

86. Borik M. A., Bredikhin S. I., Kulebyakin A. V., Kuritsyna I. E., Lomonova E. E., Milovich F. O., Myzina V. A., Osiko V. V., Panov V. A., Ryabochkina P. A., Seryakov S. V., Tabachkova N. Yu. Melt growth, structure and properties of $(ZrO_2)_{1-x}(Sc_2O_3)_x$ solid solution crystals. *Journal of Crystal Growth*. 2016;443: 54–61. <https://doi.org/10.1016/j.jcrysgro.2016.03.004>

87. Agarkov D. A., Borik M. A., Volkova T. V., Eliseeva G. A., Kulebyakin A. V., Larina N. A., Lomonova E. E., Myzina V. A., Ryabochkina P. A., Tabachkova N. Yu. Phase composition and local structure of scandia and yttria stabilized zirconia solid solution. *Journal of Luminescence*. 2020;222: 117170. <https://doi.org/10.1016/j.jlumin.2020.117170>

88. Guo X., Schober T. Water incorporation in tetragonal zirconia. *Journal of the American Ceramic Society*. 2004;87(4): 746–748. <https://doi.org/10.1111/j.1551-2916.2004.00746.x>

89. Serena S., Sainz M. A. de Aza S., Caballero A. Thermodynamic assessment of the system ZrO_2 -CaO-MgO using new experimental results: Calculation of the isoplethal section MgO-CaO- ZrO_2 . *Journal of the European Ceramic Society*. 2005;25(5): 681–694. <https://doi.org/10.1016/j.jeurceramsoc.2004.02.011>

90. Guo X. Property degradation of tetragonal zirconia induced by low-temperature defect reaction with water molecules. *Chemistry of Materials*. 2004;16(21): 3988–3994. <https://doi.org/10.1021/cm040167h>

91. Fujimori H., Yashima M., Kakihana M., Yoshimura M. Beta-cubic phase transition of scandia-doped zirconia solid solution calorimetry, X-ray diffraction, and Raman scattering. *Journal of Applied Physics*. 2002;91: 6493–6498. <https://doi.org/10.1063/1.1471576>

92. Hirano M., Kato E. Transformation of Sc_2O_3 -doped tetragonal zirconia polycrystals by aging under hydrothermal conditions. *Journal of Materials Science*. 1999;34: 1399–1405. <https://doi.org/10.1023/A:1004583023044>

93. Haering C., Roosen A., Schichl H., Schnoller M. Degradation of the electrical conductivity in stabilized zirconia system. Part. II: Scandia-stabilized zirconia. *Solid State Ionics*. 2005;176(3-4): 261–268. <https://doi.org/10.1016/j.ssi.2004.07.039>

94. Rouanet A. Contribution a l'etude des systems zircon-oxydes des lanthanides au voisinage fe la fusion. *Rev. Int. Hautes et Refract*. 1971;8: 161–180.

95. Noguchi T., Mizuno M., Yamada T. The liquidus curve of the ZrO_2 - Y_2O_3 system as measured by a solar furnace. *Bull. Chem. Soc. Japan*. 1970;43(8): 2614–2616. <https://doi.org/10.1246/bcsj.43.2614>

96. Almashev V. I., Barrachin M., Bechta S. V., Bottomley D., Defoort F., Fischer M., Gusarov V. V., Hellmann S., Khabensky V. B., Lopukh D. B., Mezentsseva L. P., Miassoedov A., Petrov Yu. B., Vitol S. A. Phase equilibria in the FeO_{1+x} - UO_2 - ZrO_2 system in the FeO_{1+x} -enriched domain. *Journal Nuclear Materials*. 2010;400(2): 119–126. <https://doi.org/10.1016/j.jnucmat.2010.02.020>

97. Sakka Y., Oishi Y., Ando K. Zr-Hf interdiffusion in polycrystalline Y_2O_3 - $(Zr+Hf)O_2$. *Journal of Materials Science*. 1982;17(11): 3101–3105. <https://doi.org/10.1007/BF01203471>

98. Sazonova L. V., Glushkova V. G., Krzhizhanovskaya V. A. Sintez tsirkonatov neodima i prazeodima [Synthesis of neodymium and praseodymium zirconates]. *Izvestiya Akademii nauk SSSR. Neorganicheskie materialy (Inorganic Materials)*. 1990;26(9): 1630–1633. (In Russ.)

99. Duran P. The system erbia- zirconia. *Journal of the American Ceramic Society*. 1977;60(11-12): 510–513. <https://doi.org/10.1111/j.1151-2916.1977.tb14095.x>

100. Yashima M., Ishizawa N., Nama T., Yoshimura M. Stable and metastable phase relationships in the system ZrO_2 - $ErO_{1.5}$. *Journal of the American Ceramic Society*. 1991;74(3): 510–513. <https://doi.org/10.1111/j.1151-2916.1991.tb04052.x>

101. Aleksandrov V. I., Voron'ko Yu. K., Ignat'ev B. V., Lomonova E. E., Osiko V. V., Sobol' A. A. Issledovanie strukturnykh prevrashcheniei v tverdykh rastvorakh na sonove dvoukisi tsirkoniya i gafniya metodom kombinatsionnogo rasseyaniya seta [Investigation of structural transformations in solid solutions based on zirconium dioxide and hafnium by the method of Raman set scattering]. *Physics of the Solid State*. 1978;20(2): 528–534. (In Russ.)
102. Voronko Y. K., Sobol A. A., Shukshin V. E. Monoclinic-tetragonal phase transition in zirconium and hafnium dioxides: A high-temperature Raman scattering investigation. *Physics of the Solid State*. 2007;49: 1963–1968. <https://doi.org/10.1134/S1063783407100253>
103. Agarkov D. A., Borik M. A., Korableva G. M. et al. Effect of heat treatment on the thermal conductivity of single crystals of ZrO₂-based solid solutions stabilized with scandium and yttrium oxides. *Physics of the Solid State*. 2020;62: 2357–2364 <https://doi.org/10.1134/S1063783420120021>
104. Vasilevskaya A., Almjasheva O. V., Gusarov V. V. Peculiarities of structural transformations in zirconia nanocrystals. *Journal of Nanoparticle Research*. 2016;18: 188. <https://doi.org/10.1007/s11051-016-3494-y>
105. Popov P. A., Solomennik V. D., Lomonova E. E. et al. Thermal conductivity of single-crystal ZrO₂-Y₂O₃ solid solutions in the temperature range 50–300 K. *Physics of the Solid State*. 2012;54: 658–661. <https://doi.org/10.1134/S1063783412030250>
106. Borik M. A., Volkova T. V., Kulebyakin A. V. et al. Thermal conductivity of cubic ZrO₂ single crystals stabilized with yttrium oxide. *Physics of the Solid State*. 2020;62: 235–239. <https://doi.org/10.1134/S1063783420010072>
107. Kuz'minov Yu. S., Lomonova E. G., Osiko V. V. *Tugoplavkie materialy iz kholodnogo tiglya* [Refractory materials from a cold crucible]. Moscow: Nauka Publ.; 2004. 372 p. (In Russ.)
108. Kornilov N. I., Solodova Yu. P. *Yuvelirnye kamni* [Jewelry stones]. Moscow: Nedra Publ.; 1986. 282 p. (In Russ.)
109. Golenko V. P., Polyanskii E. V., Yarotskaya E. G., Yarotskii V. G. *Baddeleit i flyurit. Sintez mineralov* [Baddeleyite and fluorite. Synthesis of minerals.]. Aleksandrov: VNIISIMS Publ.; 2000(2). 136–141. (In Russ.)
110. Borik M. A., Lomonova E. E., Osiko V. V., Panov V. A., Porodnikov O. E., Vishnyakova M. A., Voron'ko Yu. K. Voronov V. V. Partially stabilized single crystals: growth from the melt and investigation of the properties. *Journal of Crystal Growth*. 2005;275(1-2): e2173–e2179. <https://doi.org/10.1016/j.jcrysgro.2004.11.244>
111. King A. G., Yavorsky P. J. Stress relief mechanisms in magnesia and yttria-stabilized zirconia. *Journal of the American Ceramic Society*. 1968;51(1): 38–42. <https://doi.org/10.1111/j.1151-2916.1968.tb11825.x>
112. Agarkova E. A., Borik M. A., Kulebyakin A. V. et al. Structural, mechanical, and transport properties of scandia and yttria partially stabilized zirconia crystals. *Inorganic Materials*. 2019;55: 748–753. <https://doi.org/10.1134/S0020168519070021>
113. Kuznetsov V. A., Sidorenko O. V. Kristallizatsiya ZrO₂-HfO₂ v gidrotermal'nykh usloviyakh [Crystallization of ZrO₂-HfO₂ under hydrothermal conditions]. *Kristallografiya*. 1968;13: 748–749. (In Russ.)
114. Vil'ke K.-T. *Vyrashchivanie kristallov* [Growing crystals]. Leningrad: Nedra Publ.; 1977. 600 p. (In Russ.)
115. Al'myasheva, O.V., Ugolkova, V.L. & Gusarov, V.V. Thermochemical analysis of desorption and adsorption of water on the surface of zirconium dioxide nanoparticles. *Russian Journal of Applied Chemistry*. 2008;81: 609. <https://doi.org/10.1134/S1070427208040071>
116. Almjasheva O. V., Denisova T. A. Water state in nanocrystals of zirconium dioxide prepared under hydrothermal conditions and its influence on structural transformations. *Russian Journal of General Chemistry*. 2017;87: 1–7. <https://doi.org/10.1134/S1070363217010017>
117. Golovin Yu. I., Farber B. Ya., Korenkov V. V., Tyurin A. I., Shuklinov A. V., Stolyarov R. A., Zhigachev A. O. Synthesis and physical- mechanical properties of stabilized zirconia ceramics prepared from baddeleyite. *Tambov University Reports. Series Natural and Technical Sciences*. 2012;17(3): 875–879. Available at: <https://elibrary.ru/item.asp?id=17839540> (In Russ., abstract in Eng.)
118. Zhigachev A. O., Golovin Y. I. Nanostructured zirconia ceramic based on baddeleyite domestic raw. *Nanotechnologies in Russia*. 2017;12: 400–408. <https://doi.org/10.1134/S1995078017040176>
119. Scian A. N., Aglietti E. F., Caracocche M. C., Rivas P. C., Pasquevich A. F., Lopez Garcia A. R. Phase transformation in monoclinic zirconia caused by milling and subsequent annealing. *Journal of the American Ceramic Society*. 1994;77(6): 1525–1530. <https://doi.org/10.1111/j.1151-2916.1994.tb09752.x>
120. Degueldre C., Paratte J. M. Concepts for an inert matrix fuel, an overview. *Journal of Nuclear Materials*. 1999;274(1-2): 1–6. [https://doi.org/10.1016/S0022-3115\(99\)00060-4](https://doi.org/10.1016/S0022-3115(99)00060-4)
121. Pöml P., Konings R. J. M., Somers J., Wiss T., de Haas G. J. L. M., Klaassen F. C. Inert matrix fuel. In: *Comprehensive Nuclear Materials*. 2012;3: 237–256. <https://doi.org/10.1016/b978-0-08-056033-5.00057-4>
122. Degueldre C. Zirconia inert matrix for plutonium utilization and minor actinides disposition in reactors. *Journal of Alloys and Compounds*. 2007;444: 36–41. <https://doi.org/10.1016/j.jallcom.2006.11.203>

123. Ewing R. C., Weber W. J., Lian J. Nuclear waste disposal-pyrochlore ($A_2B_2O_7$): Nuclear waste form for the immobilization of plutonium and “minor” actinides. *Journal of Applied Physics*. 2004;95(11): 5949–5971. <https://doi.org/10.1063/1.1707213>
124. Nästren C., Jardin R., Somers J., Walter M., Brendebach B. Actinide incorporation in a zirconia based pyrochlore ($Nd_{1.8}An_{0.2}Zr_2O_{7+x}$ ($An = Th, U, Np, Pu, Am$)). *Journal of Solid State Chemistry*. 2009;182: 1–7. <https://doi.org/10.1016/j.jssc.2008.09.017>
125. Huang Z., Li Q., Zhang Y., Duan J. Wang H., Tang Z., Yang Y., Qi J., Lu T. Densifications and mechanical properties of single phase $Gd_2Zr_2O_7$ ceramic waste forms with improved TRPO waste load. *Journal of the European Ceramic Society*. 2020;40(13): 4613–4622.
126. Nandi C., Jain D., Grover V., Dawar R., Kaity S., Prakash A., Tyagi A. $Zr_{0.70}[Y_{1-x}Nd_x]_{0.30}O_{1.85}$ as a potential candidate for inert matrix fuel: Structural and thermophysical property investigations. *Journal of Nuclear Materials*. 2018;510: 178–186. <https://doi.org/10.1016/j.jnucmat.2018.08.008>
127. Tananaev I. V., Fedorov V. B., Morokhov I. D., Malyukova L. V. Osnovy fizikokhimii veshchestv v metastabil'nom ul'tradispersnom sostoyanii i perspektivy ikh ispol'zovaniya [Fundamentals of physical chemistry of substances in a metastable ultrafine state and prospects for their use]. *Izvestiya Akademii nauk SSSR. Neorganicheskie materialy (Inorganic Materials)*. 1984;20(6): 1026–1033. (In Russ.)
128. Fedorov P. P. Heterovalent isomorphism and solid solutions with a variable number of ions in the unit cell. *Russian Journal of Inorganic Chemistry*. 2000;45: S268–S291. Available at: <https://elibrary.ru/item.asp?id=13360696>
129. Fedorov P. P., Sobolev B. P. Ob usloviyakh obrazovaniya maksimumov na krivykh plavleniya tverdykh rastvorov v solevykh sistemakh [On the conditions for the formation of maxima on the melting curves of solid solutions in salt systems]. *Russian Journal of Inorganic Chemistry*. 1979;24(4): (In Russ.)
130. Sobolev B. P. *The rare earth trifluorides. Pt. 1. The high-temperature chemistry of the rare earth trifluorides*. Barcelona: Inst. d'estudies catalans; 2000. 520 p.
131. Kaminskii A. A., Agamalyan N. R., Denisenko G. A., Sarkisov S. E., Fedorov P. P. Spectroscopy and laser emission of disordered GdF_3 - CaF_2 : Nd^{3+} trigonal crystals. *Physica Status Solidi (a)*. 1982;70(2): 397–406. <http://dx.doi.org/10.1002/pssa.2210700206>
132. Tsvetkov V. B., Proidakova V. Yu., Kuznetsov S. V., Subbotin K. A., Lis D. A., Yapyntsev A. D., Ivanov V. K., Fedorov P. P. Growth of $Yb:Na_2SO_4$ crystals and study of their spectral–luminescent characteristics. *Quantum Electronics*. 2019;49(11): 1008–1011. <https://doi.org/10.1070/qel17107>
133. Fedorov P. P. Third law of thermodynamics as applied to phase diagrams. *Russian Journal of Inorganic Chemistry*. 2010;55: 1722–1739. <https://doi.org/10.1134/S0036023610110100>
134. Yin Y., Argent B. B. Phase diagrams and thermodynamics of the systems ZrO_2 – CaO and ZrO_2 – MgO . *Journal of Phase Equilibria*. 1993;14(4): 439–450. <https://doi.org/10.1007/bf02671962>
135. Wang K., Li Ch. H., Gao Y. H., Lu X. G., Ding W. Z. Thermodynamic reassessment of ZrO_2 – CaO system. *Journal of the American Ceramic Society*. 2009;92(5): 1098–1104. <https://doi.org/10.1111/j.1551-2916.2009.02942.x>
136. Jacobson N. S., Liu Z.-K., Kaufman L., Zhang F. Thermodynamic modeling of $YO_{1.5}$ – ZrO_2 system. *Journal of the American Ceramic Society*. 2004;87(8): 1559–1566. <https://doi.org/10.1111/j.1551-2916.2004.01559.x>
137. Zinkevich M., Djurovic D., Aldinger F. Thermodynamic modeling of the cerium-oxygen system. *Solid State Ionics*. 2006;177(11–12): 989–1001. <https://doi.org/10.1016/j.ssi.2006.02.044>
138. Morozova L. V., Tikhonov P. A., Gushkova V. B. Fazovye sootnosheniya v sisteme ZrO_2 – In_2O_3 , sintez i fiziko-khimicheskie svoystva tverdykh rastvorov [Phase relationships in the ZrO_2 – In_2O_3 system, synthesis and physicochemical properties of solid solutions]. *Doklady of the USSR Academy of Sciences*. 183: 140–143. (In Russ)
139. Artamonova O. V., Al'myasheva O. V., Mittova I. Ya., Gusarov V. V. Spekanie nanoporoshkov i svoystva keramiki v sisteme ZrO_2 – In_2O_3 [Sintering of nanopowders and properties of ceramics in the ZrO_2 – In_2O_3 system]. *Perspektivnye Materialy*. 2009;9: 91–94. Available at: <https://elibrary.ru/item.asp?id=11779849> (In Russ.)
140. Fedorov P. P. Nanotechnology and material science. *Nanosystems: Physics, Chemistry, Mathematics*. 2020;11(3): 314–315. <https://doi.org/10.17586/2220-8054-2020-11-3-314-315>

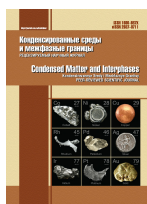
Information about the authors

Pavel P. Fedorov, DSc in Chemistry, Professor, Chief Researcher of Prokhorov General Physics Institute of the Russian Academy of Sciences, Moscow, Russian Federation; e-mail: ppfedorov@yandex.ru. ORCID ID: <https://orcid.org/0000-0002-2918-3926>.

Evgeniya G. Yarotskaya, PhD in Chemistry, Prokhorov General Physics Institute of the Russian Academy of Sciences, Moscow, Russian Federation; e-mail: yar461@yandex.ru. ORCID ID: <https://orcid.org/0000-0001-6704-1964>.

Received 28 December 2020; Approved after reviewing 30 March 2021; Accepted for publication 15 May 2021; Published online on 25 June 2021.

Translated by Valentina Mittova
Edited and proofread by Simon Cox



Condensed Matter and Interphases

Kondensirovannye Sredy i Mezhfaznye Granitsy
<https://journals.vsu.ru/kcmf/>

Original articles

Research article

<https://doi.org/10.17308/kcmf.2021.23/3428>

Study of the formation of structures in solutions of chitosan – polyvinyl alcohol polymer blends

R. M. Akhmetkhanov, V. V. Chernova, A. S. Shurshina, M. Yu. Lazdina, E. I. Kulish✉

Bashkir State University,
32, Zaki Validi str., Ufa 450076, Russian Federation

Abstract

The aim of this work was the investigation of the formation of structures in solutions of individual polymers, as well as their blends with each other in buffer solvents with different values of pH. In this study we used a sample of chitosan (degree of deacetylation ~ 84 %, M = 130,000), which is a polycation when dissolved, and polyvinyl alcohol ($\rho = 1.25 \text{ g/cm}^3$, M = 5000). Buffer systems based on acetic acid and sodium acetate with pH = 3.8, 4.25, and 4.75 were used as solvents. Viscosimetry was used to determine the intrinsic viscosity, the degree of structuring, and the Huggins constant. The Kriegbaum method was used to determine the nature of the aggregates formed by the blend of the studied polymers.

In the course of the research, it was shown that an increase in the pH of the acetate buffer used as a solvent was accompanied by a compression of the macromolecular coil (a decrease in intrinsic viscosity values), a deterioration in the quality of the solvent (an increase in Huggins constant values), and an increase in the degree of polymer aggregation in a solution for chitosan polyelectrolyte. At the same time for a solution of polyvinyl alcohol the pH of the buffer practically did not affect the nature of the polymer-solvent interaction. It has been proved that polymer blends are characterized by an increase in aggregation processes and a decrease in the thermodynamic quality of the solvent in comparison with solutions of individual polymers. The size of the “combined” macromolecular coil, characterized by the intrinsic viscosity value for the polymer blend, which can be both above (buffer solvent with pH = 3.80) and below (buffer solvent with pH = 4.25 and 4.75) additive values, changed depending on the type of formed polymer-polymer aggregates (homo- or hetero-). It was established that the type of aggregates (homo- or hetero-) formed in solutions of polymer blends was determined not only by the thermodynamic quality of the used solvents, but also by the concentration of the polymers in the initial solutions.

Keywords: Polymer blends, Viscometry, Structure formation, Chitosan, Polyvinyl alcohol

For citation: Akhmetkhanov R. M., Chernova V.V., Shurshina A.S., Lazdina M. Yu., Kulish E. I. Study of the formation of structures in solutions of chitosan – polyvinyl alcohol polymer blends. *Kondensirovannye sredyimezhfaznyegrantsy = Condensed Matter and Interphases*. 2021;23(2): 188–195. <https://doi.org/10.17308/kcmf.2021.23/3428>

Для цитирования: Ахметханов Р. М., Чернова В. В., Шуршина А. С., Лаздина М. Ю., Кулиш Е. И. Исследование структурообразования в растворах смесей полимеров хитозан – поливиниловый спирт. *Конденсированные среды и межфазные границы*. 2021;23(2): 188–195. <https://doi.org/10.17308/kcmf.2021.23/3428>

✉ Elena I. Kulish, e-mail: onlyalena@mail.ru

© R. M. Akhmetkhanov, V. V. Chernova, A. S. Shurshina, M. Yu. Lazdina, E. I. Kulish, 2021



1. Introduction

It is known that the prehistory of the formation of a polymer material from a solution can affect a number of its characteristics: elasticity, strength, thermal stability, and many others [1–4]. This is due to the fact that even after the careful removal of the solvent, the nature and thermodynamic quality of the solvent used, the initial concentration of polymers in the solution, and the ratio of the components in the blend affect the properties and structure of films or fibres formed from a solution [4–7]. For example, due to the use of solvents of different thermodynamic qualities in relation to the polymer, various supramolecular structures were created in solutions, which remain in the metastable systems formed after the removal of solvents and further in the solid phase [8]. Thus, even in the case of obtaining materials from polymer-solvent systems, the hierarchy of the structures being formed, both in a dilute solution and in a condensed state, is complex and diverse, not to mention polymer-polymer-solvent systems.

Taking these facts into account, it becomes clear that it is extremely important to study the formation of the structures of polymers, as well as their blends in solutions, not only for the solution of specific applied problems, but also for obtaining new knowledge about the structures of polymers in solutions. The aim of this study was the investigation of the formation of structures in solutions of individual polymers (chitosan (ChTS) and polyvinyl alcohol (PVA)), as well as their blends with each other. The choice of polymers was due to their physiological activity [9], as well as a number of properties, such as biocompatibility, biodegradability, atraumaticity, high sorption capacity, minimal immune response of the organism, etc. [10–

17]. It should be noted that, when dissolved in acidic media, ChTS acquires the properties of a polyelectrolyte, namely, a polycation, which has a major effect on its physiological activity.

2. Experimental

For the study we used a sample of chitosan ChTS (manufactured by ZAO Bioprogress, Shchelkovo), obtained by the alkaline deacetylation of crab chitin (degree of deacetylation ~ 84 %), $M = 130000$, which, upon dissolution is a polycation (Fig. 1a), and polyvinyl alcohol PVA (Fig. 1b), grade 11/2 produced by OOO Reakhim $\rho = 1.25 \text{ g/cm}^3$, $M = 5000$.

Acetate buffers with $\text{pH} = 3.8$ (buffer solution 1), 4.25 (buffer solution 2), and 4.75 (buffer solution 3) were used as solvents. The acetate buffers were prepared by mixing 0.2 M acetic acid and 0.2 M sodium acetate: $\text{pH} = 3.8$ –12 ml and 88 ml, $\text{pH} = 4.25$ –32 ml and 68 ml, $\text{pH} = 4.75$ –60 ml and 40 ml, respectively.

For the determination of the intrinsic viscosity $[\eta]$, the polymer was dissolved in an acetate buffer (for the exclusion of the effect of polyelectrolyte swelling for chitosan) for 24 h at room temperature with constant stirring. The intrinsic viscosity was determined viscometrically according to the standard method using an Ubbelohde viscometer at $25 \text{ }^\circ\text{C}$ [8] (by extrapolating to zero using the Huggins and Kroemer equations), the polymer concentration in the solution was varied from 0.1 to 0.5 g/dl. The experimental error was not higher than 1 %.

The degree of structuring of the solution (d) was determined as the slope of the line of the experimental dependences of the specific viscosity of solutions on the concentration of the polymer in the solution in logarithmic coordinates [18] (Fig. 2a).

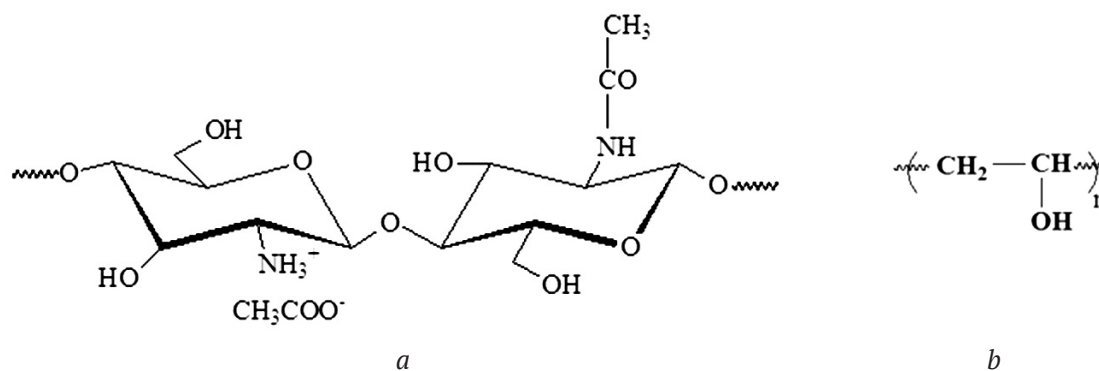


Fig. 1. Structural formulas of chitosan (a) and polyvinyl alcohol (b)

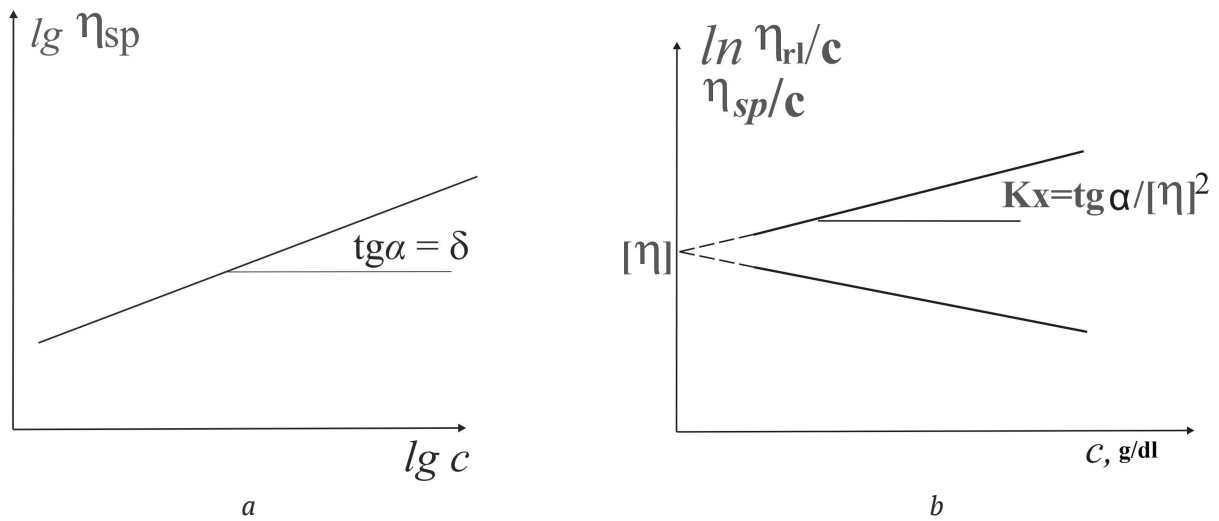


Fig. 2. Graphical methods for determining the degree of structuring of the solution (a) and Huggins constant (b)

The experimental data were analysed using the Kriegbaum method: according to the Huggins equation:

$$\eta_{\text{specific}}/C = [\eta] + bC;$$

where $b = [\eta]^2 K_x$.

The parameter of intermolecular interaction for individual polymers (b_{11}, b_{22}) was determined as the slope of the linear part of the dependence of the reduced viscosity on the polymer concentration (Fig. 2b).

Then, at each fixed concentration, the experimental parameter of intermolecular interaction ($b_{12(\text{exp})}$) for a blend was determined according to the formula:

$$b_{12(\text{exp})} = \frac{h_{\text{blend}} - [h]_1 C_1 - [h]_2 C_2 - b_{11} C_1^2 - b_{22} C_2^2}{2C_1 C_2}.$$

The parameter of intermolecular interaction Δb_{12} ($\Delta b_{12} = b_{12(\text{exp})} - b_{12(\text{theor})}$; $b_{12(\text{theor})} = (b_{11} b_{22})^{0.5}$) was determined by comparing $b_{12(\text{exp})}$ and $b_{12(\text{theor})}$. The types of the associates formed can be determined by the change of Δb_{12} : positive values of Δb_{12} indicate the presence of associates between dissimilar macromolecules in the solution and negative values indicate the presence of homoassociates.

3. Results and discussions

The study of the dynamic properties of macromolecules in solutions, in particular their hydrodynamic behaviour, provides information on the intermolecular interactions. In the description of the viscosity properties of dilute solutions,

as a rule, the interaction of macromolecules is neglected and their description is based on the linear dependence of the increase in viscosity on the concentration of the polymer solution. In the region of transition from dilute to semi-dilute solutions (crossover region), where the mechanism of mass transfer and the conformational regime of macromolecules change, and the formation of entangled network occurs. In accordance with the scaling theory in this region there is a deviation from the linearity of the concentration dependence of viscosity $\eta \sim c^\delta$. This is revealed by the change in the slope of the corresponding dependence in double logarithmic coordinates. According to generally accepted concepts, the tangents to the initial and final sections of this dependence intersect in the region of c^* , and the slopes are equal to 1 and 15/4 [19, 20].

Indeed, as was shown by viscometric studies of ChTS and PVA solutions in aqueous solutions with different values of pH (buffer solution 1 – pH = 3.80, buffer solution 2 – pH = 4.25, buffer solution 3 – pH = 4.75), the representation of the dependences of the specific viscosity of polymer solutions on concentration in logarithmic coordinates allows determining the concentration of c^* as the value from which the experimental curve deviates from a straight line. It should be noted that in the case of ChTS solutions, which have a polyelectrolyte nature, the value of c^* changes with changes in the pH of the medium (see Table 1).

As can be seen from Table 1, with an increase in the pH of the aqueous solution, the crossover

Table 1. Characteristics of the studied polymers obtained from viscometric data

Polymer	Solvent	c^* , g/dl	δ	K_χ	$[\eta]$, dl/g
ChTS	Buffer1 (pH = 3.80)	0.24	1.25	0.54	6.80
	Buffer2 (pH = 4.25)	0.26	1.28	0.60	5.70
	Buffer3 (pH = 4.75)	0.28	1.35	0.62	5.00
PVA	Buffer1 (pH = 3.80)	–	1.10	0.80	0.50
	Buffer2 (pH = 4.25)	–	1.15	0.80	0.50
	Buffer3 (pH = 4.75)	–	1.20	0.81	0.49

occurred somewhat later, which indicates a slight decrease in the size of the macromolecular coils. For PVA solutions, a crossover in the studied concentration range (up to 1 g/dL) was not observed due to the low molecular weight of PVA.

In addition, the description of the viscosity properties of polymer solutions, should consider the possibility of reversible aggregation processes, which can occur not only in the region of high concentrations, but also in the region $c < c^*$.

It is known that in the translational mechanism of mass transfer in aggregated suspensions, the contribution to the viscosity is made not by individual particles with a volume V_0 , but by their aggregates, the volume of which $V(n)$ depends not only on the number of constituent particles n , but also on the density of their packing, characterized by the fractal dimension D :

$$V(n) = V_0 \cdot n^{3/D}. \quad (1)$$

As a result of the loose packing of the suspension particles in the aggregate, their contribution to the viscosity starts to depend non-linearly on the concentration:

$$\Delta\eta \sim \eta_0 \cdot C^\delta, \quad \delta > 1. \quad (2)$$

A similar reasoning extends to polymer solutions when considering the dynamic properties of polymer coils taking into account the excluded volume effect (the model of impermeable coils) [18].

The processing of the experimental dependences of the specific viscosity of polymer solutions on the concentration in double logarithmic coordinates allows determining the power value d in the scaling dependence (2), the corresponding values of which are presented in Table 1.

A comparison of the obtained values shows that in all considered cases, the values of the scaling parameter exceed 1, which unambiguously

indicates that the processes of aggregation in the polymer solution begin in the region of dilute solutions.

Table 1 shows the values of the intrinsic viscosity and the Huggins constant (K_χ) of the studied polymers, which allowed the quality of the used solvents to be estimated. An analysis of these data for PVA and ChTS solutions in buffer solutions with different pH confirms the conclusions about the deterioration of the solvent quality and a decrease in the coil size with increasing pH in the case of ChTS. The sizes of PVA coils practically did not change with a change in the pH of the medium, which should be expected, considering that PVA is not a polyelectrolyte.

As a result of mixing ChTS and PVA solutions with equal concentrations, both the additive behaviour of the mixed solutions and deviations from additivity due to the rearrangement of the structure of polymer solutions, caused by both the different nature (ChTS is polyelectrolyte, PVA is not), and by the difference in molecular weight of macromolecules can be expected. An increase in the structuring of mixed solutions in comparison with solutions of individual polymers can be indicated, first of all, by the degree of aggregation (δ).

As can be seen from data presented in Fig. 3, polymer blends and solutions of individual polymers, are aggregated systems in all used buffers, regardless of the pH of the solvent, and for all compositions of ChTS: PVA blends. It should be noted that the values of the degree of aggregation are always higher than the additive values, which characterizes an increase in the intermolecular interaction of macromolecules. However, a general pattern was noted: with the deterioration of the thermodynamic quality of the solvent, e.g. with the transition to a more alkaline buffer, higher deviations from the additive values were observed.

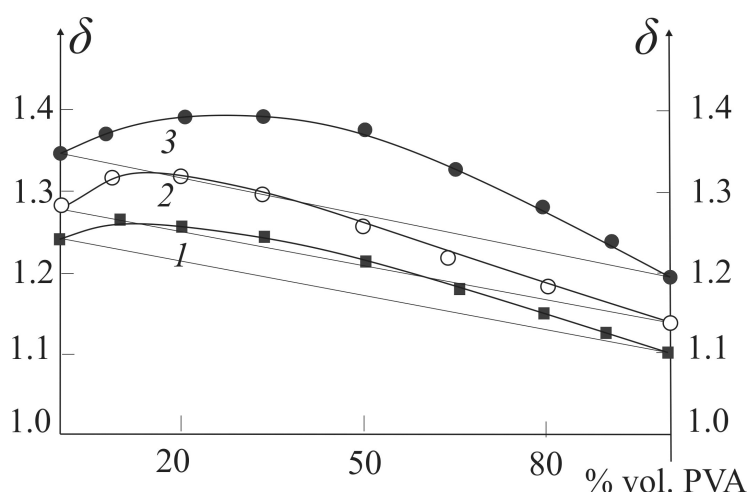


Fig. 3. The dependence of the aggregation δ degree of ChTSZ-PVA solutions in buffer solution 1 (1), in buffer solution 2 (2), in buffer solution 3 (3)

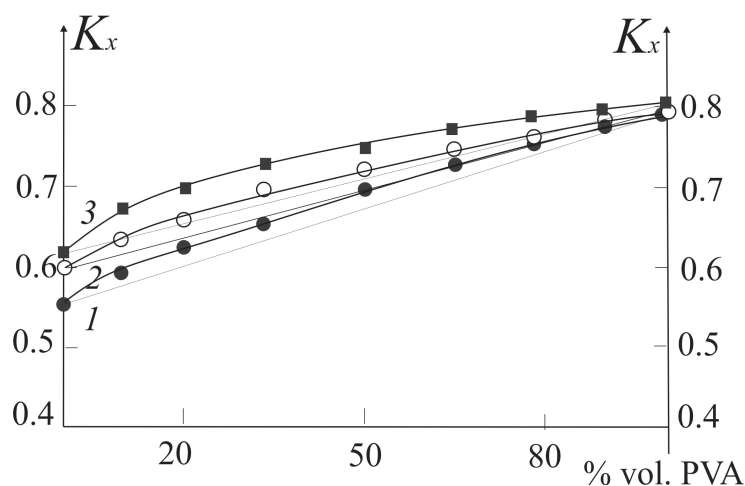


Fig. 4. The dependence of the Huggins constant of ChTS-PVA solutions in buffer solution 1 (1), buffer solution 1 (2) and in buffer solution 3 (3)

The increase in the degree of structuring of the solution was also evidenced by the values of Huggins constant (Fig. 4). As can be seen from the data presented, deviations from the additive values were observed for all solvents (buffer systems) used in the study.

Based on the values of the degree of aggregation and Huggins constant it can be stated that the formation of structures in solutions increases with polymer mixing. However, the analysis of the dependence of the intrinsic viscosity (reflecting the conformational state of macromolecules) on the composition of the polymer blend solutions indicates that the nature of the formed aggregates is different when using solvents with different values of pH (Fig. 5).

As can be seen from the data in Fig. 5, representing the dependence of the intrinsic viscosity on the composition of the blend for solutions with different pH, in a more acidic medium (with pH = 3.8) the mixed macromolecular coils “swell”, while in a more alkaline buffer - 3, the coils are “squeezed”, as evidenced by the negative nature of the deviation of the intrinsic viscosity from the additive values.

The processing of the viscometric data by the Krigbaum method allowed determining the nature of the aggregates formed by the PVA-ChTS blend. It was found that the nature of the aggregates in the polymer blend depends not only on the pH of the used solvent, but also on the concentration of the initial polymer solutions (Fig. 6).

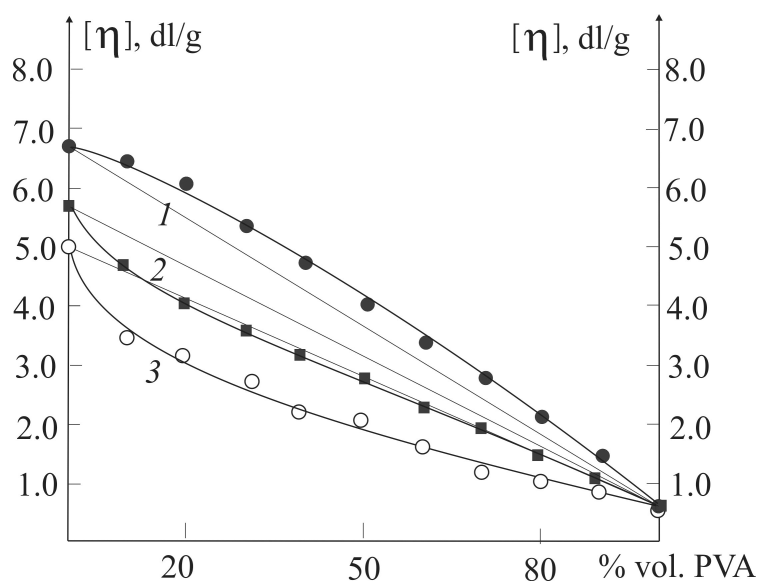


Fig. 5. The dependence $[\eta]$ of ChTS-PVA solutions in buffer solution 1 (1), in buffer solution 2 (2), in buffer solution 3 (3)

Thus, in buffers with $\text{pH} = 4.25$ and 4.75 , the formation of homoaggregates from macromolecules occurred with all investigated concentrations of the initial solutions of ChTS and PVA. This was evidenced by the negative values of the intermolecular aggregation parameter (Δb_{12}) (Fig. 6 b, c).

In the case of a more acidic solution with $\text{pH} = 3.80$, a complex dependence of the values of the intermolecular aggregation parameter on the concentration of the initial polymer solutions was observed. Thus, at concentrations lower and slightly exceeding c^* , positive Δb_{12} values (Fig. 6, curves 1, 2, 3) were revealed, which

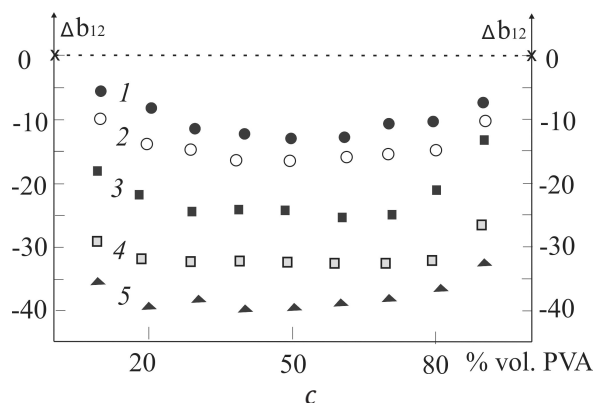
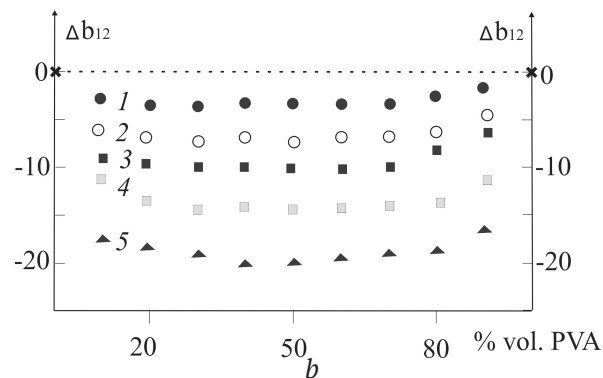
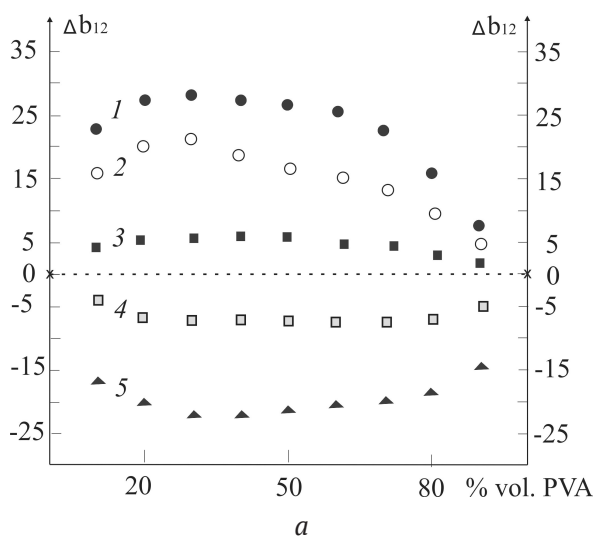


Fig. 6. The dependence of the intermolecular aggregation Δb_{12} parameter of ChTS-PVA solutions in buffer solution 1 (a), in buffer solution 2 (b), in buffer solution 3 (c). Concentrations of the initial polymer solutions were 0.1 (1), 0.2 (2), 0.3 (3), 0.4 (4), and 0.5 (5) g/dl

indicate the formation of mixed associates. At high concentrations of the initial ChTS and PVA solutions, negative values of intermolecular aggregation (Fig. 6, curves 4, 5) and, accordingly, the formation of homoaggregates were detected.

Probably, in a more acidic solution with concentrations slightly exceeding the crossover, the capture of PVA molecules by the ChTS macromolecules with the corresponding formation of heteroaggregates occurs. In more basic media (buffer solvents 2 and 3) and when c^* in buffer solvent 1 is exceeded, ChTS macromolecules were compressed, as a result of which each of the polymers aggregates separately from each other.

Thus, the performed studies showed that the formation of aggregates from macromolecules is possible in the case of solutions of individual polymers and in the case of their blends even in the region of dilute and semi-dilute solutions of polymer blends, which are a single-phase solution without a visible interface. The type of formed aggregates was largely determined by the nature and thermodynamic quality of the selected solvent, as well as by the concentration of the initial polymer solutions.

4. Conclusions

1. It was shown that for ChTS polyelectrolyte solutions, an increase in the pH of the acetate buffer used as a solvent is accompanied by a shrinkage of the macromolecular coil (a decrease in the intrinsic viscosity values), a deterioration in the quality of the solvent (an increase in the Huggins constant), and an increase in the degree of polymer aggregation in the solution. For PVA solutions, the pH of the solution practically did not affect the nature of the polymer-solvent interaction.

2. It has been proven that polymer blends are characterized by an intensification of aggregation processes and a decrease in the thermodynamic quality of the solvent in comparison with solutions of individual polymers. The size of the “combined” macromolecular coil (intrinsic viscosity value for a polymer blend) in this case can be both higher (buffer 1 with pH = 3.80) and below (buffer 2 with pH = 4.25 and buffer 3 with pH = 4.75) the additive values, which is determined by the type of (homo- or hetero-) formed polymer-polymer aggregates.

3. It was found that the type of aggregates formed in solutions of polymer blends (homo- or hetero-) are determined not only by the thermodynamic quality of the used solvents, but also by the concentration of polymers in the initial solutions.

Author contributions

All authors made an equivalent contribution to the preparation of the publication.

Conflict of interests

The authors declare that they have no known competing financial interests or personal relationships that could have influenced the work reported in this paper.

References

- Matevosyan M. S., Askadskii A. A., Slonimskii G. L. Mechanical relaxational properties of polymer films as a function of the prehistory of their preparation from solutions. *Polymer Science U.S.S.R.* 1987;29(4): 843–850. [https://doi.org/10.1016/0032-3950\(87\)90457-6](https://doi.org/10.1016/0032-3950(87)90457-6)
- Kulish E. I., Chernova V. V., Vildanova R. F., Volodina V. P., Kolesov S. V. The influence of the prehistory of the formation of film samples of chitosan on the process of their enzymatic decomposition. *Bulletin of the Bashkir University.* 2011;16(2): 339–340. Available at: <https://elibrary.ru/item.asp?id=16461557> (In Russ., abstract in Eng.)
- Kulish E. I., Lazdina R. Yu., Shurshina A. S., Kolesov S. V., Zakharova E. M., Zakharov V. P. Structure formation as a method of forming physicomaterial characteristics of films obtained from aqueous solutions of certain polysaccharides. *Polymer Science, Series A.* 2021;63 (1): 54–62. <https://doi.org/10.1134/s0965545x21010053>
- Alig I., Lellinger D., Skipa T. Influence of thermorheological history on electrical and rheological properties of polymer-carbon nanotube composites. In: *Polymer-Carbon Nanotube Composites.* 2011; 295–328. <https://doi.org/10.1533/9780857091390.2.295>
- Mazinov A. S., Tyutyunik A. S., Gurchenko V. S. Changes in the spectral characteristics and conductivity of fullerene films depending on the type of solvent. *Applied Physics = Prikladnaya Fizika.* 2020;2: 64–70. Available at: <https://elibrary.ru/item.asp?id=43064333> (In Russ., abstract in Eng.)
- Gorodnyakova I. S., Shcherbina L. A., Budkute I. A. Influence of the composition of the precipitation bath on the structure and properties of the fiber obtained by the wet method from solutions of poly[acrylonitrile-co-methyl acrylate-co-2-acrylamide-2-methylpropane sulfonic acid] in aprotic and hydrotropic solvents.

Polimernye materialy i tekhnologii. 2020;6(4): 42–57. <https://doi.org/10.32864/polymmattech-2020-6-4-42-57> (In Russ., abstract in Eng.)

7. Liu B., Zhang H., Ren J., Ma T., Yu M., Xie L., Lu D. Effect of solvent aromaticity on poly(9,9-dioctylfluorene) (PFO) chain solution behavior and film condensed state structure. *Polymer*. 2019;185(17): 121986. <https://doi.org/10.1016/j.polymer.2019.121986>

8. Rafikov S. R., Budtov V. P., Monakov Yu. B. *Vvedeniye v fiziko-khimiya rastvorov polimerov* [Introduction to the physicochemistry of polymer solutions]. Moscow: Khimiya Publ.; 1978. 320 p. (in Russ.)

9. Plate N. A., Vasilyev A. Ye. *Fiziologicheski aktivnyye polimery* [Physiologically active polymers]. Moscow: Khimiya Publ., 1986. 296 p. (in Russ.)

10. Anwar H., Ahmad M., Minhas, M. U., Rehmani S. Alginate-polyvinyl alcohol based interpenetrating polymer network for prolonged drug therapy, Optimization and in-vitro characterization. *Carbohydrate Polymers*. 2017;166: 183–194. <https://doi.org/10.1016/j.carbpol.2017.02.080>

11. Timofejeva A., D'Este M., Dagnija L. Calcium phosphate/polyvinyl alcohol composite hydrogels: A review on the freeze-thawing synthesis approach and applications in regenerative medicine. *European Polymer Journal*. 2017;95: 547–565. <https://doi.org/10.1016/j.eurpolymj.2017.08.048>

12. Matyjaszewski K., Möller M. Copper-mediated atom transfer radical polymerization. In: *Polymer Science: A Comprehensive Reference*. Elsevier Science; 2012;3: 377–428. <https://doi.org/10.1016/b978-0-444-53349-4.00071-6>

13. Schmitz C., Auza L. G., Koberidze D., Rasche S., Fischer R., Bortesi L. Conversion of chitin to defined chitosan oligomers: current status and future prospects. *Marine Drugs*. 2019;17(8): 452. <https://doi.org/10.3390/md17080452>

14. Crini G. Historical review on chitin and chitosan biopolymers. *Environmental Chemistry Letters*. 2019;17: 1623–1643. <https://doi.org/10.1007/s10311-019-00901-0>

15. Shukla S. K., Mishra A. K., Arotiba O. A., Mamba B. B. Chitosan-based nanomaterials: a state-of-the-art review. *International Journal of Biological Macromolecules*. 2013;59: 46–58. <https://doi.org/10.1016/j.ijbiomac.2013.04.043>

16. Keong L. C., Halim A. S. In Vitro models in biocompatibility assessment for biomedical-grade chitosan derivatives in wound management. *International Journal of Molecular Sciences*. 2009;10(3): 1300–1313. <https://doi.org/10.3390/ijms10031300>

17. Li J., Wu Y., Zhao L. Antibacterial activity and mechanism of chitosan with ultra high molecular weight. *Carbohydrate Polymers*. 2016;148: 200–205. <https://doi.org/10.1016/j.carbpol.2016.04.025>

18. Arinshtein A. E. Effect of aggregation processes on the viscosity of suspensions. *Sov. Phys. JETP*. 1992;74(4): 646–648. Available at: http://jetp.ac.ru/cgi-bin/dn/e_074_04_0646.pdf

19. Doi M., Edwards S. F. *The theory of polymer dynamics*. New York: The Clarendon Press, Oxford University Press; 1986. 391 p.

20. Gennes P. G. de *Scaling concepts in polymer physics*. Ithaca, N.Y.: Cornell University Press; 1979. 324 p.

Information about the authors

Rinat M. Akhmetkhanov, DSc in Chemistry, Associate Professor, Dean, Bashkir State University, Ufa, Russian Federation; e-mail: rimasufa@rambler.ru. ORCID iD: <https://orcid.org/0000-0003-0016-0218>.

Valentina V. Chernova, PhD in Chemistry, Associate Professor, Bashkir State University, Ufa, Russian Federation; e-mail: my_life82@mail.ru. ORCID iD: <https://orcid.org/0000-0002-3443-8911>.

Angela S. Shurshina, PhD in Chemistry, Associate Professor, Bashkir State University, Ufa, Russian Federation; e-mail: anzhela_murzagil@mail.ru. ORCID iD: <https://orcid.org/0000-0001-6737-7265>.

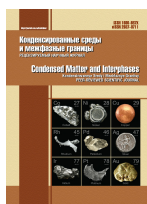
Mariya Yu. Lazdina, student, Bashkir State University, Ufa, Russian Federation; e-mail: mashalazdina@mail.ru.

Elena I. Kulish, DSc in Chemistry, Professor, Head of Department, Bashkir State University, Ufa, Russian Federation; e-mail: onlyalena@mail.ru. ORCID iD: <https://orcid.org/0000-0002-6240-0718>.

Received 16 February 2021; Approved after reviewing 30 March 2021; Accepted for publication 15 May 2021; Published online 25 June 2021.

Translated by Valentina Mittova

Edited and proofread by Simon Cox



Original articles

Research article

<https://doi.org/10.17308/kcmf.2021.23/3429>

Sol-gel synthesis, crystal structure and magnetic properties of nanocrystalline praseodymium orthoferrite

Bui Xuan Vuong¹, Nguyen Anh Tien²✉

¹Faculty of Natural Sciences, Sai Gon University,
Ho Chi Minh City 700000, Vietnam

²Faculty of Chemistry, Ho Chi Minh City University of Education,
Ho Chi Minh City 700000, Vietnam

Abstract

In this work, nano-sized crystalline praseodymium orthoferrite was successfully synthesized via sol-gel method using water – methanol co-solvent. Single-phase PrFeO₃ nanoparticles were formed after annealing the precursors at 650, 750, 850, and 950 °C during 60 min. The crystal size, lattice volume and coercivity (H_c) of nanocrystalline PrFeO₃ increase with the annealing temperature. The obtained praseodymium orthoferrite exhibited paramagnetic properties with $H_c = 28 - 34$ Oe.

Keywords: Sol-gel synthesis, Methanol, Praseodymium orthoferrite, Magnetic property

For citation: Bui X. V., Nguyen A. T. Sol-gel synthesis, crystal structure and magnetic properties of nanocrystalline praseodymium orthoferrite. *Kondensirovannye sredy i mezhfaznye granitsy = Condensed Matter and Interphases*. 2021;23(2): 196–203. <https://doi.org/10.17308/kcmf.2021.23/3429>

Для цитирования: Буй Х. В., Нгуен А. Т. Золь-гель синтез, кристаллическая структура и магнитные свойства нанокристаллического ортоферрита празеодима. *Конденсированные среды и межфазные границы*. 2021;23(2): 196–203. <https://doi.org/10.17308/kcmf.2021.23/3429>

✉ Nguyen Anh Tien, e-mail: tienna@hcmue.edu.vn

© Bui Xuan Vuong, Nguyen Anh Tien, 2021



The content is available under Creative Commons Attribution 4.0 License.

1. Introduction

Amongst nano-sized metal oxide semiconductors, rare earth orthoferrites $AFeO_3$ ($A = La, Y, Pr, Sm, Ho$) have been studied for application in many fields such as inorganic dyes, optical catalysts, gas sensors, magnetic materials or electrodes for Li-ion battery [1–8]. The properties of this type of materials depend on not only the particle size and morphology, but also the dopant concentration and preparation methods [5–9].

Recently, the sol-gel method has been used for preparation of $AFeO_3$ orthoferrite nanomaterials owing to many advantage of this method: low annealing temperature, narrow particle size distribution, high purity, facile synthesize highly doped $AFeO_3$ materials, [1–3, 10–12]. However, the challenge of this method lies in the selection of appropriate organic polymer for gel formation and the experimental time is usually prolonged. In previous works [13–14], orthoferrite $AFeO_3$ ($A = Nd$ and Ho) nanomaterials of particle size < 100 nm were synthesized by co-precipitation method using hot ethanol via the hydrolysis of $A(III)$ and $Fe(III)$ cations in hot water ($T > 95$ °C) and NH_3 5 % solution as the precipitant. Methanol and ethanol have similar dipole moments ($\mu(C_2H_5OH) = 1.66$ D, $\mu(CH_3OH) = 1.69$ D) [15], which are lower than that of water ($\mu(H_2O) = 1.85$ D) [16]. Meanwhile, the viscosity of CH_3OH ($5.9 \cdot 10^{-4}$ Pa·s) is lower than that of C_2H_5OH ($1.2 \cdot 10^{-3}$ Pa·s), and is also very low compared to organic polymers [15]. As a result, the interaction between $A(III)$ and $Fe(III)$ cations with CH_3OH is smaller than with C_2H_5OH , which leads to the decrease of the size of orthoferrite $AFeO_3$ particles synthesized by sol-gel method using methanol.

In this work, the formation, as well as structural and magnetic properties of nano-sized orthoferrite praseodymium (o- $PrFeO_3$) prepared by sol-gel method using methanol have been studied and characterized.

2. Experimental and methods

All solvents and chemicals for the synthesis of used nanocrystalline praseodymium orthoferrite were purchased and used as-received: $Pr(NO_3)_3 \cdot 6H_2O$ (99.8 % purity, Merck), $Fe(NO_3)_3 \cdot 9H_2O$ (99.6 % purity, Sigma-

Aldrich), methanol absolute (99.7 % purity, $d = 0.792$ g/mL), ammonia solution (Xilong purity, 85 %, $d = 0.901$ g/mL).

A mixture of $Pr(NO_3)_3 \cdot 6H_2O$ and $Fe(NO_3)_3 \cdot 9H_2O$ (1:1 mol to mol ratio) was dissolved in 50 mL solvent of $H_2O - CH_3OH$ (1:1, V/V). The mixture solution was then added dropwise to a round-bottom flask containing 150 mL boiling $H_2O - CH_3OH$ co-solvent ($T \sim 85$ °C). The slow addition of $Pr(III)$ and $Fe(III)$ mixture to the co-solvent at 85 °C would increase the hydrolysis process, thus hinder and control the particle size of orthoferrite $PrFeO_3$. Details of optimized conditions can be found in previous reports on the synthesis of $LnFeO_3$ ($Ln = Y, La, Nd$) orthoferrites [17–19]. The system continued to be refluxed for an additional 30 minutes before cooling down to ~ 30 °C, resulted in a brownish-yellow mixture. By refluxing, the solvent volume was maintained and the diffusion of toxic CH_3OH vapor to the environment could be minimized. Next, NH_3 5 % solution was added dropwise to the system until $pH \sim 9-10$ (tested by pH paper). The system was stirred for 30 minutes, then vacuum filtered. After removing all the filtrate, the residue was dry at 50 °C during 3 hours and grounded to obtain brownish-yellow powder (precursor for the synthesis of o- $PrFeO_3$).

Thermogravimetry and differential scanning calorimetry (TG-DSC) curves were recorded under dried air at the heating rate of 10 K·min⁻¹, maximum temperature 950 °C, platinum crucibles, using Labsys Evo – TG-DSC 1600 °C (France).

X-ray diffraction (XRD) patterns of $PrFeO_3$ samples were recorded using X-ray powder diffractometer (XRD, D8-ADVANCE, Germany) with CuK_α radiation ($\lambda = 1.5406$ Å), range $2\theta = 10-75^\circ$, step size 0.019 °/s. Crystal size (D_{XRD} , nm) of $PrFeO_3$ samples was determined according to Debye-Scherrer equation, lattice parameters (a, b, c, V) were calculate according to previous works [12, 19-20]. Phase composition was determined by Rietveld refinement, Fullprof 2009.

The content and surface distribution of the elements (Pr, Fe, O) were studied by energy-dispersive X-ray spectroscopy (EDX and EDX-mapping), FE-SEM S-4800 (Japan). The quantitative elemental composition were taken as the average of 5 different positions of each sample.

Crystal size and morphology of PrFeO_3 samples were characterized by transmission electron spectroscopy (TEM), Joel JEM-1400 (Japan). The crystal size distribution of were determined by IMAGE J.

Hysteresis loop and magnetic properties including coercive force (H_c , Oe), remanent magnetization (M_r , emu/g) and saturation magnetization (M_s , emu/g) were recorded on vibrating sample magnetometer (VSM, MICROSENE EV11) under the magnetic field in the range of -21 000 Oe to +21 000 Oe.

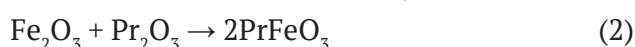
3. Results and discussion

Fig. 1 shows the TG-DSC curves of precursors for the synthesis of o- PrFeO_3 nanomaterial. The total mass loss from room temperature to 950 °C was 23.67 %. This result proves the formation of bonds between Pr(III) and Fe(III) cation with CH_3 - group in the precipitate [21]. Indeed, if this precipitate had only included $\text{Pr}(\text{OH})_3\downarrow$ and $\text{Fe}(\text{OH})_3\downarrow$, mass loss deduced from equation (1) would have been 18.07 %.



The mass loss by decomposition of $\text{M}^{3+}\text{-CH}_3$ ($\text{M} = \text{Pr}, \text{Fe}$) bonds corresponds to the exothermic peak at 270.56 °C on the DSC curve (Fig. 1). The endothermic peaks at 113.37 and 358.52 °C are the

dehydrate and decomposition of praseodymium (III) and iron (III) hydroxides. Similar results were also observed in previous works [13, 19] for HoFeO_3 and NdFeO_3 orthoferrite. The exothermic peak at 617.31 °C correspond to the phase formation of PrFeO_3 orthoferrite from Pr_2O_3 and Fe_2O_3 according to equation (2). This inference is in good agreement with the mass change on the TG curve (there were no observable changes in the sample's mass from ~650 °C). From the TG-DSC results, the sample was annealed at 650, 750, 850, and 950 °C for 60 min to characterize the structural properties of PrFeO_3 crystals by XRD.



XRD patterns of praseodymium orthoferrite precursor after annealing at different temperatures for 60 min were shown in Fig. 2. The results give single phase orthorhombic PrFeO_3 . All obtained peaks match well with the standard peaks of PrFeO_3 (JCPDS: 74-1472), without any observable oxide peaks such as Pr_2O_3 , Pr_6O_{11} or Fe_2O_3 . The degree of crystallinity and crystal phase content of PrFeO_3 samples increased with the annealing temperature, however, this increment was not linear (Table 1). The crystallinity of the sample annealed at 750 °C (592.04 cts) and that annealed at 950 °C (614.66 cts) were approximate, but the PrFeO_3 crystal phase content of the sample

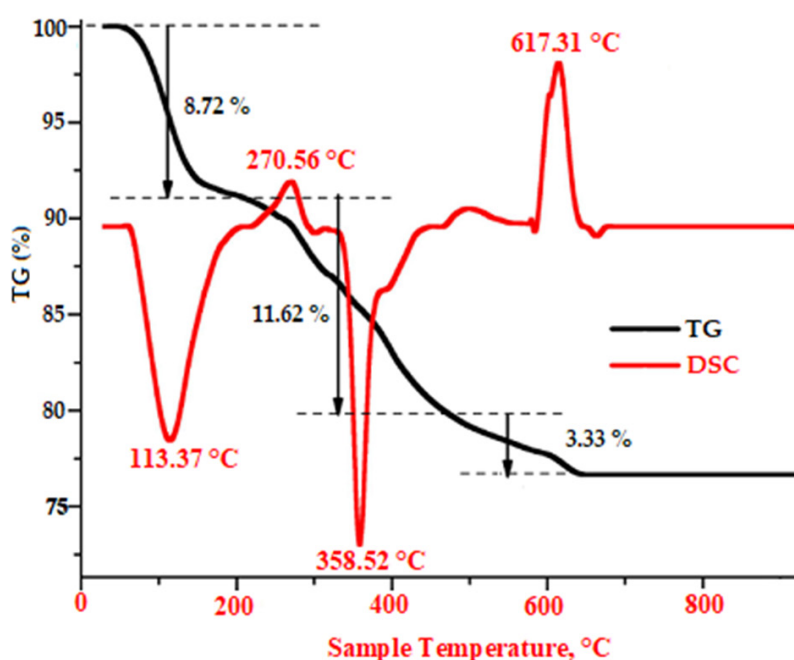


Fig. 1. TG-DSC curves of the dried gel powders

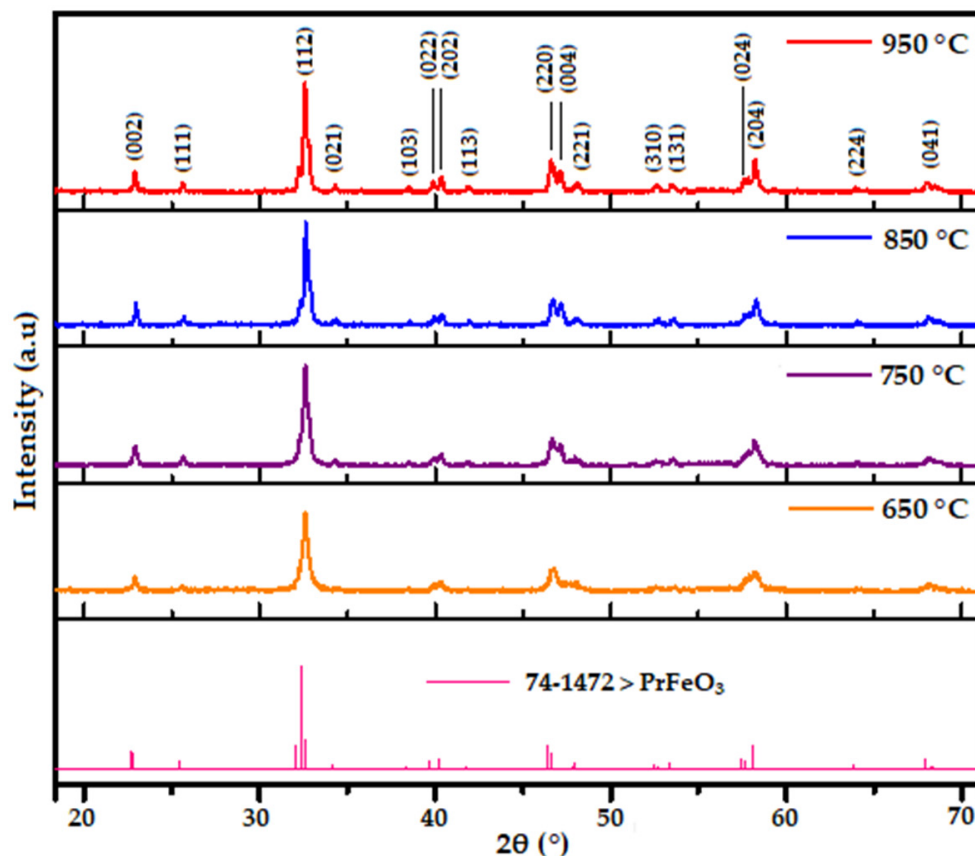


Fig. 2. PXRD patterns of PrFeO_3 nanopowders annealed at 650, 750, 850, and 950 °C for 60 min

Table 1. Characteristics of PrFeO_3 samples annealed at different temperatures for 60 min

T	650 °C	750 °C	850 °C	950 °C
2θ , °	32.6092	32.5659	32.6185	32.5584
Height, cts	288.26	592.04	490.86	614.66
Crystal phase, %	68.8	93.4	80.5	89.7
Amorphous phase, %	31.2	6.6	19.5	10.3
FWHM, °	0.1309	0.1683	0.1122	0.1122
d-spacing, Å	2.74604	2.74960	2.74529	2.75022
D , nm	62.5	48.6	73.0	73.0
a , Å	5.4556	5.4521	5.4509	5.4501
b , Å	5.5753	5.5840	5.6206	5.6218
c , Å	7.8113	7.7245	7.8169	7.8145
V , Å ³	237.59	235.17	239.49	239.43
H_c , Oe	28.0	30.8	33.7	–
M_r , emu/g	0.22	0.13	0.76	–
M_s , emu/g	0.24	1.10	0.73	–

annealed at 750 °C was much higher than the others. The full-width at half maximum (FWHM, °) of the sample annealed at 750 °C was the widest, leading to the smallest Debye-Scherrer crystal size ($D_{\text{XRD}} = 48.6$ nm) and lattice volume ($V = 235.17$ Å³) (Table 1). Thus, it can be

assumed that 750 °C for 60 min is the appropriate conditions for the formation of single phase praseodymium orthoferrite (o- PrFeO_3) by sol-gel method using water-methanol co-solvent.

From the EDX and EDX-mapping analysis of PrFeO_3 sample annealed at 750 °C, only

praseodymium, iron and oxygen peaks were observable without any other signals of impurity elements (Fig. 3). The averages of weight percentage and atomic percentage of the elements Pr, Fe, O from five different positions are shown in Table 2. The obtained results are consistent with expected chemical composition (Table 2).

Particle size and morphology of PrFeO₃ powder annealed at 750 °C are shown in the TEM image (Fig. 4a). The obtained particles have slightly angular spherical shape with the size mostly in the range of 20–60 nm (Fig. 4b). Average

size calculated by IMAGE J was 46.28 nm. This result is rather close to the crystal size by Debye-Scherrer equation ($D_{XRD} = 48.6$ nm) (Table 1).

Field dependence of the magnetization of PrFeO₃ nanomaterials at 300K are shown in Fig. 5. The coercive force ($H_c = 20.8 \div 30.7$ Oe) and saturation magnetization ($M_r = 0.13 \div 0.76$ emu/g) (Table 1) of all three PrFeO₃ samples in this work are much lower than those of PrFeO₃ prepared by co-precipitation method reported by Sudandararaj T. S. A. et. al. [22] ($H_c = 505.45$ Oe, $M_r = 27.63$ emu/g). The low value of H_c and

Table 2. EDX analysis of PrFeO₃ nano-sized powders annealed at 750 °C

Pr		Fe		O	
Wt%	At%	Wt%	At%	Wt%	At%
56.39	21.02	22.35	18.28	21.36	60.70

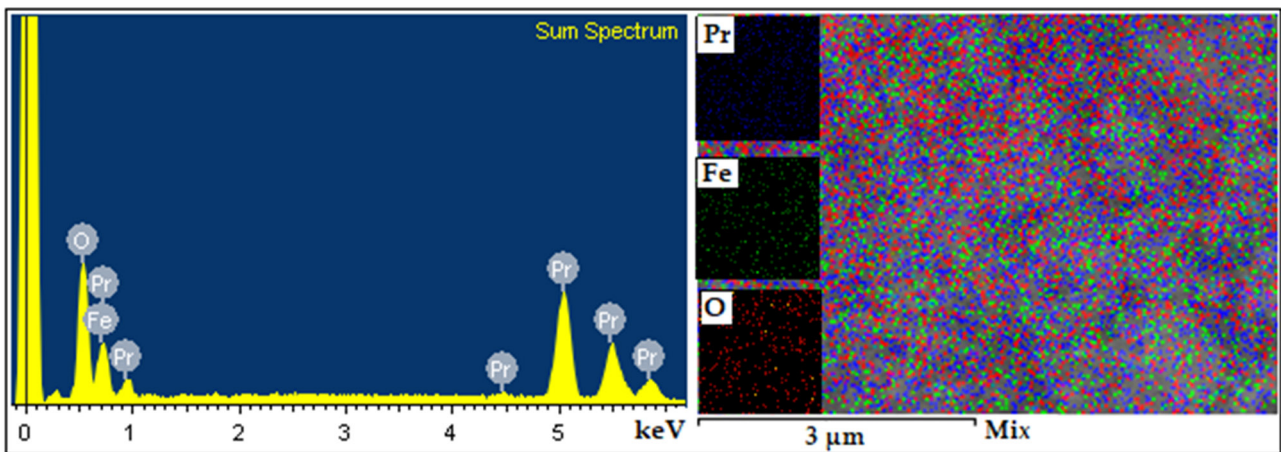


Fig 3. EDX and EDX-mapping images of PrFeO₃ sample annealed at 750 °C

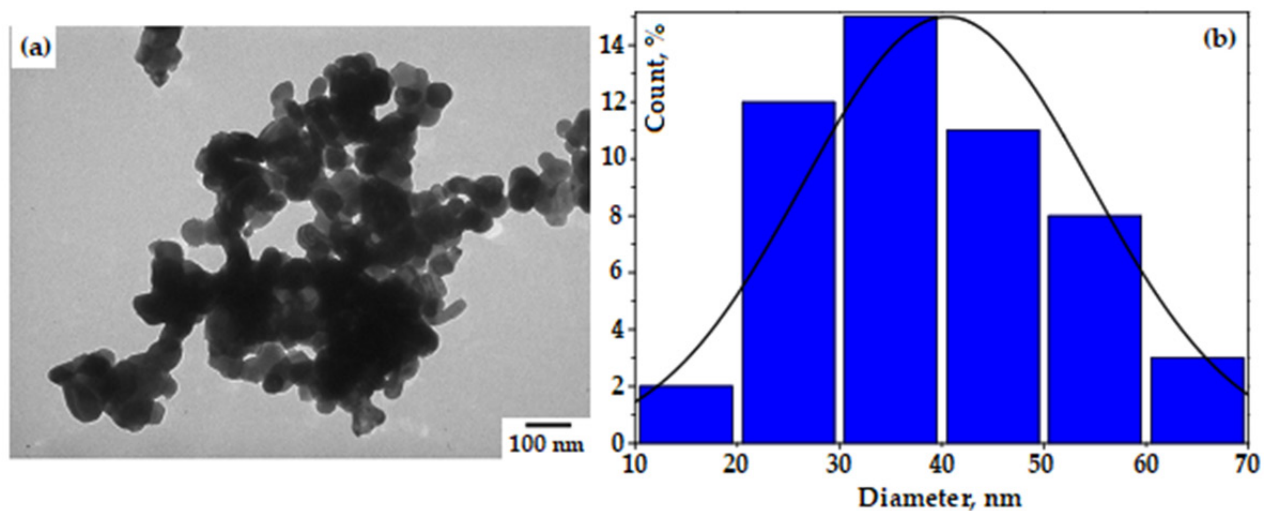


Fig. 4. (a) TEM image of PrFeO₃ sample annealed at 750 °C and (b) Particle size distribution

M_r could be originated from the homogeneity in shape and size of the PrFeO_3 nanoparticles with clear particle boundaries (see Fig. 4) while in the TEM image of the corresponding PrFeO_3 in [22], the particle boundaries are not observable with severe aggregation that joined the entire area of the material despite the particle size of 36.0 nm (by Image J).

Most interestingly, the magnetic parameters of PrFeO_3 nanomaterials changed irregularly with the annealing temperature (Table 1). The PrFeO_3 sample annealed at 750 °C has the lowest M_r (0.13 emu/g) while its M_s (1.10 emu/g) has the highest value. This can be ascribed by the highest crystallinity and crystal phase content of the PrFeO_3 sample annealed at 750 °C (see Table 1) which decreased the magnetocrystalline anisotropy of the material, leading to the rise in M_s and the decreased in M_r [23–24].

Thus, with low H_c , M_r and high M_s , obtained PrFeO_3 nanomaterials are soft magnetics that can be applied as material working under the external field as transformer cores, electromagnet cores, and conductive cores [24].

4. Conclusions

In this study, nanocrystalline praseodymium orthoferrite (o- PrFeO_3) was successfully synthesized by sol-gel method using water-methanol co-solvent. The PrFeO_3 nanocrystal

formed after annealing the precursor at different temperatures (650, 750, 850, and 950 °C) for 1 hour. The crystal size of PrFeO_3 samples are in the range of 45–70 nm (XRD, TEM). The PrFeO_3 sample annealed at 750 °C had the highest crystallinity (592.04 cts) and crystal phase content (93.4 %) (XRD) with smallest particle size (46.28 nm, TEM). The obtained PrFeO_3 nanomaterials are soft magnetic materials with low coercive force and remanent magnetization, high saturation magnetization.

Contribution of the authors

The authors contributed equally to this article.

Conflict of interests

The authors maintain that they have no conflict of interest to be described in this communication.

References

1. Opuchovic O., Kreiza G., Senvaitiene J., Kazlauskas K., Beganskiene A., Kareiva A. Sol-gel synthesis, characterization and application of selected sub-microsized lanthanide (Ce, Pr, Nd, Tb) ferrites. *Dyes and Pigments*. 2015;118: 176–182. <https://doi.org/10.1016/j.dyepig.2015.03.017>
2. Luxova J., Sulcova P., Trojan M. Influence of firing temperature on the color properties orthoferrite PrFeO_3 . *Thermochimica Acta*. 2014;579: 80–85, <http://dx.doi.org/10.1016/j.tca.2014.01.017>

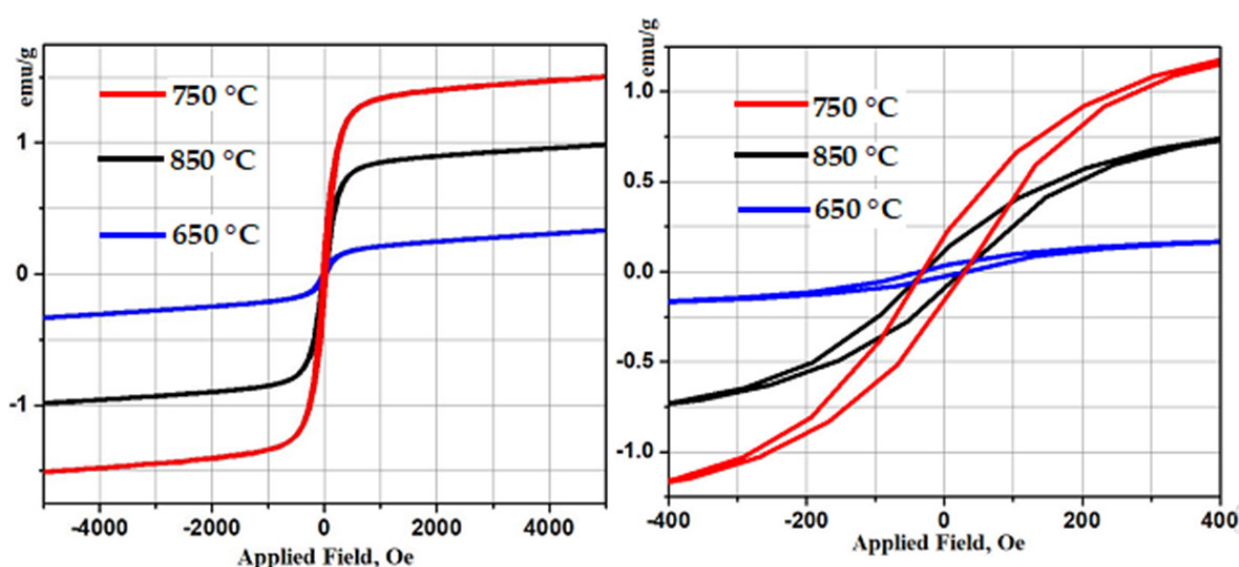


Fig. 5. Field dependence of the magnetization of PrFeO_3 nanoparticles annealed at 650, 750, and 850 °C for 1 h

3. Kondrashkova I. S., Martinson K. D., Zakharaova N. V., Popkov V. I. Synthesis of nanocrystalline HoFeO_3 photocatalyst via heat treatment of products of glycine-nitrate combustion, *Russian Journal of General Chemistry*. 2018;88(12): 2465–2471. <https://doi.org/10.1134/S1070363218120022>
4. Fergus J. W. Perovskite oxides for semiconductor-based gas sensors. *Sensors and Actuators B: Chemical*. 2007;123(2): 1169–1179. <https://doi.org/10.1016/j.snb.2006.10.051>
5. Oemar U., Ang P., Hidajat K., Kawi S. Promotional effect of Fe on perovskite $\text{LaNi}_x\text{Fe}_{1-x}\text{O}_3$ catalyst for hydrogen production via steam reforming of toluene. *International Journal Hydrogen Energy*. 2013;38(14): 5525–5534. <https://doi.org/10.1016/j.ijhydene.2013.02.083>
6. Mir F. A., Sharma S., Kumar R. Magnetizations and magneto-transport properties of Ni-doped PrFeO_3 thin films. *Chinese Physics B*. 2014;23(4): 048101. <https://doi.org/10.1088/1674-1056/23/4/048101>
7. Zhang L., Zhang X., Tian G., Zhang Q., Knapp M., Ehrenberg H., Chen G., Shen Z., Yang G., Gu L. Lithium lanthanum titanate perovskite as an anode for lithium ion batteries. *Nature communications*. 2020;11(1): 1–8. <https://doi.org/10.1038/s41467-020-17233-1>
8. Liu J., Sheha E., El-Dek S. I., Goonetilleke D., Harguindeguy M., Sharma N. SmFeO_3 and Bi-doped SmFeO_3 perovskites as an alternative class of electrodes in lithium-ion batteries. *CrystEngComm*. 2018;20(40): 6165–6172. <https://doi.org/10.1039/c8ce00780b>
9. Chen Ch., Jang P. W., Kim J. S. Ferroelectric and magnetic properties of PrFeO_3 - PbTiO_3 and PrFeO_3 - BiFeO_3 - PbTiO_3 thin films. *Japanese Journal of Applied Physics*. 2002;41(11B): 6777. <https://doi.org/10.1143/JJAP.41.6777>
10. Pekinchak O., Vasylechko L., Lutsyuk I., Vakhula Ya., Prots Yu., Carrillo-Cabrela W. Sol-gel-prepared nanoparticles of mixed praseodymium cobaltites-ferrites. *Nanoscale Research Letters*. 2016;11: 75. <https://doi.org/10.1186/s11671-016-1295-y>
11. Peisong T., Xinyu X., Haifeng Ch., Chunyan L., Yangbin D. Synthesis of nanoparticulate PrFeO_3 by sol-gel method and its visible-light photocatalytic activity. *Ferroelectrics*. 2019;546: 181–187. <https://doi.org/10.1080/00150193.2019.1592470>
12. Tijare S. N., Bakardjieva S., Subrt J., Joshi M. V., Rayalu S. S., Hishita S., Labhsetwar N. Synthesis and visible light photocatalytic activity of nanocrystalline PrFeO_3 perovskite for hydrogen generation in ethanol-water system. *Journal of Chemical Sciences*. 2014;126(2): 517–525. <https://doi.org/10.1007/s12039-014-0596-x>
13. Nguyen T. A., Nguyen L. T. Tr., Bui V. X., Nguyen D. H. T., Lieu H. D., Le L. M. T., Pham V. Optical and magnetic properties of HoFeO_3 nanocrystals prepared by a simple co-precipitation method using ethanol. *Journal of Alloys and Compounds*. 2020;834: 155098. <https://doi.org/10.1016/j.jallcom.2020.155098>
14. Nguyen A. T., Nguyen V. Y., Mittova I. Ya., Mittova V. O., Viryutina E. L., Hoang C. Ch. T., Nguyen Tr. L. T., Bui X. V., Do T. H. Synthesis and magnetic properties of PrFeO_3 by the co-precipitation method using ethanol. *Nanosystems: Physics, Chemistry, Mathematics*. 2020;11(4): 468–473. <https://doi.org/10.17586/2220-8054-2020-11-4-468-473>
15. Housecroft C. E., Sharpe A. G. *Inorganic Chemistry, 2nd edition*. Pearson: Prentice Hall; 2005.
16. Klein D. *Organic Chemistry, 2nd edition*. Wiley; 2016. chapter 13.
17. Nguyen A. T., Mittova I. Ya., Almjashaeva O. V., Kirillova S. A., Gusarov V. V. Influence of the preparation condition on the size and morphology of nanocrystalline lanthanum orthoferrite. *Glass Physics and Chemistry*. 2008;34(6): 756–761. <https://doi.org/10.1134/S1087659608060138>
18. Nguyen A. T., Mittova I. Ya., Almjashaeva O. V. Influence of the synthesis condition on the particle size and morphology of yttrium orthoferrite obtained. *Russian Journal of Applied Chemistry*. 2009;82(11): 1915–1918. <https://doi.org/10.1134/S1070427209110020>
19. Nguyen T. A., Pham V., Pham Th. L., Nguyen L. T. Tr., Mittova I. Ya., Mittova V. O., Vo L. N., Nguyen B. T. T., Bui V. X., Viryutina E. L. Simple synthesis of NdFeO_3 by the so-precipitation method based on a study of thermal behaviors of Fe (III) and Nd (III) hydroxides. *Crystals*. 2020;10: 219. <https://doi.org/10.3390/cryst10030219>
20. Abdollahi M., Abhari A. Sh., Bahmanpour M. Preparation and characterization of orthoferrite PrFeO_3 nanoceramic. *Ceramics International*. 2016;42(4): 4637–4641. <http://dx.doi.org/10.1016/j.ceramint.2015.12.027>
21. Brinker C. J., Scherer G. W. (eds.) *Sol-gel science: the physics and chemistry of sol-gel processing*. I Boston: Academic Press; 1990. 908 p.
22. Sudandararaj T. A. S., Kumar G. S., Dhivya M., Eithiraj R. D., Banu I. B. S. Spin reorientation transition in nanoscale multiferroic PrFeO_3 and its band structure calculation. *Journal of Alloys and Compounds*. 2020;817: 152747. <https://doi.org/10.1016/j.jallcom.2019.152747>
23. Nada F. A., Ahmed G., Ekram H. E-A. *Perovskite nanomaterials: Synthesis, characterization, and appli-*

cations, 1st ed. / Likun Pan, Guang Zhu (eds.). London: InTechOpen; 2016. Chapter 4, pp. 107–151. <https://doi.org/10.5772/61280>

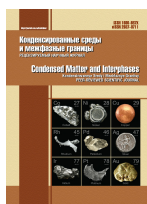
24. Cullity B. D., Graham C. D. *Introduction to magnetic materials, 2nd ed.* Canada: John Wiley & Sons, Inc., Publication; 2009. <https://doi.org/10.1002/9780470386323>

Information about the authors

Xuan Vuong Bui, PhD in Chemistry, Lecturer of Faculty of Natural Sciences, Sai Gon University, Ho Chi Minh City, Vietnam; e-mail: bxvuong@sgu.edu.vn. ORCID iD: <https://orcid.org/0000-0002-3757-1099>.

Anh Tien Nguyen, PhD in Chemistry, Chief of General and Inorganic Chemistry Department, Ho Chi Minh City University of Education, Vietnam; E-mail: tienna@hcmue.edu.vn. ORCID iD: <http://orcid.org/0000-0002-4396-0349>.

Received 13 April 2021; Approved after reviewing 30 April 2021; Accepted 15 May 2021; Published online 25 June 2021.



Condensed Matter and Interphases

Kondensirovannye Sredy i Mezhfaznye Granitsy
<https://journals.vsu.ru/kcmf/>

Original articles

Research article

<https://doi.org/10.17308/kcmf.2021.23/3430>

Growing epitaxial layers of InP/InGaAsP heterostructures on the profiled InP surfaces by liquid-phase epitaxy

M. G. Vasil'ev[✉], A. M. Vasil'ev, A. D. Izotov[✉], Yu. O. Kostin, A. A. Shelyakin

*Kurnakov Institute of General and Inorganic Chemistry of the Russian Academy of Sciences,
31 Leninsky prospekt, Moscow 119991, Russian Federation*

Abstract

The effect of various planes was studied when growing epitaxial layers by liquid-phase epitaxy (LPE) on the profiled InP substrates. The studies allowed obtaining buried heterostructures in the InP/InGaAsP system and creating highly efficient laser diodes and image sensors.

It was found that protruding mesa strips or in-depth mesa strips in the form of channels formed by the {111}A, {111}B, {110}, {112}A, or {221}A family of planes can be obtained with the corresponding selection of an etching agent, strip orientation, and a method of obtaining a masking coating. It was noted that in the case of the polarity of axes being in the direction of <111>, the cut of mesa strips was conducted along the most densely packaged planes. This cut led to the difference in rates of both chemical etching and epitaxial burying of profiled surfaces.

The cut was made along the planes at a low dissolution rate {111}A for a sphalerite lattice, to which the studied material, indium phosphide, belongs. Analysis of planes {110} and $\bar{1}10$ showed that the location of the most densely packaged planes {111}A and {111}B relative to them is different.

Keywords: Heterostructures, Laser diodes, Indium phosphide, Buried heterostructures, Channel in the substrate

Acknowledgements: the work was supported by the Ministry of Science and Higher Education of Russia as part of the state assignment of Kurnakov Institute of General and Inorganic Chemistry of the Russian Academy of Sciences.

For citation: Vasil'ev M. G., Vasil'ev A. M., Izotov A. D., Kostin Yu. O., Shelyakin A. A. Growing epitaxial layers of InP/InGaAsP heterostructures on the profiled InP surfaces by liquid-phase epitaxy. *Kondensirovannye sredy i mezhfaznye granitsy = Condensed Matter and Interphases*. 2021;23(2): 204–211. <https://doi.org/10.17308/kcmf.2021.23/3430>

Для цитирования: Васильев М. Г., Васильев А. М., Изотов А. Д., Костин Ю. О., Шелякин А. А. Выращивание эпитаксиальных слоев гетероструктур InP/InGaAsP на профилированных поверхностях InP методом жидкофазной эпитаксии. *Конденсированные среды и межфазные границы*. 2021;23(2): 204–211. <https://doi.org/10.17308/kcmf.2021.23/3430>

✉ Mikhail G. Vasil'ev, e-mail: mgvas@igic.ras.ru

✉ Alexander D. Izotov, e-mail: izotov@igic.ras.ru

© Vasil'ev M. G., Vasil'ev A. M., Izotov A. D., Kostin Yu. O., Shelyakin A. A., 2021



The content is available under Creative Commons Attribution 4.0 License.

1. Introduction

InP/InGaAsP heterostructures are the main type of structures used for obtaining quantum electronics devices, such as semiconductor lasers, superluminescent radiation sources, and photodiodes with a wavelength range from 1.20 to 1.65 μm which is the most important for the systems of fibre optic communication channels and fibre optic sensors [1–6]. The uniqueness of these structures is that InGaAsP solid solutions are isoperiodic to indium phosphide, which allows creating “perfect” heterojunctions suitable for wide application in engineering [7–9].

There are various methods for obtaining such heterostructures: liquid-phase epitaxy (LPE) [10,11], molecular-beam epitaxy (MBE) [12, 13], and metalorganic chemical vapour deposition (MOCVD) [14–16]. All these methods are aimed at the creation of heterostructures forming the basis of chips for quantum electronics devices. Creating chips from the structures that are grown using MBE and MOCVD methods requires foreign equipment and a unique post-growth technology for processing structures, which makes the technological cycle of the production of devices more complicated and expensive. It also requires high-precision and expensive technological equipment and is conducted under conditions of nonequilibrium growth, which complicates their creation on profiled surfaces.

At the same time, there are methods of obtaining epitaxial heterostructures on profiled surfaces [17, 18] that allow simplifying the technological cycle and creating chips for quantum electronics devices from solutions-melts in growth modes close to equilibrium using a rather simple and cheap LPE method and Russian equipment. These growth modes allow creating device structures with a high level of perfection of layers by simple doping of different layers of the structure in a wide range of concentrations of the dopant. Forming an initial profiled surface of substrates, it is possible to use a selective growth mode on various sides, thus creating the specified electrical and optical limitations for light transmission in laser diodes. The aim of this work was to study the modes of formation of profiled surfaces of indium phosphide as well as the growth of InP/InGaAsP heterostructures on profiled surfaces

and production of laser diodes with a spectral range of wavelengths 1300–1650 nm.

2. Experimental

2.1. Creating and burying a “fishtail” laser pinned structure

To determine the modes of formation of the profiled surface of indium phosphide and rates of epitaxial growth of InP layers and solid solutions InGaAsP, the samples of substrates InP with the orientation of planes $\{100\}$ were used. The orientation accuracy was ± 0.5 degrees.

The substrates with *n*-type conductivity were doped with Sn or S to a concentration of 10^{18} – 10^{19} cm^{-3} , the substrates with *p*-type conductivity were doped with Zn to the concentration of $(4\text{--}5)\cdot 10^{18}$ cm^{-3} . The substrates were mechanically polished to a thickness of 320 ± 10 μm . Then, after the mechanical polish, the samples were washed three times in organic solvents and etched in a polishing etching agent $\text{Br} : \text{CH}_3\text{COOH}$ to eliminate the damaged surface layer of ~ 10 μm . The masking coating for the further formation of a “fishtail” mesa was a SiO_2 film deposited using the method of pyrolytic reaction of SiH_4 and O_2 with the temperature of the InP substrate being 450 $^\circ\text{C}$. The thickness of the oxide film was 0.15 μm . The processes of liquid-phase epitaxy were conducted in the hydrogen atmosphere with the dew point of -80 $^\circ\text{C}$ in a plate made of high-purity MPG-7 graphite with a limited growth cell volume [19].

The profile of a strip was formed along the cleavage in the directions of $[110]$ or $[\bar{1}10]$. The direction of the strip in relation to the plane of the substrate was determined by etching an InP

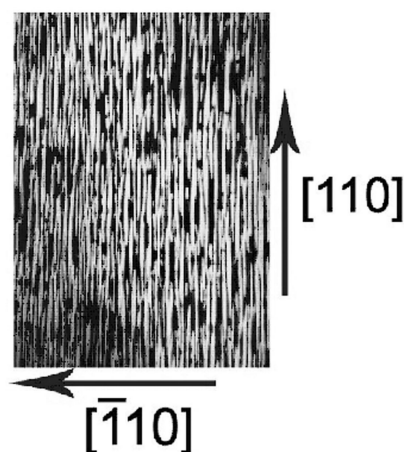


Fig. 1. Etching figures on plane (100)

substrate fragment ~ 1 mm wide with further etching in concentrated HCl for 2 minutes. Characteristic “straws” were formed on the surface of the InP substrate fragment, and their elongated part indicated the direction of [110]. The direction of $[\bar{1}10]$ was perpendicular to the elongated part of the “straws”.

Mesa strips were formed using a standard photolithography method. The width of a strip was 10 μm with the 400 μm interval between the strips. Further etching for the creation of a mesa strip structure was conducted at room temperature with normal lighting conditions and slight stirring of the solution. There are different chemical etching agents for indium phosphide [20]. The composition of the Br : CH_3COOH etching agent was used in this work as the most preferable for InP [21]. Geometric sizes of the profile were determined by the measurements in the “Epival” optical microscope with an amplification of $\times 450$. The cleavage for the determination of geometric sizes was made parallel to the planes {110}. The etching rate was calculated by the etching depth defined by the cleavage using an optical microscope. After the formation of the strips, the etched surface between them was mirror-smooth without any visible defects. Various volume ratios of this etching agent were used (1:160; 1:80; 1:25; 1:9). With the specified direction of the strip, the shape of the mesa strip structure did not change with different ratios of the etching agent. In our opinion, the most suitable ratio for Br : CH_3COOH was 1:9. The etching rate of this etching agent was 2 μm per minute on the samples without a masking coating. Further experiments on the formation of mesa strips were conducted by chemical etching in the Br : CH_3COOH mixture

with the 1:9 ratio. Depending on the orientation of masking strips, two types of mesa structures were obtained, see Fig. 2.

This etching agent was also used for test multi-layer InP/InGaAsP heterostructures without any deviations from the selected modes.

Analysis of planes (110) and $(\bar{1}10)$ showed [22] that the position of the most densely packaged planes {111}A in relation to them is different, see Fig. 3.

During the etching of the InP layer with the strip orientation along the direction of [110], the mesa strip had a shape of a fishtail limited by planes $(\bar{1}\bar{1})\text{A}$ and $(\bar{1}\bar{1})\text{A}$ which were located at an angle of $125^\circ 16'$ to (001) and by planes $(1\bar{1}2)$ and $(\bar{1}12)$ (angle $35^\circ 16'$). However, when the etching was conducted along the direction of $[\bar{1}10]$, the mesa strip had a shape of a hill limited by planes $(111)\text{A}$ and $(\bar{1}\bar{1}\bar{1})\text{A}$ which were located at an angle of $54^\circ 44'$ to (001). We studied the etching rates of indium phosphide substrates with different crystallographic orientations (111)A; (111)B; (100); (001). The changes in the etching rate of the substrates with different orientation are shown in Fig. 4.

We can see that $V_{(111)\text{B}} > V_{(100)} > V_{(111)\text{A}}$. It should be noted that the slowly etched plane (111)A always remains matt while planes (111)B, (100), and (001) are mirror-like. Such significant differences in the etching rates for various crystallographic orientations are apparently related to polar properties of the sphalerite lattice in the direction of $\langle 111 \rangle$.

Fig. 5 shows the etching rates of the mesa strip structure in the strip direction of $\langle 110 \rangle$. We can see that the etching rate of mesa strips in the Br : CH_3COOH etching agent greatly depends

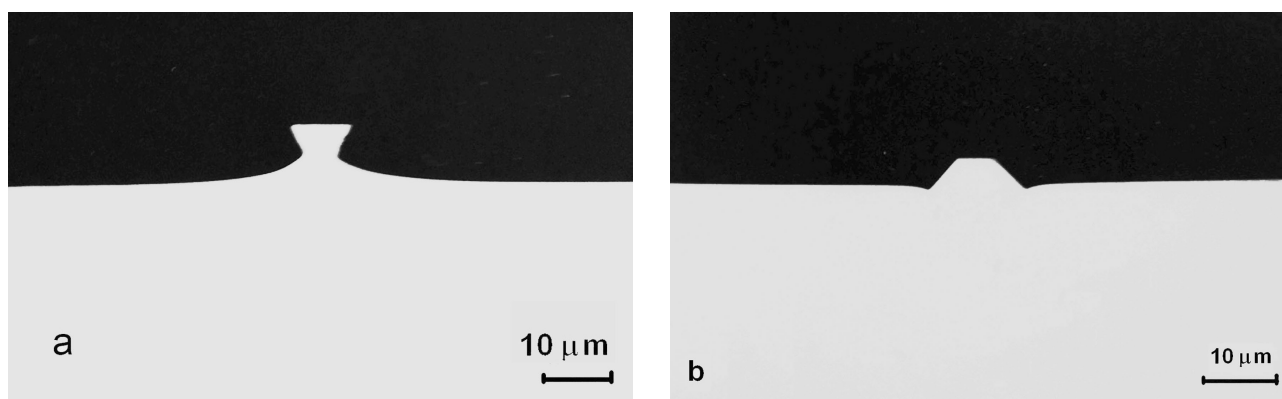


Fig. 2. Types of mesa strips depending on the orientation of the masking strips: a-[110], b- $[\bar{1}10]$

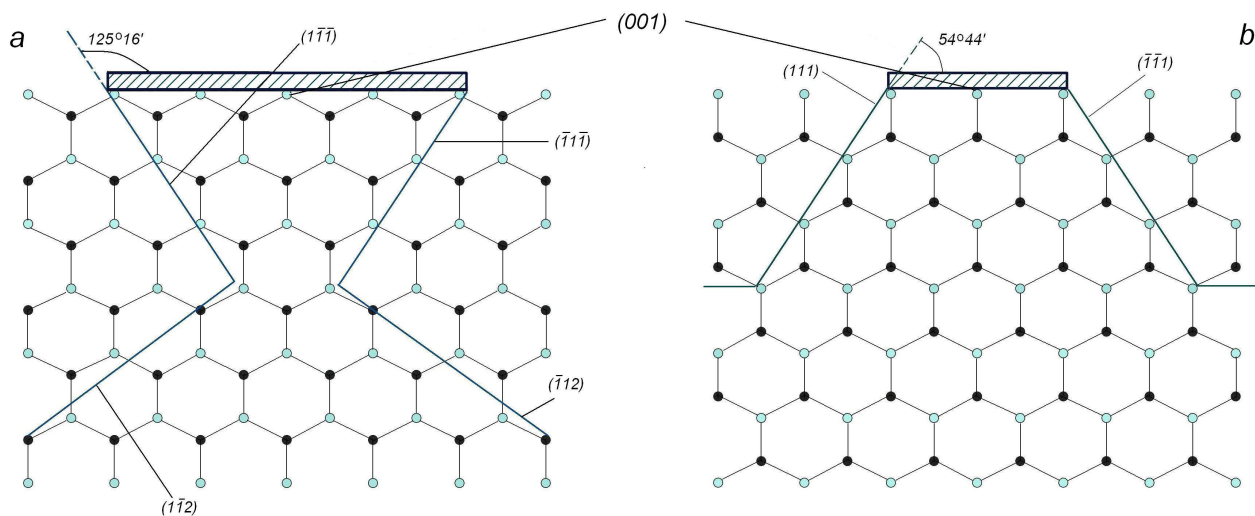


Fig. 3. Projection of the InP crystal structure on plane (110) – a and $(\bar{1}10)$ – b

on the mutual combination of planes cutting the mesa strip. It was also noted that the absolute values of the etching rates of the mesa strips changed their values when the etching agent was stirred, while the relative value of the rates remained constant.

Diffusion is important for determining the etching rate and can conceal the difference in the absolute rates of some low-index planes, although it cannot hide the insufficient reactivity properties of planes {111}A. We can also assume that masking coatings are highly significant both for diffusion processes during the formation of mesa strips and for their burying using the method of liquid-phase epitaxy.

A laser heterostructure was grown on the substrates of indium phosphide with the p-type conductivity. At first, an initial heterostructure was grown, an InP layer with the p-type conductivity, then an undoped layer of the GaInAsP solid solution and an InP layer with the n-type conductivity doped to the concentration of $1 \times 10^{19} \text{ cm}^{-3}$. After that, a mesa strip in the form of a fishtail was formed. A protruding mesa strip was buried with two layers of InP of the n-type and p-type conductivity respectively. These layers were “blocking layers” that limited the the flow of the current outside the mesa strip, so the pumping current of a laser diode flows only along the mesa strip at the lowest value outside the strip. Such limitation of current allows obtaining a laser diode with low operating current and good optical limitation of light emitted by the diode. The use

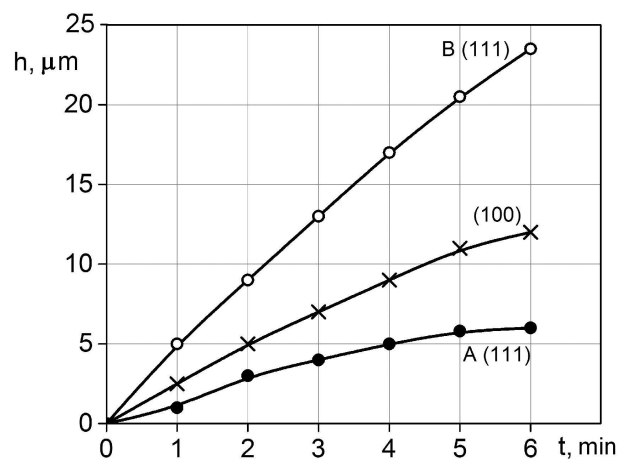


Fig. 4. Changing the rate of InP etching depending on the orientation of the substrate

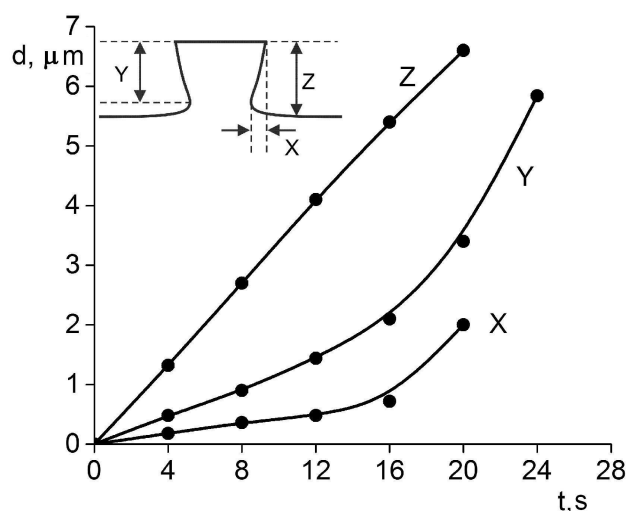


Fig. 5. Etching rate for mesa strips along the direction of [110] in the etching agent Br : CH_3COOH

of the InP substrates with the p-type conductivity allowed reducing the leakage currents outside the mesa strip and avoid using an additional contact layer of the GaInAsP solid solution required for the creation of an ohmic contact of the laser diode [21]. Burying was conducted in the temperature range of 620–600 °C with different degrees of supercooling of the solution-melt. A disadvantage of this structure is low reproducibility of the narrow part of the “fishtail” (active area of the laser diode) due to adsorption of the Br : CH₃COOH etching agent on the surface of the masking coating and its further diffusion into the etching area free from the masking coating. The same adsorption is also observed in the form of “excrescences” of crystals along the mesa strip during the process of growth from the solution-melt. These excrescences had a negative effect on the further formation of chips of laser diodes.

3. Results and discussion

During the experiments, it was shown that the masking coating must be removed from the surface of the mesa strip and epitaxial burying must be conducted without a masking coating in order to eliminate the adsorption.

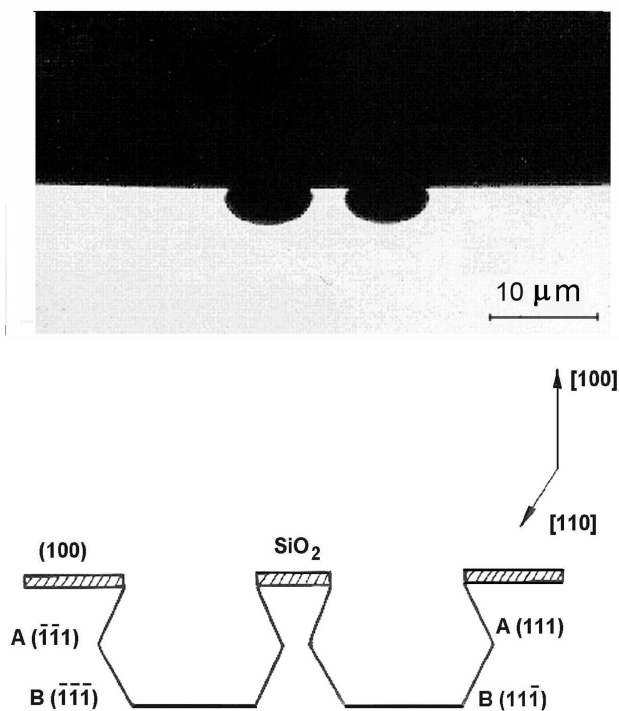


Fig. 6a Two-channel mesa strip

The experiment was conducted on the InP substrates with the p-type conductivity. Two barrier layers *n*-InP and *p*-InP were grown sequentially. It was noted that there was no growth on the surface when the mesa strip without a masking coating was less than 6 μm wide. This effect can presumably be explained by the fact that the growth of a more densely packaged plane (111)B requires a larger amount of InP as compared to plane (100). Therefore, InP actively moves towards plane (111)B in the solution-melt and is completely weakened above the surface of the mesa strip with the specified growth modes.

3.1. Creating and burying a two-channel laser strip structure

From a practical perspective, mesa strips with the minimum sizes of the radiation area of a future device are of special interest. For this reason, we considered an option of a mesa strip limited by two etched channels, see Fig. 6 (a, b). This structure of a mesa strip allows creating the “top” of a strip with a size less than 1–2 μm, which is highly important for the future laser structure, as this size is responsible for the size of the active area of the laser diode, and the size of 1.5–2.5 μm is considered optimal for lasers with a spectral range of wavelengths 1210–1650 nm.

A photoresist was used to create a two-channel mesa-strip structure, which considerably simplified the process of formation of the two-channel structure. A photoresist, placed using a standard photolithography method, was left on the surface after the formation of a pattern.

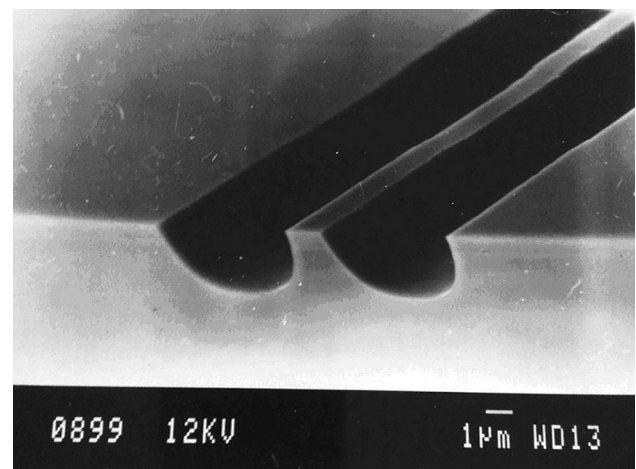


Fig. 6b Two-channel mesa strip structure after etching in the Br : CH₃COOH = 1:9 mixture

A two-channel mesa strip structure was formed on the InP (100) substrate with the direction of the strips [110] by chemical etching in the Br : CH₃COOH = 1 : 9 mixture. After the formation of the two-channel mesa strip, the photoresist was removed from the profiled surface (Fig. 6b).

In this case, there is no classic cut with planes (111)A; (1 $\bar{1}\bar{1}$)A; ($\bar{1}\bar{1}\bar{1}$)B; (11 $\bar{1}$)B, and (100), and the etching profile of the two-channel structure has a smooth transition between planes ($\bar{1}\bar{1}\bar{1}$)B; (11 $\bar{1}$)B, and (100). This smooth transition allowed levelling the growth rates of indium phosphide and GaInAsP solid solutions between the planes with a high index of the cut of the channels.

The buried two-channel laser structure on the InP/InGaAsP heterojunction was created in three stages: the first stage was growing the initial laser heterostructure InP/GaInAsP, the second stage was etching the mesa strips and removing the protective coating from the photoresist, and the third stage was growing blocking layers on the mesa strip structure.

At the first stage of LPE, the following layers were grown on the *n*-InP (001) substrate.

- An emitter layer of *n*-InP doped with Sn, $n = 2 \cdot 10^{18} \text{ cm}^{-3}$, 7 μm thick.

- An active layer of InGaAsP, undoped, 0.15 μm thick.

- An emitter layer of *p*-InP doped with Zn, $p = 3 \cdot 10^{17} \text{ cm}^{-3}$, 0.5 μm thick.

- A technological layer of InGaAsP, undoped, 0.5 μm thick.

At the second stage, a mesa strip was formed under the mask of the photoresist along direction $\langle 110 \rangle$ using photolithography. The geometry

of the strip before burying had the following sizes: width – 2.0–2.5 μm , height and width of side channels 7 μm each – 3 μm . After that, the photoresist was removed, and the profiled structure was sent to burying (Fig. 7b).

At the third stage of LPE, the mesa strip without a coating was buried with the blocking layers of *p*-InP and the layer of *n*-InP. Due to the set orientation, the selected geometry of mesa strips, and the controlled technological mode of growth from the liquid phase in the quasi-equilibrium mode, the blocking layers were grown only in the channels and on the planar section of the surface between the channels, but there was no growth on the mesa strip itself. Then the next blocking layer of *p*-InP and a contact layer of *p*+InGaAsP were grown, which made the surface of the two-channel buried heterostructure almost planar. The buried InP/GaInAsP two-channel laser heterostructure is presented in Figs. 7a and b.

After that, a part of the substrate was removed by chemical-dynamic polishing [22] and ohmic contacts were deposited: Au + Sn on the *n*-side, Au + Zn on the *p*-side. The planar structure was cleaved into separate chips 400 μm wide and 350 μm long. The chips were mounted on a copper cold conductor using an indium solder, and the parameters of laser diodes were measured.

Laser diodes made from the chips of the buried two-channel structure had the following parameters:

- The threshold current was $\sim 10 \div 15 \text{ mA}$ at 25 °C.

- The differential quantum efficiency was $\sim 50 \%$.

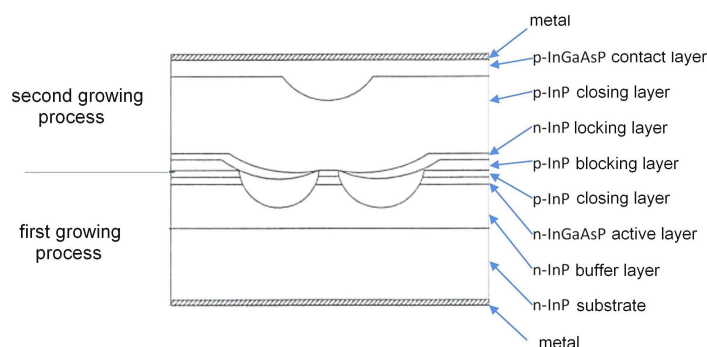


Fig. 7a A schematic representation of the buried two-channel laser heterostructure InP/GaInAsP

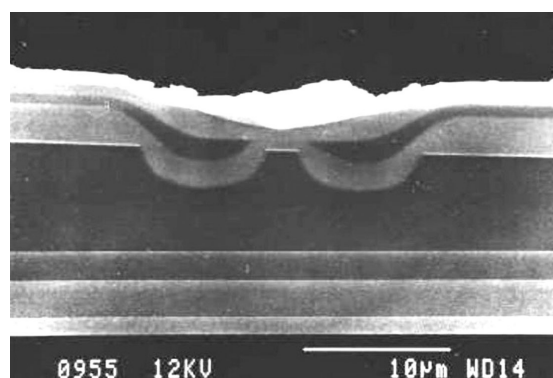


Fig. 7b Microphoto of the buried two-channel laser heterostructure InP/GaInAsP

- The linearity of watt-ampere characteristics was observed up to a power of ~ 20 MW.
- The radiation wavelength was 1320 nm.
- The yield ratio was ~ 30 %.

4. Conclusions

We studied the mechanisms of the formation of profiled surfaces of indium phosphide with different orientations of a substrate and mesa strips. We determined the modes of creation of profiled surfaces for obtaining laser diodes in the wavelength range of 1210–1650 nm. The modes of growing laser heterostructures on the InP profiled surfaces were also studied. We proposed a Russian technology for the creation of laser diode chips using Russian equipment. It was shown that the conditions of nonequilibrium growth of thin layers from the liquid phase on a profiled surface allowed conducting unique processes of local growth.

Based on the buried two-channel laser heterostructures we obtained highly efficient Russian laser diode chips working in a continuous mode of generation. The suggested technology allows obtaining laser diodes in the wavelength range from 1210 to 1650 nm. The diode chips can be used in fibre optic communication channels, environmental monitoring systems, and other quantum electronics devices.

We studied the processes of creation of buried laser mesa structures InP/GaInAsP on the profiled surfaces of indium phosphide.

It was shown that the set orientation of mesa strips along the directions of $\langle 110 \rangle$ with the orientation of the substrates on plane (001) is highly important for obtaining these structures. We determined optimal etching agents and etching modes for creation of the profiled surface of indium phosphide. We discovered masking coatings for the creation of a complex profiled relief of the surface of indium phosphide. We described an original technology for the creation of an InP/GaInAsP two-channel laser heterostructure on the profiled surface without a protective growth coating with the width of the active area of 1.5–2.5 μm , which allows obtaining single-mode laser diodes with high quantum efficiency.

Contribution of the authors

All authors have contributed equally to the publication.

Conflict of interests

The authors declare that they have no known competing financial interests or personal relationships that could have influenced the work reported in this paper.

References

1. Andreev D. S., Boltar K. O., Vlasov P. V., Irodov N. A., Lopuhin A. A. Investigation of planar photodiodes of a focal plane array based on a heteroepitaxial InGaAs/InP structure. *Journal of Communications Technology and Electronics*. 2016;61(10): 1220–1225. <https://doi.org/10.1134/S1064226916100028>
2. Kong J., Ouyang X. W., Zhou A., Yuan L. B. Highly sensitive directional bending sensor based on eccentric core fiber Mach–Zehnder modal interferometer. *IEEE Sensors Journal*. 2016;16 (18): 6899–6902. <https://doi.org/10.1109/jsen.2016.2589262>
3. Khan M. Z. M., Ng T. K., Ooi B. S. High-Performance 1.55- μm superluminescent diode based on broad gain InAs/InGaAlAs/InP quantum dash active region. *IEEE Photonics Journal*. 2014;6(4): 1–8. <https://doi.org/10.1109/jphot.2014.2337892>
4. Eichler H. J., Eichler J., Lux O. Semiconductor lasers. In: *Lasers. Springer Series in Optical Sciences. Vol 220*. Springer, Cham.; 2018. p. 165–203. https://doi.org/10.1007/978-3-319-99895-4_10
5. Guin S., Das N. R. Modeling power and linewidth of quantum dot superluminescent light emitting diode. *Journal of Applied Physics*. 2020;128(8): 083102. <https://doi.org/10.1063/1.5131550>
6. Sychikova Ya. A. *Nanorazmernye struktury na poverkhnosti fosfida indiya* [Nanoscale structures on the surface of indium phosphide]. LAP Lambert Academic Publishing; 2014. 132 p. (In Russ.)
7. Lei P. H., Yang C. D., Wu M., et al. Optimization of active region for 1.3- μm GaInAsP compressive strain multiple-quantum-well ridge waveguide laser diodes. *Journal of Electronic Materials*. 2006;35(2): 243–249. <https://doi.org/10.1007/BF02692442>
8. Emelyanov V. M., Sorokina S. V., Khvostikov V. P., Shvarts M. Z. Simulation of the characteristics of InGaAs/InP-based photovoltaic laser-power converters. *Semiconductors*. 2016;50(1): 132–137. <https://doi.org/10.1134/S1063782616010097>
9. Andreeva E. V., Ilchenko S. N., Ladugin M. A., Marmalyuk A. A., Pankratov K. M., Shidlovskii V. R., Yakubovich S. D. Superluminescent diodes based on asymmetric double-quantum-well heterostructures. *Quantum Electronics*. 2019;49(10): 931–935. <https://doi.org/10.1070/qel17071>
10. Saidov A. S., Usmonov Sh. N., Saidov M. S. Liquid-phase epitaxy of the $(\text{Si}_2)_{1-x-y}(\text{Ge}_2)_x(\text{GaAs})_y$ substitutional solid solution ($0 \leq x \leq 0.91, 0 \leq y \leq 0.94$)

and their electrophysical properties. *Semiconductors*. 2015;49(4): 547–550. <https://doi.org/10.1134/s106378261504020x>

11. Vorotyntsev V. M., Skupov V. D. *Bazovye tekhnologii mikro- i nanoelektroniki* [Basic technologies of micro- and nanoelectronics]. Prospekt Publ.; 2017. 520 p. (In Russ.)

12. Preobrazhenskii V. V., Putyato M. A., Semyagin B. R. Measurements of parameters of the low-temperature molecular-beam epitaxy of GaAs. *Semiconductors*. 2002;36(8): 837–840. <https://doi.org/10.1134/1.1500455>

13. Abramkin D. S., Bakarov A. K., Putyato M. A., Emelyanov E. A., Kolotovkina D. A., Gutakovskii A. K., Shamirzaev T. S. Formation of low-dimensional structures in the InSb/AlAs heterosystem. *Semiconductors*. 2017;51(9): 1233–1239.

<https://doi.org/10.1134/s1063782617090020>

14. Akchurin R. Kh., Marmalyuk A. A. *MOS-gidridnaya zpitaksiya v tekhnologii materialov fotoniki i elektroniki* [MOS-hydride absorption in photonics and electronics materials technology]. Tekhnosfera Publ.; 2018. 487 p. (In Russ.)

15. Gagis G. S., Vasil'ev V. I., Levin R. V., Marichev A. E., Pushnyi B. V., Kuchinskii V. I., Kazantsev D. Yu., Ber B. Ya. Investigation of the effect of doping on transition layers of anisotype GaInAsP and InP heterostructures obtained by the method of MOCVD. *Technical Physics Letters*. 2020;46: 961–963. <https://doi.org/10.1134/S1063785020100053>

16. Hasan S., Richard O., Merckling C., Vandervorst W. Encapsulation study of MOVPE grown InAs QDs by InP towards 1550 nm emission. *Journal of Crystal Growth*. 2021;557: 126010. <https://doi.org/10.1016/j.jcrysgro.2020.126010>

17. Vasil'ev M. G., Izotov A. D., Marenkin S. F., Shelyakin A. A. Preparation of shaped indium phosphide surfaces for edge-emitting devices. *Inorganic Materials*. 2019;55(1): 105–108. <https://doi.org/10.1134/s0020168519010175>

18. Mamutin V. V., Ilyinskaya N. D., Bedarev D. A., Levin R. V., Pushnyi B. V. Study of postgrowth processing in the fabrication of quantum-cascade lasers. *Semiconductors*. 2014;48(8): 1103–1108. <https://doi.org/10.1134/s1063782614080181>

19. Vasil'ev M. G., Vasil'ev A. M., Kostin Yu. O., Shelyakin A. A. and Izotov A. D. Study of linear light edge-emitting diodes based on InP/InGaAsP/InP heterostructure with the crescent active region. *Inorganic Materials: Applied Research*. 2018;9(5): 813–816. <https://doi.org/10.1134/S2075113318050295>

20. Vasil'ev M. G., Vasil'ev A. M., Vilk D. M., Shelyakin A. A. LPE growth of InP/InGaAsP/InP

heterostructures and separate preparation of high-temperature solutions. *Inorganic Materials*. 2007;43(7): 683–688. <https://doi.org/10.1134/s0020168507070011>

21. Blank T. V., Gol'dberg Yu. A. Mechanisms of current flow in metal-semiconductor ohmic contacts. *Semiconductors*. 2007;41(11): 1263–1292. <https://doi.org/10.1134/s1063782607110012>

22. Vasil'ev M. G., Vasil'ev A. M., Izotov A. D., Shelyakin A. A. Preparation of indium phosphide substrates for epilayer growth. *Inorganic Materials*. 2018;54(11): 1109–1112. <https://doi.org/10.1134/s0020168518110158>

Information about the authors

Mikhail G. Vasil'ev, DSc in Technical Sciences, Professor, Head of the Laboratory of Semiconductor and Dielectric Materials, Kurnakov Institute of General and Inorganic Chemistry of the Russian Academy of Sciences, Moscow, Russian Federation, e-mail: mgvas@igic.ras.ru. ORCID iD: <https://orcid.org/0000-0002-4279-1707>.

Anton M. Vasil'ev, Researcher Fellow, Kurnakov Institute of General and Inorganic Chemistry of the Russian Academy of Sciences, Moscow, Russian Federation, e-mail: toto71@bk.ru. ORCID iD: <https://orcid.org/0000-0002-9901-5856>.

Alexander D. Izotov, DSc in Chemistry, Corresponding Member of Russian Academy of Sciences, Chief Researcher at the Laboratory of Semiconductor and Dielectric Materials, Kurnakov Institute of General and Inorganic Chemistry of the Russian Academy of Sciences, Moscow, Russian Federation, e-mail: izotov@igic.ras.ru. ORCID iD: <https://orcid.org/0000-0002-4639-3415>.

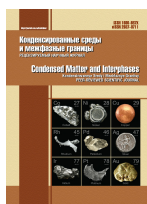
Yuriy O. Kostin, PhD in Technical Science, Senior Researcher, Kurnakov Institute of General and Inorganic Chemistry of the Russian Academy of Sciences, Moscow, Russian Federation, e-mail: mgvas@igic.ras.ru. ORCID iD: <https://orcid.org/0000-0001-8172-3988>.

Alexey A. Shelyakin, PhD in Technical Science, Senior Researcher at the Laboratory of Semiconductor and Dielectric Materials, Kurnakov Institute of General and Inorganic Chemistry of the Russian Academy of Sciences, Moscow, Russian Federation, e-mail: mgvas@igic.ras.ru. ORCID iD: <https://orcid.org/0000-0003-0028-005X>.

Received 16 February 2021; Approved after reviewing 30 March 2021; Accepted for publication 15 May 2021; Published online 25 June 2021.

Translated by Valentina Mittova

Edited and proofread by Simon Cox



Original articles

Research article

<https://doi.org/10.17308/kcmf.2021.23/3431>

Anomalous behaviour of dynamic electrical conductivity in semiconductor ferroelectric ceramics near the phase transition temperature

G. S. Grigoryan✉, A. M. Solodukha

Voronezh State University,
1 Universitetskaya pl., Voronezh 394018, Russian Federation

Abstract

The article presents the results of a study of the electrical properties of semiconductor perovskite ceramics based on a solid solution of barium-strontium titanate with the addition of the rare earth element of cerium with the initial formula $Ba_{1-x-y}Sr_xCe_yTiO_3$ ($x = 0.05$, $y = 0.003$). A scanning electron microscope was used to obtain images of the sample surfaces and the elemental composition data. The measurements were performed by impedance spectroscopy in the temperature range of 348–385 K in the frequency range of 10^2 – 10^6 Hz using an LCR metre. It was found that there is an anomalous behaviour in the dynamic electrical conductivity of the samples in the temperature range close to the ferroelectric-paraelectric phase transition. This is expressed by a decrease in the value of the real part of the dynamic conductivity with an increase in frequency. An analysis of the simplified equivalent circuit of the intergranular barrier showed that this anomaly can be explained by introducing an inductive element into the circuit. This element can be considered a “negative capacitance element”. Following the results of the study, a conclusion was made about the generalised character of the phenomenon.

Keywords: Semiconductor ceramics, Impedance spectroscopy, Negative capacitance effect, Posistor

Acknowledgements: The authors are grateful to the Centre for the Collective Use of Scientific Equipment of Voronezh State University for qualified assistance in conducting structural studies.

For citation: Grigoryan G. S., Solodukha A. M. Anomalous behaviour of dynamic electrical conductivity in semiconductor ferroelectric ceramics near the phase transition temperature. *Kondensirovannye sredyimezhfaznyegranitsy=Condensed Matter and Interphases*. 2021; 23 (2): 212–217. <https://doi.org/10.17308/kcmf.2021.23/3431>

Для цитирования: Григорян Г. С., Солодуха А. М. Аномальное поведение динамической электропроводности в полупроводниковой сегнетоэлектрической керамике вблизи температуры фазового перехода. *Конденсированные среды и межфазные границы*. 2021;23(2): 212–217. <https://doi.org/10.17308/kcmf.2021.23/3431>

✉ Gevorg S. Grigoryan, e-mail: gri7287@yandex.ru
© G. S. Grigoryan, A. M. Solodukha, 2021



The content is available under Creative Commons Attribution 4.0 License.

1. Introduction

The study of barium-strontium titanate (BST) ceramics with rare earth elements has attracted the attention of researchers for many years [1–4]. Such interest is due to the fact that above the Curie temperature, there is a sharp increase in sample resistance, i.e. there is an effect of positive temperature coefficient resistance (PTCR), which enables the extensive practical use of the material. The mechanism of this effect has not been fully understood yet. Various models have been proposed, but the most widely recognised was the Heywang model [5], in which the temperature behaviour of doped titanates is attributed to phenomena occurring at the grain boundaries. The idea of the model is that at the grain boundary (GB) there are acceptor states with trapped electrons. This leads to the formation of a barrier layer similar to the Schottky barrier. The transition from the ferroelectric phase to the paraelectric phase leads to an increase of the barrier height and as a consequence the PTCR effect.

At the same time, an anomalous behaviour of electric quantities (so called “negative capacitance effect”) is observed in some oxide heterostructures, Schottky diodes, and metal-dielectric (ferroelectric)-semiconductor structures (MIS structures). This shows as a change in the nature of a sample’s impedance from capacitive to inductive. The study of this effect can give way to new micro and nanoelectronic devices, in particular to an increase in the capacity superdense dynamic RAM systems [6–17]. Since the negative capacitance effect can be found in heterophase structures, it is reasonable to assume that it is associated with phenomena at interphase boundaries of a different nature: at the grain boundaries in polycrystals, the barriers in the semiconductor diodes, at the metal-semiconductor or semiconductor-insulator barriers in MIS-structures.

Therefore, the aim of this work was to study the negative capacitance effect within the radio range of the test signal frequency at the Schottky barriers which are formed in the grain boundaries of posistor ceramics.

2. Experimental

Ceramic samples with the initial formula $\text{Ba}_{1-x-y}\text{Sr}_x\text{Ce}_y\text{TiO}_3$ ($x = 0.05$, $y = 0.003$) in the form

of tablets 10 mm in diameter and 1 mm thick were prepared by the technology of solid-phase pressing for posistors [18]. Trivalent cerium ions penetrate into the perovskite lattice and substitute divalent barium ions, which leads to the formation of semiconductor ceramics with an electronic type of conductivity, i.e. the following reaction takes place:



Following the preparation of samples, a microscopic examination of their morphology and elemental composition was conducted using a JEOL JSM 6380LV scanning electron microscope. Fig. 1 shows a micrograph of the mechanically chipped surfaces of the BST ceramics, which allows thoroughly analysing the shape and size of the crystallites, as well as the intercrystalline space. By the nature of the mechanical chipping it is obvious that the microcrystalline ceramic structure is fairly homogeneous and the size of most grains varies between 5 and 8 μm . The elemental analysis showed that the ratio between the sum of the N_{Ba} and strontium atom concentrations and the concentration of titanium atoms $\frac{N_{\text{Ba}} + N_{\text{Sr}} + N_{\text{Ce}}}{N_{\text{Ti}}} = 0.96$ corresponds (within the measurement accuracy) to the initial composition.

Electrical measurements were performed in the frequency range of 10^2 – 10^6 Hz and the temperature range of 348–385 K by impedance spectroscopy using a WK 4270 LCR metre. In-

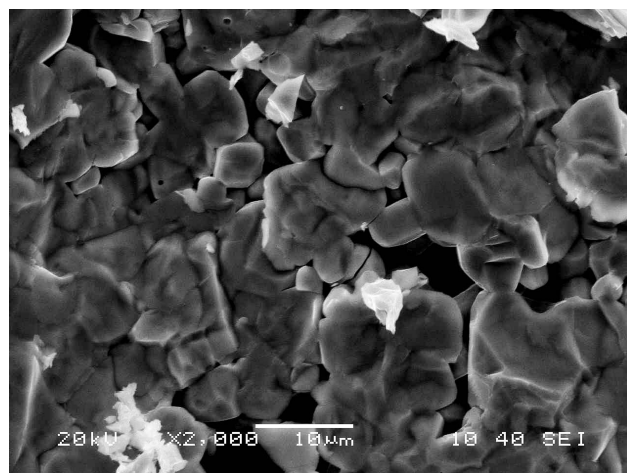


Fig. 1. Electron microscope image of the ceramic grains

Ga electrodes were previously deposited on the sample surfaces. It was found that for a temperature range of 293–348 K the contact resistance is negligible compared to the resistance of the sample.

The test signal amplitude was 0.3 V, the sample temperature was recorded with a thermocouple with an accuracy of ± 1 °C.

The indications of the LCR metre allowed determining the sample impedance module and the phase angle displacement between current and voltage. The dynamic conductivity Y was calculated from the impedance Z data using following formulas:

$$Y = \text{Re}Y + i\text{Im}Y = \frac{1}{Z}; Z = z \cos \varphi - iz \sin \varphi,$$

where Y and Z are complex values, z is the impedance module, φ is the phase angle displacement between current and voltage, i is an imaginary number.

3. Results and discussion

Fig. 2 shows the frequency dependence of the real part of the complex conductivity at various temperatures. In the range of high temperatures, the conductivity monotonously grows as, according to [5], there is an increase in the height of the potential barrier due to a decrease in

values of the dielectric permittivity near the grain boundaries (Fig. 2a). However, in the temperature range below the phase transition when the PTCR effect is slightly manifested, the behaviour is atypical: with an increase in frequency the conductivity first decreases and then increases, i.e. frequency dependencies show the minimum conductivity (Fig. 2b). Such behaviour may be due to the presence of the inductive circuit element or the “negative capacitance” effect. Structures, in which this effect was detected, have one thing in common: inertial conductivity whose mechanism can have its own peculiarities in each particular case.

We are not talking here about a real effect of the self-induced electromotive force, i.e. such an effect should be enhanced with an increase in frequency, while in the studied samples it is observed in the low-frequency region. However, the inductance can be considered as an inertial factor caused by the presence of a “delayed barrier” at grain boundaries as proposed in [19].

Let’s consider a simplified equivalent circuit (Fig. 3) of the grain boundary (GB) where one R - L link reflects the Joule energy dissipation and the inertance of the charge carriers, and the other R - C link considers the displacement current and dielectric losses of bound carrier oscillations in the space charge region (SCR).

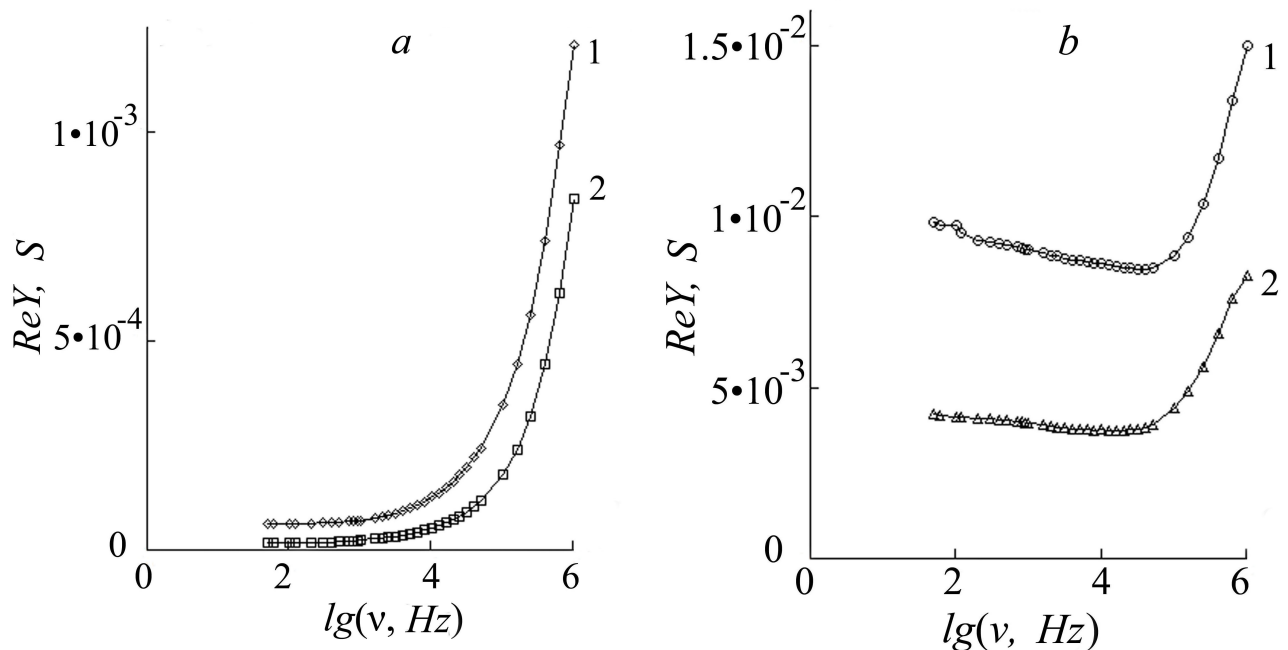


Fig. 2. Frequency dependence of the real part of the complex conductivity at different temperatures: a – curve 1 at $t = 75$ °C, curve 2 at $t = 81$ °C; b – curve 1 at $t = 103$ °C, curve 2 at $t = 102$ °C

Let Y_1 and Y_2 be admittance of the first and second link, respectively (see Fig. 3). Then admittance of the whole chain is $Y = Y_1 + Y_2$. As $Y = 1/Z$, then:

$$Y_1 = \frac{1}{Z_1} = \frac{1}{R_1 + i\omega L} = \frac{R_1}{R_1^2 + (\omega L)^2} - i \frac{\omega L}{R_1^2 + (\omega L)^2};$$

$$Y_2 = \frac{1}{Z_2} = \frac{1}{R_2 - \frac{i}{\omega C}} = \frac{R_2}{R_2^2 + \frac{1}{(\omega C)^2}} + i \frac{1}{R_2^2 + \frac{1}{(\omega C)^2}};$$

$$\text{Re}(Y_1) = \frac{R_1}{R_1^2 + (\omega L)^2}; \text{Re}(Y_2) = \frac{R_2}{R_2^2 + \frac{1}{(\omega C)^2}};$$

$$\text{Re}Y = \text{Re}(Y_1) + \text{Re}(Y_2).$$

where $\omega = 2\pi\nu$ is the cyclic frequency.

Fig. 4 shows the frequency dependences of real admittance components for each link and the whole chain. It is obvious that $\text{Re}Y$ in the range of $10^2 - 10^3$ Hz decreases and then increases with an increase in frequency. Thus, even a simplified circuit with an inductive element allows qualitatively interpreting the results of the experiment.

[20] proposed a method for presenting experimental data for a particular frequency band using CY – diagrams, where C and Y are real components of electric capacity and conductivity, respectively. Such an approach allows identifying the characteristic features of equivalent circuits with the inductance and capacitance elements.

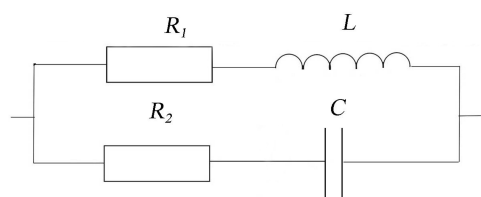


Fig 3. Simplified equivalent circuit of the grain boundary

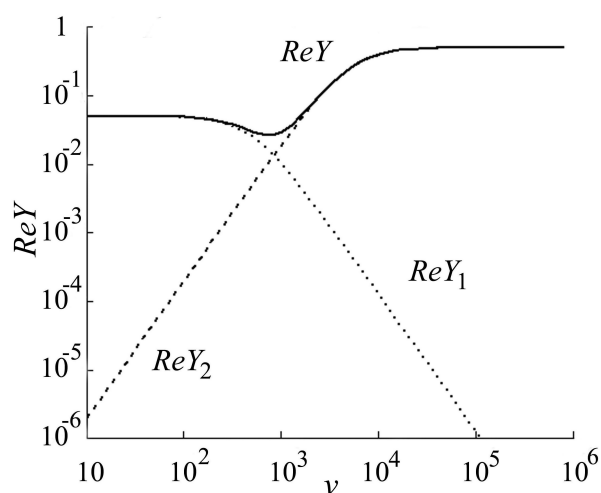


Fig 4. Frequency dependences of real admittance components for each link and the whole chain. The calculations are performed using the MathCAD package at the following values of parameters (in measurement units) $R_1 = 20, R_2 = 2, C = 10^{-4}, L = 4 \cdot 10^{-2}$

The results obtained for coordinates CY are shown in Fig. 5. It is seen that with an increase in temperature the shape of the curves is changed from the characteristic loops to a nearly vertical dip. Curves 1 and 2 exactly correspond to the theoretical calculations with regard to the

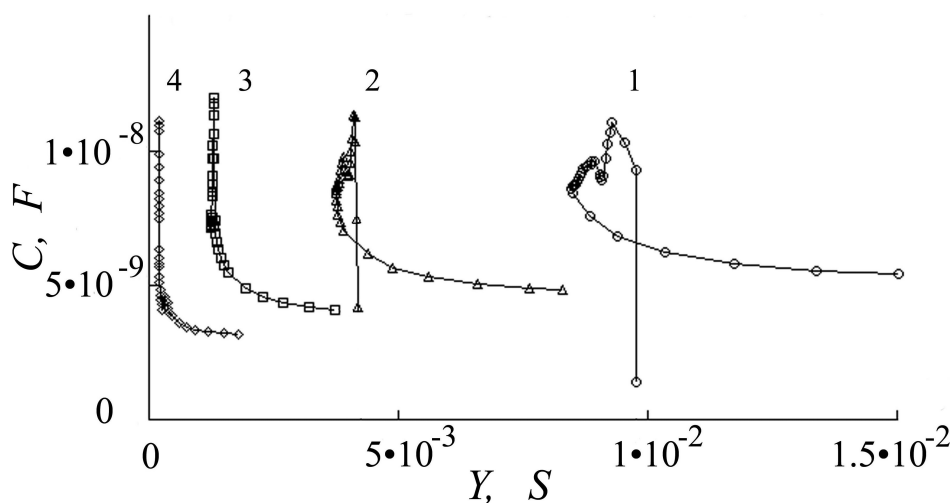


Fig 5. Capacity dependence on conductivity at different temperatures (in °C) 1 – 75; 2 – 81; 3 – 87; 4 – 97

equivalent circuit with an inductive element, obtained in [21].

4. Conclusions

The experiments showed that a ceramic posistor based on a solid solution of barium-strontium titanate with the addition of cerium (0.3 at%) demonstrates an anomalous behaviour of the dynamic conductance. The analysis of the simplified circuit of the grain boundary indicates a manifestation of the negative capacitance effect. Considering the fact that this effect occurs both in devices with p - n transitions and in semiconductor ceramic samples of different compositions, we can assume that it is connected to processes of charge carrier capture in the energy barrier areas, and is possibly of a generalised character.

Contribution of the authors

A. M. Solodukha – research concept, results analysis, text editing. G. S. Grigoryan – conducting research, methodology development, writing of text, final conclusions.

Conflict of interests

The authors declare that they have no known competing financial interests or personal relationships that could have influenced the work reported in this paper.

References

1. Lines and M. E., Glass A. M. *Principles and applications of ferroelectrics and related Materials*. Oxford University Press; 2001. <https://doi.org/10.1093/acprof:oso/9780198507789.001.0001>
2. Moulson A. J. *Electroceramics: Materials, Properties*. Wiley; 2003. p. 576. <https://doi.org/10.1002/0470867965>
3. Chen Y. L., Yang S. F. PTCR effect in donor doped barium titanate: review of compositions, microstructures, processing and properties. *Advances in Applied Ceramics*. 2011; 110(5): 257–269. <https://doi.org/10.1179/1743676111Y.0000000001>
4. Katsu H. *Crystal- and defect-chemistry of fine grained thermistor ceramics on BaTiO₃ basis with BaO-excess*. Schriften des Forschungszentrums Jülich. Reihe Information; 2011;18: p. 163.
5. Heywang W. Semiconducting barium titanate. *Journal of Materials Science*. 1971;6: 1214–1226. <https://doi.org/10.1007/BF00550094>
6. Champness C. H., Clark W. R. Anomalous inductive effect in selenium Schottky diodes. *Applied Physics Letters*. 1990;56(12): 1104–1106. <https://doi.org/10.1063/1.102581>
7. Wu X., Yang E. S., Evans H. L. Negative capacitance at metal-semiconductor interfaces *Journal of Applied Physics*. 1990;68(6): 2845–2848. <https://doi.org/10.1063/1.346442>
8. Gavriyachenko V. G., Kabirov Y. V., Panchenko E. M., Sitalo E. I., Gavriyachenko T. V., Milov E. V., Lyanguzov N. V. Specific features of the dielectric spectrum of CaCu₃Ti₄O₁₂ in the low-frequency range. *Physics of the Solid State*. 2013;55(8): 1651–1654. <https://doi.org/10.1134/s1063783413080131>
9. Zagni N., Pavan P., Alam M. A. Two-dimensional MoS₂ negative capacitor transistors for enhanced (super-Nernstian) signal-to-noise performance of next-generation nano biosensors. *Applied Physics Letters*. 2019;114: 233102. <https://doi.org/10.1063/1.5097828>
10. Ko E., Shin J., Shin C. Steep switching devices for low power applications: negative differential capacitance/resistance field effect transistors. *Nano Convergence*. 2018;5(2): 1–9. <https://doi.org/10.1186/s40580-018-0135-4>
11. Li J., Liu Y., Han G., Zhou J., Hao Y. Comparative study of negative capacitance field-effect transistors with different MOS capacitances. *Nanoscale Research Letters*. 2019;14(171): 1–6. <https://doi.org/10.1186/s11671-019-3013-z>
12. Peng Y., Liu Y., Han G., Zhang J., Hao Y. Germanium negative capacitance field effect transistors: impacts of Zr Composition in Hf_{1-x}Zr_xO₂. *Nanoscale Research Letters*. 2019;14(25): 1–8. <https://doi.org/10.1186/s11671-019-2927-9>
13. Peng Y., Han G., Xiao W., Wu J., Liu Y., Zhang J., Hao Y. Nanocrystal-embedded-insulator (NEI) ferroelectric FETs for negative capacitance device and non-volatile memory applications. *Nanoscale Research Letters*. 2019;14(115): 1–9. <https://doi.org/10.1186/s11671-019-2943-9>
14. Starzonek S., Drozd-Rzoska A., Rzoska J. S., Zhang K., Pawlikowska E., Kedzierska-Sar A., Szafran M., Gao F. Polymer matrix ferroelectric composites under pressure: Negative electric capacitance and glassy dynamics. *The European Physical Journal E*. 2019;42(118): 1–7. <https://doi.org/10.1140/epje/i2019-11876-9>
15. Zhang S., Liu H., Zhou J., Liu Y., Han G., Hao Y. ZrO_x Negative capacitance field-effect transistor with sub-60 subthreshold swing behavior. *Nanoscale Research Letters*. 2021;16(21): 2–6. <https://doi.org/10.1186/s11671-020-03468-w>
16. Wong C., Salahuddin S. Negative capacitance transistors. *Proceedings of the IEEE*. 2019;107(1): 49–62. <https://doi.org/10.1109/JPROC.2018.2884518>
17. Gupta A. K., Raman A., & Kumar N. Charge-plasma-based negative capacitance ring-FET: Design,

investigation and reliability analysis. *Journal of Electronic Materials*. 2020;49(3): 4852–4863. <https://doi.org/10.1007/s11664-020-08205-8>

18. Macklen E. D. NTC Thermistor Materials. In: *Concise Encyclopedia of Advanced Ceramic Materials*. 1991. p. 328–331. <https://doi.org/10.1016/b978-0-08-034720-2.50091-5>

19. Sekushin N. A. Istomin P. V., Ryabkov Y. I., Goldin B. A. Electrical properties of ceramic synthesized from natural ilmenite-containing raw materials. *Proceedings of the Komi Science Centre of the Ural Division of the Russian Academy of Sciences*. 2012;2(10): 20–28. Available at: <https://elibrary.ru/item.asp?id=17954194> (In Russ., abstract in Engl.)

20. Sekushin N. A. Method of presentation of experimental data in impedance spectroscopy. *Russian Journal of Electrochemistry*. 2009;45(11): 1300–1305. <https://doi.org/10.1134/S1023193509110123>

21. Sekushin N. A. Two-frequency criterion of the presence of inductive component in the electrochemical

cell impedance. *Russian Journal of Electrochemistry*. 2010;46(3): 345–353. <https://doi.org/10.1134/S102319351003013>

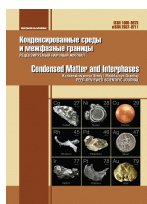
Information about the authors

Gevorg S. Grigoryan, PhD in Physics and Mathematics, Department of Experimental Physics, Voronezh State University, Voronezh, Russian Federation; e-mail: gri7287@yandex.ru. ORCID iD: <https://orcid.org/0000-0002-9850-8341>.

Alexander M. Solodukha, DSc in Physics and Mathematics, Professor at the Department of Experimental Physics, Voronezh State University, Voronezh, Russian Federation; e-mail: asn2@yandex.ru. ORCID iD: <https://orcid.org/0000-0002-4373-3883>.

Received 5 April 2021; Approved after reviewing 26 April 2021; Accepted 15 May 2021; Published online 25 June 2021.

*Translated by Irina Charychanskaya
Edited and proofread by Simon Cox*



Original articles

Research article

<https://doi.org/10.17308/kcmf.2021.23/3432>

On the limitations of the applicability of Young's equations temperature

M. P. Dokhov 

*Kabardino-Balkarian State Agricultural University named after V. M. Kokov
1“V” Prospekt Lenina, Nalchik 360030, Kabardino-Balkarian Republic, Russian Federation*

Abstract

The article uses the thermodynamics of interfacial phenomena to justify the fact that Young's equations can correctly describe the three-phase equilibrium with any type of interatomic bonds.

Wetting, adhesion, dissolution, surface adsorption, and other surface phenomena are important characteristics, which largely determine the quality and durability of materials, and the development of a number of production techniques, including welding, soldering, baking of metallic and non-metallic powders, etc. Therefore, it is important to study them.


Using experimental data regarding surface energies of liquids (melts) and contact angles available in the literature, we calculated the surface energies of many solid metals, oxides, carbides, and other inorganic and organic materials without taking into account the amount of the interfacial energy at the solid-liquid (melt) interface. Some researchers assumed that in case of an acute contact angle the interfacial energy is low. Therefore, they neglected it and assumed it to be zero. Others knew that this value could not be measured, that is why they measured and calculated the difference between the surface energy of a solid and the interfacial energy of a solid and a liquid (melt), which is equal to the product of the surface energy of this liquid by the cosine of the contact angle. It is obvious that these methods of determining the surface energy based on such oversimplified assumptions result in poor accuracy.

Through the use of examples this paper shows how the surface energies of solids were previously calculated and how the shortcomings of previous calculations can be corrected.

Keywords: Surface energy, Interfacial energy, Wetting angle, Nickel, Cobalt, Graphite, Titanium carbide

For citation: Dokhov M. P. On the limitations of the applicability of Young's equations. *Kondensirovannyye sredy i mezhfaznye granitsy = Condensed Matter and Interphases*. 2021;23(2): 218–222. <https://doi.org/10.17308/kcmf.2021.23/3432>

Для цитирования: Духов М. П. О пределах применимости уравнений Юнга. *Конденсированные среды и межфазные границы*. 2021;23(2): 218–222. <https://doi.org/10.17308/kcmf.2021.23/3432>

 Magomed Pashevich Dokhov, e-mail: innagubachikova@mail.ru

© M. P. Dokhov, 2021



The content is available under Creative Commons Attribution 4.0 License.

1. Introduction

Since T. Young derived the two equations named after him, some researchers of interfacial phenomena have subjected them to revision. Some of them have denied their validity, others have noted their limited applicability, and yet others have tried to derive new alternative equations.

As we know, the first of Young's equations associates the work of adhesion W_A with the surface energy of the liquid (melt) σ_{LV} and the contact angle Θ :

$$W_A = \sigma_{LV} (1 + \cos \Theta). \quad (1)$$

Equation (1) is theoretically and practically reasonable, however, some authors do not recognize the validity of Young's first equation. In [1], N. K. Adam wrote in regards to it that Young not only formulated equation (1) with adhesion, but he also indicated its meaninglessness when W_A is more than $2\sigma_{LV}$.

According to Yu. V Naidich [2], in other words, Young also pointed out the limitations of the applicability of equation (1), although this is sometimes forgotten, and the equation is unjustly criticised due to its inapplicability at $\Theta = 0$.

The second equation derived by Young is represented as following:

$$\cos \Theta = \frac{\sigma_{SV} - \sigma_{SL}}{\sigma_{LV}}, \quad (2)$$

where σ_{SV} , σ_{SL} , σ_{LV} are the surface energies on the respective three interphase boundaries: solid – vapour, solid – melt, and melt – vapour.

In the case of equation (2) things are more complicated. Despite the fact that equation (2) is over 215 years old, that there are numerous works devoted to its theoretical derivation, and that it is widely applied in practice during analyses of the wettability phenomena, the equation (in the case of solid – liquid – vapour) has still not been experimentally verified. The latter circumstance is due to the fact that to date there are no sufficiently reliable methods to determine the absolute values of the interfacial energies. All this means that Young's equation (2) has regularly been a matter of debate since the moment it was derived [2].

The purpose of this work is to show that in general Young's equations correctly describe the three-phase equilibrium.

2. Methods for calculating the surface energy of solid titanium carbide and graphite

[3] analysed the existing measurement methods and results regarding the surface energy of solid carbides obtained by various authors with the help of Young's equation (2).

The authors of [3] examined the liquid nickel – titanium carbide system (Ni-TiC). The wetting angle of nickel on titanium carbide equals 4° in a vacuum at a temperature of 1728 K. Assuming that σ_{SL} is zero, and the surface energy of nickel equals 1934 mJ/m², the authors inserted the respective values in Young's equation (2) and found the surface energy of titanium carbide:

$$\sigma_{SV} = 0 + 1934 \cdot 0.998 = 1930 \text{ mJ/m}^2 \quad (3)$$

The authors then pointed out that their assumption that $\sigma_{SL} = 0$ may be wrong, and the surface energy of titanium carbide can be expected to have higher values of σ_{SV} .

Similar calculations were performed by the authors of [3] to determine the minimum surface energy of graphite. Pure liquid cobalt with graphite in a vacuum at a temperature of 1773 K has a contact angle of 35° . The authors assumed that the surface energy of liquid cobalt was equal to 1942 mJ/m² and σ_{SL} was equal to zero, and according to equation (2) the value for the minimum surface energy of graphite in an atmosphere of cobalt vapour was equal to 1590 mJ/m². In this case, this value was also underestimated by the unknown value of σ_{SL} .

Until recently, researchers were unable to calculate the interfacial energy σ_{SL} . Therefore, they had to be satisfied with calculating either the difference of $\sigma_{SV} - \sigma_{SL}$ or they assumed that at the contact angle of $\sigma < \pi/2$ the interfacial energy was low and neglected it as stated above, for example in [3–7].

Earlier in [8], a thermodynamic formula was obtained to calculate σ_{SL} using the known values of the surface energy of the liquid (melt) σ_{LV} and the wetting angle Θ :

$$\sigma_{SL} = \sigma_{LV} \left(\frac{2 - 3 \cos \Theta + \cos^3 \Theta}{4} \right)^{1/3}. \quad (4)$$

If we insert the above-mentioned numerical values in formula (4) or use a table based on formula (4), then for the Ni-TiC system [8–9]:

$$\sigma_{SL} = 1934 \cdot \left(\frac{2 - 3 \cdot 0.9976 + 0.9976^3}{4} \right)^{1/3} = 32 \text{ mJ/m}^2. \quad (5)$$

A similar calculation for the system of cobalt-graphite will have a result where $\sigma_{SL} = 553 \text{ mJ/m}^2$.

During calculations, we used a previously prepared table of relative values of σ_{SL}/σ_{LV} depending on the contact angle.

Taking into account the recent results for σ_{SL} , the surface energies of solid titanium carbide and graphite will be equal to 1962 and 2144 mJ/m² respectively.

The work of adhesion of nickel to titanium carbide and cobalt to graphite can be calculated by two identical equations: by equation (1) and by the Dupré equation:

$$W_A = \sigma_{SV} + \sigma_{LV} - \sigma_{SL}. \quad (6)$$

By inserting numerical values, for example, in (6), we will obtain the following:

$$W_{A1}(\text{Ni-TiC}) = 3864 \text{ mJ/m}^2,$$

$$W_{A2}(\text{Co-graphite}) = 3532 \text{ mJ/m}^2.$$

Inserting numerical values in (1) with an accuracy of $\pm 1 \text{ mJ/m}^2$ produced results consistent with the results obtained from equation (6).

And here is another example:

[4] studied the influence of silicon on the interfacial properties of low-carbon liquid steel. The researchers calculated the contact angles formed by steel on a substrate of chromium oxide Cr_2O_3 depending on the silicon concentration in the steel.

In [4], we were interested in the numerical values of contact angles, but the authors presented them in the form of graphs, so based on the differences of $\sigma_{SV} - \sigma_{SL}$ provided by the authors and their experimental data regarding the surface tension of liquid steel, we calculated contact angles Θ for each concentration of silicon in steel. The differences of $\sigma_{SV} - \sigma_{SL}$ for a substrate of Cr_2O_3 not only decreased with increasing silicon concentration, but even changed the sign, which indicates the good wettability by liquid silicon and chromium oxide melts. Then, knowing the contact angles and the surface tensions of melts, we were able to calculate the interfacial characteristics: σ_{SL} , σ_{SV} , and W_A . What is more, σ_{SV}

and σ_{SL} were calculated as separate values rather than as differences.

Hereinafter, we will consider another aspect of the problem concerning the determination of interfacial energy at the solid-liquid (melt) interface. For this purpose, we will use the data of the surface energy of solid chromium oxide provided in [10]. The authors provided the value for the surface energy of chromium oxide at $T = 0 \text{ K}$: $\sigma_{SV} = 1400 \text{ mJ/m}^2$. The value of the temperature coefficient is $d\sigma_{SV}/dT = -0.25 \text{ mJ}/(\text{m}^2 \cdot \text{K})$. If we combine these data with the data obtained in [4], namely the isotherm of contact angles Θ , and use the concentration relation of the surface tension of liquid silicon at the measurement temperature for contact angles $T_{\text{mes}} = 1823 \text{ K}$, then:

$$\begin{aligned} \sigma_{SV}(1823 \text{ K}) &= 1400 - 0.25(1823 - 0) = \\ &= 1400 - 456 = 944 \text{ mJ/m}^2. \end{aligned}$$

After that, we will find the interfacial energy at the solid oxide - liquid steel interface by formula (2) using the value of $\sigma_{SV} = 944 \text{ mJ/m}^2$ and compare them with our calculations.

Tables 1 and 2 show the results obtained.

3. Discussion

It follows from the above that until recently, it was impossible to take into consideration the interfacial energy σ_{SL} when calculating the surface energy of solids since it was not experimentally measurable and there was no separate formula to calculate it. The formula derived by us allows determining σ_{SL} within the range of the contact angle starting from 1° up to 180° . A wetting angle equal to zero is a singular point at which the interfacial energy σ_{SL} is zero, which also follows from formula (4).

For this three-phase system the smaller the contact angle, the lower the interfacial energy at the solid-liquid (melt) interface. In case of ($\Theta < 90^\circ$) the value of the surface free energy of a solid at the interface with saturated vapour of a liquid is determined as a sum of the interfacial energy σ_{SL} and $\sigma_{LV} \cdot \cos \Theta$, wherein with an increasing contact angle the contribution of σ_{SL} grows much faster than that of σ_{LV} . At ($\Theta > 90^\circ$), on the contrary, the closer to 180° , the smaller the surface energy of a solid is. If a wetting angle of 180° was achievable, the surface energy of the solid would be equal to zero.

Table 1. The dependence of the interfacial characteristics on the silicon concentration in the system of solid chromium oxide - low carbon liquid steel

Si, at%	Cr ₂ O ₃ substrate					W _A , mJ/m ²
	σ _{LV} , mJ/m ²	Θ, degree	-(σ _{SV} - σ _{SL}), mJ/m ²	σ _{SL} , mJ/m ²	σ _{SV} , mJ/m ²	
1.0	1430	110	490	1297	808	940
4.0	1360	98	190	1150	960	1170
9.5	1300	87	-65	1004	1072	1365
18.0	1200	87	-63	927	990	1263
25.4	1040	76	-250	713	964	1291
34.0	820	62	-385	458	843	1205
45.0	715	48	-460	299	777	1193

Table 2. Deviation of Δσ_{SV} and Δσ_{SL} from the initial calculations

1	Δσ _{SL1} = 136
2	Δσ _{SV1} = 136
3	Δσ _{SL2} = -86
4	Δσ _{SV2} = -86
5	Δσ _{SL3} = -128
6	Δσ _{SV3} = -128
7	Δσ _{SL4} = -46
8	Δσ _{SV4} = -46
9	Δσ _{SL5} = -20
10	Δσ _{SV5} = -20
11	Δσ _{SL6} = 101
12	Δσ _{SV6} = 101
13	Δσ _{SL7} = 167
14	Δσ _{SV7} = 167

Table 2 implies the most interesting fact that an increase in σ_{SL} means a similar increase in σ_{LV}. The reduction in σ_{SL} results in a similar reduction in σ_{LV}. At the same time, the work of adhesion remains unchanged. This is understandable, since in the Dupré expression the surface energy of a solid and the interfacial energy at the solid - liquid (melt) interface have different signs. The changing surface energy of a solid is compensated with interfacial energy. This surprising phenomenon is probably due to the effect of the adsorption of liquid vapours on the surface energy of a solid which causes a simultaneous modification of σ_{LV} and σ_{SL} when the contact angle changes.

4. Conclusions

1. The validity of Young’s equations was shown by examples of contact between highly energetic surfaces.

2. Interfacial energies of titanium carbide at the interface with liquid nickel and graphite with liquid cobalt were calculated for the first time.

3. Surface energies of solid titanium carbide and graphite were determined considering the interfacial energies of the respective systems.

4. The work of adhesion of liquid metals to titanium carbide and graphite were calculated respectively.

5. The deviations between interfacial energies σ_{SL} and surface energies σ_{SV} calculated using a constant value and by our method were found.

6. It was shown that the larger the contact angle is, the greater is the contribution of interfacial energy to the surface energy of solids within an acute contact angle.

Conflict of interests

The author declares that they have no known competing financial interests or personal relationships that could have appeared to influence the work reported in this paper.

References

1. Adam N. K. Use of Term “Young’s Equation” for contact angles. *Nature*. 1957;180(4590): 809-810. <https://doi.org/10.1038/180809a0>
2. Naidich Yu. V. *Contact phenomena in metallic melts*. Kiev: Nauk. Dumka Publ.; 1972. 196 p. (In Russ.)
3. *Cermets*. Ed. by J. R. Tinklepaugh and W. B. Crandall. New York, Reinhold; London: Chapman and Hall; 1960. 173 p.
4. Vatolin N. A., Ukhov F. V. Vliyanie kremniya na mezhfaznye svoistva malouglerodistoi stali. *Smachivaemost’ i poverkhnostnye svoistva rasplavov i*

tverdykh tel [The effect of silicon on the interfacial properties of mild steel. In: Wettability and surface properties of melts and solids.]. Kiev: Nauk. Dumka Publ.; 1972. p. 186-189. (In Russ.)

5. Zisman W. A. Relation of the equilibrium contact angle to liquid and solid constitution. *Advances in Chemistry*. 1964;43: 1-51. <https://doi.org/10.1021/ba-1964-0043.ch001>

6. Good J. R., Girifalco L. A. A theory for estimation of surface and interfacial energies. III. Estimation of surface energies of solids from contact angle data. *The Journal of Physical Chemistry*. 1960;64(5): 561-565. <https://doi.org/10.1021/j100834a012>

7. Kingery W. D. Metal-ceramic interactions: IV, Absolute measurement of metal-ceramic interfacial energy and the interfacial adsorption of silicon from iron-silicon alloys. *Journal of the American Ceramic Society*. 1954;37(2): 42-45. <https://doi.org/10.1111/j.1151-2916.1954.tb14002.x>

8. Dokhov M. P., Kokoeva M. N. Interface energy of the several polymer surface with water solution spirituous. *Sovremennye Naukoemkie Tekhnologii*. 2014;55(9): 64-66. Available at: <https://www.elibrary.ru/item.asp?id=22025127> (In Russ., abstract in Eng.)

9. Dokhov M. P. O svyazi mezhfaznoi energii na granitse razdela tverdoe telo-rasplav s poverkhnostnoi

energii ot del'nykh faz [On the relationship of interphase energy at the solid-melt interface with the surface energy of individual phases]. *Uspekhi sovremennogo estestvoznaniya*. 2007;10: 85-87. Available at: <https://www.elibrary.ru/item.asp?id=9935322> (In Russ.)

10. Vatolin N. A., Timofeev A. I. Svobodnaya poverkhnostnaya energiya tverdykh kristallicheskikh oksidov [Free surface energy of solid crystalline oxides]. *Doklady Akademii Nauk SSSR*. 1988;302(2): 358-362. (In Russ.)

Information about the author

Magomed Pashevich Dokhov, DSc in Technical Sciences, Professor, Department of Technical Mechanics and Physics, Kokov Kabardino-Balkarian State Agricultural University, Nalchik, Kabardino-Balkarian Republic, Russian Federation; e-mail: innagubachikova@mail.ru. ORCID iD: <https://orcid.org/0000-0002-3224-9850>.

Received 5 April 2021; Approved after reviewing 17 April 2021; Accepted for publication 15 May 2021; Published online 25 June 2021.

*Translated by Anastasiia Ananeva
Edited and proofread by Simon Cox*



Original articles

Research article

<https://doi.org/10.17308/kcmf.2021.23/3433>

The structure of carbon nanotubes in a polymer matrix

G. V. Kozlov¹, Gas. M. Magomedov², Gus. M. Magomedov², I. V. Dolbin¹✉

¹*Kabardino-Balkarian State University named after H. M. Berbekov,
173 Chernyshevsky str., Nalchik 360004, Kabardafterino-Balkarian Republic, Russian Federation*

²*Dagestan State Pedagogical University,
57 Yaragского ul., Makhachkala 367003, the Republic of Dagestan, Russian Federation*

Abstract

We carried out an analytical structural analysis of interfacial effects and differences in the reinforcing ability of carbon nanotubes for polydicyclopentadiene/carbon nanotube nanocomposites with elastomeric and glassy matrices. In general, it showed that the reinforcing (strengthening) element of the structure of polymer nanocomposites is a combination of the nanofiller and interfacial regions. In the polymer matrix of the nanocomposite, carbon nanotubes form ring-like structures. Their radius depends heavily on the volume content of the nanofiller. Therefore, the structural reinforcing element of polymer/carbon nanotube nanocomposites can be considered as ring-like formations of carbon nanotubes coated with an interfacial layer. Their structure and properties differ from the characteristics of the bulk polymer matrix. According to this definition, the effective radius of the ring-like formations increases by the thickness of the interfacial layer. In turn, the level of interfacial adhesion between the polymer matrix and the nanofiller is uniquely determined by the radius of the specified carbon nanotube formations. For the considered nanocomposites, the elastomeric matrix has a higher degree of reinforcement compared to the glassy matrix, due to the thicker interfacial layer. It was shown that the ring-like nanotube formations could be successfully modelled as a structural analogue of macromolecular coils of branched polymers. This makes it possible to assess the effective (true) level of anisotropy of this nanofiller in the polymer matrix of the nanocomposite. When the nanofiller content is constant, this level, characterised by the aspect ratio of the nanotubes, uniquely determines the degree of reinforcement of the nanocomposites.

Keywords: Nanocomposite, Carbon nanotubes, Structure, Interfacial layer, Ring-like formations, Reinforcement degree

For citation: Kozlov G. V., Magomedov Gas. M., Magomedov Gus. M., Dolbin I. V. The structure of carbon nanotubes in a polymer matrix. *Kondensirovannye sredy i mezhfaznye granitsy = Condensed Matter and Interphases*. 2021;23(2): 223–228. <https://doi.org/10.17308/kcmf.2021.23/3433>

Для цитирования: Козлов Г. В., Магомедов Гас. М., Магомедов Гус. М., Долбин И. В. Структура углеродных нанотрубок в полимерной матрице. *Конденсированные среды и межфазные границы*. 2021;23(2): 223–228. <https://doi.org/10.17308/kcmf.2021.23/3433>

✉ Igor V. Dolbin, e-mail: i_dolbin@mail.ru

© Kozlov G. V., Magomedov Gas. M., Magomedov Gus. M., Dolbin I. V., 2021



The content is available under Creative Commons Attribution 4.0 License.

1. Introduction

The authors of [1] showed that carbon nanotubes (CNTs), both in solution and in the polymer matrix of the nanocomposite, form ring-like structures that look like macromolecular coils of branched polymers [1, 2]. In [2], the formation of these structures was analytically studied, a number of methods were proposed to calculate their radius, this study also reveals the dependence of the properties of polymer/carbon nanotube (nanofiber) nanocomposites on the structure of CNTs. With regard to this issue, one well-known effect is of interest: the degree of reinforcement of the same nanocomposite, regardless of the type of its filler, is always significantly higher for a nanocomposite with an elastomeric matrix as compared to a glassy matrix [3–5]. The same effect was observed for polymer/carbon nanotube nanocomposites [6–9]. Obviously, the radius of the ring-like formations of CNTs cannot change abruptly during the indicated transition, since the elastomeric matrix (especially the cross-linked one) has sufficiently high parameters of viscosity and strength to prevent any significant change in the structure of the ring-like formations of CNTs, i.e., their radius. Therefore, the aim of this study is to study the aforementioned effect and to develop a structural model to describe it quantitatively.

2. Experimental

The nanofillers were multi-walled carbon nanotubes (MWCNTs) with 15–20 nm outer diameter, 5–10 nm inner diameter, and 0.5–20 μm length. These MWCNTs were functionalized with norbornene to increase the level of interfacial adhesion between the polymer matrix and the nanofiller. Polydicyclopentadiene (PDCPD) was used as the polymer matrix [10].

To obtain nanocomposites, functionalized MWCNTs were dispersed in an aqueous solution of PDCPD and were sonicated to improve the dispersion of the nanofiller. Then this mixture was stirred with a catalyst (dichloro-(3-methyl-2-butenylidene) bis-(tricyclofentyl) ruthenium phosphine) until a homogeneous solution was obtained. Then it was cross-linked for 2 h at 343 K and 1.5 h at 443 K [10].

Mechanical uniaxial tension tests were performed using an Instron 5569 universal testing

machine according to ASTM D638 (type V samples) at a temperature of 293 K and a crosshead speed of 1 mm/min. Each result was obtained as an average of the data from four tests [10].

Dynamic mechanical analysis (DMA) was performed using a TA Instruments Q800 DMA. The tension tests of the samples were carried out at a frequency of 1 Hz in the temperature range of 303–583 K at a heating rate of 3 K/min. The samples were 35×5×1 mm in size [10].

3. Results and discussion

The authors of [2] used several methods for calculating the radius of ring-like formations of CNTs, R_{CNT} . One of them, proposed in [11], takes into account only the geometric parameters of carbon nanotubes and their volume content φ_n :

$$(2R'_{\text{CNT}})^3 = \frac{\pi L_{\text{CNT}} r_{\text{CNT}}^2}{\varphi_n}, \quad (1)$$

where L_{CNT} and r_{CNT} are the length and radius of carbon nanotubes, respectively.

The value of φ_n can be determined using a well-known formula [12]:

$$\varphi_n = \frac{W_n}{\rho_{\text{CNT}}}, \quad (2)$$

where W_n and ρ_{CNT} are the weight content and density of carbon nanotubes, respectively. For PDCPD/MWCNT nanocomposites, the value of W_n ranged from 0.05 to 0.40 wt.%.

For carbon nanotubes, the value of ρ_{CNT} can be calculated as follows [12]:

$$\rho_{\text{CNT}} = 188(D_{\text{CNT}} - d_{\text{CNT}})^{1/3}, \text{ kg/m}^3, \quad (3)$$

where D_{CNT} and d_{CNT} are the outer and inner diameters of a nanotube, respectively.

Another method for calculating R_{CNT} (R''_{CNT}) takes into account the actual conditions for the formation of a CNT structure in the polymer matrix of the nanocomposite (for example, sonication [13], functionalisation [14, 15], etc.) and uses the following empirical formula [2]:

$$b_\alpha = 57 \left[(R''_{\text{CNT}})^2 - 0.022 \right], \quad (4)$$

where b_α is a dimensionless parameter characterising the level of interfacial adhesion in the polymer nanocomposites, and the value of R''_{CNT} is given in μm .

The value of b_α can be determined according to the following percolation relation [12]:

$$\frac{E_n}{E_m} = 1 + 11(cb_\alpha\varphi_n)^{1.7}, \quad (5)$$

where E_n and E_m are the elastic moduli of the nanocomposite and the original matrix polymer, respectively (the E_n/E_m ratio is usually called the reinforcement degree of a nanocomposite), and c is a constant coefficient, which is ~ 2.86 for CNTs [12].

Fig. 1 shows a comparison of the dependences R'_{CNT} and R''_{CNT} on the weight content of nanofiller W_n for PDCPD/MWCNT nanocomposites with a glassy and elastomeric matrix. We can see that the values of R'_{CNT} and R''_{CNT} are similar in the absolute value for the first of the specified series of nanocomposites (their average discrepancy is less than 9 %). However, in the case of an elastomeric matrix, the value of R''_{CNT} is double the value of R'_{CNT} . As noted above, the two-fold “swelling” of the ring-like formations of CNTs in the cross-linked elastomer matrix is unlikely. Therefore, the physical basis of the observed effect should be considered.

So far, two facts have been well established. First, it was shown experimentally [10] and theoretically [16] that the elastic modulus of interfacial regions in polymer nanocomposites significantly exceeds the corresponding parameter for a bulk polymer matrix. It is close in absolute value to the elastic modulus of nanofiller aggregates. Second, in polymer/carbon nanotube nanocomposites with low nanofiller content, very extended interfacial regions are formed. Their thickness l_{if} can exceed the radius of the nanotube by an order of magnitude or more [10]. Thus, for the considered nanocomposites with an elastomeric matrix with an average radius of MWCNTs $r_{CNT} = 8.75$ nm, l_{if} ranges from 125 to 226 nm [10], i.e., exceeds the value of r_{CNT} 14.3–25.8 times. From the above observations, it follows that the reinforcing element of polymer/carbon nanotube nanocomposites is ring-like CNT formations surrounded by an interfacial layer. Then the effective radius of such reinforcing element R'''_{CNT} can be described as follows:

$$R'''_{CNT} = R'_{CNT} + l_{if}. \quad (5)$$

The values of l_{if} for PDCPD/MWCNT nanocomposites with an elastomeric matrix are

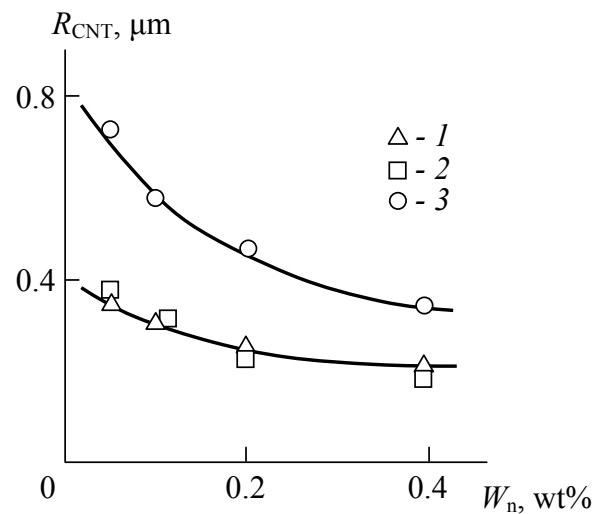


Fig. 1. Dependences of the radius of ring-like formations of MWCNTs R_{CNT} on the weight content of nanofiller W_n for PDCPD/MWCNT nanocomposites with a glassy (1, 2) and elastomeric (3) matrix. R_{CNT} was calculated using equations (4) (for 1, 3) and (1) (for 2)

provided in [10]. For the same nanocomposites with a glassy matrix, the l_{if} values were determined as described below. First, the relative fraction of interfacial regions φ_{if} was estimated using the following relation [12]:

$$\frac{E_n}{E_m} = 1 + 11(\varphi_n + \varphi_{if})^{1.7}. \quad (6)$$

Then we calculated the value of l_{if} , using the following equation [16]:

$$\varphi_{if} = \left(\frac{l_{if}^2 + 2r_{CNT}l_{if}}{r_{CNT}^2} \right) \varphi_n. \quad (7)$$

Fig. 2 shows a comparison of the values of the radii of ring-like formations R''_{CNT} and R'''_{CNT} , calculated according to equations (4) and (5), respectively, for PDCPD/MWCNT nanocomposites with elastomeric and glassy matrices. We can see that the R_{CNT} values calculated by these two methods are in good agreement. This correspondence confirms the above assumption about the nature of the reinforcing element in polymer/carbon nanotube nanocomposites. It should be noted that in the case of PDCPD/MWCNT nanocomposites with a glassy matrix, the use of the radius of ring-like formations R'''_{CNT} instead of R'_{CNT} (Fig. 1) gives even a slightly better agreement of this parameter. The average discrepancy between R''_{CNT} and R'''_{CNT} is less than 7 %.

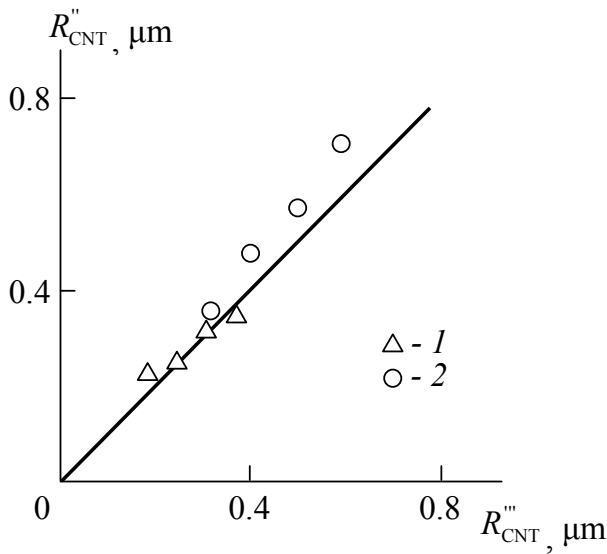


Fig. 2. Comparison of the radii of the ring-like formations of MWCNTs R''_{CNT} and R'''_{CNT} , calculated using equations (4) and (5), respectively, for PDCPD/MWCNT nanocomposites. A straight line means a ratio of 1:1

It is known [17] that carbon nanotubes are considered the most promising nanofiller for polymer nanocomposites due to two factors: a high longitudinal elastic modulus of the nanofiller, which can reach 1000–2000 GPa, and a high nominal degree of anisotropy. However, in practice, these expectations are usually not met. The reason for this is well-known: generally, nanocomposites are reinforced not by nanoparticles, but by their aggregates. In the case of carbon nanotubes, the aggregates are their ring-like formations [1, 2]. The true level of anisotropy of CNTs in such aggregates can be determined by modelling the ring-like formations of CNTs as macromolecular coils of branched polymers [1, 18]. In this case, the persistent length of a ring-like formation L_p is determined using the following equation [19]:

$$\left(R'''_{CNT}\right)^2 = \frac{L_{CNT}L_p}{6}, \quad (8)$$

and the true aspect ratio is calculated as the ratio [20]:

$$\alpha = \frac{L_p}{D_{CNT}}. \quad (9)$$

It is known [12] that the level of interfacial adhesion, characterised by the parameter b_α , largely determines the properties of nanocom-

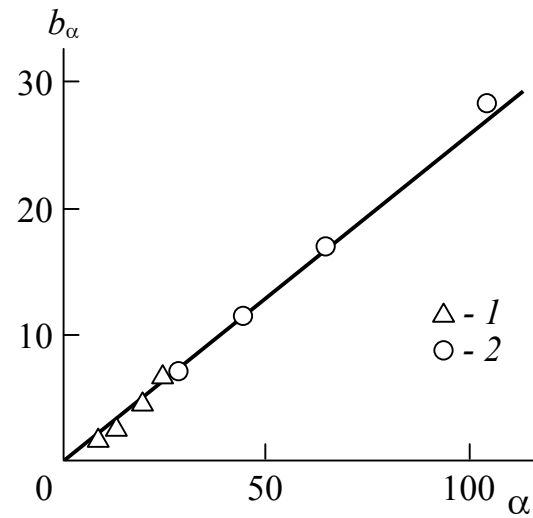


Fig. 3. Dependence of the parameter b_α , characterising the level of interfacial adhesion, on the MWCNTs' true aspect ratio α for PDCPD/MWCNT nanocomposites

posites. Fig. 3 shows the dependence of the parameter b_α on the actual degree of anisotropy of carbon nanotubes, characterised by the aspect ratio α . As we can see, a linear correlation was obtained between these parameters, which can be described analytically by the following empirical equation:

$$b_\alpha = 0.257\alpha. \quad (10)$$

If we substitute formula (10) into relation (5), we obtain the following equation, which can be used to determine the degree of reinforcement of polymer/carbon nanotube nanocomposites:

$$\frac{E_n}{E_m} = 1 + 11(0.72\alpha\phi_n)^{1.7}. \quad (11)$$

Fig. 4 shows a comparison of the experimentally obtained and equation-based (11) dependences of the reinforcement degree E_n/E_m on the volume content of the nanofiller ϕ_n for PDCPD/MWCNT nanocomposites with glassy and elastomeric matrices. As can be seen, both cases show a good agreement between theory and experiment (their average discrepancy is ~ 2 %, which corresponds to the experimental error for this parameter [10]). Note that the difference in the E_n/E_m values at the same values of ϕ_n is determined by only one parameter, the true aspect ratio of MWCNTs α . In turn, according to equations (5), (8), and (9), the difference in values of α for nanocomposites with

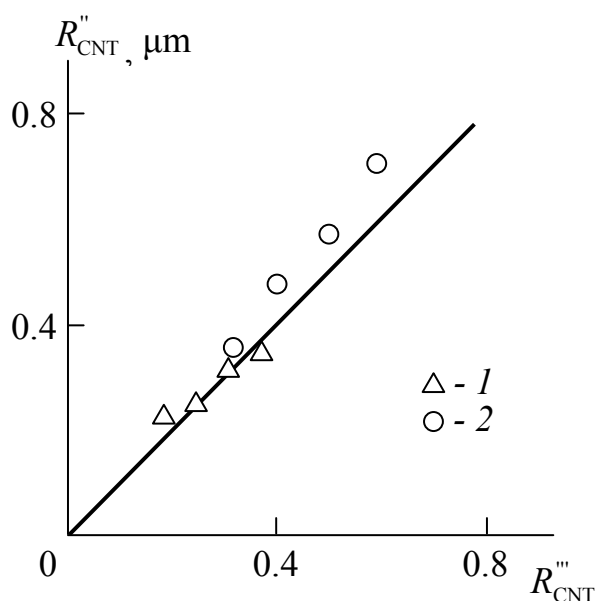


Fig. 4. Comparison of the dependences of the reinforcement degree E_n/E_m on the nanofiller volume content φ_n for PDCPD/MWCNT nanocomposites with elastomeric (1, 3) and glassy (2, 4) matrices, calculated according to equation (11) (1, 2) and obtained experimentally (3, 4)

elastomeric and glassy matrices is determined only by the thickness of the interfacial layer l_{if} .

4. Conclusions

Thus, the results of this study showed that the reinforcing element in polymer/carbon nanotube nanocomposites is a ring-like formation (aggregate) of carbon nanotubes surrounded by an interfacial layer. This predetermines the fact that the effective radius of the specified formation increases by the thickness of the interfacial layer. Modelling the ring-like formation of nanotubes as a macromolecular coil of a branched polymer showed that the actual level of anisotropy of carbon nanotubes is determined by the effective radius of this structural reinforcing element of the nanocomposite. This level is characterised by the true aspect ratio of the nanotubes. When the volume content of the nanofiller is constant, it is the only factor that determines the degree of reinforcement of the nanocomposite.

Author contributions

All authors made an equivalent contribution to the preparation of the publication.

Conflict of interests

The authors declare that they have no known competing financial interests or personal relationships that could have influenced the work reported in this paper.

References

- Schaefer D. W., Justice R. S. How nano are nanocomposites? *Macromolecules*. 2007;40(24): 8501–8517. <https://doi.org/10.1021/ma070356w>
- Atlukhanova L. B., Kozlov G. V *Fizikokhimiya nanokompozitov polimer-uglerodnye nanotrubki* [Physics and chemistry of polymer/carbon nanotube nanocomposites]. Moscow: Sputnik + Publ.; 2020. 292 p. (In Russ.)
- Cho H., Lee H., Oh E., Lee S.-H., Park H. J., Yoon S.-B., Lee C.-H., Kwak G.-H., Lee W. J., Kim J., Kim J. E., Lee K.-H. Hierarchical structure of carbon nanotube fibers, and the change of structure during densification by wet stretching. *Carbon*. 2018;136: 409–416. <https://doi.org/10.1016/j.carbon.2018.04.071>
- Ata M. S., Poon R., Syed A. M., Milne J., Zhitomirsky I. New developments in non-covalent surface modification, dispersion and electrophoretic deposition of carbon nanotubes. *Carbon*. 2018;130: 584–598. <https://doi.org/10.1016/j.carbon.2018.01.066>
- Li H., Branicio P. S. Ultra-low friction of graphene/C₆₀/graphene coatings for realistic rough surfaces. *Carbon*. 2019;152: 727–737. <https://doi.org/10.1016/j.carbon.2019.06.020>
- Tan W., Stallard J. C., Smail F. R., Boies A. M., Fleck N. A. The mechanical and electrical properties of direct-spun carbon nanotube mat-epoxy composites. *Carbon*. 2019;150: 489–504. <https://doi.org/10.1016/j.carbon.2019.04.118>
- Smail F., Boies A., Windle A. Direct spinning of CNT fibres: Past, present and future scale up. *Carbon*. 2019;152: 218–232. <https://doi.org/10.1016/j.carbon.2019.05.024>
- Zhang S., Hao A., Nguen N., Oluwalowo A., Liu Zh., Dessureault Y., Park J. G., Liang R. Carbon nanotube/carbon composite fiber with improved strength and electrical conductivity via interface engineering. *Carbon*. 2019;144: 628–638. <https://doi.org/10.1016/j.carbon.2018.12.091>
- Schaefer D. W., Zhao J., Dowty H., Alexander M., Orlor E. B. Carbon nanofibre reinforcement of soft materials. *Soft Matter*. 2008;4(10): 2071–2078. <https://doi.org/10.1039/b805314f>
- Jeong W., Kessler M. R. Toughness enhancement in ROMP functionalized carbon nanotube/polydicyclopentadiene composites. *Chemistry of materials*. 2008;20(22): 7060–7068. <https://doi.org/10.1021/cm8020947>

11. Bridge B. Theoretical modeling of the critical volume fraction for percolation conductivity in fibre-loaded conductive polymer composites. *Journal of Materials Science Letters*. 1989;8(2): 102–103. <https://doi.org/10.1007/BF00720265>
12. Mikitaev A. K., Kozlov G. V., Zaikov G. E. *Polymer Nanocomposites: Variety of Structural Forms and Applications*. New York: Nova Science Publishers, Inc.; 2008. 319 p.
13. Li W., Zhao J., Xue Y., Ren X., Zhang X., Li Q. Merge multiple carbon nanotube fibers into a robust yarn. *Carbon*. 2019;145: 266–272. <https://doi.org/10.1016/j.carbon.2019.01.054>
14. Qiu L., Guo P., Yang X., Ouyang Y., Feng Y., Zhang X., Zhao J., Zhang X., Li Q. Electro curing of oriented bismaleimide between aligned carbon nanotubes for high mechanical and thermal performances. *Carbon*. 2019;145: 650–657. <https://doi.org/10.1016/j.carbon.2019.01.074>
15. Liang X., Gao Y., Duan J., Liu Z., Fang Sh., Baughman R.H., Jiang L., Cheng Q. Enhancing the strength, toughness, and electrical conductivity of twist-spun carbon nanotube yarns in π bridging. *Carbon*. 2019;150: 268–274. <https://doi.org/10.1016/j.carbon.2019.05.023>
16. Coleman J. N., Cadek M., Ryan K. P., Fonseca A., Nady J. B., Blau W. J., Ferreira M. S. Reinforcement of polymers with carbon nanotubes. The role of an ordered polymer interfacial regions. Experiment and modeling. *Polymer*. 2006;47(23): 8556–8561. <https://doi.org/10.1016/j.polymer.2006.10.014>
17. Schadler L. S., Giannaris S. C., Ajayan P. M. Load transfer in carbon nanotube epoxy composites. *Applied Physics Letters*. 1998;73(26): 3842–3844. <https://doi.org/10.1063/1.122911>
18. Zhong-can O.-Y., Su Z.-B., Wang C.-L. Coil formation in multishell carbon nanotubes: competition between curvature elasticity and interlayer adhesion. *Physical Review Letters*. 1997;78(21): 4055–4058. <https://doi.org/10.1103/physrevlett.78.4055>
19. Kozlov G. V., Dolbin I. V., Zaikov G. E. (eds.) *The fractal physical chemistry of polymer solutions and melts*. Toronto, New Jersey: Apple Academic Press; 2013. 316 p. <https://doi.org/10.1201/b16305>
20. Moniruzzaman M., Winey K. I. Polymer nanocomposites containing carbon nanotubes. *Macromolecules*. 2006;39(16): 5194–5205. <https://doi.org/10.1021/ma060733p>

Information about the authors

Georgii V. Kozlov, Senior Research Fellow, Kabardino-Balkarian State University named after H. M. Berbekov, Nalchik, Kabardino-Balkarian Republic, Russian Federation; e-mail: i_dolbin@mail.ru. ORCID iD: <https://orcid.org/0000-0002-9503-9113>.

Gasam M. Magomedov, DSc in Physics and Mathematics, Professor, Head of the Department of Physics and Teaching Methods, Dagestan State Pedagogical University, Makhachkala, the Republic of Dagestan, Russian Federation; e-mail: gasam_mag@mail.ru. ORCID iD: <https://orcid.org/0000-0002-1278-9278>.

Gusein M. Magomedov, PhD in Physics and Mathematics, Associate Professor, Professor at the Department of Professional Pedagogy, Technology, and Teaching Methods, Dagestan State Pedagogical University, Makhachkala, the Republic of Dagestan, Russian Federation; e-mail: mgusein@mail.ru. ORCID iD: <https://orcid.org/0000-0002-5525-5970>.

Igor V. Dolbin, PhD in Chemistry, Associate Professor, Department of Organic Chemistry and High-Molecular Compounds, Kabardino-Balkarian State University named after H. M. Berbekov, Nalchik, Kabardino-Balkarian Republic, Russian Federation; e-mail: i_dolbin@mail.ru. ORCID iD: <https://orcid.org/0000-0001-9148-2831>.

Received 9 February 2021; Approved after reviewing 5 March 2021; Accepted 15 May 2021; Published online 25 June 2021.

*Translated by Anastasiia Ananeva
Edited and proofread by Simon Cox*



Condensed Matter and Interphases

Kondensirovannye Sredy i Mezhfaznye Granitsy
<https://journals.vsu.ru/kcmf/>

Original articles

Research article

<https://doi.org/10.17308/kcmf.2021.23/3434>

Features of the discharge of zinc in the background solution of sodium sulphate under stirring conditions

A. V. Kolesnikov✉, E. I. Ageenko

Chelyabinsk State University,
129 ul. Brat'yev Kashirinykh, Chelyabinsk 454001, Russian Federation

Abstract

The production technology of hydrometallurgical zinc uses various surfactants to thicken pulps, stabilise the electrolysis process, and obtain high-quality cathode deposits. Numerous researches were conducted to study the cathodic and anodic processes in a wide range of the composition of aqueous solutions using various solid electrodes in the absence of intense stirring of the electrolyte and with a high contribution of the migration component of the discharge of metals. This approach to the study of the surfactants' influence rarely provided a high degree of statistical reliability in observing the effect of differently charged surfactants on electrode processes, which is of great importance in the hydrometallurgical production of zinc. In this work, the task was to practically eliminate the contribution of the migration component due to the following factors: conducting electrolysis in a background solution of sodium sulphate, organising electrolyte stirring, performing calculations of current densities at the beginning of electrolysis, and establishing polarisation curves at an increased potential sweep rate from 20 to 100 mV/s. This approach provided a greater degree of statistical reliability in presenting the mechanism of the effect of additions of cationic and anionic surfactants during the stage of zinc discharge on a solid electrode, which was the purpose of the article.

Electrolysis was conducted in the potential range from -1050 to -1250 mV relative to the silver chloride electrode (AgCl/Ag) in the presence of a background sodium sulphate solution (0.5 M of Na₂SO₄ solution) containing 0.005, 0.0125, and 0.025 M ZnSO₄ with the introduction of high-molecular surfactants: cationic and anionic coagulants (floculants) and foaming agents (lignosulphonate – LSTP).

During the electrolysis in a background solution of sodium sulphate with stirring, it was found that the process of discharge of zinc ions on a solid electrode occurs in a mixed-kinetic mode. It was shown that positively charged additives, such as lignosulphonate and cationic coagulant (floculant) Besfloc K6645, have a negative effect on the dynamics of zinc cation discharge, while negatively charged Besfloc K4034 has practically no effect. The approach proposed in this work allows evaluating the influence of additions of cationic and anionic surfactants on the stage of zinc discharge on a solid electrode, which was the practical and scientific value of this work.

Keywords: Zinc, Current density, Potential, Polarisation, Coagulant, Lignosulphonate, Sodium sulphate, Electrode

For citation: Kolesnikov A. V., Ageenko E. I. Features of the discharge of zinc in the background solution of sodium sulfate under stirring conditions. *Kondensirovannye sredy i mezhfaznye granitsy = Condensed Matter and Interphases*. 2021;23(2): 229–235. <https://doi.org/10.17308/kcmf.2021.23/3434>

Для цитирования: Колесников А. В., Агеенко Е. И. Особенности разряда цинка в фоновом растворе сульфата натрия в условиях перемешивания. *Конденсированные среды и межфазные границы*. 2021;23(2): 229–235. <https://doi.org/10.17308/kcmf.2021.23/3434>

✉ Alexander V. Kolesnikov, e-mail: avkzinc@csu.ru

© Kolesnikov A.V., Ageenko E. I., 2021



The content is available under Creative Commons Attribution 4.0 License.

1. Introduction

As we know, different surfactants present in hydrometallurgical production solutions influence the process of the cathodic reduction of zinc [1–9]. Among surfactants are foaming agents used for zinc electrolysis and coagulants (flocculants) which are added to solutions to increase the settling rate of pulps and separate the solution from the insoluble mass (zinc cake) under the leaching of heat treatment products.

Numerous researches were conducted to study the cathodic and anodic processes in a wide range of the composition of aqueous solutions using various electrodes [10–17] in the absence of intense stirring of the electrolyte and with a high contribution of the migration component of the discharge of metals. This approach to the study of the influence of surfactants rarely provided a high degree of statistical reliability in observing the effect of differently charged surfactants on electrode processes, which is of great importance in the hydrometallurgical production of zinc. To eliminate the possibility of migration transport, a background electrolyte was introduced in the studied solution with a concentration exceeding the depolariser concentration by at least one hundred times [18, 19, 21]. The elimination of migration transport from the process of electrolysis allows increasing the contribution of the charge transfer stage into the dynamics of the reduction of cations through the “metal – electrolyte” interphase.

In this work, the task was to increase the contribution of the electrochemical stage into the dynamics of zinc discharge due to the following factors:

- Conducting electrolysis in a background solution of sodium sulphate.
- Organising electrolyte stirring (the Reynolds number Re was 1500).
- Performing calculations of current densities at the beginning of electrolysis.
- Establishing polarisation curves at an increased potential sweep rate.

This approach provided a greater degree of statistical reliability in evaluating the effect of additions of cationic and anionic surfactants during the stage of zinc discharge on a solid electrode, which was the purpose and the novelty of this study.

2. Experimental

Electrochemical studies were conducted in a sulphate electrolyte containing 0.005, 0.0125, and 0.025 M $ZnSO_4$ in the background 0.5 M solution of Na_2SO_4 with the introduction of high-molecular surfactants: 50 mg/l of cationic and anionic coagulants (flocculants) with the trade names Besfloc K6645 and Besfloc K4034, as well as 80 mg/l of a foaming agent (lignosulphonate – LSTP). Potentiostatic and galvanostatic measurements and establishing polarisation curves in the dynamic mode were conducted on a PotentiostatP-30Jcom (Elins) using a three-electrode cell [1]. The working electrode (cathode) was made of copper with an area of 0.1 cm², the auxiliary electrode (anode) was made of a platinum plate with an area of 0.2 cm², and the reference electrode was silver chloride (AgCl/Ag). The working copper electrode was polished, degreased in ethanol, and washed with water. The auxiliary electrode was etched in a nitric acid solution (1 : 2 = acid : water) for 5 seconds and washed with distilled water. The measurements were performed at room temperature with and without stirring. At first, before establishing the experimental curves, zinc was increased on a copper cathode with a constant potential of –1200 mV (AgCl/Ag) for 5 min using an electrolyte with a composition of 0.25 M $ZnSO_4$. The results of potentiostatic measurements are presented in the form of average data obtained over the initial period of 1 s of electrolysis while the results of galvanostatic measurements are presented in the form of average data obtained over the initial period of 5 s of electrolysis. The polarisation curves were obtained using a potentiodynamic method with linear potential sweep in the potential range –1050 ÷ –1250. Maximum current density was registered on polarisation curves in the potential range from –1200 to –1250 mV.

Confidence intervals were calculated for the experimental data on the figures. With the value $p = 0.05$, the intervals changed in the range from 0.015 to 1.14 mA/cm² (for current densities) and from 6.82 to 8.77 mV (for polarisation) and amounted to 0.11 lg I , μA when plotting the logarithmic dependence of the current value on the concentration of zinc in an electrolyte.

3. Results and discussion

In this work, the following studies were conducted with and without stirring in a background solution of sodium sulphate: the dependences of the current density on time were obtained during the potentiostatic measurements with various cathodic potentials: -1100 , -1150 , -1200 , -1250 mV (AgCl/Ag) (Fig. 1 a,b) and additions of the LSTP foaming agent (Fig. 2 a,b). The dependences of the current density on the concentration of zinc in an electrolyte were

obtained in the potentiodynamic mode with the linear potential sweep of 20 and 100 mV/s (Fig. 3) and on the square root of the linear potential sweep of rate (Fig. 4).

During electrolysis in the presence of a background sodium sulphate solution, zinc deposited on an electrode darkens with cathodic potentials of more than -1150 mV in magnitude. It is related to the oxidation of reduced zinc and possible side reaction of the reduction of sulphate ions on a cathode, as noted in [20, 22],

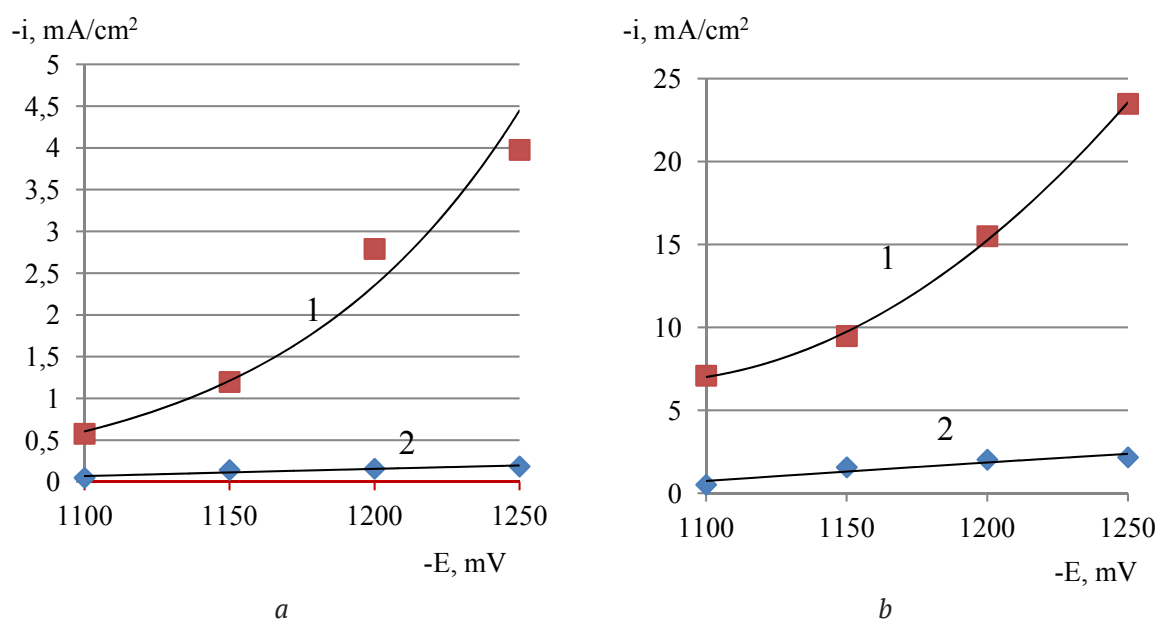


Fig. 1. Dependence of current density (i) on the cathode potential (E): 1 – with stirring; 2 – without stirring. The content of sodium sulphate 0.5 M and zinc sulphate in the electrolyte: a – 0.005 M; b – 0.025 M. The confidence interval at significance levels ($p = 0.05$) was 0.30 mA/cm² (a) and 1.14 mA/cm² (b)

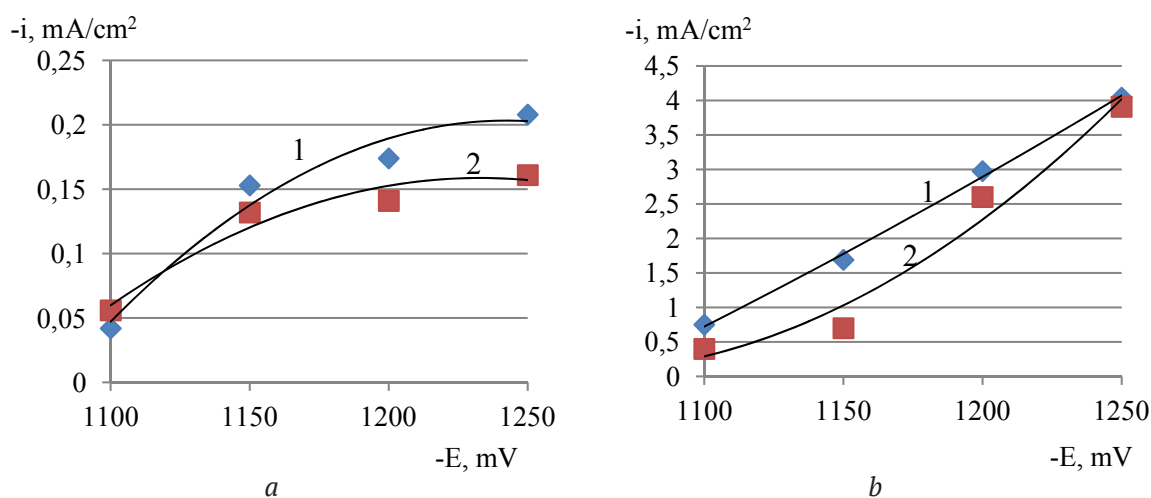


Fig. 2. Dependence of current density (i) on the cathode potential (E) under conditions without stirring (a) and with stirring (b). The content of sodium sulphate in the electrolyte is 0.5 M and the content of zinc sulphate is 0.005 M: 1 – without the addition; 2 – with the addition of 50 mg/l of LSTP. The confidence interval ($p = 0.05$) was 0.015 mA/cm² (2a) and 0.125 mA/cm² (b)

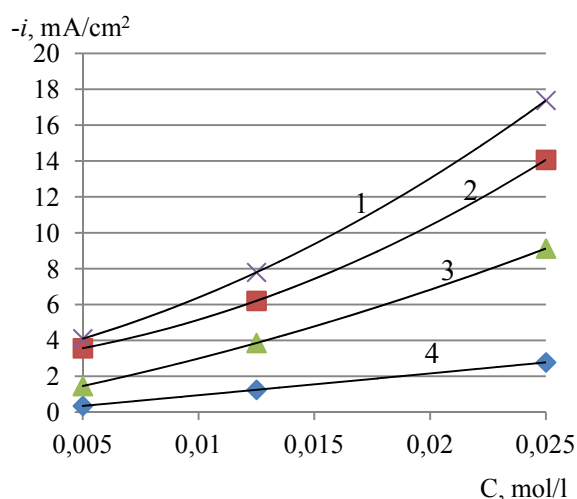


Fig. 3. The dependence of the maximum current density (i) on the concentration of zinc sulphate (C) in the background solution of 0.5 M sodium sulphate under the linear potential sweep in the potential range from -1050 to -1250 mV at a speed of 100 mV/s (1 – with stirring; 3 – without stirring) and with a sweep rate of 20 mV/s (2 – with stirring; 4 – without stirring). The confidence interval ($p = 0.05$) was 0.85 mA/cm^2

and justified by the conducted thermodynamic calculations and the obtained experimental data.

If we compare the polarisation curves (Fig. 1 a,b), a considerable increase in current densities (by ten times and more) can be observed under stirring with all potentials. Without stirring, the polarisation curves have linear dependence, while with stirring, the dependence of the current density change on the potential can be identified as a quadratic dependence. The obtained experimental data allow making an assumption about the increased contribution of the electrochemical stage into the overall rate of the zinc discharge process under stirring. Similar data were obtained when establishing polarisation curves using a potentiodynamic method with linear potential sweep in the potential range of $-1050 \div -1250$ mV (Fig. 4). When building the dependences of the current values on the square root of the linear potential sweep, it can be noted that the straight lines do not pass through the origin of coordinates. In this case, in [23] a conclusion is made that the process occurs in the mixed mode.

Without stirring, the effect of LSTP addition is not really seen at low cathodic potentials ($-1100, -1150$ mV) and the concentration of zinc in the solution 0.005 M. At the same time, under intense stirring we can observe a decrease in the

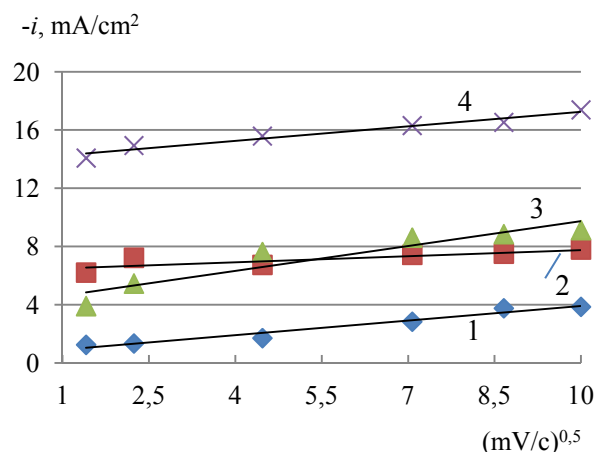


Fig. 4. Dependence of the maximum current density value (i) in a background solution of 0.5 M sodium sulphate on the square root of the linear potential sweep of rate in the potential range from -1050 to -1250 mV. 1 – zinc concentration (C) = 0.0125 M without stirring, 2 – $C = 0.0125$ M with stirring; 3 – $C = 0.025$ M without stirring, 4 – $C = 0.025$ M with stirring. The confidence interval ($p = 0.05$) was 0.85 mA/cm^2

current density in the above-mentioned potential range if we add 50 mg/l of LSTP (Fig. 2b). Based on the obtained data, we can make a conclusion that under stirring the LSTP foaming agent has greater influence on the stage of charge transfer through the “metal – electrolyte” interphase. Also, we assume that the addition of 50 mg/l of LSTP should not greatly influence the transport stage of zinc discharge process.

To study the mechanism of zinc electrolysis in a background solution of sodium sulphate under intense stirring, the reaction order was calculated by zinc ion with four potentials. The data of the discharge current values determined using the potentiostatic method [24] during the first second of the beginning of the process were used for the calculations. The calculations which were performed using the equation of the logarithmic dependence of the current values on the concentration of zinc in a solution are presented below:

$$I = K \cdot (C_{\text{Zn}^{2+}})^z$$

$$\lg I = \lg K + z \lg C_{\text{Zn}^{2+}},$$

where I is discharge current, μA , z is the reaction order for zinc ion, and K is a constant. The results are presented in Figs. 5 and 6.

Figs. 5 and 6 show that all dependences with high correlation coefficients ($R^2 = 0.98–0.99$ and higher) are described by straight lines. With the addition of the foaming agent, the reaction order for zinc for the studied system increases on average with 4 potentials from 1.224 ± 0.059 (without the addition) to 1.475 ± 0.126 . We believe that the increase of the reaction order over one in the concentration of zinc in an electrolyte in the system with stirring is related to the transition of the process from the diffusion to the mixed mode.

As the data obtained in galvanostatic mode showed, polarisation of the electrode in the presence and in the absence of the additives decreases under intense stirring. For example, with the current density of 1.7 mA/cm^2 (Fig. 7 a,b) polarisation decreases by 1.6 times with the addition of a cationic coagulant and almost by 3 times in the presence of the anionic coagulant without the addition. The obtained data showed a change in the mechanism of zinc electrolysis under stirring conditions, when the mass transfer

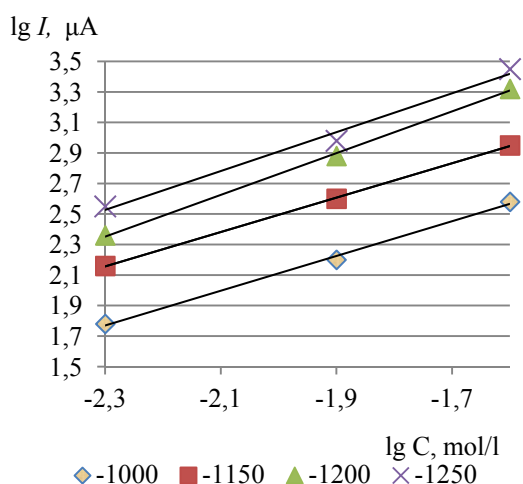


Fig. 5. The logarithmic dependence of the initial current density ($\lg I$) (for 1 s) on the concentration of zinc ($\lg C$) in the electrolyte with the Na_2SO_4 background (0.5 mol/l) at different potentials (-1100; -1150; -1200; -1250) mV according to (Ag/AgCl). Solution without foaming agent. Under stirring. The confidence interval ($p = 0.05$) was 0.11 ($\lg I, \mu\text{A}$)

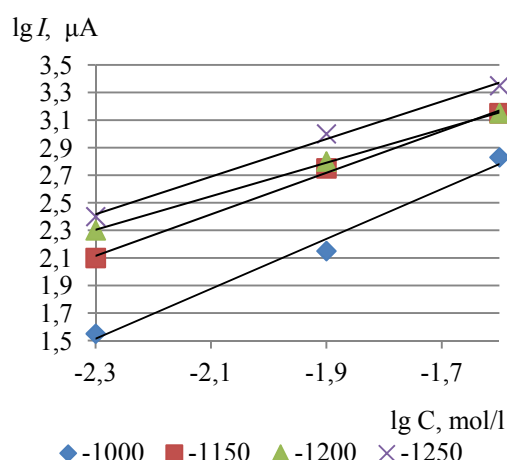


Fig. 6. The logarithmic dependence of the initial current ($\lg I$) (for 1 s) on the concentration of zinc ($\lg C$) in the electrolyte with the Na_2SO_4 background (0.5 mol/l) at different potentials (-1100; -1150; -1200; -1250) mV according to (Ag/AgCl). Solution with the addition of 80 mg/l of foaming agent. Under stirring. The confidence interval ($p = 0.05$) was 0.11 ($\lg I, \mu\text{A}$)

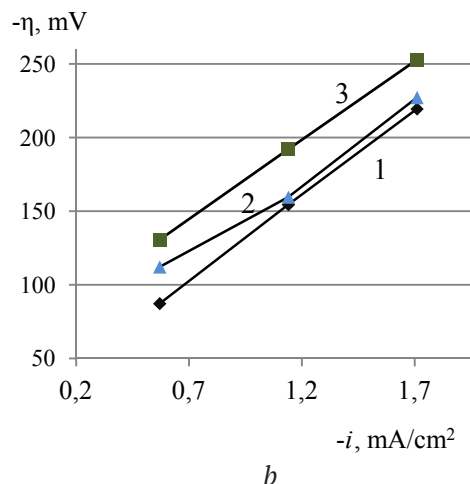
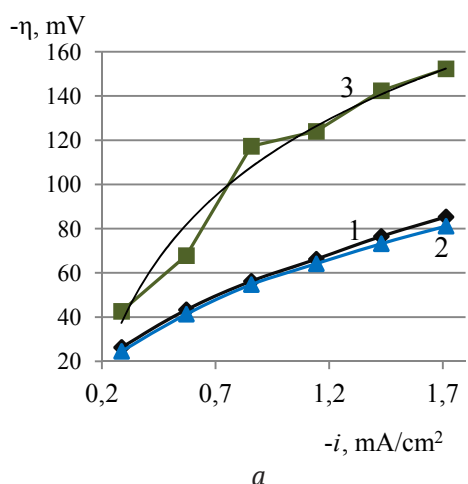


Fig. 7. Dependence of polarisation ($-\eta$) on current density (i) during electrolysis of a solution of $0.025 \text{ M ZnSO}_4 + 0.5 \text{ M Na}_2\text{SO}_4$. 1 – without coagulant; 2 – anionic; 3 – cationic. With stirring, the confidence interval ($p = 0.05$) was 8.77 mV (a). Without stirring, the confidence interval ($p = 0.05$) was 6.82 mV (b)

process greatly accelerated and the contribution to the dynamics of the process of charge transfer stage through the “metal – electrolyte” interphase, the so-called electrochemical stage, started increasing. It was confirmed by the experimental data on the influence of cationic and anionic surfactants on the process of zinc discharge. In our opinion, if the process of zinc discharge was limited only by the transport stage (concentration polarisation), the unequal influence of differently charged coagulants on the cathodic process would be unlikely.

Therefore, the obtained experimental data under intense stirring in the presence of a background sodium sulphate solution, a foaming agent, and cationic and anionic coagulants (flocculants) correspond to the theoretical concepts of electrochemical processes [25–26].

4. Conclusions

The data obtained in this work, including quadratic dependence of current density of zinc discharge on the value of the cathode potential, the fact that the straight lines of dependence of current density of zinc discharge on the square root of the linear potential sweep of rate do not pass through the origin of coordinates, change in the reaction order for zinc electrolysis in the presence of surfactants, and an increase in the influence interval of differently charged surfactants on electrode processes, allow determining that the process of discharge of zinc ions in a background solution on a solid electrode occurs in a mixed-kinetic mode, where it is difficult to identify a significant contribution to the dynamics of the process of the stage of mass-transfer of ions or the charge transfer stage through the “metal – electrolyte” interphase.

Thus, the approach suggested in this work provided a greater degree of statistical reliability in evaluating the effect of additions of cationic and anionic surfactants on the stage of zinc discharge, which is of great importance for hydrometallurgical technologies and outlines further lines of research in this field.

Contribution of the authors

A. V. Kolesnikov – academic advisor, setting tasks, research concept, methodology, conclusions.
E. I. Ageenko – conducting experimental work,

participating in the analysis of the obtained data, text editing.

Conflict of interests

The authors declare that they have no known competing financial interests or personal relationships that could have influenced the work reported in this paper.

References

1. Kolesnikov A. V., Kozlov P. A. Electrolysis of zinc in sulfate solutions. *Tsvetnye Metally*. 2018;(8): 45–49. <https://doi.org/10.17580/tsm.2018.08.05> (In Russ., abstract in Eng.)
2. Ivanov I., Stefanov Y. Electroextraction of zinc from sulphate electrolytes containing antimony ions and hydroxyethylated-butyne-2-diol-1,4: Part 3. The influence of manganese ions and a divided cell. *Hydrometallurgy*. 2002;64(3): 181–186. [https://doi.org/10.1016/S0304-386X\(02\)00039-7](https://doi.org/10.1016/S0304-386X(02)00039-7)
3. Stefanov Y., Ivanov I. The influence of nickel ions and triethylbenzylammonium chloride on the electrowinning of zinc from sulphate electrolytes containing manganese ions. *Hydrometallurgy*. 2002;64(3): 193–203. [https://doi.org/10.1016/S0304-386X\(02\)00037-3](https://doi.org/10.1016/S0304-386X(02)00037-3)
4. Kolesnikov A. V. Investigations of the influence of di-2-ethyl-hexyl phosphoric acid on the parameters of electrolysis of zinc from acidic solutions. *Butlerov Communications*. 2018;55(8): 127–133. Available at: <https://www.elibrary.ru/item.asp?id=35659982> (In Russ., abstract in Eng.)
5. Kolesnikov A. V., Kozlov P. A., Fominykh I. M. Investigations of the influence of white spirit on the parameters of electrolysis of zinc from acidic solutions. *Butlerov Communications*. 2018;55(8): 120–126. Available at: <https://www.elibrary.ru/item.asp?id=35659981> (In Russ., abstract in Eng.)
6. Karavasteva M. The effect of some surfactants on the dissolution of zinc in sulfuric acid solutions containing ions of metallic impurities. *Canadian Metallurgical Quarterly*. 2004;43(4): 461–468. <https://doi.org/10.1179/cm.2004.43.4.461>
7. Kolesnikov A. V. The electroreduction are investigated zinc from the background solution of sodium sulfate in the presence of cationic and anionic flocculants. *Butlerov Communications*. 2017;49(2): 130–136. Available at: <https://www.elibrary.ru/item.asp?id=29197189> (In Russ., abstract in Eng.)
8. Ivanov I. Increasing the current efficiency during zinc electroextraction in the presence of metal impurities by adding organic inhibitors. *Hydrometallurgy*. 2004;72(1-2): 73–78. [https://doi.org/10.1016/S0304-386X\(03\)00129-4](https://doi.org/10.1016/S0304-386X(03)00129-4)

9. Tripathy B. C., Das S. C., Misra V. N. Effect of antimony(III) on the electrocrystallisation of zinc from sulphate solutions containing SLS. *Hydrometallurgy*. 2003;69(1-3): 81–88. [https://doi.org/10.1016/S0304-386X\(02\)00204-9](https://doi.org/10.1016/S0304-386X(02)00204-9)
10. Kolesnikov A. V. Copper recovery of zinc metal in aqueous solutions in the presence of high surfactant. *Kondensirovannye sredy i mezhfaznye granitsy = Condensed Matter and Interphases*. 2016;18(1): 46–55. Available at: <https://journals.vsu.ru/kcmf/article/view/107/128> (In Russ., abstract in Eng.)
11. Krstajic N. V., Grgur B. N., Mladenovic N. S., Vojnovic M. V., Jaksic M. M. Determination of the kinetic parameters of hydrogen evolution. *Electrochimica Acta*. 1997;42(2): 323–330. [https://doi.org/10.1016/0013-4686\(96\)00188-0](https://doi.org/10.1016/0013-4686(96)00188-0)
12. Tseluykin V. N., Koreshkova A. A., Invalid O. G., Tseluykina G. V., Solovieva N. D. Electrodeposition and properties of zinc composite coatings modified by carbon nanotubes. *Kondensirovannye sredy i mezhfaznye granitsy = Condensed Matter and Interphases*. 2013;15(4): 466–469. Available at: <https://journals.vsu.ru/kcmf/article/view/936/1018> (In Russ.)
13. Sapronova L. V., Sotskaya N. V., Dolgikh O. V. Kinetics of electrodeposition of nickel from complex electrolytes containing amino acids. *Kondensirovannye sredy i mezhfaznye granitsy = Condensed Matter and Interphases*. 2013;15(4): 446–452. Available at: <https://journals.vsu.ru/kcmf/article/view/933/1015> (In Russ.)
14. Kolesnikov A. V., Kazanbaev L. A., Kozlov P. A. Influence of organic substances on cementation and zinc electrolysis processes. *Tsvetnye Metally*. 2006;(8): 24–28. Available at: <https://www.elibrary.ru/item.asp?id=9245180> (In Russ., abstract in Eng.)
15. Kichigin V. I., Shein A. B. Effect of anodization on the kinetics of the hydrogen evolution on cobalt silicides in sulfuric acid solution. *Kondensirovannye sredy i mezhfaznye granitsy = Condensed Matter and Interphases*. 2017;19(3): 359–367. <https://doi.org/10.17308/kcmf.2019.21/2365> (In Russ., Abstract in Eng.)
16. Skibina L. M., Duran Delgado O. A., Sokolenko A. I. Kinetics of electrodeposition and surface morphology of cadmium and organo-cadmium coatings containing e-caprolactan. *Kondensirovannye sredy i mezhfaznye granitsy = Condensed Matter and Interphases*. 2017;19(3): 430–440. Available at: <https://doi.org/10.17308/kcmf.2017.19/220> (In Russ., abstract in Eng.)
17. Kondrashin V. Yu., Shafrava M. F. Copper dissolution in persulfate environment at cathodic potentials. *Kondensirovannye sredy i mezhfaznye granitsy = Condensed Matter and Interphases*. 2017;19(4): 517–522. <https://doi.org/10.17308/kcmf.2017.19/230> (In Russ., abstract in Eng.)
18. Galyus Z. *Theoretical foundations of electrochemical analysis*. Moscow: Mir Publ.; 1974. 552 p. (In Russ.)
19. Alfantazi A. M. An investigation on the effects of orthophenylene diamine and sodium lignin sulfonate on zinc electrowinning from industrial electrolyte. *Hydrometallurgy*. 2003;69(1-3): 99–107. [https://doi.org/10.1016/S0304-386X\(03\)00030-6](https://doi.org/10.1016/S0304-386X(03)00030-6)
20. Kolesnikov A. V., Fominykh I. M. Parameters of electrolysis of zinc sulfate solutions. *Butlerov Communications*. 2017;51(8): 89–97. Available at: <https://www.elibrary.ru/item.asp?id=30506038> (In Russ., abstract in Eng.)
21. Solmaz R., Kardas G., Yazici B., Erbil M. Adsorption and anticorrosive properties of 2-amino-5-mercapto-1,3,4-thiadiazole on mild steel in hydrochloric acid media *Colloids and Surfaces A: Physicochemical and Engineering Aspects*. 2008;(312): 7–17. <https://doi.org/10.1016/j.colsurfa.2007.06.035>
22. Kolesnikov A. V. Cathodic and anodic processes in zinc sulfate solutions in the presence of surfactants. *ChemChemTech*. 2016;59(1): 53–57. Available at: <https://www.elibrary.ru/item.asp?id=25501669> (In Russ.)
23. Minin I. V., Solovyova N. D. Kinetics of zinc electroreduction from the sulfate electrolyte in the presence of surfactant additives. *Vestnik Saratovskogo tekhnicheskogo universiteta*. 2013;69(1): 58–60. Available at: <https://www.elibrary.ru/item.asp?id=19415711> (In Russ., abstract in Eng.)
24. Rotinyan A. L., Tikhonov K. I., Shoshina I. A. *Theoretical electrochemistry*. Leningrad: Khimiya Publ.; 1981. 424 p. (In Russ.)
25. Atkins P. *Physical chemistry*. New York: W. H. Freeman; 2002.
26. Skorcheleti V. V. *Theoretical electrochemistry*. Ed. 4th, rev. and add. Leningrad: Khimiya Publ; 1974. 567 p. (In Russ.)

Information about the authors

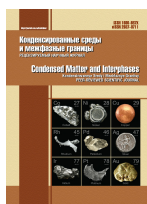
Alexander V. Kolesnikov, DSc in Chemistry, Senior Researcher, Head of the Department of Analytical and Physical Chemistry, Faculty of Chemistry, Chelyabinsk State University, Chelyabinsk, Russian Federation; e-mail: avkzinc@csu.ru. ORCID iD: <https://orcid.org/0000-0002-9747-1241>.

Egor I. Ageenko, Assistant, Department of Analytical and Physical Chemistry, Faculty of Chemistry, Chelyabinsk State University, Chelyabinsk, Russian Federation; e-mail: ag-40@mail.ru. ORCID iD: <https://orcid.org/0000-0002-2701-9831>.

Received 28.01.2021; Approved after reviewing 17.03.2021; Accepted 15.05.2021; Published online 25.06.2021.

Translated by Marina Strepetova

Edited and proofread by Simon Cox



Condensed Matter and Interphases

Kondensirovannye Sredy i Mezhfaznye Granitsy
<https://journals.vsu.ru/kcmf/>

Original articles

Research article

<https://doi.org/10.17308/kcmf.2021.23/3435>

Phase relations in the CuI-SbSI-SbI₃ composition range of the Cu-Sb-S-I quaternary system

P. R. Mammadli^{1,2,✉}, V. A. Gasymov², G. B. Dashdiyeva³, D. M. Babanly^{1,2}

¹Azerbaijan State Oil and Industry University, French - Azerbaijani University,
183 Nizami str., Baku AZ-1010, Azerbaijan

²Institute of Catalysis and Inorganic Chemistry of the Azerbaijan National Academy of Sciences,
113 H. Javid ave., Baku AZ-1143, Azerbaijan

³Baku Engineering University,
120 Hasan Aliyev str., Baku AZ-0102, Azerbaijan

Abstract

The phase equilibria in the Cu-Sb-S-I quaternary system were studied by differential thermal analysis and X-ray phase analysis methods in the CuI-SbSI-SbI₃ concentration intervals. The boundary quasi-binary section CuI-SbSI, 2 internal polythermal sections of the phase diagram, as well as, the projection of the liquidus surface were constructed. Primary crystallisation areas of phases, types, and coordinates of non- and monovariant equilibria were determined. Limited areas of solid solutions based on the SbSI (β -phase) and high-temperature modifications of the CuI (α_1 - and α_2 - phases) were revealed in the system. The formation of the α_1 and α_2 phases is accompanied by a decrease in the temperatures of the polymorphic transitions of CuI and the establishment of metatectic (375°C) and eutectoid (280°C) reactions. It was also shown, that the system is characterised by the presence of a wide immiscibility region that covers a significant part of the liquidus surface of the CuI and SbSI based phases.

Keywords: Copper (I) iodide, Antimony iodide, Antimony sulfoiodide, Cu-Sb-S-I system, Phase diagram, Solid solutions

Acknowledgements: the work has been partially supported by the Science Development Foundation under the President of the Republic of Azerbaijan, a grant № EIF-BGM-4-RFTF-1/2017-21/11/4-M-12.

For citation: Mammadli P. R., Gasymov V. A., Dashdiyeva G. B., Babanly D. M. Phase relations in the CuI-SbSI-SbI₃ composition range of the Cu-Sb-S-I quaternary system. *Kondensirovannye sredy i mezhfaznye granitsy = Condensed Matter and Interphases*. 2021;23(2): 236–244. <https://doi.org/10.17308/kcmf.2021.23/3435>

Для цитирования: Маммадли П. Р., Гасымов В. А., Дашдиева Д. Б., Бабанлы Д. М. Фазовые равновесия в области составов CuI-SbSI-SbI₃ системы Cu-Sb-S-I. *Конденсированные среды и межфазные границы*. 2021;23(2): 236–244. <https://doi.org/10.17308/kcmf.2021.23/3435>

✉ Parvin Rovshan Mammadli, e-mail: parvin.mammadli@ufaz.az
© Mammadli P. R., Gasymov V. A., Dashdiyeva G. B., Babanly D. M., 2021



1. Introduction

Copper-antimony chalcogenides and phases based on them are considered to be potential candidates for the preparation of environmentally friendly, low-cost functional materials possessing novel desired characteristics [1–3]. The majority of ternary Cu–Sb–sulphides are naturally occurring minerals that have been widely explored as valuable electronic materials displaying high photoelectric, photovoltaic, radiation detector, thermoelectric, etc. properties. Earth abundance and environmental compatibility of these substances highlight the recent advances of investigations on these materials [4–7].

As it is known, one of the ways to increase the efficiency of thermoelectric materials is to complicate their composition and crystal structure [8]. In this regard, Cu-Sb chalcogenides could be considered promising research objects in terms of the search and design of new eco-friendly functional materials. However, we could not find literary information about the phase equilibria of the Cu–Sb–S–I quaternary system. There is a literary report about the formation, crystal structure, and conductivity of the $\text{Cu}_5\text{SbS}_3\text{I}_2$ compound [9]. $\text{Cu}_5\text{SbS}_3\text{I}_2$ crystallises in the orthorhombic system, space group $Pn\bar{m}$ with the following lattice parameters $a = 10.488(2)$, $b = 12.619(2)$, $c = 7.316(1)$ Å, and $Z = 4$ [9]. Electric conductivity and dielectric parameters of the Cu–Sb–S–I glasses have been investigated in order to evaluate their practical importance in memory switching, electrical threshold, optical switching devices, and so forth [10].

The search and design of new complex functional materials require investigation of the respective phase diagrams. The information accumulated in phase diagrams of the corresponding systems is always helpful in materials science for the development of advanced materials [11–13].

Considering above mentioned facts, in terms of the search for new multicomponent phases, the concentration plane $\text{Cu}_2\text{S}-\text{CuI}-\text{SbI}_3-\text{Sb}_2\text{S}_3$ of the Cu–Sb–S–I quaternary system is of great interest. The present contribution is dedicated to the study of physicochemical interaction in the CuI–SbSI–SbI₃ (A) concentration area of the above-mentioned concentration plane.

Primary compounds of the system (A) possessing interesting functional properties

have been studied in detail. Copper (I) iodide CuI is a non-poisonous, wide-gap semiconductor possessing stable p-type electrical conductivity at room temperature, fast-ionic conductivity at high temperatures, an unusually large temperature dependency, negative spin-orbit splitting, etc [14–16]. It has wide application in light-emitting diodes, solid-state dye-sensitised solar cells, high-performance thermoelectric elements, etc [17, 18]. Antimony triiodide SbI₃ has been intensively studied as a dopant in thermoelectric materials, as a potential material for radiation detectors, as cathodes in solid-state batteries, in high-resolution image microrecording, information storage, etc. [19–21]. SbSI exhibits important ferroelectricity, piezoelectricity, photoconduction, dielectric polarisation properties and is widely used in the fabrication of nanogenerators and nanosensors [22–25].

CuI melts at 606 °C without decomposition and has 3 modifications [26, 27]. The low-temperature γ -modification transforms to the β -phase at 369 °C. The β -CuI phase exists in a small temperature range (~ 10 K) and transforms into α -phase at 407 °C. SbI₃ melts at 172 °C [28] and crystallises to rhombohedral lattice [29]. SbSI melts congruently at 300 °C [22,30]. Three phases of SbSI have been reported: ferroelectric ($T < 20$ °C), antiferroelectric (20 °C $< T < 140$ °C) and paraelectric ($T < 140$ °C) [31]. Both in the paraelectric and ferroelectric phases, SbSI crystallises in the orthorhombic structure [32, 33].

Crystallographic parameters of the constituent compounds of the system A are represented in Table 1.

CuI–SbI₃ and SbSI–SbI₃ boundary quasi-binary sections of the quasi-ternary CuI–SbSI–SbI₃ system have been investigated by [35–37], respectively. CuI–SbI₃ system forms a monotectic phase diagram. At the monotectic equilibrium temperature (~ 220 °C) the immiscibility region ranges within ~ 15 – 93 mol% SbI₃ concentration interval [35]. SbSI–SbI₃ quasi-binary section is characterised by a eutectic equilibrium at 160 °C [12, 30].

2. Experimental part

A CuI binary compound, as well as, antimony and iodine elementary components of the *Alfa*

Table 1. Crystal lattice types and parameters of the CuI, SbI₃, and SbSI compound

Compound, modification	Crystal lattice type and parameter, Å
LT–CuI	Cubic lattice; SpGr. F; $a = 6.05844(3)$ Å [27]
HT1–CuI	Trigonal: SpGr. P3; $a = 4.279 \pm 0.002$; $c = 7.168 \pm 0.007$ (673 K) [34]
	Trigonal: SpGr. R-3; $a = 4.29863(11)$; $c = 21.4712(6)$ (603 K) [26]
HT2–CuI	Trigonal: SpGr. R-3 $a = 4.30571$ (12); $c = 21.4465(7)$ (608 K) [26]
	Cubic: SpGr. F $a = 6.16866(6)$ [27]
SbI ₃	Rhombohedral: SpGr. ; $a = 7.48$; $c = 20,90$; $Z = 6$ [29]
SbSI	Orthorhombic: SpGr. Pnam; $a = 8.556(3)$; $b = 10.186(4)$; $c = 4.111(2)$; $z = 4$ [32]
	Orthorhombic: SpGr. Pna2 ₁ ; $a = 8.53$; $b = 10.14$; $c = 4.10$ [33]

The symbols HT2, HT1, and LT indicate high, intermediate, and low-temperature modifications of CuI, respectively.

Aesar German brand (99.999 % purity) were used in the course of experimental studies.

Binary SbI₃ and ternary SbSI compounds were synthesised from the elemental components in evacuated ($\sim 10^{-2}$ Pa) silica ampoules followed by a specially designed method taking into account the high volatility of iodine and sulphur. The synthesis was performed in an inclined two-zone furnace, with the hot zone kept at a temperature 20–30 °C higher than the corresponding melting point of the synthesised compound, whereas the temperature of the cold zone was kept at about 130 °C. After the main portion of iodine and sulphur had reacted, the ampoules were relocated such that the products could melt at 230 °C (SbI₃) and 450 °C (SbSI). After stirring the homogeneous liquid at this temperature, the furnace gradually cooled. The purity and individuality of the obtained products were monitored using DTA and PXRD methods.

Two sets of samples (0.5 g by mass each) were prepared by co-melting of different proportions of the preliminarily synthesised compounds and CuI of the *Alfa Aesar* company. After melting, most of the alloys were annealed at about ~ 20 –30 °C below the solidus temperature for ~ 1000 hours in order to achieve complete homogenisation.

The DTA and PXRD methods were used to monitor the purity and individuality of the synthesised compounds and to conduct experimental studies. DTA of the samples was carried out in evacuated quartz ampoules on a differential scanning calorimeter of the 404 F1 Pegasus System (NETZSCH). Results of measurements were processed using the NETZSCH Proteus Software. The accuracy of the temperature measurements was within ± 2 °C. X-ray analysis of the annealed alloys was carried

out at room temperature on the Bruker D2 PHASER diffractometer with $\text{CuK}\alpha_1$ radiation. The diffraction patterns were indexed using the Topas 4.2 Software (Bruker).

3. Results and discussion

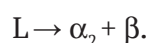
A co-analysis of experimental results together with the literature data regarding boundary binary systems helped us to obtain the full description of phase equilibria in the CuI–SbSI–SbI₃ concentration triangle.

3.1. CuI–SbSI boundary quasi-binary system

The powder X-ray diffraction patterns of the thermally treated CuI–SbSI alloys are given in Fig. 1. As can be seen, diffraction patterns of samples in the full composition range consist of the diffraction peaks of the SbSI and low-temperature modification of CuI.

The T - x phase diagram of the system (Fig. 2) was constructed using DTA results (Table 2). Note that, α_1 and α_2 are solid solutions based on the HT1 – CuI and HT2 – CuI respectively, and β – is a solid solution based on SbSI.

The system is quasi-binary and forms a eutectic phase diagram. Eutectics has a ~ 45 mol% SbSI composition and crystallises at 327 °C by the reaction:



The formation of α_1 and α_2 solid solution areas based on the high-temperature modifications of CuI is accompanied by a decrease in temperature of its' both phase transformations and these phase transitions occur by metatectic and eutectoid reactions.

Isotherms corresponding to the 375 and 280 °C temperatures on the phase diagram, reflect metatectic

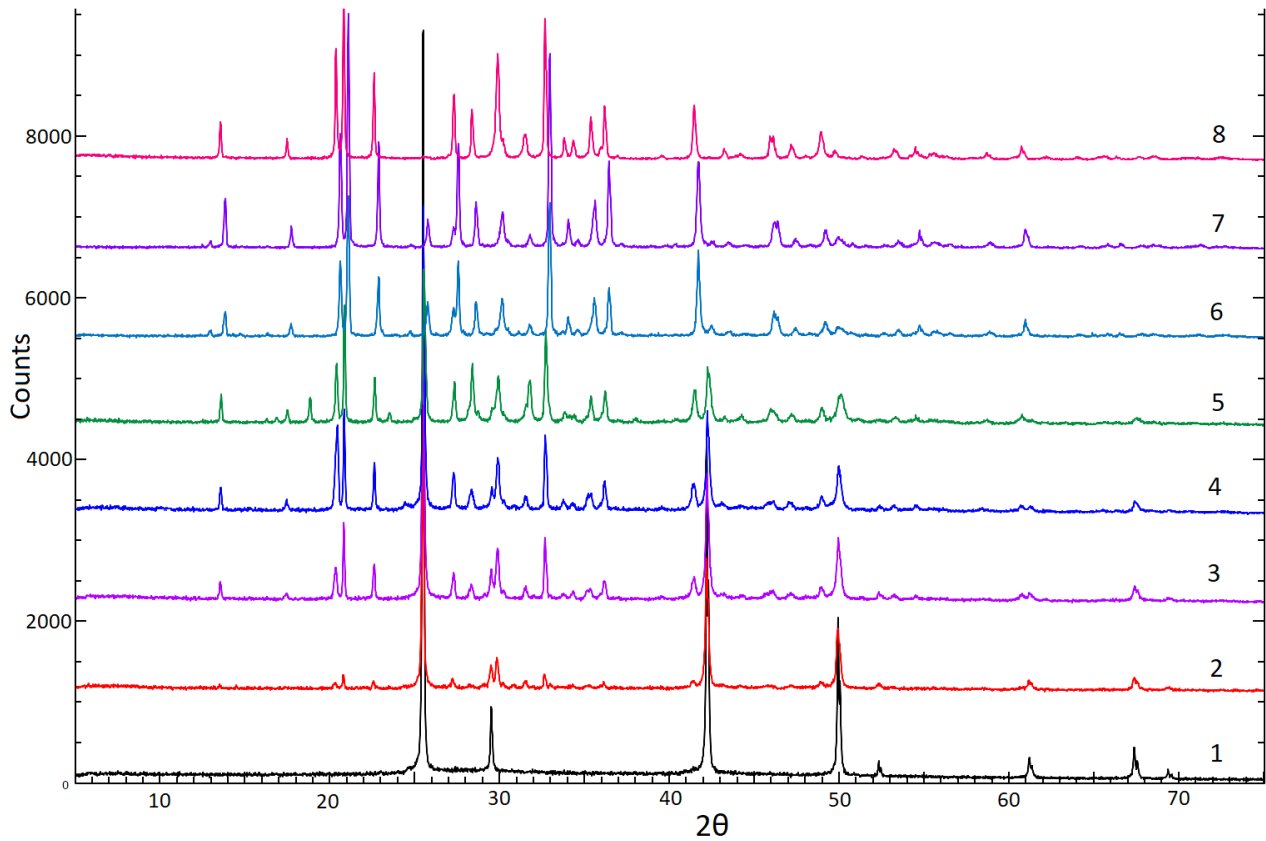


Fig. 1. X-ray images of different alloys of the CuI–SbSI system: 1 – CuI, 2 – 10 mol% CuI, 3 – 20 mol% CuI, 4 – 40 mol% CuI, 5 – 60 mol% CuI; 6 – 80 mol% CuI; 7 – 90 mol% CuI; 8 – SbSI

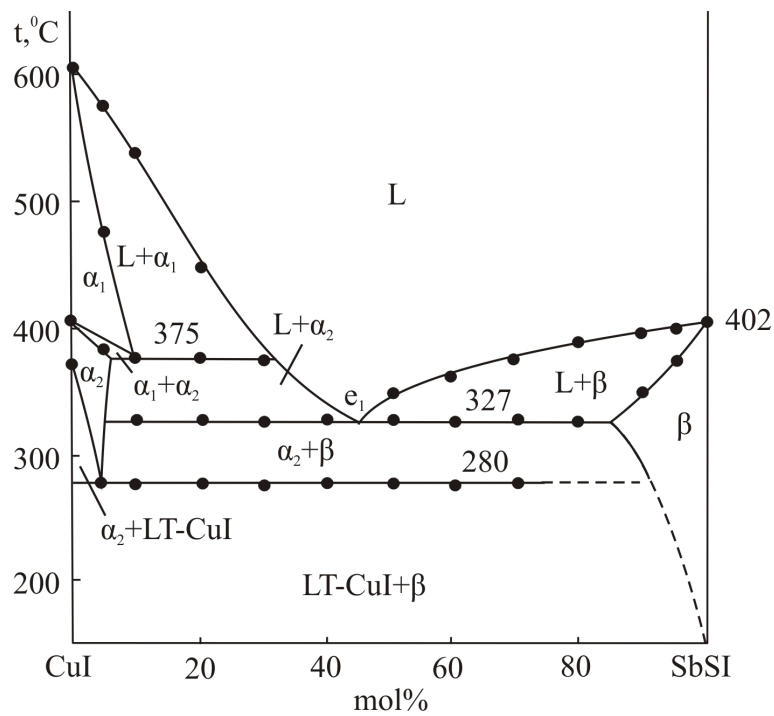
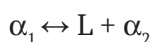


Fig. 2. *T-x* phase diagram of the CuI–SbSI system

Table 2. DTA results of the CuI–SbSI system

Composition, mol% SbSI	Thermal effects, °C	
	Isothermal	Polythermal
0 (pure CuI)	369; 407; 606	–
5	280; 385	470–573
10	280; 325; 375	375–534
20	282; 327; 373	373–455
30	280; 328; 376	–
40	278; 327	–
50	280; 327	327–343
60	280; 328	328–360
70	279; 327	327–375
80	327	327–382
90	–	352–394
95	–	380–398
100 (pure SbI ₃)	402	–



and eutectoid



equilibriums, respectively.

The homogeneity region of the β -phase based on SbSI is maximum (~15 mol%) at the eutectic temperature (Fig. 2). Moreover, reflection angles belonging to LT-CuI and SbSI phases on powder diffractograms are fully compatible with appropriate pure compounds. It shows that the mutual solubility of these compounds is negligible at room temperature. Therefore, in Fig. 2, the decomposition curve of the β -phase is extrapolated to the SbSI compound.

3.2. Projection of the liquidus surface (Fig. 3)

Fig. 3 represents a projection of the T - x - y diagram of the CuI–SbSI–SbI₃ system, where liquidus isotherms are given in blue. The liquidus surface consists of three fields describing the primary crystallisation of the α_1 (α_2), β -phases, and SbI₃. The latter occupies a small region near the appropriate corner of the concentration triangle.

Primary crystallisation surfaces of phases are limited by a number of monovariant equilibrium curves and non-variant equilibrium points (Table 3).

The L_1+L_2 immiscibility region in the CuI–SbI₃ boundary system sharply penetrates into the concentration triangle and covers part of

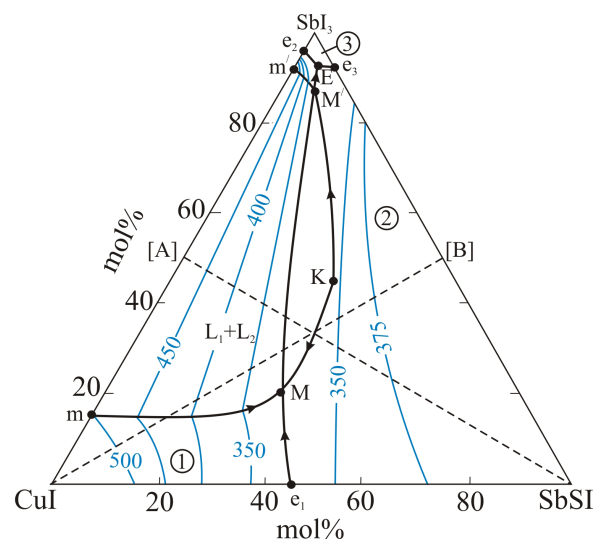


Fig. 3. Projection of the liquidus surface of the system CuI–SbSI–SbI₃. Primary crystallisation fields: 1 – α_1 (α_2); 2 – β phase; 3 – SbI₃. Dotted lines are studied polythermal sections

the liquidus area of the β phase by crossing the eutectic curve from the point e_1 . Consequently, the $L \leftrightarrow \alpha_2 + \beta$ monovariant eutectic equilibrium shifts to the $L_1 \leftrightarrow L_2 + \alpha_2 + \beta$ nonvariant monotectic equilibrium (Fig. 3, Table 1 – MM' conjugate pair). K is the critical point of stratification and has a temperature of ~350 °C.

Crystallisation across the whole system ends at 165 °C by nonvariant eutectic (E) reaction.

3.3. Polythermal sections

The CuI–[B] (Fig. 4) and [A]–SbSI (Fig. 5) polythermal sections of the phase diagram of the CuI–SbSI–SbI₃ ternary system are given below and analysed in context with the projection of the liquidus surface of the system. Here, [A] and [B] are 1:1 mix ratios of the constituent compounds of the CuI–SbI₃ and SbSI–SbI₃ side binary systems, consequently.

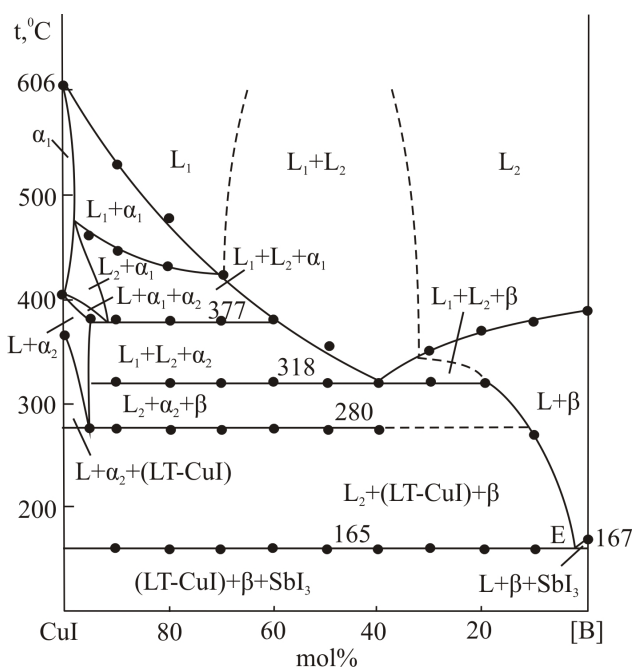
The system CuI–[B] (Fig. 4). This section passes through the initial crystallisation areas of the α_1 (α_2) and β -phases and the immiscibility area in the ~ 30–70 mol% CuI concentration range. Crystallisation in the compositions rich in CuI initially continues by the monovariant monotectic $L_1 \leftrightarrow L_2 + \alpha_1$ reaction and leads to the formation of the $L_1 + L_2 + \alpha_1$ three-phase area. At 377 °C this phase field is replaced by the $L_1 + L_2 + \alpha_1$ three-phase area as a result of the $\alpha_1 \leftrightarrow \alpha_2$ phase transition. Crystallisation in the 20–40 mol% CuI

Table 3. Non- and monovariant equilibria of the CuI–SbSI–SbI₃ system

Point in Fig. 3	Equilibrium	Composition, mol%		Temperature, °C
		SbSI	SbI ₃	
e ₁	L ↔ α ₂ + β	45	–	327
e ₂	L ↔ LT-CuI + SbI ₃	–	97	168
e ₃	L ↔ SbSI + SbI ₃	7	93	167
m (m')	L ₁ ↔ L ₂ + α ₁	–	15 (93)	493
M (M')	L ₁ ↔ L ₂ + α ₂ + β	34 (6)	20 (87)	318
E	L ↔ LT-CuI + β + SbI ₃	–	–	165
Curve in Fig. 3	Equilibrium	Temperature interval, °C		
mM (m'M')	L ₁ ↔ L ₂ + α ₁	493–318		
KM (KM')	L ₁ ↔ L ₂ + β	340–318		
e ₁ M	L ↔ α ₂ + β	327–318		
M'E	L ↔ α ₂ (LT-CuI) + β	318–165		
e ₂ E	L ↔ LT-CuI + SbI ₃	168–165		
e ₃ E	L ↔ β + SbI ₃	167–165		

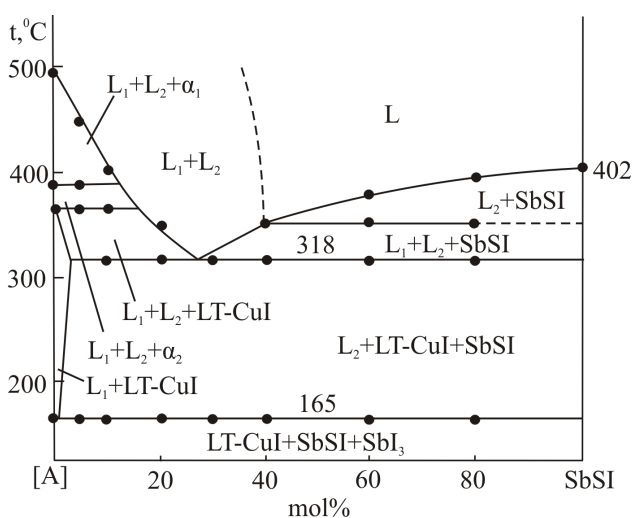
composition range continues by the L₁ ↔ L₂ + β monotectic scheme and forms the L₁ + L₂ + β phase area. Horizontal line at 318 °C belongs to the L₁ ↔ L₂ + α₂ + β nonvariant monotectic reaction (Table 2). After this reaction, the L₂ + α₂ + β three-phase area forms in the system. At 280 °C, the α₂ ↔ LT-CuI phase transitions occur and the latter phase area passes to the L₂ + β + LT-CuI.

Crystallisation of all samples along the system ends at 165 °C by the nonvariant eutectic reaction


Fig. 4. T-x phase diagram of the system CuI–[B]

(E) and the β + LT-CuI + SbI₃ three-phase mixture forms.

The system [A]–SbSI (Fig. 5). This polythermal section is situated in the L₁ + L₂ immiscibility area at the 0–40 mol% SbSI composition range and crystallisation processes occur by monotectic reactions (Fig. 3, mM/K and m'M'/K' conjugate curves). In the course of those processes the L₁ + L₂ + α₁, L₁ + L₂ + α₂, L₁ + L₂ + LT-CuI and L₁ + L₂ + β three-phase areas are formed. In the alloys rich in SbSI, crystallisation of this compound initially occurs from the liquid solution, then continues by the L₁ ↔ L₂ + SbSI monotectic scheme. All alloys are exposed to the nonvariant monotectic


Fig. 5. T-x phase diagram of the system [A]–SbSI

reaction (m) at 318 °C and fully crystallise by the nonvariant eutectic reaction at 165 °C.

Fig. 6 shows the DTA heating curves of selected annealed samples along the boundary quasi-binary system CuI–SbSI and the above-mentioned internal sections. Comparison of these curves with the corresponding T - x diagrams (Fig. 2, 4, 5), the projection of the liquidus surface (Fig. 3) and the table shows that they accurately reflect the character and temperatures of the processes occurring in the system.

4. Conclusion

The phase equilibria in the CuI–SbSI–SbI₃ composition range of the Cu–Sb–S–I quaternary system have been studied for the first time. Several polythermal sections of the phase diagram including the CuI–SbSI boundary system and T - x - y projection of the liquidus surface of the system was obtained by co-analysis of experimental results along with the literature data on boundary binary systems. It was determined that there are limited solid solutions based on SbSI (β -phases) and HT-CuI (α_1 - and α_2 -phases) and the system is characterised by the formation of a large immiscibility area. The types and coordinates of non- and monovariant equilibria, as well as, primary crystallisation areas of phases were determined.

Contribution of the authors

P. R. Mammadli – experimental investigations, writing original draft, making conclusions. V. A. Gasymov – powder X-ray analysis. G. B. Dashdiyeva – research concept, methodology development. D. M. Babanly – scientific management, review and editing.

Conflict of interests

The author declares that they have no known competing financial interests or personal relationships that could have appeared to influence the work reported in this paper.

References

1. Ivanov-Shhic A. K., Murin. I. V. *Ionika tverdogo tela. V 2-h tomah* [Ionic Solid State (in 2 vol.)]. St. Petersburg: Izd-vo S.- Peterb. un-ta Publ. 2000;1: 616. (In Russ.)
2. Babanly M. B., Mashadiyeva L. F., Babanly D. M., Imamaliyeva S. Z., Tagiyev D. B., Yusibov Y. A.. Some issues of complex studies of phase equilibria and thermodynamic properties in ternary chalcogenide systems involving Emf measurements. *Russian Journal of Inorganic Chemistry*. 2019;64(13): 1649–1672. <https://doi.org/10.1134/s0036023619130035>
3. Peccerillo E., Durose K. Copper–antimony and copper–bismuth chalcogenides—Research opportunities and review for solar photovoltaics. *MRS Energy & Sustainability*. 2018;5(9): 1–59. <https://doi.org/10.1557/mre.2018.10>

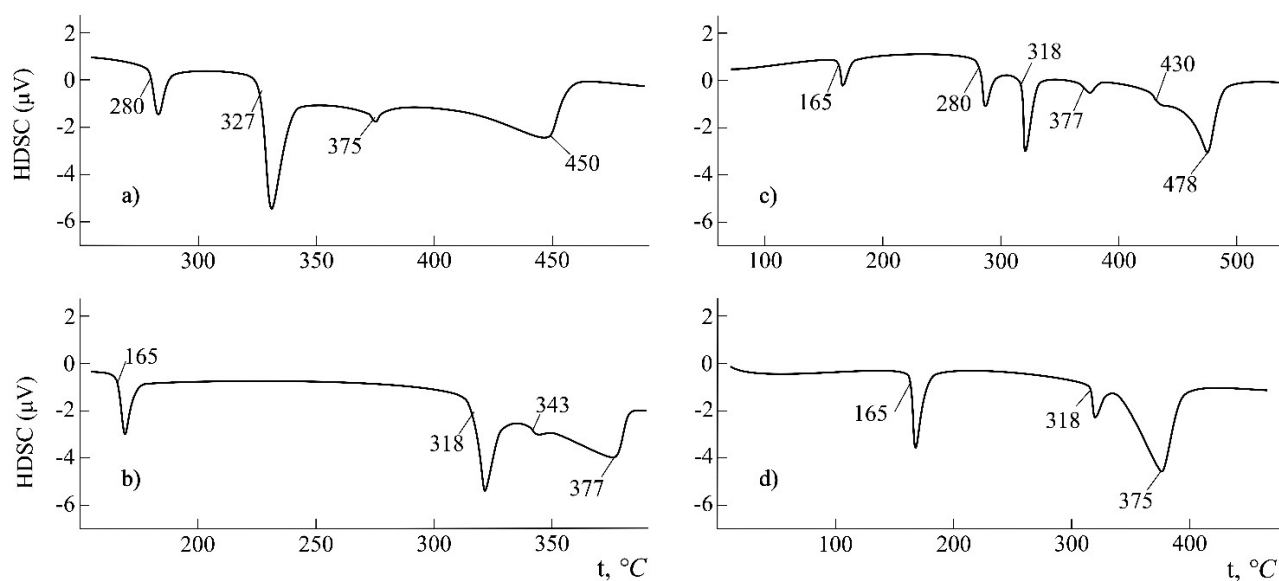


Fig.6. DTA heating curves of some samples: alloy of composition 20 mol% SbSI of the CuI–SbSI system (a); alloys with compositions 30 (b) and 80 mol% CuI (c) along the section CuI–[B]; and 60 mol% SbSI (d) along the section [A] – SbSI

4. Loranca-Ramos F. E., Diliegros-Godines C. J., Silva-González R., Pal M. Structural, optical and electrical properties of copper antimony sulfide thin films grown by a citrate-assisted single chemical bath deposition. *Applied Surface Science*. 2018;427: 1099–1106. <https://doi.org/10.1016/j.apsusc.2017.08.027>
5. Chetty R., Bali A., Mallik R. C. Tetrahedrites as thermoelectric materials: an overview. *Journal of Materials Chemistry C*. 2015;3(48): 12364–12378. <https://doi.org/10.1039/C5TC02537K>
6. Van Embden J., Latham K., Duffy N. W., Tachibana Y. Near-infrared absorbing $\text{Cu}_{12}\text{Sb}_4\text{S}_{13}$ and Cu_3SbS_4 nanocrystals: Synthesis, characterization, and photoelectrochemistry. *Journal of the American Chemical Society*. 2013;135(31): 11562–11571. <https://doi.org/10.1021/ja402702x>
7. Lu X., Morelli D. T., Xia Y., Zhou F., Ozolins V., Chi H., Zhou X., Uher C. High performance thermoelectricity in earth-abundant compounds based on natural mineral tetrahedrites. *Advanced Energy Materials*. 2013;3(3): 342–348. <https://doi.org/10.1002/aenm.201200650>
8. Ioffe A. F. *Semiconductor thermoelements and thermoelectric cooling*. London: Infosearch Ltd; 1957.
9. Pfitzner A. $(\text{CuI})_2\text{Cu}_3\text{SbS}_3$: copper iodide as solid solvent for thiometalate ions. *Chemistry – A European Journal*. 1997;3(12): 2032–2038. <https://doi.org/10.1002/chem.19970031218>
10. Rubish V. M. Electric and dielectric properties of glasses of Cu-Sb-S-I system. *Semiconductor Physics, Quantum electronics, and Optoelectronics*. 2003;6(1): 76–80. <http://dspace.nbuv.gov.ua/handle/123456789/117961>
11. Babanly M. B., Chulkov E. V., Aliev Z. S., Shevelkov A. V., Amiraslanov I. R. Phase diagrams in materials science of topological insulators based on metal chalcogenides. *Russian Journal of Inorganic Chemistry*. 2017;62(13): 1703–1729. <https://doi.org/10.1134/S0036023617130034>
12. Aliyev Z. S., Musayeva S. S., Babanly M. B. The phase relationships in the Sb-S-I system and thermodynamic properties of the SbSI. *Journal of Phase Equilibria and Diffusion*. 2017;38(12): 887–896. <https://doi.org/10.1007/s11669-017-0601-4>
13. Babanly D. M., Tagiyev D. B. Physicochemical aspects of ternary and complex phases development based on thallium chalcogenides. *Chemical Problem*. 2018;16 (2): 153–177. <https://doi.org/10.32737/2221-8688-2018-2-153-177>
14. Koyasu S., Umezawa N., Yamaguchi A., Miyauchi M. Optical properties of single crystalline copper iodide with native defects: Experimental and density functional theoretical investigation. *Journal of Applied Physics*. 2019;125(11): 115101. <https://doi.org/10.1063/1.5082865>
15. Grundmann M., Schein F-L., Lorenz M., Böntgen T., Lenzner J., Wenckstern H. Cuprous iodide – a p-type transparent semiconductor: history and novel applications. *Physica Status Solidi A*. 2013;210(9): 1671–1703. <https://doi.org/10.1002/pssa.201329349>
16. Amalina M. N., Azilawati Y., Rasheid N. A., Rusop M. The properties of copper (I) iodide (CuI) thin films prepared by mister atomizer at different doping concentration. *Procedia Engineering*. 2013;56: 731 – 736. <https://doi.org/10.1016/j.proeng.2013.03.186>
17. Perera V. P. S., Tennakone K. Recombination processes in dye-sensitized solid-state solar cells with CuI as the hole collector. *Solar Energy Materials and Solar Cells*. 2003;79(2): 249–255. [https://doi.org/10.1016/S0927-0248\(03\)00103-X](https://doi.org/10.1016/S0927-0248(03)00103-X)
18. Christians J. A., Fung R. C. M., Kamat P. V. An inorganic hole conductor for organo-lead halide perovskite solar cells. Improved hole conductivity with copper iodide. *Journal of the American Chemical Society*. 2014;136(2): 758–764. <https://doi.org/10.1021/ja411014k>
19. Onodera T., Baba K., Hitomi K. Evaluation of antimony tri-iodide crystals for radiation detectors. *Science and Technology of Nuclear Installations*. 2018;1532742: 1–7. <https://doi.org/10.1155/2018/1532742>
20. Mohan D. B., Philip A., Sunandana C. S. Iodization of antimony thin films: XRD, SEM, and optical studies of nanostructured SbI_3 . *Vacuum*. 2008;82(6): 561–565. <https://doi.org/10.1016/j.vacuum.2007.08.014>
21. Kępińska M., Starczewska A., Bednarczyk I., Szala J., Szperlich P., Mistewicz K. Fabrication and characterisation of SbI_3 -opal structures. *Materials Letters*. 2014;130: 17–20. <http://dx.doi.org/10.1016/j.matlet.2014.05.063>
22. Toron B., Szperlich P., Koziol M. SbSI composites based on epoxy resin and cellulose for energy harvesting and sensors - the influence of SbSI nanowires conglomeration on piezoelectric properties. *Materials*. 2020;13(4): 902. <https://doi.org/10.3390/ma13040902>
23. Purusothaman Y., Alluri N.R., Chandrasekhar A., Kim S. J. Photoactive piezoelectric energy harvester driven by antimony sulfoiodide (SbSI): $\text{AA}_V\text{B}_{VI}\text{C}_{VII}$ class ferroelectric-semiconductor compound. *Nano Energy*. 2018;50: 256–265. <https://doi.org/10.1016/j.nanoen.2018.05.058>
24. Jesionek M., Toron B., Szperlich P., Binias W., Binias D., Rabiej S., Starczewska A., Nowak M., Kępińska M., Dec J. Fabrication of a new PVDF/SbSI nanowire composite for smart wearable textile. *Polymer*. 2019;180: 121729. <https://doi.org/10.1016/j.polymer.2019.121729>

25. Szperlich P., Toron B. An ultrasonic fabrication method for epoxy resin/SbSI nanowire composites, and their application in nanosensors and nanogenerators. *Polymers*. 2019;11(3): 479. <https://doi.org/10.3390/polym11030479>
26. Shan Y., Li G., Tian G., Han J., Wang Ch., Liu Sh., Du H., Yang Y. Description of the phase transitions of cuprous iodide. *Journal of Alloys and Compounds*. 2009;477(1-2): 403–406. <https://doi.org/10.1016/j.jallcom.2008.10.026>
27. Yashima M., Xu Q., Yoshiasa A., Wada S. Crystal structure, electron density, and diffusion path of the fast-ion conductor copper iodide CuI. *Journal of Materials Chemistry*. 2006;16(45): 4393–4396. <https://doi.org/10.1039/B610127E>
28. Rolsten R. F. *Iodide metals and metal iodides*. New York: John Wiley and Sons; 1961.
29. Trotter J., Zobel T. The crystal structure of SbI_3 and BiI_3 . *Zeitschrift für Kristallographie - Crystalline Materials*. 1966;123(1-6): 67–72. <https://doi.org/10.1524/zkri.1966.123.16.67>
30. Ryazantsev T. A., Varekha L. M., Popovkin B. A., Lyakhovitskaya V. A., Novoselova A. V. *P-T-x* phase diagram of the SbI_3 - Sb_2S_3 system. *Izv. Akad. Nauk. Neorg. Mater.* 1969;5(7): 2196–2197. (in Russ.)
31. Audzijonis A., Sereika R., Zaltauskas R. Antiferroelectric phase transition in SbSI and SbSeI crystals. *Solid State Commun.* 2008;147(3-4): 88–89. <https://doi.org/10.1016/j.ssc.2008.05.008>
32. Lukaszewicz K., Pietraszko A., Stepen' Damm Yu., Kajokas A. Crystal structure and phase transitions of the ferroelectric antimony sulfoiodide SbSI. Part II. Crystal structure of SbSI, in Phases I, II, and III. *Polish Journal of Chemistry*. 1997;71: 1852–1857.
33. Itoh K., Matsunaga H. A Study of the crystal structure in ferroelectric SbSI. *Zeitschrift für Kristallographie - Crystalline Materials*. 1980;152(1-4): 309–315. <https://doi.org/10.1524/zkri.1980.152.14.309>
34. Sakuma T. Crystal structure of β -CuI. *Journal of the Physical Society of Japan*. 1988;57(2): 565–569. <https://doi.org/10.1143/JPSJ.57.565>
35. Mammadli P. R. Physico-chemical interaction of the copper and antimony iodides. *Azerbaijan Chemical Journal*. 2021;1: 43–49. <https://doi.org/10.32737/0005-2531-2021-1-43-47>

Information about the authors

Parvin R. Mammadli, PhD student in Chemistry, a Chemistry Teacher at French-Azerbaijani University, Azerbaijan State Oil and Industry University, Baku, Azerbaijan; e-mail: parvin.mammadli@ufaz.az. ORCID iD: <https://orcid.org/0000-0002-8062-1485>.

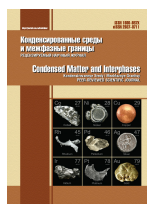
Vagif A. Gasymov, PhD in Chemistry, Assistance Professor, Institute of Catalysis and Inorganic Chemistry, Azerbaijan National Academy of Sciences, Baku, Azerbaijan; e-mail: v-gasymov@rambler.ru. ORCID iD: <https://orcid.org/0000-0001-6233-5840>.

Ganira B. Dashdiyeva, PhD in Chemistry, Chemistry Teacher, Baku Engineering University, Baku, Azerbaijan; e-mail: ganira.dasdiyeva@mail.ru.

Dunya M. Babanly, DSc in Chemistry, Coordinator of the Chemistry Department, Lecturer at French-Azerbaijani University, Senior Researcher of the Institute of Catalysis and Inorganic Chemistry, Azerbaijan National Academy of Sciences, Baku, Azerbaijan; e-mail: dunya.babanly@ufaz.az. ORCID iD: <https://orcid.org/0000-0002-8330-7854>.

Received 16 February 2021; Approved after reviewing 9 April 2021; Accepted 15 May 2021; Published online 25 June 2021.

Edited and proofread by Simon Cox



Original articles

Research article

<https://doi.org/10.17308/kcmf.2021.23/3436>

Gender differences in lipid metabolism

V. O. Mittova✉, A. O. Khoroshikh, O. V. Zemchenkova, S. V. Ryazantsev, O. V. Maslov, E. V. Korzh,
L. S. Rysnaya-Lokinskaya, V. V. Alabovsky

Voronezh State Medical University named after N. N. Burdenko of the Ministry of Health of the Russian Federation,
10 Studencheskaya str., Voronezh 394036, Russian Federation

Abstract

The search for early markers of atherosclerosis is an effective method for providing personalized medicine allowing the prevention of the progression of this pathology. The aim of this study was the determination of the total indices of dyslipidemia and the identification of the gender indices of the extended lipid profile in the population of residents of the Southern and Central Federal Districts (Voronezh, Belgorod, Lipetsk, Kursk and Rostov regions) for the identification of early markers of atherogenicity. In a simultaneous clinical study, involving 339 patients (mean age 48 years), the concentrations of total cholesterol, triglycerides, LDL (low density lipoproteins), HDL (high density lipoproteins), apolipoproteins B and A1, the ApoB/ApoA1 ratio and the atherogenic coefficient were determined. For the identification of the relationship between changes in lipid profile indicators with cytotoxicity syndrome and indicators of carbohydrate metabolism, the activity of ALAT (alanine aminotransferase), GGTP (gamma-glutamyl transpeptidase) and glucose content were also studied. Analysis of the results of the lipid spectrum of the population sample of the middle age group revealed significant metabolic disorders of lipid metabolism with a predominance of atherogenic lipid fractions and a significant excess of indicators of atherogenic lipid fractions in middle-aged men in comparison with women. It has been shown that the apoB/apoA1 index can be used as an auxiliary marker for early assessment of the prevalence of atherogenic lipid fractions, allowing the identification of risk groups for the development of diseases associated with metabolic disorders.

Keywords: Lipid metabolism, Atherosclerosis, Metabolic syndrome, Cholesterol, Triglycerides, LDL, HDL, ApoV / ApoA1, Atherogenic coefficient

For citation: Mittova V. O., Khoroshikh A. O., Zemchenkova O. V., Ryazantsev S. V., Maslov O. V., Korzh E. V., Rysnaya-Lokinskaya L. S., Alabovsky V. V. Gender differences in lipid metabolism. *Kondensirovannye sredy i mezhfaznye granitsy = Condensed Matter and Interphases*. 2021;23(2): 245–259. <https://doi.org/10.17308/kcmf.2021.23/3436>

Для цитирования: Миттова В. О., Хороших А. О., Земченкова О. В., Рязанцев С. В., Маслов О. В., Корж Е. В., Рясная-Локинская Л. С., Алабовский В. В. Гендерные особенности липидного обмена. *Конденсированные среды и межфазные границы*. 2021;23(2): 245–259. <https://doi.org/10.17308/kcmf.2021.23/3436>

✉ Mittova Valentina Olegovna, e-mail: vmittova@mail.ru

© Mittova V. O., Khoroshikh A. O., Zemchenkova O. V., Ryazantsev S. V., Maslov O. V., Korzh E. V.,
Rysnaya-Lokinskaya L. S., Alabovsky V. V., 2021



1. Introduction

Cardiovascular diseases (CVD) associated with atherosclerosis represent a global medical and social problem and are the main cause of mortality and disability in the population [1]. The PESA study showed that worldwide 71 % of middle-aged men and 43 % of women have signs of subclinical atherosclerosis [2], mortality from CVD in the Russian Federation in 2017 amounted to 587.6 cases per 100 thousand population [3, 4].

The concept of high cardiovascular risk is associated primarily with dyslipidemia due to an increase in the concentration of atherogenic lipids. Under normal conditions, insulin limits lipolysis, however, with the development of insulin resistance it is unable to suppress this process [5]. The production of very-low-density lipoproteins (VLDL) and triglycerides in the liver and their retention in tissues increases with the development of insulin resistance and dyslipidemia is formed [6]. The nosological spectrum of diseases associated with dyslipidemia, has a similar pathogenesis, determined by laboratory markers of the disease: metabolic syndrome; obesity; diseases of the biliary tract and liver; steatohepatitis; arterial hypertension; hypothyroidism and adrenal gland pathology, thromboembolism, COVID-19 [7–13].

The studies using PCSK9 inhibitors [14] and the results of the ODYSSEY OUTCOMES study with alirocumab [15] have shown that lowering LDL cholesterol decreases the incidence of cardiovascular heart disease [14, 15]. Although LDL is recognized as the main source of intracellular lipid accumulation in plaque, native LDL does not induce significant lipid accumulation in cultured cells. The modification of LDL, which changes the physicochemical characteristics of the particles is atherogenic [16]. During the course of its modification, the LDL particle is first desialylated, followed by an increase in the particle density, a decrease in size, and the acquisition of a negative charge [17]. Modified LDL is utilized mainly by the non-specific phagocytosis, which leads to the accumulation of intracellular cholesterol and the formation of foam cells [18]. Foam cells are an important structural component of atherosclerotic plaque, and modified LDL forms immune complexes that have a damaging effect

on the vascular wall, narrowing the vessel lumen and promoting thrombus formation [19].

Despite the leading role of LDL in the development of CVD, associated with atherosclerosis, the role of other lipoproteins, in particular apolipoprotein B (apoB), which is the main component of LDL was demonstrated [20]. It has been shown that the concentration of apoB can be considered a direct indicator of the total amount of atherogenic lipoproteins in the bloodstream [21]. The largest studies, INTERHEART [22] and AMORIS [23], showed that the determination of the levels of apoB and apoA1 in blood plasma seems to be the most informative indicator of the risk of developing CVD [22, 24].

Previously, the main role in the development of atherosclerosis was attributed to hypercholesterolemia, but recent clinical studies showed the participation of any hyperlipidemia in the onset and further development of atherosclerosis [25]. Thus, it was shown that although triglyceride levels above 1.7 mM/l are a factor of increased risk of CVD, the positive effect of lowering triglycerides has not been confirmed by evidence-based medicine [26]. The leading “pacemaker” of the pathological process and the degree of functional abnormalities which is not always determined by functional and visual diagnostic methods, are determined based on the presence and combination of biochemical abnormalities [27–29].

The role of dyslipidemic disorders in the etiopathogenesis of CVD, diabetes mellitus, hypertension, non-alcoholic steatohepatosis, diseases of the biliary tract, menopausal disorders determine the relevance of the search for early markers for predicting the risk of dyslipidemia in men and women [30,31].

Possible methods to search for biomarkers are:

1. In-depth/extended study of the lipid profile.
2. Inclusion in the analysis of new markers characterizing the functioning of the main metabolic systems and their disorders, which are involved in the pathogenesis of atherosclerosis in addition to the traditional factors of cardiovascular risk [32].

For the identification of the specificity and predictive value of apolipoproteins apoA1 and apoB in comparison with cholesterol, HDL,

LDL, and triglycerides we decided to analyse the extended lipid spectrum during the stage of transition of women to menopause and the indicators of men of a similar age group in order to determine the basic risks of development of atherogenic dyslipidemia. This approach determines the resources of health during the formative stage of risks associated with age, regardless of hormonal changes. The aim of this study was the determination of the total indices of dyslipidemia and the identification of the gender indices of the extended lipid profile in the population of residents of the Southern and Central Federal Districts (Voronezh, Belgorod, Lipetsk, Kursk and Rostov regions) in order to search for early markers of atherogenicity.

2. Experimental

The results of research obtained in the laboratory of OOO New Medical Technologies, Voronezh were used in the study.

For the identification of the relationship between changes in lipid profile parameters with cytotoxicity syndrome and indicators of carbohydrate metabolism, the activity of alanine aminotransferase (ALAT), gamma-glutamyl transpeptidase (GGTP), and glucose content was also studied in patients. The clinical study was carried out simultaneously, in the period from January to October 2019, the blood of 339 patients (242 women and 97 men) was examined, their average age was 48 years.

The participants were examined according to a unified scheme. A single blood sample with a volume of 10 ml on an empty stomach in the morning was carried out using a venipuncture of the superficial veins at the bend of the elbow for biochemical analysis. Serum was obtained from venous blood by standard methods.

Determination of total cholesterol, triglycerides, high density lipoprotein cholesterol was carried out by the colorimetric enzymatic method using Beckman Coulter AU analysers (USA) [33, 34, 35].

The determination of total cholesterol was carried out by the enzymatic method [33]. The reaction mixture included: 103 mM/l phosphate buffer (pH = 6.5), 0.31 mM/l 4-aminoantipyrine, 5.2 mM/l phenol, 3.3 μ kat/l cholesterol esterase, 3.3 μ kat/l cholesterol oxidase, 166.7 μ kat/l

peroxidase. The colour intensity of the reaction mixture, measured at 540/600 nm, is directly proportional to the total cholesterol concentration in the sample.

The method for measuring the concentration of triglycerides is based on the enzymatic method for the determination of glycerol [34]. Triglycerides present in the sample are hydrolysed to glycerol and fatty acids under the action of several bacterial lipases. The absorption intensity at 660/800 nm is proportional to the triglyceride content. The colorimetric mixture contained: 50 mM/l PIPES buffer (pH = 7.5), 25 μ kat/l lipase, 4.6 mM/l Mg^{2+} , 8.3 μ kat/l glycerol kinase, 0.25 mM/l MADB, 16.3 μ kat/l peroxidase, 0.5 mM/l 4-aminoantipyrine, 24.6 μ kat/l ascorbic acid oxidase, 1.4 mM/l ATP, 24.6 μ kat/l glycerol-3-phosphate oxidase.

The level of HDL was determined by the formation of a coloured product of the enzymatic reaction after antibodies against human β -lipoprotein, which are part of the reagent, bound to lipoproteins other than HDL (LDL, VLDL and chylomicrons), as a result, antigen-antibody complexes were formed, which are incapable of participating in enzymatic reactions [35]. The reaction mixture for determination of HDL-cholesterol contained: anti-human β -lipoprotein antibodies, 0.8 IU/ml cholesterol esterase, 4.4 IU/ml cholesterol oxidase, 1.7 IU/ml peroxidase, 2.0 IU/ml ascorbic acid oxidase, 30 mM/l Good's buffer (pH = 7.0), 0.20 mM/l N-ethyl-N-(2-hydroxy-3-sulfopropyl)-3,5-dimethoxy-4-fluoroaniline, 0.67 mM/l 4-aminoantipyrine.

The LDL concentration was calculated using the formula:

$$\text{LDL} = \text{Total Cholesterol} - (\text{Triglycerides}/2.2) - \text{HDL} \text{ [36].}$$

The atherogenic index (AI) was calculated using the following formula:

$$\text{AI} = (\text{total cholesterol} - \text{HDL})/\text{HDL} \text{ [36].}$$

Apoproteins: apo A1 and apo B were determined by the immunoturbidimetric method using Beckman Coulter reagents (USA). The method is based on measuring the absorption intensity of insoluble aggregates formed as a result of the immunological reaction of anti-apoproteins with antibodies. The concentration

of apoproteins was estimated based on the degree of turbidity development [37, 38, 39]. The compositions of the reaction mixtures for the determination of apoproteins A1 and B included the following components, respectively: 8 mM/l Tris buffer (pH = 7.4), 106 mM/l sodium chloride, 3.5 % polyethylene glycol 6000, goat anti-apoprotein A1 antibodies \approx 0.14 g/l and 8.6 mM/l Tris buffer (pH = 7.4), 125 mM/l sodium chloride, 4 % polyethylene glycol 6000, goat anti-lipoproteins B antibodies \approx 1.93 g/l.

ALAT activity (EC 2.6.1.2) was determined by the decrease in optical density at 340 nm caused by the oxidation of NADH in a coupled reaction in the presence of LDH [40]. The reaction mixture for the determination of ALAT contained: 100 mM/l Tris buffer (pH = 7.15), 500 mM/l L-alanine, 12 mM/l 2-oxoglutarate, 1.8 kU/l lactate dehydrogenase, 0.20 mM/l NADH, 0.1 mM/l pyridoxal phosphate.

GGTP activity (EC 2.3.2.2) was determined by the rate of formation of 5-amino-2-nitrobenzoate at 405 nm, in a reaction mixture containing: 150 mM/l glycylglycine (pH = 7.7), 6 mM/l L- γ -glutamyl-3-carboxy-4-nitroanilide [41].

For the quantitative determination of glucose, we used the hexokinase method based on an increase in optical density at 340 nm caused by the formation of NADH [42]. Determination of glucose concentration was carried out in a reaction mixture

containing: 24 mM/l PIPES buffer (pH = 7.6), 2.0 mM/l ATP, 1.32 mM/l NAD⁺, 2.37 mM/l Mg²⁺, 0.59 kU/l hexokinase, 1.58 kU/l G6F-DG.

Statistical data processing: quantitative analysis data are presented as $M \pm m$, where M is the mean, m is the standard error of the mean. For the identification of correlations between the studied indicators, the Pearson coefficient (r) was used. This study discusses the values of the average (0.30–0.50), significant (0.50–0.70), and high (0.70–0.90) degrees of correlation. The statistical processing was carried out using the Microsoft Excel program. Differences were considered significant at $p < 0.05$.

3. Results and discussion

As a result of the analysis, the presence of an average, significant, and high correlation of the total cholesterol (TC) concentration with the level of triglycerides (TG), LDL, HDL, apolipoproteins B and A1, ApoB/ApoA1 and the atherogenic index was revealed (Table 1). At the same time, there was no correlation of TC with the activities of ALAT, GGTP, or glucose concentration (data not shown). However, the average level of correlation between the TG level and these indicators was revealed (Table 2). For further research, the patients were divided into groups: a control group (patients with a normal TC level/or a normal TG level) and patients with an increased level of TC

Table 1. Values of lipid metabolism indicators and their correlation with blood cholesterol concentration

Indicators	Mean \pm standard error of the mean ($M \pm m$)	Pearson's correlation coefficient r , $p < 0.05$
Total cholesterol, mM/l	5.54 \pm 0.08	
Triglycerides, mM/l	1.52 \pm 0.06	0.26
LDL cholesterol, mM/l	3.60 \pm 0.07	0.94
HDL cholesterol, mM/l	1.28 \pm 0.02	0.38
Apolipoprotein B, mg/dl	124.60 \pm 2.02	0.87
Apolipoprotein 1, mg/dl	180.89 \pm 1.81	0.26
ApoB/ApoA1	0.71 \pm 0.01	0.64
Atherogenic index	3.55 \pm 0.08	0.53

Table 2. The values of lipid metabolism indicators and their correlation with the concentration of blood triglycerides

Indicators	Mean \pm standard error of the mean ($M \pm m$)	Pearson's correlation coefficient r , $p < 0.05$
Triglycerides, mM/l	1.52 \pm 0.06	
ALAT, U/l	26.46 \pm 1.30	0.22
GGTP, U/l	39.75 \pm 3.86	0.22
Glucose, mM/l	5.85 \pm 0.12	0.38

or TG. The comparison was made between the respective groups (normal TC-increased TC and normal TG-increased TG).

In the course of the study, it was revealed that 59.5 % of patients had an increased level of total cholesterol (TC, mean value – 6.51 mM/l, reference value – 3.63–5.20 mM/l) (Table 3). Elevated cholesterol levels were observed in 56.4 % of women (mean value – 6.69 mM/l) and 52.1 % of men (mean value – 6.29 mM/l) (Fig. 1).

The TG level in the group of patients with elevated TC was increased in 15 % of patients (3.68 mM/l, reference value <2.2 mM/l), in the group of patients with normal TC this indicator was 9 % (Table 3). Among patients with an increased TC level, an increase in TG was found in 17.3 % of women (mean value 3.22 mM/l) and 30.6 % of

men (mean value – 3.55 mM/l, the number of men or women in the group with normal or increased TC was taken as 100 %). Among patients with a normal TC level, an increase was found in 7.9 % of women and 11.6 % of men (Fig. 2).

Among patients with an increased TC level, 61.4 % had an increase in the LDL content (on average 4.94 mM/l, reference value < 3.9 mM/l) (Table 3). In this group, an increase in LDL was detected in 66.1 % of women (mean value – 4.93 mM/l) and 63.6 % of men (mean value – 4.77 mM/l) (Fig. 3).

The blood concentration of apolipoprotein B contained in atherogenic lipoproteins correlates well with these data. Despite the fact that the mean value of the concentration of apolipoprotein in the group of patients with increased TC level

Table 3. Diagnostic indicators of the development of pathology in the control group and group with high cholesterol level

Indicators	Mean \pm standard error of the mean ($M \pm m$) in patients with normal cholesterol	Percentage of patients with pathology	Mean \pm standard error of the mean ($M \pm m$) in patients with normal cholesterol	Percentage of patients with pathology
Total cholesterol, mM/l	4.34 \pm 0.05	0%	6.51 \pm 0.09	100%
Triglycerides, mM/l	3.03 \pm 0.26	9.0%	3.68 \pm 0.23	15.9%
LDL cholesterol, mM/l	<3.9 mM/l	0%	4.94 \pm 0.10	61.4%
HDL cholesterol, mM/l	1.01 \pm 0.02	69.3%	1.08 \pm 0.02	49.7%
Apolipoprotein B, mg/dl	141.63 \pm 5.82	4.6%	161.94 \pm 3.14	64.0%
Apolipoprotein 1, mg/dl	227.01 \pm 4.62	13.2%	230.46 \pm 3.34	27.4%
ApoB/ApoA1	1.25 \pm 0.21	1.3%	1.25 \pm 0.04	11.8%
Atherogenic index	4.33 \pm 0.12	24.0%	4.9 \pm 0.11	60.4%
ALAT, U/l	46.12 \pm 3.44	22.6%	48.84 \pm 3.33	25.3%
GGTP, U/l	76.49 \pm 16.15	36.0%	57.91 \pm 5.34	52.4%
Glucose, mM/l	7.44 \pm 0.54	21.6%	7.75 \pm 0.53	25.9%

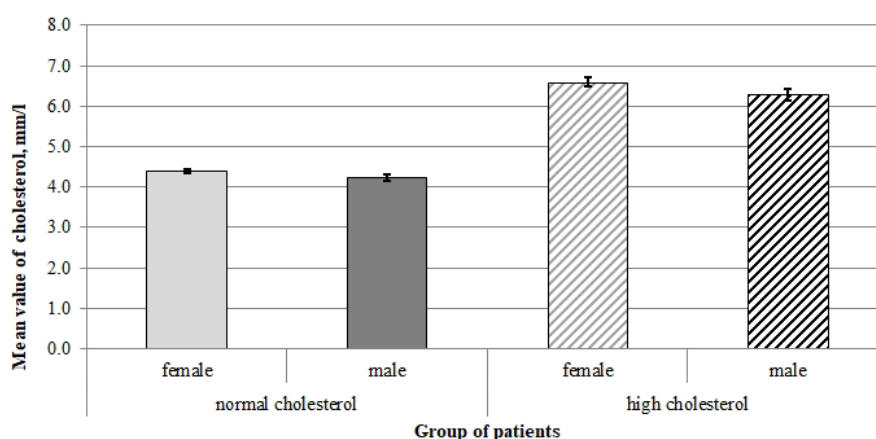


Fig. 1. Cholesterol level in the control group of patients and patients with increased cholesterol

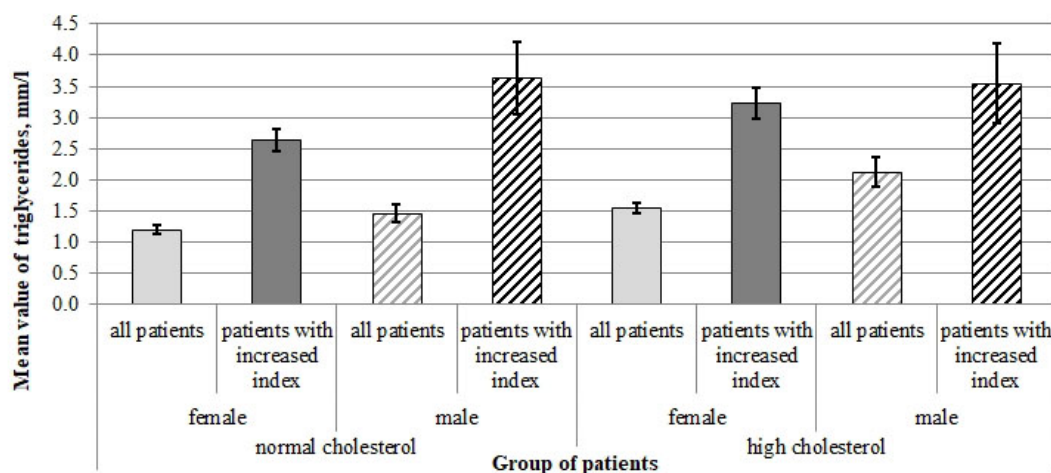


Fig. 2. Triglycerides level in the control group of patients and patients with increased cholesterol

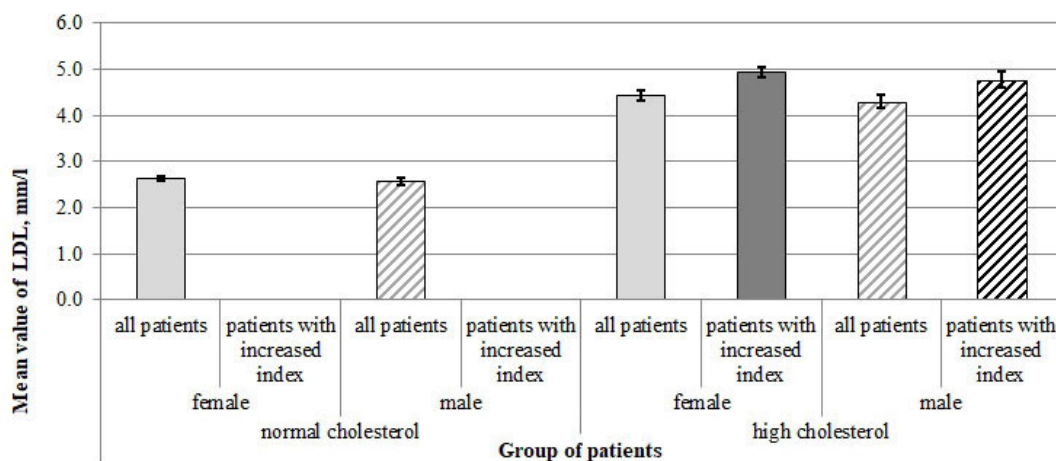


Fig. 3. LDL level in the control group of patients and patients with increased cholesterol

was 144.47 mg/dl with a reference value of 55–130 mg/dl, a significant increase to 161.4 mg/dl was found in 65.4 % of women and increase up to 169.6 mg/dl was revealed in 50 % of men (Fig. 4).

In some patients (13.2 %), with normal levels of total cholesterol, an increase in the level of apolipoproteins A1 to mean value of 227.0 mg/dl was observed (Table 3) (reference value – 105–205 mg/dl), which has a positive prognostic character, since these proteins are part of HDL and are responsible for receptor recognition of lipoproteins by cells. In patients with elevated TC levels, the average apoA1 value did not exceed the reference value and was 192.4 mg/dl. However, in 31.6 % of women and 16 % of men, the level of apoA1 was significantly increased and comprised 233.6 and 218.8 mg/dl, respectively. In the group of people with normal TC, an increase in the level of apoA1 was observed in 15.2 % of women and 8.7 % of men (Fig. 5).

The apoB/apoA1 ratio can be considered as an alternative assessment of the risk of complications of cardiovascular diseases. An increased risk of coronary artery disease was observed when the ratio was > 0.9 in men and > 0.8 in women. However, current clinical guidelines do not propose to consider the apoB/apoA1 ratio as a target when prescribing lipid-lowering therapy (LDL, HDL, and apoB cholesterol are used for therapeutic purposes). Our study showed that the apoB/apoA1 ratio was increased in 11.0 % of women (average value – 1.29) and 14 % of men (average value – 1.14) in the group of patients with high TC (Fig. 6). In the group of patients with normal TC, an increase in this indicator was not detected in women and was observed only in 4.3 % of men (Fig. 6). The association of an increased risk of coronary artery disease with an increased apoB/apoA1 ratio has been shown in a number of studies [43,44], and recent data have not confirmed

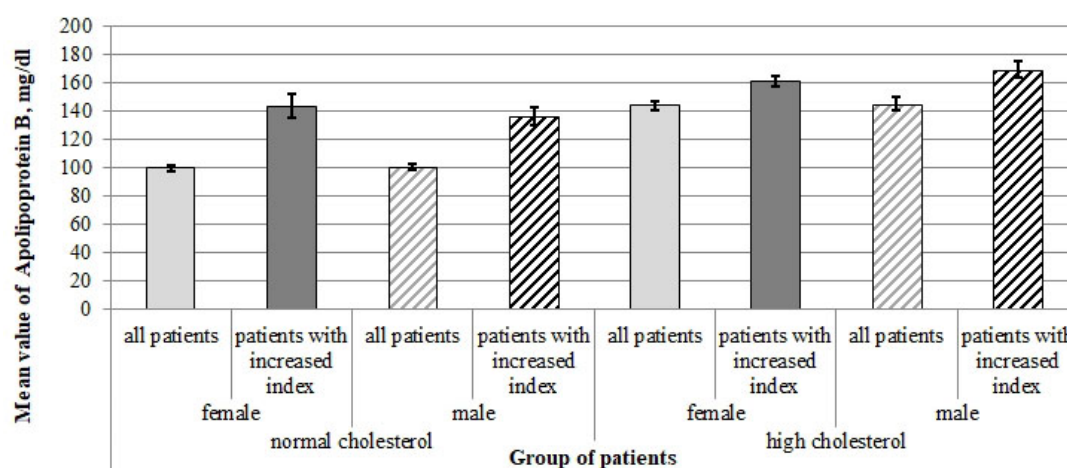


Fig. 4. Apolipoprotein B level in the control group of patients and patients with increased cholesterol

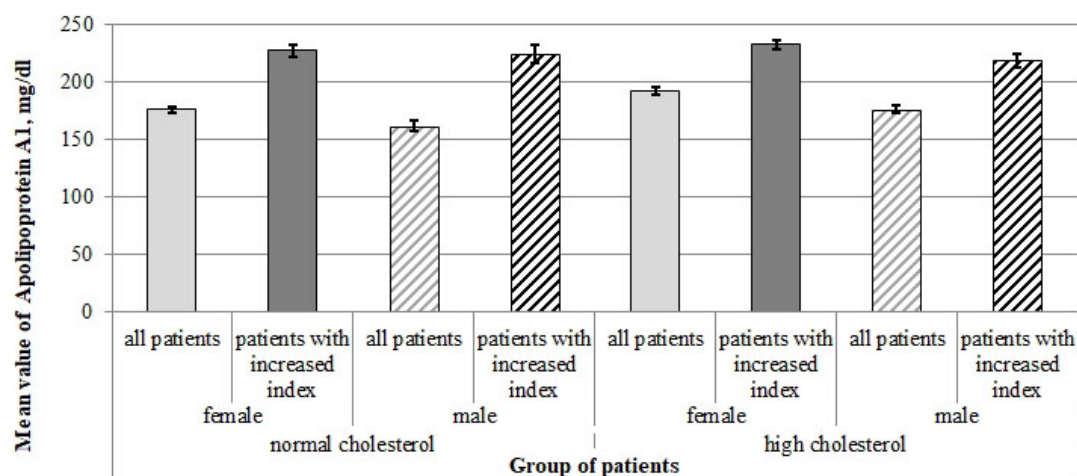


Fig. 5. Apolipoprotein A1 level in the control group of patients and patients with increased cholesterol

the role of isolated hypertriglyceridemia in the prediction of risk for cardiovascular diseases. As was noted by the authors, this criterion can only be valid in combination with LDL and HDL levels [45, 46]. The same diagnostic value of the value of the apoB/apoA1 ratio and the TG level for the diagnosis of metabolic syndrome was shown [47]. Also, some authors discuss the technical inconvenience associated with the requirement of fasting for 12 h before taking blood for analysis for TG and HDL cholesterol [48]. In contrast, the measurement of ApoB and ApoA1 does not require 12 hours of fasting. Thus, the ApoB/ApoA1 ratio appears to be more appropriate in the clinical setting than TG, LDL, and HDL levels for identifying patients with metabolic syndrome and CVD risk.

An increase in the atherogenic index of plasma, as a result of a decrease in HDL, was found in 24 % of patients with normal TC levels, which indicates the risk of developing

atherosclerosis despite normal TC and LDL levels. HDL was decreased in 44.4 % of women (mean value – 1.12 mM/l, reference value > 1.3) and 63.8 % of men with high cholesterol (mean value – 1.01 mM/l) (Fig. 7). The AI was increased in 60.4 % of patients in the group with increased TC level (mean value – 4.90, reference value < 3.5) (Table 3). In the group of patients with normal cholesterol, a decrease was observed in 62.6 % of women and 90.2 % of men (Fig. 8). In the group of patients with normal TC levels, an increase in AI was found in 17.6 % of women and 39.5 % of men. A similar trend was found in the group of patients with increased TC levels: AI was increased in 55.2 % of women (mean value – 4.83) and 76.7 % of men (mean value – 4.99) (Fig. 8). The data obtained unambiguously indicate a greater predisposition of men to atherosclerosis.

The established gender differences in atherogenic indices in different nosologies

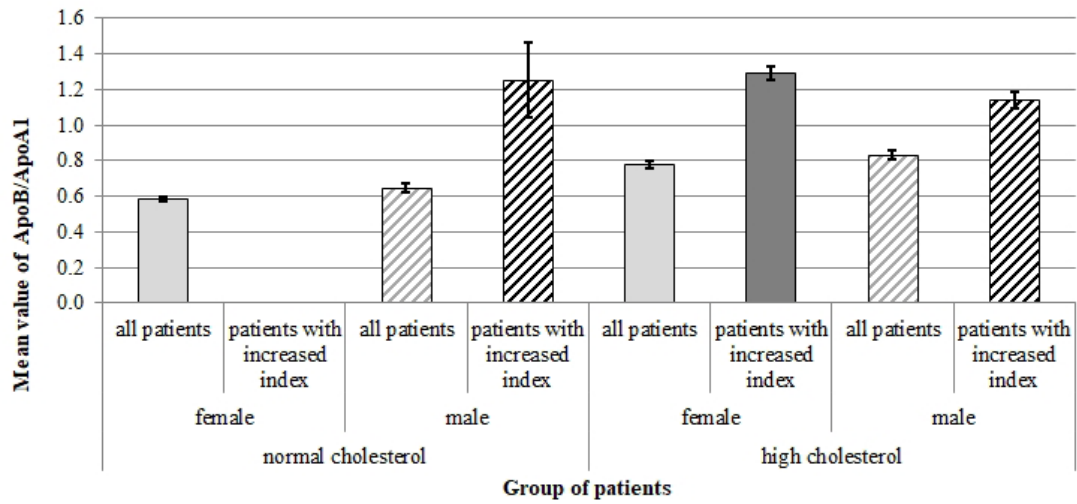


Fig. 6. ApoB/ApoA1 ratio in the control group of patients and patients with increased cholesterol

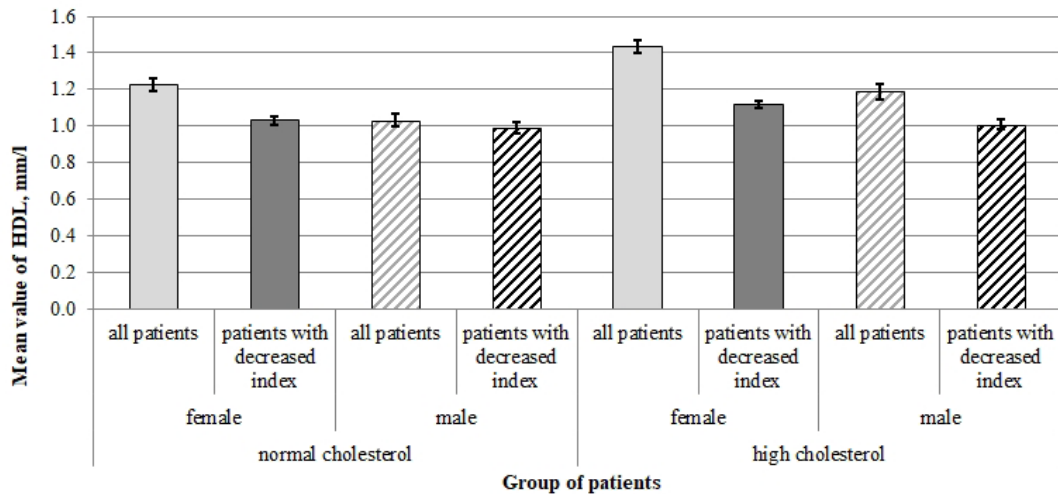


Fig. 7. HDL level in the control group of patients and patients with increased cholesterol

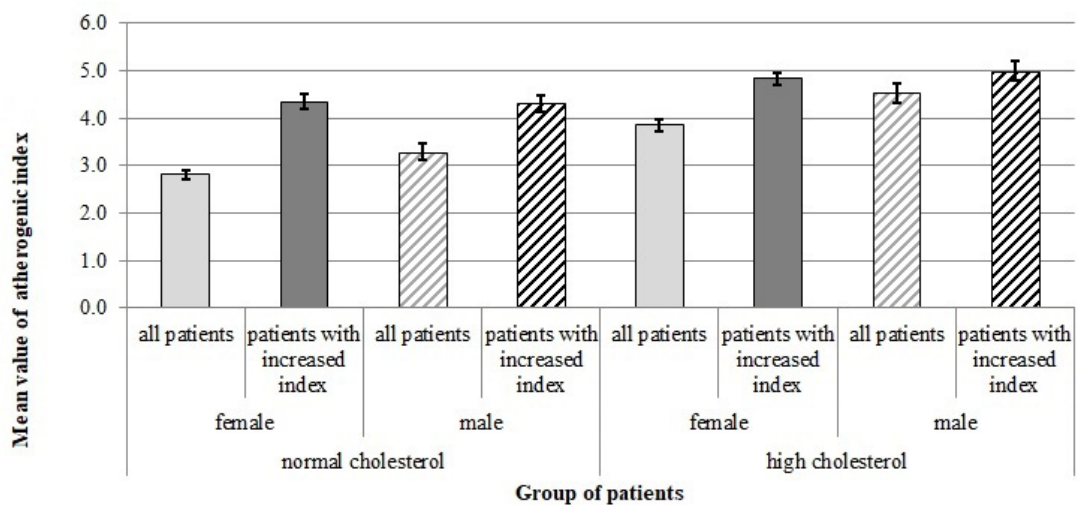


Fig. 8. Atherogenic index in the control group of patients and patients with increased cholesterol

and in different age subgroups characterize men as initially predisposed to the development of abdominal obesity in metabolic disorders, since abdominal obesity is androgen-dependent. In addition, with the formation of deposits of visceral fat due to metabolic syndrome, insulin sensitivity is impaired, which triggers a vicious circle and aggravates insulin resistance [49].

Interestingly, the role of the atherogenic lipid spectrum in the development of type 2 diabetes mellitus and hypertension in women over 60 is higher than in men. At the same time, the risk group is composed of women with early menarche, and the frequency and severity of cardiovascular events and thromboembolic complications correlates with the duration of the menopause. In women, the transition of the “silent” course of ischemic heart disease with the late appearance of clinical syndromes in the form of pain syndrome is recorded. Certain erasure of the clinical manifestations of diabetes mellitus, coronary artery disease, characteristic of women, contributes to a later detection of diseases in comparison with men. Ten years after the onset of menopause (postmenopause), the risk of cardiovascular disease in women is similar to that in men of the same age [50].

Statistically significant differences between men and women were not revealed in the study of the correlation between the level of TG and ALAT, GGTP and glucose, and, accordingly, patients were not divided according to gender.

In the group of patients with elevated TG levels, 29.2 % of patients showed an increase in ALAT levels (mean value – 46.12 U/l, reference

value – up to 40 U/l for men and 35 U/l for women) (Fig. 9).

An increase in the indices of the enzymatic activity of ALAT, as an enzyme contained in liver cells, and to a lesser extent in the kidneys, muscles, heart and pancreas, reflect destructive damage in the above organs or secondary liver changes in metabolic disorders. It was shown that increased ALAT levels are clinically and histologically associated with steatohepatosis [51, 52].

In the same group, the GGTP activity was increased in 60 % of patients (the norm was up to 32 U/L). Among patients with normal TG levels, ALAT activity was increased in 14.6 % of patients, and GGTP activity increased in 38 % of patients (Fig. 10). An increase in GGTP indicates the destruction of parenchymal organs. Small increase in levels of GGTP and ALAT have been shown in patients with steatohepatosis [53].

Depending on the presence/absence of abdominal obesity, mild and moderate steatohepatosis was determined 11 times more often in women than in men, while cirrhosis, an extreme degree of damage to hepatocytes, prevailed in men. Clinical signs of steatohepatosis are an increase in the concentration of insulin (however, its numbers are not proportional to the degree of liver damage), C-peptide, hypertriglyceridemia, an increase in the activities of ALAT and aspartate aminotransferase (ASAT). It has been proven that an increase in liver function tests is less informative in women, which is probably due to the reaction of ALAT and ASAT as the ability of the liver to immediately respond

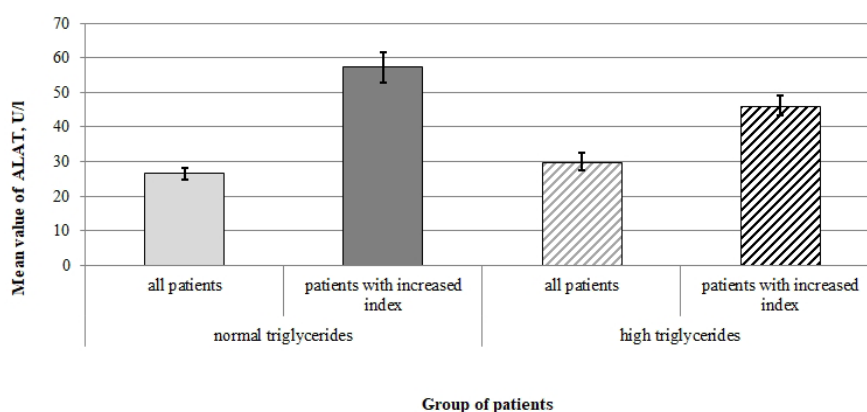


Fig. 9. ALAT activity in the control group of patients and patients with increased triglycerides

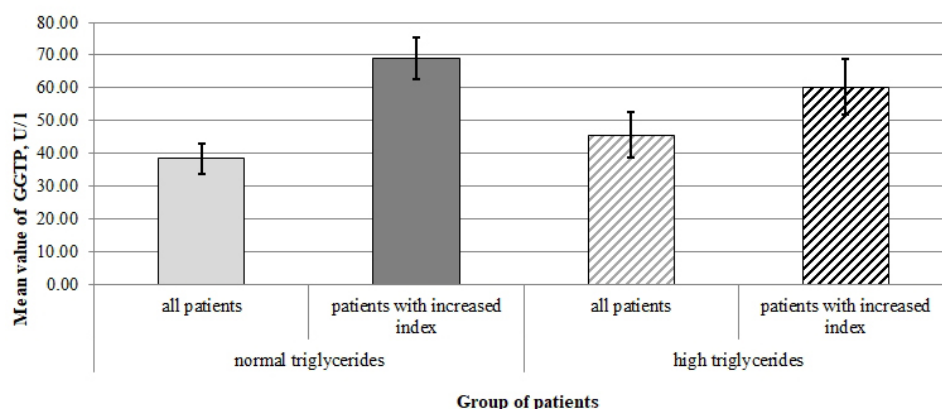


Fig. 10. GGTP activity in the control group of patients and patients with increased triglycerides

to hepatotoxic effects. In men, this potential is reduced under conditions of systematic damage to hepatocytes due to the systematic consumption of fried, spicy foods, heavy alcohol use, etc. A similar mechanism is triggered in women with abusive drinking behaviour, in this case, liver function tests can remain low for a long time.

In the group of patients with normal TG, an increase in glucose content was detected in 21.6 % (mean value – 7.43 mM/l, reference value – up to 6.2 mM/l), while in the group of patients with elevated TG an increase in glucose was more significant (mean value – 8.44 mM/l) and was detected in 42.3 % of patients (Fig. 11). This correlation reflects the need for the ABC strategy proposed by the National Diabetes Education Program: diabetologists and patients with diabetes should pay attention not only to the control of glycemia (“A” - HbA1c) and blood pressure (“B” - blood pressure), but also to the level of blood lipids (“C” - cholesterol) [54]. The main cause of hypertriglyceridemia in diabetes mellitus

is the low sensitivity of visceral adipose tissue to the anti-lipolytic action of insulin, which leads to increased lipolysis, the entry of large amounts of free fatty acids into the portal bloodstream and, in combination with hyperinsulinemia, an increase in the synthesis of triglycerides and VLDL by the liver. In addition, in patients with type 2 diabetes with hyperglycemia, the activity of endothelial lipoprotein lipase, which is responsible for the catabolism of triglycerides and VLDL, is reduced, which aggravates this disorder.

4. Conclusions

Thus, as a result of the conducted studies of lipid metabolism indicators in middle-aged group (from 32 to 61 years) of Southern and Central Federal Districts of Russia (Voronezh, Belgorod, Lipetsk, Kursk and Rostov regions) the following distinguishing features were identified:

- significant metabolic disorders of lipid metabolism in the middle age group with a predominance of atherogenic lipid fractions,

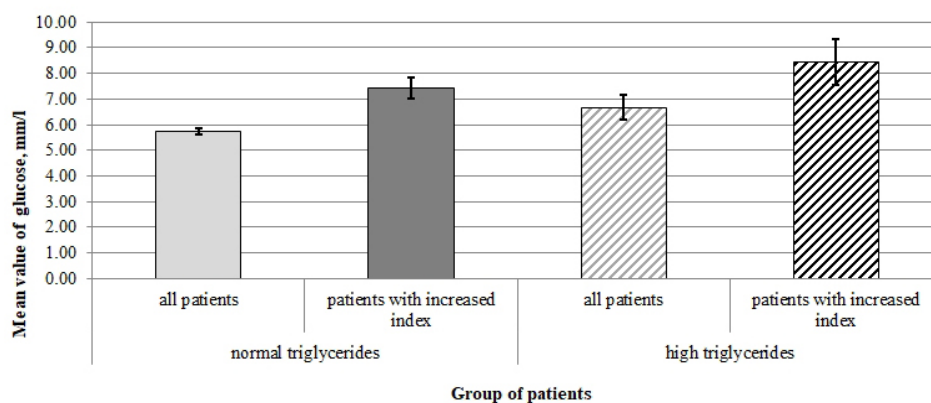


Fig. 11. Glucose content in the control group of patients and patients with increased triglycerides

which can serve as a negative indicator of the health status of the working-age population;

– in the absence of a universal marker of lipid atherogenicity for the early diagnosis of pathological changes in the body, a comprehensive screening of LDL fractions, triglycerides, glucose indicators for the isolation of risk groups in relation to the development of metabolic disorders leading to the development of atherogenic vascular lesions is justified. The feasibility of determination of insulin, conducting a glucose tolerance test, C-peptide is determined by the specialists in order to clarify the basic diagnosis, and their results do not always correlate with the severity of atherogenic changes;

– the results of the study showed that the apoB/apoA1 ratio can be used as an auxiliary marker for the early assessment of the prevalence of atherogenic lipid fractions, allowing to identify risk groups for the development of diseases associated with metabolic disorders;

– the revealed significant excess of atherogenic lipid fractions in men of the middle age group in comparison with women, at the stage of addition of natural menopausal changes in lipid metabolism, determines an almost two-fold increase in the risks of developing cardiovascular lesions in men in the age category up to 50 years;

– the revealed correlation of the TG level and the increase in glucose content shows the need for constant monitoring of the blood lipid profile in patients with diabetes;

– screening detection of indicators of hypertriglyceridemia and/or dyslipidemia, even in the absence of a somatic pathology, should be an indication for in-depth clinical and laboratory examination: exclusion of organic lesions of parenchymal organs (primarily of the liver and biliary tract).

Author contributions

Mittova V. O. – writing text; research design development. Khoroshikh A. O. – analysis of scientific literature, bibliography design. Zemchenkova O. V. – preparation and revision of the research part of the text. Ryazantsev S. V. – experimental research, data collection and analysis. Maslov O. V. – development of methodology, data processing. Corzh E. V. – interpretation of data, final conclusions,

preparation of a literature review. Ryasnaya-Lokinskaya L. S. – writing of the clinical part of the discussion of the results, analysis of scientific literature. Alabovsky V. V. – scientific leadership, research concept.

Conflict of interests

The authors declare that they have no known financial conflicts of interest or personal relationships that might affect the work presented in this article.

References

1. Mc Namara K., Alzubaidi H., Jackson J. K. Cardiovascular disease as a leading cause of death: how are pharmacists getting involved? *Integrated Pharmacy Research and Practice*. 2019; 8: 1–11. <https://doi.org/10.2147/IPRP.S133088>
2. Fernández-Friera L., Peñalvo J. L., Fernández-Ortiz A., Ibañez B., López-Melgar B., Laclaustra M., Oliva B., Moco-roa A., Mendiguren J., Martínez de Vega V., García L., Molina J., Sánchez-González J., Guzmán G., Alonso-Farto J. C., Guallar E., Civeira F., Sille-sen H., Pocock S., Ordovás J. M., Sanz G., Jiménez-Borreguero L. J., Fuster V. Prevalence, vascular distribution, and multiterritorial extent of subclinical atherosclerosis in a middle-aged cohort: the PESA (Progression of Early Subclinical Atherosclerosis) study. *Circulation*. 2015;131: 2104–2113. <https://doi/10.1161/CIRCULATIONAHA.114.014310>
3. Strategiya razvitiya zdravookhraneniya v Rossiiskoi Federatsii na period do 2025 goda. Ukaz Prezidenta Rossiiskoi Federatsii ot 06 iyunya 2019 g. No254. [Healthcare development strategy in the Russian Federation for the period until 2025. Decree of the President of the Russian Federation of June 6, 2019 No. 254.]. Moscow, 2019. (In Russ.)
4. Poznyak A., Orekhov A. N., Grechko A. V., Poggio P., Myasoedova V. A., Alfieri V. The Diabetes Mellitus–Atherosclerosis Connection: The role of lipid and glucose metabolism and chronic inflammation. *International Journal of Molecular Sciences*. 2020;21(5): 1835. <https://doi/10.3390/ijms21051835>
5. Diagnostika i korrektsiya lipidnogo obmena s tsel'yu profilaktiki i lecheniya ateroskleroza. Rossiiskie rekomendatsii, VI peresmotr, M; 2017. 44 s. [Diagnosis and correction of lipid metabolism with the aim of prediction and treatment of atherosclerosis, Russian recommendations, VI revision, M; 2017. 44 p.] (In Russ.)
6. Faintuch J., Faintuch S. *Obesity and Diabetes-Scientific Advances and Best Practice, 2nd Edition*. Springer; 2020. 994 p. <https://doi.org/10.1007/978-3-030-53370-0>

7. Komissarenko I. A., Levchenko S. V. *Metabolicheskiy sindrom: mezhdistsiplinarnaya problema-optimal'noe reshenie*. [Metabolic syndrome: interdisciplinary problem – optimal solution]. Moscow: Prima-print Publ.; 2019. 44–46. (In Russ.)
8. Kuz'mina-Krutetskaya S. R., Repina M. A. *Metabolicheskiy sindrom u zhenshchin: metodicheskie rekomendatsii* [Metabolic syndrome in women: methodological recommendations]. Sankt-Peterburg: Eko-Vektor Publ.; 2019. 72 p. (In Russ.)
9. Durrer Schutz D., Busetto L., Dicker D., Farpour-Lambert N., Pryke R., Toplak H., Widmer D., Yumuk V., Schutz Y. European practical and patient – centred guidelines for adult obesity management in primary care. *Obesity Facts*. 2019;12: 40–66. <https://doi.org/10.1159/000496183>
10. Anderson M. R., Geleris J., Anderson D. R., Zucker J., Nobel Y. R., Freedberg D., Small-Saunders J., Rajagopalan K. N., Greendyk R., Chae S. R., Natarajan K., Roh D., Edwin E., Gallagher D., Podolanczuk A., Barr R. G., Ferrante A. W., Baldwin M. R. Body mass index and risk for intubation or death in SARS-CoV-2 infection: a retrospective cohort study. *Annals of Internal Medicine*. 2020;173: 82–90. <https://doi.org/10.7326/M20-3214>
11. Canoy D., Beral V., Balkwill A., Wright F. L., Kroll M. E., Reeves G. K., Green J., Cairns B. J. Age at menarche and risks of coronary heart and vascular diseases in a large UK cohort. *Circulation*. 2015;131: 237–244. <https://doi.org/10.1161/circulationaha.114.010070>
12. Dobner J, Kaser S. Body mass index and the risk of infection – from underweight to obesity. *Clinical Microbiology and Infection*. 2018;24: 248. <https://doi.org/10.1016/j.cmi.2017.02.013>
13. Targher G., Mantovani A., Wang X. B., Yan H. D., Sun Q. F., Pan K. H., et al. Patients with diabetes are at higher risk for severe illness from COVID-19. *Diabetes & Metabolism*. 2020;46: 335–337. <https://doi.org/10.1016/j.diabet.2020.05.001>
14. Sabatine M. S., Giugliano R. P., Keech A. C., et al., Evolocumab and clinical outcomes in patients with cardiovascular disease. *The New England Journal of Medicine*. 2017;376: 1713–1722. <https://doi.org/10.1056/nejmoa1615664>
15. Schwartz G. G., Steg P. G., Szarek M., et al. Alirocumab and cardiovascular outcomes after acute coronary syndrome. *The New England Journal of Medicine*. 2018;379: 2097–2107. <https://doi.org/10.1056/nejmoa1801174>
16. Summerhill V. I., Grechko A. V., Yet S. F., Sobenin I. A., Orekhov A. N. The atherogenic role of circulating modified lipids in atherosclerosis. *International Journal of Molecular Sciences*. 2019;20: 3561. <https://doi.org/10.3390/ijms20143561>
17. Berneis K. K., Krauss R. M. Metabolic origins and clinical significance of LDL heterogeneity. *Journal of Lipid Research*. 2002;43: 1363–1379. <https://doi.org/10.1194/jlr.R200004-JLR200>
18. Maguire E. M., Pearce S. W. A., Xiao Q. Foam cell formation: A new target for fighting atherosclerosis and cardiovascular disease. *Vascular Pharmacology*. 2019;112: 54–71. <https://doi.org/10.1016/j.vph.2018.08.002>
19. Ference B. A., Ginsberg H. N., Graham I., Ray K. K., Packard C. J., Bruckert E., Hegele R. A., Krauss R. M., Raal F. J., Schunkert H., Watts G. F., Borén J., Fazio S., Horton J. D., Masana L., Nicholls S. J., Nordestgaard B. G., van de Sluis B., Taskinen M. R., Tokgözoğlu L., Landmesser U., Laufs U., Wiklund O., Stock J. K., Chapman M. J., Catapano A. L. Low-density lipoproteins cause atherosclerotic cardiovascular disease. 1. Evidence from genetic, epidemiologic, and clinical studies. A consensus statement from the European Atherosclerosis Society Consensus Panel. *European Heart Journal*. 2017;38(32): 2459–2472. <https://doi.org/10.1093/eurheartj/ehx144>
20. Borén J., Chapman M. J., Krauss R. M., Packard C. J., Bentzon J. F., Binder C. J., Daemen M. J., Demer L. L., Hegele R. A., Nicholls S. J., Nordestgaard B. G., Watts G. F., Bruckert E., Fazio S., Ference B. A., Graham I., Horton J. D., Landmesser U., Laufs U., Masana L., Pasterkamp G., Raal F. J., Ray K. K., Schunkert H., Taskinen M. R., van de Sluis B., Wiklund O., Tokgözoğlu L., Catapano A. L., Ginsberg H. N. Low-density lipoproteins cause atherosclerotic cardiovascular disease: pathophysiological, genetic, and therapeutic insights: a consensus statement from the European Atherosclerosis Society Consensus Panel. *European Heart Journal*. 2020;41(24): 2313–2330. <https://doi.org/10.1093/eurheartj/ehz962>
21. Stock J. Triglycerides and cardiovascular risk: Apolipoprotein B holds the key. *Atherosclerosis*. 2019;284: 221–222. <https://doi.org/10.1016/j.atherosclerosis.2019.03.004>
22. Yusuf S., Hawken S., Ounpuu S., Dans T., Avezum A., Lanas F., McQueen M., Budaj A., Pais P., Varigos J., Lisheng L. Effect of potentially modifiable risk factors associated with myocardial infarction in 52 countries (the INTERHEART study): case-control study. *Lancet*. 2004;364: 937–952. [https://doi.org/10.1016/s0140-6736\(04\)17018-9](https://doi.org/10.1016/s0140-6736(04)17018-9)
23. Walldius G., Jungner I., Holme I., Aastveit A. H., Kolar W., Steiner E. High apolipoprotein B, low apolipoprotein A-I, and improvement in the prediction of fatal myocardial infarction (AMORIS study): a prospective study. *Lancet*. 2001;358: 2026–2033. [https://doi.org/10.1016/s0140-6736\(01\)07098-2](https://doi.org/10.1016/s0140-6736(01)07098-2)
24. Walldius G., Jungner I., Aastveit A. H., Holme I., Furberg C. D., Sniderman A. D. The apoB/apo A-I ratio

is better than the cholesterol ratios to estimate the balance between plasma proatherogenic and antiatherogenic lipoproteins and to predict coronary risk. *Clinical Chemistry and Laboratory Medicine*. 2004;42: 1355–1363. <https://doi.org/10.1515/cclm.2004.254>

25. Gubergrits N. B., Belyaeva N. V., Klochkova A. E., Lukashevich G. M., Fomenko P. G. *Metabolicheskii sindrom: kak izbezhat' polipragmazii?* [Metabolic syndrome: how to avoid Polypharmacy?]. Moscow: Prima Print Publ.; 2017. 96 p. (In Russ.)

26. HSE/ICGP Healthy weight management guidelines before, during & after pregnancy, 2013. Available at: <https://www.icgp.ie/go/library/catalogue/item/73ACFC19-4195-4F57-91E5F973ED955D72>

27. Xie J., Zu Y., Alkhatib A., Pham T. T., Gill F., Jang A., Radosta S., Chaaya G., Myers L., Zifodya J. S., Bojanowski C. M., Marrouche N. F., Mauvais-Jarvis F., Denson J. L. Metabolic syndrome and COVID-19 mortality among adult black patients in New Orleans. *Diabetes Care*. 2021;44(1): 188–193. <https://doi.org/10.2337/dc20-1714>

28. Zheng K. I., Gao F., Wang X. B., Sun Q. F., Pan K. H., Wang T. Y., Ma H. L., Chen Y. P., Liu W. Y., George J., Zheng M. H. Obesity as a risk factor for greater severity of COVID-19 in patients with metabolic associated fatty liver disease. *Metabolism Clinical and Experimental*. 2020;108: 154244. <https://doi.org/10.1016/j.metabol.2020.154244>

29. Cho S. M. J., Lee, H. J., Shim, J. S., Song B. M., Kim H. C. Associations between age and dyslipidemia are differed by education level: The Cardiovascular and Metabolic Diseases Etiology Research Center (CMERC) cohort. *Lipids in Health and Disease*. 2020;19, 12. <https://doi.org/10.1186/s12944-020-1189-y>

30. Cui J. Overview of risk prediction models in cardiovascular disease research. *Annals of Epidemiology*. 2009;19(10): 711–17. <https://doi.org/10.1016/j.annepidem.2009.05.005>

31. Dallmeier D., Koenig W. Strategies for vascular disease prevention: the role of lipids and related markers including apolipoproteins, low-density lipoproteins (LDL)-particle size, high sensitivity C-reactive protein (hs-CRP), lipoprotein-associated phospholipase A2 (Lp-PLA₂) and lipoprotein(a) (Lp(a)). *Best Practice & Research Clinical Endocrinology & Metabolism*. 2014;28(3): 281–94. <https://doi.org/10.1016/j.beem.2014.01.003>

32. Metelskaya V. A. Multimarker diagnostic panels for atherosclerosis. *Russian Journal of Cardiology*. 2018;(8): 65–73. <https://doi.org/10.15829/1560-4071-2018-8-65-73> (In Russ.)

33. Riesen W. F. Lipid metabolism. In: Thomas L, (ed.) *Clinical laboratory diagnostics. Use and assessment of clinical laboratory results*. Frankfurt/Main: TH-Books

Verlagsgesellschaft; 1998: 171–173. <https://doi.org/10.1515/cclm.1999.37.7.771>

34. Koditschek L. K., Umbreit W. W. Alpha-glycerophosphate oxidase in streptococcus faecium F 24. *Journal of Bacteriology*. 1969;98: 1063–1068. <https://doi.org/10.1128/jb.98.3.1063-1068.1969>

35. Young D. S. Effects of drugs on clinical laboratory tests. *Annals of Clinical Biochemistry*. 1997;34: 579–581. <https://doi.org/10.1177/000456329703400601>

36. Friedewald W. T., Levy R. I., Fredrickson D. S. Estimation of the concentration of low-density lipoprotein cholesterol in plasma, without use of the preparative ultracentrifuge. *Clinical Chemistry*. 1972;18; 499–502. <https://doi.org/10.1093/clinchem/18.6.499>

37. Stein E. A. Lipids, lipoproteins, and apolipoproteins. In: Tietz N. W. (ed.) *Fundamentals of clinical chemistry*. Philadelphia: WB Saunders Company; 1987:454–456.

38. Riesen W. F. Lipid metabolism. In: Thomas L, (ed.) *Clinical laboratory diagnostics. Use and assessment of clinical laboratory results*. Frankfurt/Main: TH-Books Verlagsgesellschaft; 1998: 172–173. <https://doi.org/10.1515/cclm.1999.37.7.771>

39. Bhatnagar D., Durrington P. N. Measurement and clinical significance of apolipoproteins A-1 and B. In: Rifai N., Warnick G. R., Dominiczak M. H. (eds.) *Handbook of lipoprotein testing*. Washington: AAC Press; 1997: 177–198.

40. Schumann G., Bonora R., Ceriotti F., Clerc-Renaud P., Ferrero C. A., Féraud G., Franck P. F., Gella F. J., Hoelzel W., Jørgensen P. J., Kanno T., Kessne A., Klauker R., Kristiansen N., Lessinger J. M., Linsinger T. P., Misaki H., Panteghini M., Pauwels J., Schimmel H. G., Vialle A., Weidemann G., Siekmann L. IFCC primary reference procedures for the measurement of catalytic activity concentrations of enzymes at 37 °C. Part 4. Reference procedure for the measurement of catalytic concentration of alanine aminotransferase. *Clinical Chemistry and Laboratory Medicine*. 2002;40: 718–24. <https://doi.org/10.1515/cclm.2002.124>

41. Shaw M., Stromme H., London L., Theodorsen L. International Federation of Clinical Chemistry, (IFCC), Scientific Committee, Analytical Section. IFCC methods for the measurement of catalytic concentration of enzymes. Part 4 IFCC method for γ -glutamyltransferase. *Journal of Clinical Chemistry and Clinical Biochemistry*. 1983;21(10): 633–646.

42. Czok R., Barthelmai W. Enzymatische Bestimmungen der Glucose in Blut, Liquor und Harn. *Wiener klinische Wochenschrift*. 1962;40: 585–589. <https://doi.org/10.1007/BF01478633>

43. Liting P., Guoping L., Zhenyue C. Apolipoprotein B/apolipoprotein A1 ratio and non-high-density

lipoprotein cholesterol. Predictive value for CHD severity and prognostic utility in CHD patients. *Herz*. 2015;40(1): 1–7. <https://doi.org/10.1007/s00059-014-4147-5>

44. Pan L., Lu G., Chen Z. Combined use of apolipoprotein B/apolipoprotein A1 ratio and non-high-density lipoprotein cholesterol before routine clinical lipid measurement in predicting coronary heart disease. *Coronary Artery Disease*. 2014;25(5): 433–438. <https://doi.org/10.1097/mca.000000000000100>

45. Andersson C., Lyass A., Vasan R. S., Massaro J. M., D'Agostino R. B., Sr., Robins S. J. Long-term risk of cardiovascular events across a spectrum of adverse major plasma lipid combinations in the Framingham heart study. *American Heart Journal*. 2014;168: 878–883. <https://doi.org/10.1016/j.ahj.2014.08.007>

46. Miller M., Cannon C., Murphy S., Qin J., Ray K., Braunwald E. Impact of triglyceride levels beyond low-density lipoprotein cholesterol after acute coronary syndrome in the PROVE IT-TIMI 22 trial. *Journal of the American College of Cardiology*. 2008;51: 724–730. <https://doi.org/10.1016/j.jacc.2007.10.038>

47. Nurtazina A., Kozhakhmetova D., Dautov D., Shakhanova A., Chattu V. K. Apolipoprotein B/A1 ratio as a diagnostic alternative to triglycerides and HDL-Cholesterol for the prediction of metabolic syndrome among hypertensives in Kazakhstan. *Diagnostics (Basel)*. 2020;10(8): 510. <https://doi.org/10.3390/diagnostics10080510>

48. Renee Ruhaak L., van der Laarse A., Cobbaert C. M. Apolipoprotein profiling as a personalized approach to the diagnosis and treatment of dyslipidaemia. *Annals of Clinical Biochemistry*. 2019;56: 338–356. <https://doi.org/10.1177/0004563219827620>

49. Dreval' A. V. *Reproduktivnaya endokrinologiya* [Reproductive endocrinology]. Moscow: GEOETAR-Media Publ.; 2020. 240 p. (In Russ.)

50. Maas A. H., Appelman Y. E. Gender differences in coronary heart disease. *Netherlands Heart Journal*. 2010;18(12): 598–602. <https://doi.org/10.1007/s12471-010-0841-y>

51. Anty R., Iannelli A., Patouraux S., Bonnafous S., Lavallard V. J., Senni-Buratti M., Amor I. B., Staccini-Myx A., Saint-Paul M. C., Berthier F., Huet P. M., Le Marchand-Brustel Y., Gugenheim J., Gual P., Tran A. A new composite model including metabolic syndrome, alanine aminotransferase and cytokeratin-18 for the diagnosis of non-alcoholic steatohepatitis in morbidly obese patients. *Alimentary Pharmacology & Therapeutics*. 2010;32: 1315–1322. <https://doi.org/10.1111/j.1365-2036.2010.04480.x>

52. Neuschwander-Tetri B. A., Clark J. M., Bass N. M., Van Natta M. L., Unalp-Arida A., Tonascia J., Zein C. O., Brunt E. M., Kleiner D. E., McCullough A. J.,

Sanyal A. J., Diehl A. M., Lavine J. E., Chalasani N., Kowdley K. V. NASH Clinical Research Network: Clinical, laboratory and histological associations in adults with nonalcoholic fatty liver disease. *Hepatology*. 2010;52: 913–924. <https://doi.org/10.1002/hep.23784>

53. Verma S., Jensen D., Hart J., Mohanty S. R. Predictive value of ALT levels for non-alcoholic steatohepatitis (NASH) and advanced fibrosis in non-alcoholic fatty liver disease (NAFLD). *Liver International*. 2013;33: 1398–1405. <https://doi.org/10.1111/liv.12226>

54. Siminerio, L. M., Albright, A., Fradkin, J., Gallivan, J., McDivitt, J., Rodriguez, B., Tuncer, D., & Wong, F. The National Diabetes Education Program at 20 Years: Lessons Learned and Plans for the Future. *Diabetes Care*. 2018;41(2), 209–218. <https://doi.org/10.2337/dc17-0976>

Information about the authors

Valentina O. Mittova, PhD in Biology, Assistant Professor of the Department of Biochemistry, Voronezh State Medical University named after N. N. Burdenko of the Ministry of Health of the Russian Federation, Voronezh, Russian Federation; e-mail: vmittova@mail.ru. ORCID iD: <https://orcid.org/0000-0002-9844-8684>.

Anna O. Khoroshikh, student of the General Medicine Faculty, Voronezh State Medical University named after N. N. Burdenko of the Ministry of Health of the Russian Federation, Voronezh, Russian Federation; e-mail: anna.horoshih@gmail.com. ORCID iD: <https://orcid.org/0000-0001-9953-2653>.

Olga V. Zemchenkova, PhD in Biology, Teaching Assistant of the Department of Biochemistry, Voronezh State Medical University named after N. N. Burdenko of the Ministry of Health of the Russian Federation, Voronezh, Russian Federation; e-mail: zov-bio@mail.ru. ORCID iD: <https://orcid.org/0000-0003-1996-9500>.

Sergey V. Ryazantsev, PhD in Biology, Teaching Assistant of the Department of Biochemistry, Voronezh State Medical University named after N. N. Burdenko of the Ministry of Health of the Russian Federation, Voronezh, Russian Federation; e-mail: ryazantsev77@gmail.com. ORCID iD: <https://orcid.org/0000-0002-0839-103X>.

Oleg V. Maslov, PhD in Biology, Assistant Professor of the Department of Biochemistry, Voronezh State Medical University named after N. N. Burdenko of the Ministry of Health of the Russian Federation, Voronezh, Russian Federation; e-mail: maslov-oleg1205@mail.ru. ORCID iD: <https://orcid.org/0000-0001-9476-2695>.

Elena V. Korzh, PhD in Medicine, Assistant Professor of the Department of Obstetrics and Gynaecology no. 1, Voronezh State Medical University named after N. N. Burdenko of the Ministry of Health

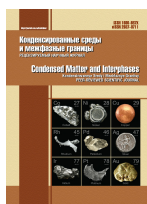
of the Russian Federation, Voronezh, Russian Federation; e-mail: elenakorzh2012@mail.ru. ORCID iD: <https://orcid.org/0000-0002-1788-2818>.

Lilia S. Rysnaya-Lokinskaya, PhD student of the Department of Hospital Therapy and Endocrinology, Resident Physician of Voronezh State Medical University named after N. N. Burdenko Ministry of Health of the Russian Federation, Voronezh, Russian Federation; e-mail: lokinskaya@rambler.ru. ORCID iD: <https://orcid.org/0000-0002-5179-7086>.

Vladimir V. Alabovsky, DSc in Medicine, Professor, Head of the Department of Biochemistry, Voronezh State Medical University named after N. N. Burdenko of the Ministry of Health of the Russian Federation, Voronezh, Russian Federation; e-mail: v.alabovsky@yandex.u. ORCID iD: <https://orcid.org/0000-0002-6306-5149>.

Received 7 April 2021; Approved after reviewing 21 April 2021; Accepted for publication 15 May 2021; Published online 25 June 2021.

*Translated by Valentina Mittova
Edited and proofread by Simon Cox*



Condensed Matter and Interphases

Kondensirovannye Sredy i Mezhfaznye Granitsy
<https://journals.vsu.ru/kcmf/>

Original articles

Research article

<https://doi.org/10.17308/kcmf.2021.23/3437>

Heat wave dynamics in frozen water droplets with eosin molecules under the femtosecond excitation of a supercontinuum

N. A. Myslitskaya^{1,2✉}, A. V. Tcibulnikova¹, I. G. Samusev¹, V. A. Slezhkin^{1,2}, V. V. Bryukhanov¹

¹Immanuel Kant Baltic Federal University,
14 A. Nevskogo ul., Kaliningrad 237041, Russian Federation

²Kaliningrad State Technical University,
1 Sovetsky prospekt, Kaliningrad 237022, Russian Federation

Abstract

In this study, we considered thermal processes in liquid and frozen water droplets with added dye molecules and metal nanoparticles at the moment of supercontinuum generation. We studied optical non-linear processes in a water droplet with a diameter of 1.92 mm, cooled (+2 °C) and frozen to -17 °C, with eosin molecules and ablative silver nanoparticles upon femtosecond laser treatment.

When we exposed a cooled water droplet and a piece of ice containing eosin molecules and ablative silver nanoparticles to a femtosecond laser beam ($\lambda = 1030$ nm), we recorded two-photon fluorescence, enhanced by plasmon processes. Also, supercontinuum generation took place, with a period of decay $t = 0.02$ s. The geometry of non-linear large-scale self-focusing ($L_{LSS} \sim 0.45\text{--}0.55$ mm) was studied. The value of microscale self-focusing ($L_{SSS} \sim 0.1$ mm) of SC radiation in the laser channel was determined experimentally. The study shows that the energy dissipation in the SC channel increases when the thermal non-linearity exceeds the electronic non-linearity. We modelled the thermal processes and determined the temperature gradient of the heating of the frozen droplet exposed to a femtosecond pulse. Based on the experimental data, the heat wave propagation velocity was calculated to be $v = 0.11$ m/s.

Keywords: Supercontinuum, Femtosecond excitation, Water, piece of ice, Eosin fluorescence, Ablative silver nanoparticles, Surface plasmons, Two-photon excitation, Thermal optical non-linearity, Temperature gradient, Heat wave, Wave propagation velocity

For citation: Myslitskaya N. A., Tcibulnikova A. V., Samusev I. G., Slezhkin V. A., Bryukhanov V. V. Heat wave dynamics in frozen water droplets with eosin molecules under the femtosecond excitation of a supercontinuum. *Kondensirovannye sredy i mezhfaznye granitsy = Condensed Matter and Interphases*. 2021;23(2): 260–272. <https://doi.org/10.17308/kcmf.2021.23/3437>

Для цитирования: Мыслицкая Н. А., Цибульникова А. В., Самусев И. Г., Слезкин В. А., Брюханов В. В. Динамика тепловой волны в сферической замороженной капле воды с молекулами эозина при фемтосекундном возбуждении суперконтинуума. *Конденсированные среды и межфазные границы*. 2021;23(2): 260–272. <https://doi.org/10.17308/kcmf.2021.23/3437>

✉ Natalia A. Myslitskaya, e-mail: myslitskaya@gmail.com

© Myslitskaya N. A., Tcibulnikova A. V., Samusev I. G., Slezhkin V. A., Bryukhanov V. V., 2021



The content is available under Creative Commons Attribution 4.0 License.

1. Introduction

For the first time, the phenomenon of the generation of white light in the range of $0.4\div 3.0\ \mu\text{m}$ with the formation of a supercontinuum (SC) with a very wide spectrum (low temporal coherence) under femtosecond laser irradiation with an intensity of about $\sim 1\ \text{GW}/\text{cm}^2$ was reported in 1970 by Alfano and Shapiro in their works [1].

Spatio-temporal high-intensity localisation of optical energy is accompanied by the non-linear polarisation of the medium and the generation of plasma filaments with the formation of a SC. To date, there have been published significant experimental and theoretical data on the spectral-energy issues of the propagation of a high-intensity electromagnetic field in various media [2–9].

Among the studies of self-focusing laser radiation with SC generation (in the wavelength range of 400–1500 nm) in various media, the most interesting are those in condensed media with silver nanoparticles (SNPs). In such cases, there are changes in the non-linear refractive index due to thermal effects [10–12]. The emergence of a laser pulse track during self-focusing is accompanied by the heating of the medium and a flash of white light, adding Δn to the refractive index due to the heating of the medium. Since the temperature derivative dn/dT can be either positive or negative, both non-linear self-focusing and defocusing can be observed [13, 14].

In this study, we consider thermal processes in liquid and frozen water droplets with eosin molecules and SNPs occurring when a SC is generated upon a femtosecond laser action on the medium. Most of the non-linear refractive index of ice (80–90 %) is associated with electronic polarisation in the optical Kerr effect. However, thermal non-linearity is significant only for nanosecond and longer pulses [15], especially under pulsed femtosecond laser irradiation.

At the same time, thermal non-linearity is an essentially non-local effect due to thermal conduction processes that occur not only in the volume where SC propagates, where radiation is absorbed, but also in neighbouring regions.

In this regard, this article is devoted to the study of the kinetics of thermal processes in the SC channel, when SC is generated in a piece of ice containing eosin and ablative silver nanoparticles.

2. Experimental

We studied water droplets with eosin and SNPs, hanging on a steel needle. In this study, we used SNPs with an average radius of 36 nm, obtained by femtosecond laser ablation of chemically pure silver in bidistilled water. The droplet diameter was 1.92 mm. It was measured using an Olympus BX43 microscope with a video camera. A droplet was cooled from room temperature to $-17\ ^\circ\text{C}$ by blowing it with gaseous nitrogen, obtained by heating liquid nitrogen in a cryostat using a thermoelement. The temperature was measured with a chromel-copel thermocouple, its wires were located inside a microsyringe on which the droplet was hanging. Spectral-energy processes were registered using a linear optical sensor (OOO LOMO FOTONIKA based on Toshiba TCD-1304 linear CCD sensor) with temporal resolution 0.2 ms and spectral resolution 2 nm, and a MotionPro X4 high-speed motion camera (REDLAKE). The study of the SC generation in aqueous solutions was carried out using an Avesta TETA-25 femtosecond laser complex with an ytterbium crystal (pulse parameters: duration $\tau = 280\ \text{fs}$, energy $W = 150\ \mu\text{J}$, wave length $\lambda = 1030\ \text{nm}$, pulse repetition frequency $\nu = 25\ \text{kHz}$, and the duration of a pulse train $t_{\text{tr}} = 0.2\ \text{s}$).

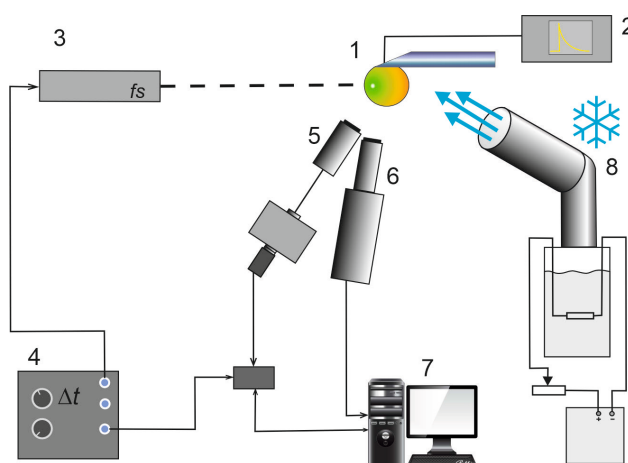


Fig. 1. Layout of the main elements of the laser system: 1 – thermocouple droplet holder; 2 – oscilloscope connected to a thermocouple, 3 – Avesta TETA-25 ytterbium femtosecond laser; 4 – G5-56 double-channel pulse generator; 5 – monochromator with optical linear scale and telescope; 6 – MotionPro X4 high-speed motion camera (by REDLAKE); 7 – computer with specialised signal processing program; 8 – nitrogen gas generator

Droplets of solutions containing eosin molecules and SNPs were frozen to temperature $T = -17\text{ }^{\circ}\text{C}$, then the formed pieces of ice were exposed to a femtosecond pulse train and emission spectra of SC were recorded.

In order to obtain a SC, we used a quartz lens with focal length $f = 50\text{ mm}$ for the optical compression of radiation. As a result, filaments were formed inside the water droplet in the SC emission channel with a diameter of less than $100\text{ }\mu\text{m}$. The power density of the pulse was about $6.8 \cdot 10^{16}\text{ W/m}^2$. The SC emission was always excited by a train of femto pulses with a repetition period of $40\text{ }\mu\text{s}$ and a total train duration of $t_{tr} = 0.2\text{ s}$ (a total of $5 \cdot 10^5$ pulses in a train).

3. Results and discussion

The study of energy processes accompanying the SC generation in condensed media is mainly aimed at studying liquid aqueous solutions [4, 7], depending on the temperature and the presence of metal nanoparticles and other substances. We wanted to carry out a comparative study of non-linear processes (optical, thermal) taking place upon the SC generation in solutions of eosin with SNPs at temperatures near zero and in frozen solutions. Dye molecules have a high quantum yield, which can be specially enhanced by plasmonic processes in the presence of nanoparticles of precious metals (silver, gold). Therefore, providing that the ingredient concentrations are constant, they can be used for studying SC processes in aqueous and frozen solutions.

In the first set of experiments, we studied the SC generation upon femtosecond laser action on aqueous eosin solutions with a concentration of $C_e = 2 \cdot 10^{-4}\text{ M}$ with added SNPs with a concentration $C_{Ag} \approx 10^{-12}\text{ M}$ at low temperature. The excitation power of aqueous solutions with SNPs and dye molecules was $< 1.0\text{ MW}$ without compression, the peak power of the pulse significantly exceeded the power threshold of self-focusing in pure distilled water, which is $P_c = 0.63\text{ MW}$ [16] ($P_c = c\lambda^2/(32\pi^2 n_2)$, where n_2 is the non-linear refractive index). Under these conditions we managed to obtain the SC emission upon irradiation self-focusing with a power density of about $6.8 \cdot 10^{16}\text{ W/m}^2$ [17]. Eosin molecules and SNPs were added to the aqueous solution in order to achieve the plasmon effect on the processes of fluorescence in the solution during the SC generation [18].

Fig. 2a shows one of the video frames of a water droplet with an exposure $t_{exp} = 0.002\text{ s}$ at a temperature $T = +2.0\text{ }^{\circ}\text{C}$.

The droplet is illuminated for the duration of the excitation laser train $t_{tr} = 0.2\text{ s}$. The laser beam ($\lambda = 1030\text{ nm}$) incident on the surface of the droplet was focused by a lens. As a result, a bright luminous white spot appeared, with a size of less than $100\text{ }\mu\text{m}$. The SC generation at this point is due to a change in the refractive index on the spherical surface of the droplet at the air-water interphase. Against the “silhouette” of a spherical water droplet, we can see bright filaments of the SC emission in different areas of the droplet. When the beam entered the water (indicated by the

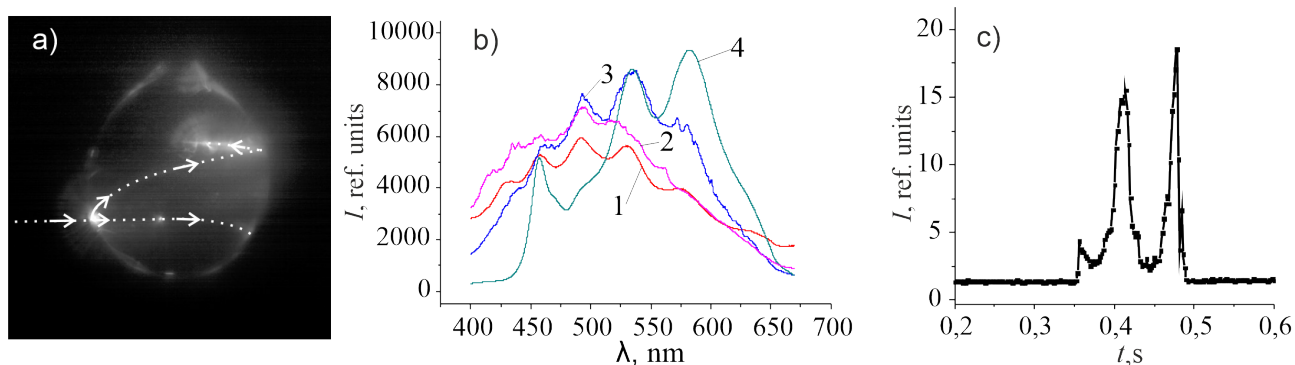


Fig. 2. Video frame of a water droplet with eosin and SNPs (a). The arrows show the propagation of laser radiation after entering the droplet. The SC spectra (b) with an envelope curve with phase modulation of the radiation signal in a water droplet at a temperature of $T = 2.0\text{ }^{\circ}\text{C}$: 1 and 2 – droplets of pure water at different excitation power; 3 and 4 – water droplets containing eosin without SNPs or with SNP, respectively. Change (c) of the integral intensity of the SC emission in a droplet with eosin and SNP during the radiation train lasting for $t = 0.2\text{ s}$

arrow), the emission of water vapour in the form of a mist was recorded. In the upper part of the SC input spot, there was a track of the refracted beam (shown by the arrow), which went in an arc to the upper part of the droplet, where the SC filament appears. According to the laws of refraction, the beam was reflected on the inner water-air interphase and the SC filament was generated, accompanied by flashes of plasma filaments. In the lower part of the SC input spot, the laser beam remained horizontal, it was an extension of the exciting beam (horizontal arrow). In this direction, along the arrow, a bright luminous point inside the droplet was recorded at some distance from the SC spot. Then the beam curved and left the droplet without generating a SC.

Two physical non-linear processes can be considered, when the laser radiation propagates in a cooled droplet at $T = +2.0$ °C. First, part of the laser light entering the droplet propagates according to the laws of linear optics along a curvilinear track (the upper beam in Fig. 2a). Meanwhile, the power of this radiation decreases and no SC is recorded. However, upon the water-air transition of the beam, the radiation self-focuses additionally at the point of refraction and the SC is generated. It rapidly decays, not reaching the centre of the droplet. Secondly, we have another part of the incoming radiation at the bottom of the SC emission spot (lower part of the figure). In the aqueous medium, a non-linear self-focusing of the infra-red radiation is recorded there at some point along the beam's track, where the eosin fluorescence occurs ($\lambda = 532$ nm) under two-photon excitation. This issue will be discussed further when studying the processes of SC generation in a frozen droplet. It should be noted that no such beam splitting processes were recorded in the water droplet at room temperature, only chaotic thin filaments of plasma spark glow and Kerr non-linear polarisation appeared (see article [17]).

Thus, in a water droplet cooled almost to the freezing point, various non-linear processes of light refraction and two-photon excitation of fluorescence of eosin with SNPs occur. When radiation transfers into another medium, SC filamentation takes place.

It is known that filaments of the SC generated by high-intensity laser action are sources of

broadband optical radiation with a maximum at the radiation wavelength. Since we studied the generation processes in aqueous solutions containing eosin molecules and SNPs, occurring under intense laser irradiation, it was of interest to obtain information on the spectral composition of the SC in water at a low temperature, $T = +2.0$ °C.

Figure 2b shows the instantaneous spectra of the SC emission in droplets of pure bidistilled water at a low temperature with broadening due to phase modulation of radiation (Fig. 2b, curves 1 and 2). It also presents the SC spectra with the emission maxima in water containing eosin molecules without SNPs (Fig. 2b, curve 3) and with SNPs (Fig. 2b, curve 4).

The presence of phase modulation in the emission channel with spectral broadening of the SC is accompanied by spectral emission of the constituent elements in samples of different physical natures. When analysing the SC generation spectra, it must be noted that self-focusing is accompanied by an uncontrolled change in the intensity of the laser pulse phase, resulting in the complex spatial dynamics of the laser beam, which is further complicated by the fluctuation of laser radiation [2]. Consequently, the spectrum will exhibit chaotic changes in the intensity of the SC emission along the front edge of the SC emission envelope. Thus, when recording the SC spectra in the 400–700 nm wavelength range, each frame with an exposure of $t_{\text{exp}} = 0.002$ s shows a set of spectral bands of absorption-emission from the components in the SC channel. Thus, by studying the features of the spectral distribution of the SC emission maxima, we can determine the SC spectra of pure water (Fig. 2b, curves 1 and 2). The obtained spectra are well known because they are scientifically valuable references [4].

When the solution contains eosin molecules and SNPs, SC generation is accompanied by the excitation of localised surface plasmons in the SNPs. It is characterised by the scattering-emission spectrum in the wavelength range of 420–460 nm (Fig. 2b, curve 3) [8,18,19]. Figure 2b, curve 4, shows the SC spectrum of the eosin solution with SNPs. This spectrum reflects the simultaneous excitation of amplified fluorescence of eosin molecules in the SC channel of a water droplet under the influence of plasmons with

maxima at wavelengths of 530 nm and 580 nm (Fig.2b, curve 4). It also shows the scattering-emission spectrum of the SNP emission in the wavelength range of 420-460 nm [20].

Thus, the instantaneous SC emission spectra of eosin solutions with SNPs near the freezing point ($T = +2.0\text{ }^{\circ}\text{C}$) reflect the processes of SC generation in pure water and the SC spectra of two-photon excitation of fluorescence of eosin molecules, when the fluorescence is amplified by plasmons under the influence of SNPs in a solution.

It should be noted that when studying the spectral features of ultrashort pulses in a condensed medium, the authors showed in article [21] that the spectral dynamics can be simulated. In this case, simulation can be carried out for SC generation processes with ultrashort femtosecond laser pulses only, due to their strong non-linearity, as well as when solitons are formed [22]. Therefore, with longer femtosecond excitations of SC, it is possible to study only the spectral-time evolution of the envelope of the radiation spectrum of a femtosecond pulse [2].

The processes of SC generation in frozen droplets with eosin molecules ($C_e = 2 \cdot 10^{-4}\text{ M}$) and SNPs ($C_{Ag} \approx 10^{-12}\text{ M}$) occur in a completely

different way. Fig. 3a shows video frames of the SC radiation in a piece of ice (the frames were recorded every $t_{\text{exp}} = 0.002\text{ s}$) until the SC completely decays. It covers a period of the current laboratory time from 0.302 to 0.322 s from the start of the shooting ($t_{\text{sc}} = 0.02\text{ s}$).

Let us consider the optical processes of energy conversion in a piece of ice under femtosecond laser excitation. It was shown above that the SC light emission channel is divided into separate glowing elements (pixels). We considered the change in the intensity of the SC pixels along the emission channel (its cross-section area is $7.85 \cdot 10^{-9}\text{ m}^2$) along the diameter of the piece of ice from the point of time and the coordinate. In addition, we determined the law relating to a decrease in the integral pixel intensity (pixel cross-section intensity) in the SC channel.

Fig. 4a selectively shows 6 intensity profiles of the SC radiation in a piece of ice at different time points of the existence of the SC. Its total duration was $t_{\text{sc}} = 0.02\text{ s}$ from initiation to complete decay. The total time of action of a laser radiation train on a piece of ice is $t_{\text{tr}} = 0.2\text{ s}$.

First, we determined that the maxima of the SC intensity profiles, which initially (frame

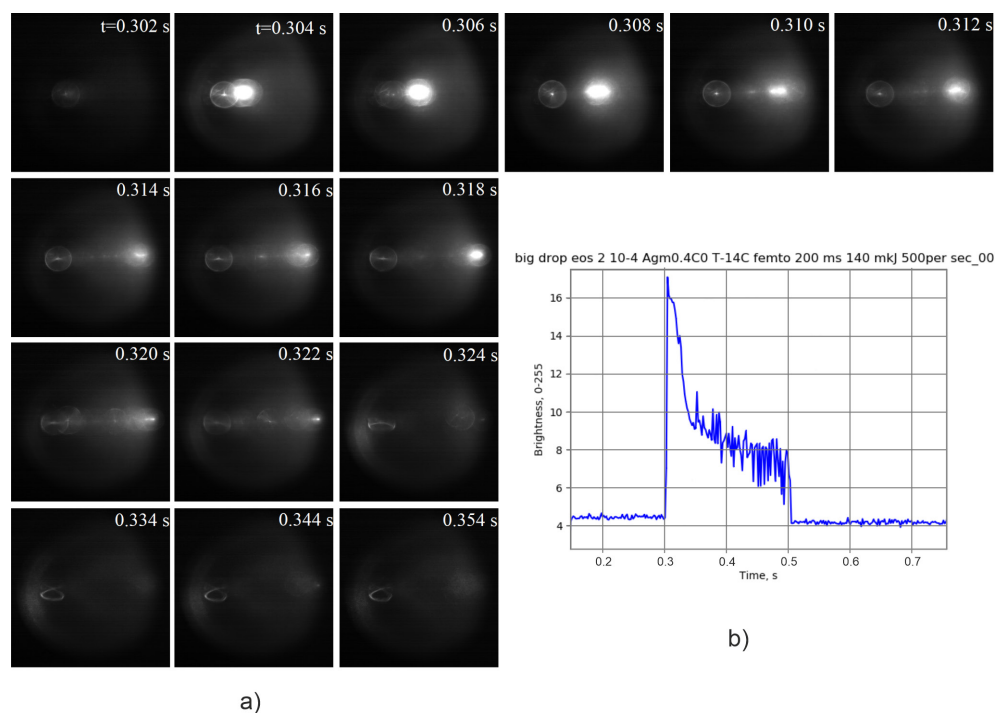


Fig. 3. Video frames (a) of the SC radiation in a frozen spherical droplet at a temperature of $-17\text{ }^{\circ}\text{C}$ with eosin molecules and SNPs along the diameter of the frozen droplet, the timestamp of the video shooting is indicated. Kinetic curve of changes in the SC radiation intensity (b)

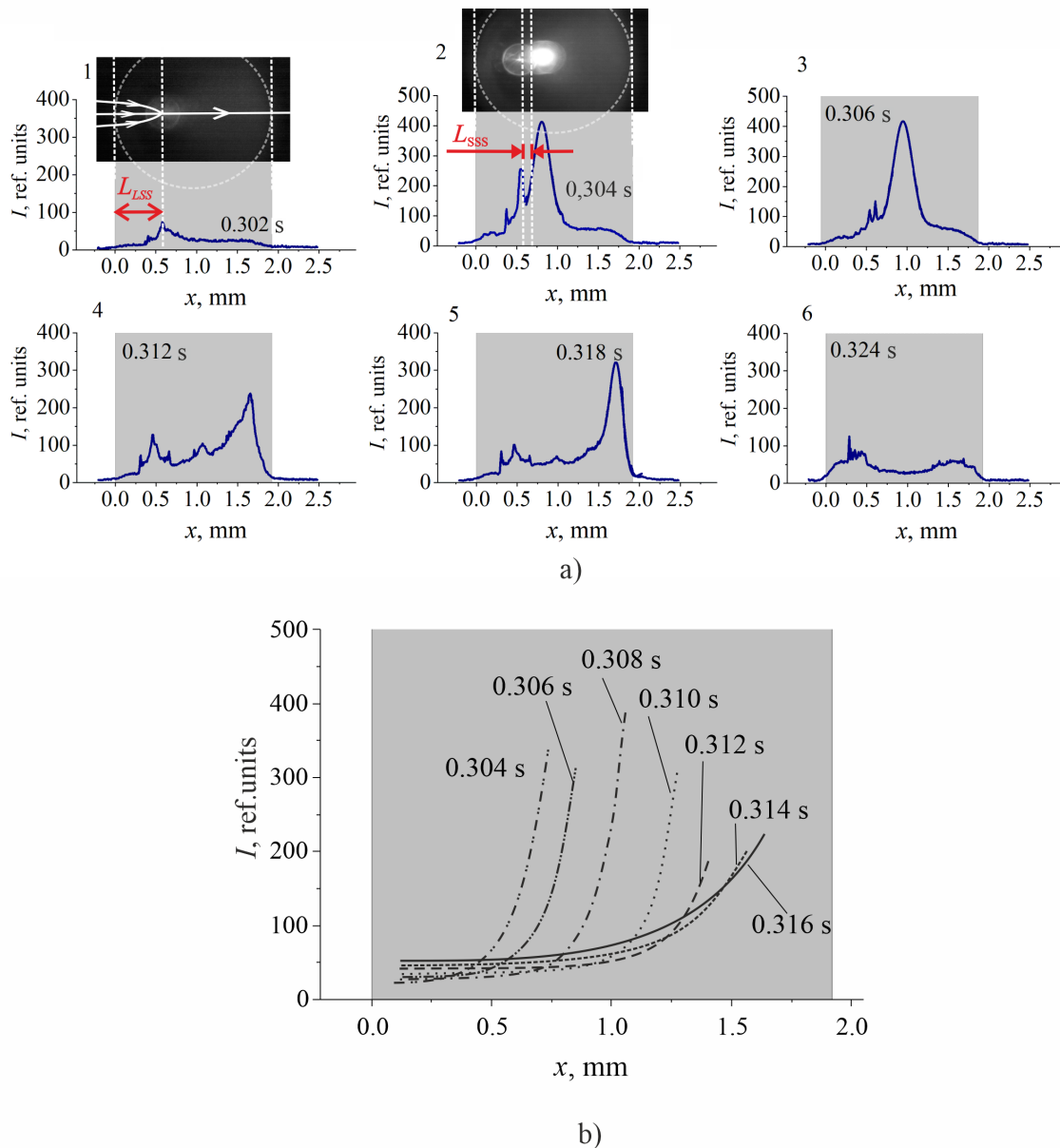


Fig. 4. Profiles (a) of the SC intensity along the diameter of the ice with a time interval of $\Delta\tau = 0.002$ s (for the frames shown in Fig. 3a). The first profile (1) shows the optical length L_{LSS} of the large-scale focusing of laser radiation entering the piece of ice. The SC intensity profile (2) shows the small-scale focusing distance L_{SSS} . Decay kinetics (b) of the SC radiation fronts along the coordinate along the diameter of the piece of ice

by frame) increased sharply, and then begin to decrease, while moving along the diameter of the piece of ice until the SC completely decays after 0.02 s. The areas of the pixel profiles proportional to the SC intensity were calculated, without taking into account the background light scattering. Then we considered the features of the registered intensities of the SC pixels.

In the first frame (Fig. 4a, profile (1), time point $t_1 = 0.302$ s), the first pixel in the SC light emission channel was recorded. We can see

that the first pixel (1) appears not at the zero coordinate $x_0 = 0.0$ mm. It is slightly shifted inside the droplet. Obviously, the first SC pixel appears due to the self-focusing of the femtosecond laser beam at a distance of L_{LSS} during the transition from air to the piece of ice. It is followed by Kerr non-linear polarisation of the medium and multiphoton processes [2, 7]. Indeed, when the laser beam passes from air to the piece of ice, non-linear self-focusing of the laser radiation in the ice occurs with the formation of a SC radiation

pixel. Profile (1) in Fig. 4a shows the optical scheme of focusing a laser beam on a spherical surface of a frozen droplet, which is a spot with a linear size of $< 100 \mu\text{m}$. The scheme is similar to the laser beam focusing on the surface of a cooled drop in Fig. 2; an additional image of the second luminous point of the SC inside the water droplet is also provided. The optical scheme (1) of self-focusing inside a piece of ice presented in Fig. 4a shows the trajectory of the beam in the piece of ice after refraction at a point on the optical axis of the piece of ice.

The appearance of the initial SC emission pixel is associated with the refraction of the laser pulse on the surface of the frozen droplet and its focusing. The focusing is determined by the value of the non-linear index of light refraction in ice:

$$n^* = n_0 + n_2 I_L(t), \quad (1)$$

where n_0 is the reference linear refractive index of ice, $n_0 = 1.32$; n_2 is the non-linear refractive index, $n_2 = 4.1 \cdot 10^{-16} \text{ cm}^2/\text{W}$ [23]; and $I_L(t)$ is the power density of the radiation incident on the surface of the piece of ice due to the laser pulse compression in air after a focusing lens (see the Experimental section). Using the mathematical model from [4, 24], we determined the focal distance at the so-called critical self-focusing of femtosecond laser radiation after non-linear refraction of radiation in ice by the formula:

$$L_{LSS} = \frac{0.367kr^2}{\left\{ \left[\sqrt{\frac{P_0}{P_{cr}}} - 0.852 \right]^2 - 0.0219 \right\}^{\frac{1}{2}}}, \quad (2)$$

where L_{LSS} is the self-focusing distance on the main optical axis; P_0 is the radiation power; $r = 50 \mu\text{m}$ is the beam radius; and P_{cr} is the critical power of self-focusing. The peak energy in water [4] for a laser pulse with $\lambda = 1032 \text{ nm}$ is $W = 150 \mu\text{J}$, the impulse length is $\tau = 280 \text{ fs}$. Thus, the peak radiation power is:

$$P_0 = \frac{E}{\tau} = 536 \text{ MW}. \quad (3)$$

The critical radiation power was determined according to Kandidov [4]:

$$P_{cr} = R_{cr} \frac{\lambda^2}{8\pi n_0 n_2} = 2.96 \text{ MW}. \quad (4)$$

Then the distance of self-focusing of radiation and the formation of the focus of the first pixel in ice is $L_{LSS} = 0.44 \text{ mm}$.

Considering the SC emission profile (Fig. 4a, profile (1)), it can be seen that the distance between the focus and the surface of the frozen droplet L_{LSS} coincides with the distance of macroscale self-focusing [23, 24] of laser radiation in ice, which is approximately at a distance of $0.44 \div 0.55 \text{ mm}$ from the surface of the droplet. It coincides with the actual position of the first SC radiation pixel. Thus, the experimental values coincide with the modelling parameters for non-linear self-focusing processes. This situation correctly reflects the physical phenomena during SC generation in a spherical piece of ice.

Considering all pixels appearing during the SC generation and decay time $t_{sc} = 0.02 \text{ s}$ frame by frame, we can see that the first pixel (1) remains still at a distance of $0.44 \div 0.55 \text{ mm}$ from the surface of the frozen droplet during the entire duration of the SC. Earlier, in [17], a study was carried out of the SC generation at low temperatures with silver NPs in water. It showed that the maximum of SC radiation moves in a medium with the speed of a heat wave. In our study, it was found that, under femtosecond excitation of SC in ice containing eosin molecules (see the Experimental), initially the first immovable SC pixel appears at the self-focusing point L_{LSS} . Moreover, on all profiles (1–6), the coordinate of the first pixel of the SC does not shift and the intensity of this pixel almost does not change.

It was assumed that this fixed pixel of the SC emission recorded in the first frame results from the fluorescence of eosin molecules upon the action of a train of high-intensity femtosecond laser pulses on the piece of ice. Since the laser (ytterbium crystal) radiation occurs at a wavelength of $\lambda = 1030 \text{ nm}$, the molecular fluorescence of eosin molecules ($\lambda_{ex} = 570 \text{ nm}$) could be excited only upon the two-photon excitation of the dye. Thus, in the case of the non-linear self-focusing of a train of laser pulses inside a piece of ice, two-photon fluorescence of eosin molecules with a constant luminous intensity is generated. Since the fluorescence lifetime of eosin molecules is $\sim 5 \text{ ns}$, the fluorescence emission remains quasi-continuous under the influence of a train of femtosecond laser pulses.

Fig. 4a, profile (2) shows the profile of SC emission in the piece of ice, obtained by analysing the following video frame, which already includes two SC emission maxima. At the coordinate of 0.4–0.5 mm, there is a complex shaped pixel with a lower intensity, which is visible even on the previous profile. Behind it, at the coordinate ~ 0.66 mm, there is a second pixel. The pixel with a smaller intensity was identified as the maximum of the eosin fluorescence emission upon two-quantum femtosecond laser excitation of the dye. The second, larger maximum on profile (2) indicates a non-linear increase in the perturbation velocity of the SC emission amplitude. Within the limits of this increase, the small-scale perturbations of the refractive index may grow [25]. Considering the intensity development within the second profile (2) at coordinates along the laser channel of the SC $x = 0.4 \div 0.5$ mm and $x = \sim 0.66$ mm, we can use formulas [23–25] to measure the coordinate shift of the amplification of small-scale radiation self-focusing in the SC:

$$\frac{L_{LSS}}{L_{SSS}} \approx \sqrt{\frac{P_0}{P_{cr}}}, \quad (5)$$

where P_0/P_{cr} is the ratio of the total and critical powers, calculated by formulas (3–4); L_{LSS}/L_{SSS} is the ratio of large-scale and small-scale self-focusing length values. In this case, $L_{SSS} \sim 0.033$ mm is associated with an increase in the amplitude of non-linear self-focusing upon a change in the refractive index. Analysing the plots (Fig. 4a), we can determine that the experimental value of the small-scale self-focusing is $L_{SSS} \sim 0.1$ mm, which is ~ 3 times higher than the calculated value of the increase in the SC intensity. It should be noted that the increase in intensity occurs according to a complex dependence, which is indicative of non-linear processes of energy conversion in a piece of ice during the SC generation. For example, Fig. 4b shows the kinetic curves of the growth of the intensity of the front edge of the SC emission in the piece of ice, calculated according to the exponential law, in different temporal coordinates of frame-by-frame recording. It can be seen (Fig. 4b) that the frame-by-frame kinetics of the SC decay in the piece of ice slows down, resulting at the “delay” of the decay time of the SC luminescence after the end of the process. We

can assume that the rate of decay of SC in the ice changes because the frozen droplet heats up, which causes a respective change in the refractive index. The resulting thermal non-linearity, as we know from [26], is an essentially non-local effect. Namely, due to heat transfer, the temperature changes not only in the volume absorbing the laser radiation, but also in the neighbouring regions [27–29].

Thus, the studied optical non-linear processes of the kinetics of frame-by-frame decay of the SC radiation in ice samples show a significant effect of thermal processes during focusing and defocusing of radiation inside the SC generation channel. It is known that defocusing occurs in liquids or solids under the conditions of thermal non-linearity, causing a decrease in the refractive index. In this case it is due to the heating of the medium under the action of laser radiation. Approximately 40 μ s before the next pulse in the train, the SC energy dissipates in the form of a radial transfer of thermal energy from the volume of the laser channel. It occurs as a result of the decay of the non-linear Kerr polarization ($\tau \sim 10^{-15}$ s). During the exposure of each frame, a train of laser radiation consisting of 50 pulses acts on the droplet. The temperature within the excitation channel and around it increases and the refractive index changes. Further, after a period of $t_{sc} = 0.02$ s, the SC light emission degrades because of the indicated reasons. When the SC in the piece of ice decays, a weakly decaying scattered glow of ice is observed, its intensity almost does not change.

It was of interest to estimate the value of the thermodynamic temperature in the spatio-temporal coordinates of the SC channel, in which the coherent supercontinuum radiation completely degrades. For this purpose, in this work, we measured the areas of all registered SC radiation pixels in the studied samples of frozen droplets frame by frame, using the units of the integral luminous intensity of the pixels.

Fig. 5 shows a graph of the change in the integrated luminous intensity of the SC pixels over the full SC lifetime, $t_{sc} = 0.02$, approximated by the exponential function

$$I(t) = I_0 + A_1 \cdot \exp\left(\frac{-t - t_1}{t_0}\right), \quad (6)$$

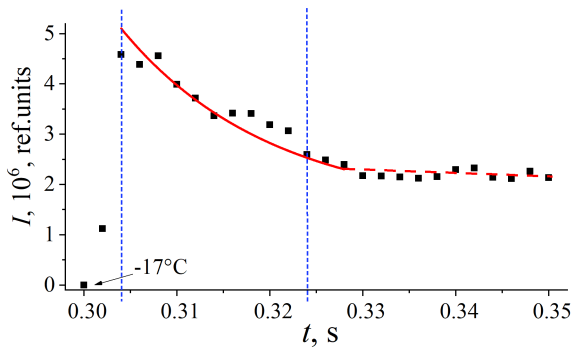


Fig. 5. Decay plot of the integral radiation intensity of the supercontinuum pixels in the frozen droplet with eosin molecules ($C = 2 \cdot 10^{-4}$ M) and silver nanoparticles ($C_{Ag} \approx 10^{-12}$ M) at an initial temperature of -17°C . The dashed lines on the time scale indicate the SC generation range

where I_0 is the integral intensity after the decay of the SC filament, background level; A_1 is the maximum increase in SC intensity relative to the background level I_0 at t_1 , a moment of time when SC generation begins; t_0 is the average time of the SC decay in the piece of ice after excitation.

When studying the intensity of the SC radiation in the channel along the diameter of the piece of ice at different timepoints of the record, it was found (Fig. 5) that at first the intensity of the SC pixels rapidly increases, reaching a certain maximum, and then exponentially decays according to formula (6). A sharp increase in the SC generation is indicative of the formation of a second radiation pixel (Fig. 4a, profile (2)), which reaches its maximum at a point with a coordinate of approximately ~ 1.0 mm, where non-linear Kerr polarisation arises [2] (at the focusing point of laser radiation). After this, the intensity values of the subsequent pixels of the SC generation decrease over time and shift along the coordinate of the SC radiation channel. The average shifting rate of the shift of the radiation maxima of the SC pixels along the diameter of the piece of ice is $v_1 = 1.92 \text{ mm}/0.018 \text{ s} = 106.6 \text{ mm/s} \approx 0.11 \text{ m/s}$.

It should be noted that the spread in the integral values of the intensities of the SC generation pixels (the pixels represent a light guide channel with an ultra-wide spectrum), observed in Fig. 5, is stochastic due to modulation instability in a medium with Kerr-type cubic non-linearity [2, 3]. In this case, possible physical processes causing a decrease in the SC intensity

occur as a result of the processes of dissipation of energy obtained during the absorption of radiation in a non-linear medium (electron-phonon interaction, destruction of the anisotropy of the medium in a light field, etc.) and the dissipation of energy with the generation of a heat wave within the SC channel.

Thus, the optical heating of ice resulting from SC generation can cause thermal processes in the SC channel. Their propagation rate is dependent on the temperature gradient and the temperature conductivity index of the medium. As shown above (formula (6)), the decay of the integrated intensity of SC generation in a piece of ice is described by an exponential dependence; simultaneously with this, thermal processes also develop according to the known laws of generation and transfer of heat during laser action [30–32]:

$$C_{(v)} \frac{\partial T}{\partial t} - a \Delta T = \delta \cdot I_L(r). \quad (7)$$

T is the thermodynamic temperature; $C_{(v)} = 1.812 \cdot 10^6 \text{ J}/(\text{m}^3 \cdot \text{K})$ is the average specific heat of ice at -17°C ; t is the duration of laser radiation; a is the thermal conductivity; δ is the absorption coefficient of ice at the laser radiation wavelength ($\delta = 10 \text{ m}^{-1}$ [33]); and $I_L(r)$ is the intensity of laser radiation in a beam with a radius of r . With a pulsed femtosecond laser action on a piece of ice, we can omit the thermal conductivity a , and, accordingly, the second summand in equation (7), and calculate the instantaneous temperature at the SC generation for a short period of time [21, 23, 34]. In this case, all temperature gradients between molecules and SNPs during the emission period of one SC pixel ($t_{\text{exp}} = 0.002 \text{ s}$) are levelled out due to the fast energy transfer. We can also omit the heat capacity and mass of eosin molecules and SNPs in the generated SC.

Let us calculate the temperature increase on the axis of the piece of ice during the entire time of the action of the train of electromagnetic laser pulse using the following equation, assuming that a stationary temperature field has been established [23]:

$$\Delta T_{fm} = \frac{\delta I r^2}{\kappa}, \quad (8)$$

where δ is the absorption coefficient of ice at the laser wavelength, $\langle I \rangle = Wv/S = 4.78 \cdot 10^8 \text{ W}/\text{m}^2$ is the average emission power density during the peri-

od of action of the train, S is the section area of the laser beam $S = \pi r^2$, and $\kappa = 2.34 \text{ W}/(\text{m}\cdot\text{K})$ is the thermal conductivity index of ice. We found that with $\Delta T_{fin} = 5.1 \text{ K}$, the temperature on the droplet axis increased to $-11.9 \text{ }^\circ\text{C}$.

Using the data on the exponential dependence of the SC radiation decay in Fig. 5, assuming that the radiation intensity is proportional to the temperature, and taking into account the obtained data that the initial temperature is $-17 \text{ }^\circ\text{C}$, and the saturation temperature is $-11.9 \text{ }^\circ\text{C}$, we can measure the initial sharp increase in the temperature in the channel during 0.002 s , when the temperature reached its maximum value, and more inertial thermal conduction processes have not yet manifested themselves. The maximum intensity value on the graph corresponds to a temperature of $-6.0 \text{ }^\circ\text{C}$.

We also estimated the temperature at the moment of the maximum intensity of the SC radiation pixel at the coordinate $x \sim 0.8 \text{ mm}$ from the surface of the frozen droplet. We took into account that heating occurs due to the linear absorption of the radiation energy of 50 laser pulses in the train during $t_{exp} = 0.002 \text{ s}$. Considering that the distance over which the heat is dissipated by heat transfer can be estimated as $l = (a \cdot t_{exp})^{1/2} \approx 51 \text{ } \mu\text{m}$ [35], the average temperature increase in the channel with a radius $r + l$ amounts to

$$\Delta T_{ch} = \frac{(1 - \exp(-\delta 2R)) W v t_{exp}}{C_{(v)} \pi (r + l)^2 2R} \approx 1.3 \text{ }^\circ\text{C},$$

but it is important to take into account the uneven distribution of heat in this volume.

We also estimated the average final temperature increment in the entire volume of heated ice after the SC decomposition over the time $t_{sc} = 0.02 \text{ s}$, which appeared to be only $\Delta T = 0.2 \text{ }^\circ\text{C}$. Therefore, in such work it is necessary to take into account that the temperature field in the volume of the droplet is distributed unevenly. For the indicated time, the SC radiation in the ice completely disappeared as a result of complex physical processes of energy dissipation, such as the decay of non-linear polarization, scattering of optical and thermal energy, etc. One of the indicators of irreversible energy dissipation of the SC in the ice was the registered scattered

glow of the ice as a whole, which may be due to the thermal heating of the ice without visible melting upon the action of a train of pulses with a duration of $t_{tr} = 0.2 \text{ s}$.

Thus, after the first pulse and focusing of the laser beam, as a result of additional refraction on the spherical surface of a frozen water droplet with eosin molecules and SNPs, the SC amplifies with maximum intensity. During the lifetime of the SC radiation in the ice ($t_{sc} = 0.02 \text{ s}$), the piece of ice in the laser channel heated up from -17 to $-11.9 \text{ }^\circ\text{C}$.

A temperature gradient in the laser channel with eosin molecules and SNPs upon femtosecond laser photoexcitation of the medium makes it possible to simulate the generation of a thermal wave in a non-linear medium. Namely, we can calculate the propagation velocity of a thermal wave according to the equation [30]:

$$v = \sqrt{\frac{\kappa}{C_{(v)} \tau_r}}, \quad (9)$$

where v is the propagation velocity of a heat wave; $\kappa = 2.34 \text{ W}/(\text{m}\cdot\text{K})$ is the thermal conductivity of ice at $-17 \text{ }^\circ\text{C}$; $C_{(v)} = C\gamma$ is the volumetric heat capacity of ice, where $C = 1.972 \cdot 10^3 \text{ J}/(\text{kg}\cdot\text{K})$ is the specific heat capacity of ice; $\gamma = 919 \text{ kg}/\text{m}^3$ is the density of ice; and $\tau_r = 1 \cdot 10^{-5} \text{ s}$ is the dielectric relaxation time of ice [36]. Calculations show that $v \approx 0.359 \text{ m/s}$.

Thus, before the complete decay of the SC in a laser-heated ice with eosin and SNPs, a thermal wave is generated with a velocity of $v = 0.11 \text{ m/s}$. Its value almost coincides with the theoretical value of the propagation velocity of a thermal wave in ice.

4. Conclusions

In this work, we studied optical non-linear processes in water droplets in liquid and frozen states with eosin molecules and SNPs at the moment of supercontinuum (SC) generation under femtosecond laser action on the medium. We obtained the following results:

1. We directed a train (duration $t_{tr} = 0.2 \text{ s}$) of femtosecond pulses at a power density of about $6.8 \cdot 10^{16} \text{ W}/\text{m}^2$ ($\lambda = 1030 \text{ nm}$) on a spherical water droplet with a temperature of $+2.0 \text{ }^\circ\text{C}$, containing eosin and SNPs. As a result, we observed a spectrum of coherent SC radiation with phase

modulation and the spectrum of SNP plasmons in the wavelength range 420–460 nm. The generation of surface plasmons on SNPs of the droplet led to an increase in the intensity of two-photon fluorescence of eosin molecules in the SC radiation filaments.

2. The action of a train of laser radiation on a piece of ice with eosin and SNPs at $-17\text{ }^{\circ}\text{C}$ led to its self-focusing after crossing the air-ice interphase and the generation of a coherent white light SC. Using a high-speed video camera, the pixels of the SC radiation in the ice were recorded frame-by-frame with a time step of $t_{\text{exp}} = 0.002\text{ s}$ until the the SC radiation decayed completely, the SC lifetime was $t_{\text{sc}} = 0.02\text{ s}$. After that, for a period of $t_{\text{tr}} = 0.2\text{ s}$, only the decaying scattered glow of a piece of ice without SC was observed.

3. When analysing the geometry of self-focusing of the first SC pixels we determined the distance of non-linear large-scale self-focusing $L_{\text{LSS}} \sim 0.44\text{--}0.55\text{ mm}$ and the experimental value of the distance of small-scale radiation self-focusing $L_{\text{SSS}} \sim 0.1\text{ mm}$. These values indicated a rapid increase in the radiation intensity in the SC channel with the first two pixels. When the excitation pulses were repeated with a black period of $t \sim 40\text{ }\mu\text{s}$, the thermal non-linearity exceeded the electron. It accelerated the energy dissipation in the SC channel. Subsequent frames also showed a temporal exponential delay of the light decay at the SC pixels along the generation channel as a result of thermal conduction processes.

4. When simulating the SC generation process, the exponential law of its decay after exposure to a laser pulse was determined. We also determined the instantaneous maximum temperature when the first pixel of the SC radiation in the piece of ice appeared, which is $T_{\text{max}} = -6.0\text{ }^{\circ}\text{C}$. The temperature of ice in the radiation channel after decay of the SC is $T \approx -11.9\text{ }^{\circ}\text{C}$. Thus, it was found that the piece of ice after exposure to a femtosecond electromagnetic pulse train did not melt.

5. The radiation kinetics of the SC pixels along the diameter of a piece of ice with eosin and SNPs indicates the presence of a temperature gradient. The gradient leads to the generation of a heat wave in a non-linear medium, the propagation velocity of which, according to modelling, is $v \approx 0.359\text{ m/s}$. If we compare the velocity value

obtained by conceptual modelling and the actual velocity value, we can see that $v_1 \sim v$.

Thus, the obtained results of the study of the femtosecond SC generation in a piece of ice containing eosin and SNPs showed that thermal optical non-linearity appears, develops, and degrades during the lifetime of the SC in ice.

Contribution of the authors

Myslitskaya N. A. – research, experimental data processing, design of figures, calculations, text writing. Tcibulnikova A. V. – research, discussion of results. Slezhkin V. A. – preparation of samples, research, discussion of results, text writing. Samusev I. G. – research concept, research methodology, discussion of results. Bryukhanov V. V. – scientific leadership, research concept, methodology development, review writing, calculations, text writing, final conclusions.

Conflict of interests

The authors declare that they have no known competing financial interests or personal relationships that could have influenced the work reported in this paper.

References

1. Alfano R. R., Shapiro S. L. Emission in the region 4000 to 7000 Å via four-photon coupling in glass. *Phys. Rev. Lett.* 1970;24(11): 584–587. <https://doi.org/10.1103/PhysRevLett.24.584>
2. Zheltikov A. M. Let there be white light: supercontinuum generation by ultrashort laser pulses. *Physics-Uspekhi.* 2006;49(6): 605. <http://dx.doi.org/10.1070/PU2006v049n06ABEH005975>
3. Couairon A., Mysyrowicz A. Femtosecond filamentation in transparent media. *Physics Reports.* 2007;441(2–4): 47–189. <https://doi.org/10.1016/j.physrep.2006.12.005>
4. Kandidov V. P., Shlemov S. A. Javlenie filamentacii moshhnyh femtosekundnyh lazernyh impul'sov i ego prakticheskie prilozhenija. [The phenomenon of filamentation of high-power femtosecond laser pulses and its practical applications] In: Panchenko V. Ja. (ed.) *Glubokoe kanalirovanie i filamentacija moshhnogo lazernogo izluchenija v veshhestve* [Deep channeling and filamentation of high-power laser radiation in matter]. Moscow, Interkontakt Nauka Publ.; 2009. p. 185–266. (In Russ.)
5. Chin S. L. *Femtosecond Laser Filamentation*. N.Y.: Springer; 2010. 130 p. <https://doi.org/10.1007/978-1-4419-0688-5>
6. Chekalin S. V., Kandidov V. P. From self-focusing light beams to femtosecond laser pulse filamen-

- tation. *Physics-Uspexhi*. 2013;56(2): 123–140. <https://doi.org/10.3367/ufne.0183.201302b.0133>
7. Apeksimov D. V., Bukin O. A., Bykova E. E., Gejnc Ju. Je., Golik S. S., Zemljanov Al. A., Zemljanov A. A., Il'in A. A., Kabanov A. M., Matvienko G. G., Oshlakov V. K., Sokolova E. B., Habibullin R. R. Interaction of GW laser pulses with water droplets. *Prikladnaja Fizika*. 2011;6: 13–21. Available at: <http://applphys.orion-ir.ru/appl-11/11-6/PF-11-6-13.pdf> (In Russ., abstract in Eng.)
8. Kudryashov S. I., Samokhvalov A. A., Ageev E. I., Veiko V. P. Ultrafast broadband nonlinear spectroscopy of a colloidal solution of gold nanoparticles. *JETP Lett.*, 2019;109(5): 298–302. <https://doi.org/10.1134/S0021364019050096>
9. Hoppius J. S., Maragkaki S., Kanitz A., Gregorcic P., Gurevich E. L. Optimization of femtosecond laser processing in liquids. *Applied Surface Science*. 2019;467–468: 255–260. <https://doi.org/10.1016/j.apsusc.2018.10.121>
10. Liu W., Kosareva O., Golubtsov I. S., Iwasaki A., Becker A., Kandidov V. P., Chin S. L. Femtosecond laser pulse filamentation versus optical breakdown in H₂O. *Applied Physics B: Lasers and Optics*. 2003;76(3): 215–229. <https://doi.org/10.1007/s00340-002-1087-1>
11. Driben R., Husakou A., Herrmann J. Supercontinuum generation in aqueous colloids containing silver nanoparticles. *Optics Letters*. 2009;34(14): 2132–2134. <https://doi.org/10.1364/OL.34.002132>
12. Sutherland R. L. *Handbook of Nonlinear Optics*. 2nd Edition. CRC Press; 2003. p. 337–499. <https://doi.org/10.1201/9780203912539>
13. Ahmanov S. A., Nikitin S. Ju. *Fizicheskaja optika [Physical optics]*. Moscow: Nauka Publ.; 2004. 656 p. (In Russ.)
14. Besprozvannyh V. G., Pervadchuk V. P. *Nelinejnaja optika: ucheb. posobie [Nonlinear Optics: A Tutorial]*. Perm': Perm. gos. tehn. un-ta Publ.; 2011. 200 p. (In Russ.)
15. Zhai S., Huang L., Weng Z., Dai W. Parabolic two-step model and accurate numerical scheme for nanoscale heat conduction induced by ultrashort-pulsed laser heating. *Journal of Computational and Applied Mathematics*. 2020;369: 112591. <https://doi.org/10.1016/j.cam.2019.112591>
16. Lee Smith W., Liu P., Bloembergen N. Superbroadening in H₂O and D₂O by self-focused picosecond pulses from a YAlG: Nd laser. *Physical Review A*. 1977;15(6): 2396–2403. <https://doi.org/10.1103/PhysRevA.15.2396>
17. Myslitskaya N. A., Tcibul'nikova A. V., Slezhkin V. A., Samusev I. G., Antipov Ju. N., Derevshhikov V. V. Generation of supercontinuum in filamentation regime in a water droplet containing silver nanoparticles at low temperature. *Optics and spectroscopy*. 2020;128(12): 1954–1962. <https://doi.org/10.1134/s0030400x20120978>
18. Klimov V. V. *Nanoplazmonika*. Moscow: Fizmatlit Publ.; 2009. 480 p. (In Russ.)
19. Balykin V. I. and Melentiev P. N. Optics and spectroscopy of a single plasmonic nanostructure. *Physics-Uspexhi*. 2018;61(2): 133. <https://doi.org/10.3367/UFNe.2017.06.038163>
20. Myslitskaya N. A., Slezhkin V. A., Borkunov R. Y., Tsar'kov M. V., Samusev I. G., Bryukhanov V. V. Spectral and temperature dynamics of the processes inside aqueous droplets containing eosine molecules and silver nanoparticles upon laser excitation in the IR and visible Ranges. *Russian Journal of Physical Chemistry A*. 2019;93(8): 1559–1566. <https://doi.org/10.1134/S003602441908020X>
21. Bespalov V. G., Kozlov S. A., Shpolyanskiy Yu. A., Walmsley I. A. Simplified field wave equations for the non-linear propagation of extremely short light pulses. *Physical Review A*. 2002;66: 013811. <https://doi.org/10.1103/PhysRevA.66.013811>
22. Rozanov N. N., Vysotina N. V., Shacev A. N., Desjatnikov A. S., Shadrivov I. V., Noskov R. E., Kivshar' Ju. S. Discrete switching and dissipative solutions in the coherently excited nanostructures and metamaterials. *Scientific and Technical Journal of Information Technologies, Mechanics and Optics*. 2012;4(80): 1–12. Available at: <https://www.elibrary.ru/item.asp?id=17799659> (In Russ. abstract in Eng.)
23. Sizmin D. V. *Nelinejnaja optika [Nonlinear optics]*. Saratov: SarFTI Publ.; 2015. 146 p. (In Russ.)
24. Marburger J. H. Self-focusing: Theory. *Progress in Quantum Electronics*. 1975;4(1): 35–110. [https://doi.org/10.1016/0079-6727\(75\)90003-8](https://doi.org/10.1016/0079-6727(75)90003-8)
25. Bespalov V. I., Talanov V. I. O nitevidnoi strukture puchkov sveta v nelineinykh zhidkostyakh [On the filamentous structure of light beams in nonlinear liquids]. *JETP Letters*. 1966;3(12): 307–309. Available at: http://jetpletters.ru/cgi-bin/articles/download.cgi/782/article_12073.pdf (In Russ.)
26. Dmitriev V. G., Tarasov L. V. *Prikladnaja nelinejnaja optika. 2nd ed.* [Applied nonlinear optics]. Moscow: FIZMATLIT Publ.; 2004. 512 p. (In Russ.)
27. Shen Y. R. *The Principles of Nonlinear Optics*. New York: Wiley; 1984. 563 p.
28. Boyd R. W. *Nonlinear optics*. 3rd ed. Boston: Academic Press; 2007. 640 p.
29. Lykov A. V. *Teoriya teploprovodnosti [Heat conduction theory]*. Moscow: Vysshaja shkola Publ.; 1966. 592 p. (In Russ.)
30. Tabiryany N. V., Luo W. Soret feedback in thermal diffusion of suspensions. *Physical Review E*. 1998;57(4): 4431–4440. <https://doi.org/10.1103/PhysRevE.57.4431>
31. Baffou G., Rigneault H. Femtosecond-pulsed optical heating of gold nanoparticles. *Physical Review*

B. 2011;84: 035415-1-13. <https://doi.org/10.1103/PhysRevB.84.035415>

32. Warren S. G., Brandt R. E. Optical constants of ice from the ultraviolet to the microwave: A revised compilation. *Journal of Geophysical Research*. 2008;113(D14220). <https://doi.org/10.1029/2007JD009744>

33. Brown A. M., Sundararaman R., Narang P., Goddard III W. A., Atwater H. A. Ab initio phonon coupling and optical response of hot electrons in plasmonic metals. *Physical Review B*. 2016;94(7): 075120-1–075120-10. <https://doi.org/10.1103/PhysRevB.94.075120>

34. Kuhling H. *Handbook of Physics*. Moscow: Mir Publ.; 1982. 519 p. (in Russ.).

35. Libenson M. N., Jakovlev E. B., Shandybina G. D. *Vzaimodejstvie lazernogo izlucheniya s veshhestvom (silovaya optika). Chast' II. Lazernyj nagrev i razrushenie materialov. Uchebnoe posobie* [Interaction of laser radiation with matter (power optics). Part II. Laser heating and destruction of materials. Tutorial]. Veiko V. P. (ed.). Sankt Petersburg: NIU ITMO Publ.; 2014. 181 p. (In Russ.)

36. Johari G. P., Whalley E. The dielectric properties of ice Ih in the range 272–133 K. *The Journal of Chemical Physics*. 1981;75(3): 1333–1340. <https://doi.org/10.1063/1.442139>

Information about the authors

Natalia A. Myslitskaya, PhD in Physics and Mathematics, senior research fellow at the Research & Education Centre “Fundamental and Applied Photonics. Nanophotonics”, Institute of Physical and Mathematical Sciences and Information Technologies, Immanuel Kant Baltic Federal University, Kaliningrad, Russian Federation; Associate Professor at the Department of Physics, Kaliningrad State Technical University, Kaliningrad, Russian Federation; e-mail: myslitskaya@gmail.com. ORCID iD: <https://orcid.org/0000-0001-6701-5328>.

Anna V. Tcibulnikova, PhD in Physics and Mathematics, senior research fellow at the Research & Education Centre “Fundamental and Applied Photonics. Nanophotonics”, Institute of Physical and Mathematical Sciences and Information Technologies, Immanuel Kant Baltic Federal University, Kaliningrad, Russian Federation; e-mail: anna.tsibulnikova@mail.ru. ORCID iD: <https://orcid.org/0000-0001-8578-0701>.

Vasily A. Slezhkin, PhD in Chemistry, senior research fellow at the Research & Education Centre “Fundamental and Applied Photonics. Nanophotonics”, Institute of Physical and Mathematical Sciences and Information Technologies, Immanuel Kant Baltic Federal University, Kaliningrad, Russian Federation; Associate Professor at the Department of Chemistry, Kaliningrad State Technical University, Kaliningrad, Russian Federation; e-mail: vslezhkin@mail.ru. ORCID iD: <https://orcid.org/0000-0002-2801-7029>.

Ilya G. Samusev, PhD in Physics and Mathematics, head of the Research & Education Centre “Fundamental and Applied Photonics. Nanophotonics”, Institute of Physical and Mathematical Sciences and Information Technologies, Immanuel Kant Baltic Federal University, Kaliningrad, Russian Federation; e-mail: is.cranz@gmail.com. ORCID iD: <https://orcid.org/0000-0001-5026-7510>.

Valeriy V. Bryukhanov, DSc in Physics and Mathematics, leading research fellow at the Research & Education Centre “Fundamental and Applied Photonics. Nanophotonics”, Institute of Physical and Mathematical Sciences and Information Technologies, Immanuel Kant Baltic Federal University, Kaliningrad, Russian Federation; e-mail: bryukhanov_v.v@mail.ru. ORCID iD: <https://orcid.org/0000-0003-4689-7207>.

Received 20.11.2020; Approved after reviewing 29.03.2021; Accepted 15.05.2021; Published online 25.06.2021.

*Translated by Anastasiia Ananeva
Edited and proofread by Simon Cox*



Condensed Matter and Interphases

Kondensirovannye Sredy i Mezhfaznye Granitsy
<https://journals.vsu.ru/kcmf/>

Original articles

Research article

<https://doi.org/10.17308/kcmf.2021.23/3438>

Thermodynamic study of manganese tellurides by the electromotive force method

E. N. Orujlu¹✉, Z. S. Aliev², Y. I. Jafarov³, E. I. Ahmadov³, M. B. Babanly^{1,3}

¹Institute of Catalysis and Inorganic Chemistry, Azerbaijan National Academy of Sciences, 113 H. Javid ave., Baku AZ-1143, Azerbaijan

²Azerbaijan State Oil and Industry University, 6/21 Azadlq ave., Baku AZ-1010, Azerbaijan

³Baku State University, 23 Z. Khalilov Street, Baku Az-1148 Azerbaijan

Abstract

The thermodynamic properties of manganese tellurides were determined using an electromotive force (EMF) method with a liquid electrolyte in a temperature range from 300 to 450 K. EMF measurements were performed using equilibrium samples taken from the two-phase regions, namely $\text{MnTe}_2 + \text{Te}$ and $\text{MnTe} + \text{MnTe}_2$, of the Mn–Te system. The phase compositions of all samples were controlled with the X-ray diffraction (XRD) method. The partial molar functions of manganese in alloys, as well as the standard thermodynamic functions of the formation and standard entropies of MnTe and MnTe_2 , were calculated. A comparative analysis of obtained results with literature data is performed.

Keywords: Electromotive force method, Thermodynamic properties, Manganese tellurides, MnTe , MnTe_2 , Partial molar functions

Acknowledgements: the work has been carried out within the framework of the international joint research laboratory “Advanced Materials for Spintronics and Quantum Computing” (AMSQC) established between the Institute of Catalysis and Inorganic Chemistry of ANAS (Azerbaijan) and Donostia International Physics Center (Basque Country, Spain) and partially supported by the Science Development Foundation under the President of the Republic of Azerbaijan – Grant № EIF-GAT-5-2020-3(37)-12/02/4-M-02.

For citation: Orujlu E. N., Aliev Z. S., Jafarov Y. I., Ahmadov E. I., Babanly M. B. Thermodynamic study of manganese tellurides by the electromotive force method. *Kondensirovannye sredy i mezhfaznye granitsy = Condensed Matter and Interphases*. 2021;23(2): 273–281. <https://doi.org/10.17308/kcmf.2021.23/3438>

Для цитирования: Оруджлу Э. Н., Алиев З. С., Джафаров Я. И., Ахмедов Э. И., Бабанлы М. Б. Термодинамическое исследование теллуридов марганца методом электродвижущих сил. *Конденсированные среды и межфазные границы*. 2021;23(2): 273–281. <https://doi.org/10.17308/kcmf.2021.23/3438>

✉ Elnur N. Orujlu, e-mail: elnur.oruclu@yahoo.com

© E. N. Orujlu, Z. S. Aliev, Y. I. Jafarov, E. I. Ahmadov, M. B. Babanly, 2021



The content is available under Creative Commons Attribution 4.0 License.

1. Introduction

Transition metal chalcogenides are considered promising candidates for spintronics, optoelectronics, and energy storage applications due to their unusual physical and chemical properties [1–4]. Among them, manganese tellurides are particularly interesting materials that provide a unique connection between semiconductivity and magnetism [5–7]. Recent studies show that ternary layered phases based on manganese telluride have the potential to combine two seemingly incompatible properties, topological insulation and magnetism, at the same time [8–12]. The first antiferromagnetic topological insulator [14] – MnBi_2Te_4 consists of a repetition of septuple blocks where magnetic MnTe bilayers are inserted into the quintuple Bi_2Te_3 layers periodically [15].

The knowledge of phase equilibria and reliable thermodynamic data of corresponding systems are crucially important for synthesizing novel complex phases and the development of modern sample-preparation techniques [16, 17].

Phase equilibria of the Mn-Te binary system have been investigated several times [18–20]. There exist two binary compounds of this type, namely MnTe and MnTe_2 . Both compounds are formed by a peritectic reaction at 1424 and 1008 K, respectively. MnTe is a p-type semiconductor and crystallizes the “NiAs” type crystal structure, while MnTe_2 has a pyrite cubic crystal structure at low temperatures. MnTe undergoes several phase transformations from the low-temperature hexagonal phase to the high-temperature cubic phase [20].

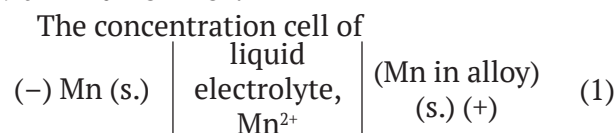
An analysis of the literature shows that the first studies on the thermodynamic properties of manganese tellurides began in the late 19th century, and data obtained from both experimentally determined (calorimetry, vapor measurements, EMF) and model-calculated values have been collected in modern handbooks and electronic databases [21–31]. It should be noted that all previous studies, including those conducted by EMF, were performed in high-temperature ranges. An analysis of these works shows that the values of standard integral thermodynamic functions calculated from high-temperature measurements are significantly different from each other. Therefore,

in order to obtain a more reliable set of standard thermodynamic functions, it is advisable to use experimental data obtained under conditions as close as possible to the standard.

Considering the above, the purpose of this work is a thermodynamic study of the Mn-Te system by EMF method with a liquid electrolyte in the temperature range from 300 to 450 K.

2. Experimental

To study the thermodynamic properties of the manganese-tellurium system, several compositions having 52, 60, 70, and 80 at% Te were synthesized from high purity (99.9999 % pure, Alfa Aesar and Sigma-Aldrich) elemental components in evacuated (10^{-2} Pa residual pressure) quartz tubes at 1300 K for 5 h. Glassy carbon crucibles were used to synthesize all samples to prevent the manganese reacting with quartz. All samples were subjected to annealing at 600 K for 240 h to reach an equilibrium state. The phase composition of the alloys was identified by means of differential thermal analysis (DTA) and powder X-ray diffraction (PXRD). DTA of the annealed alloys was carried out using the LINSEIS HDSC PT1600 system with a heating rate of 10 K/min. The temperature accuracy was better than 2 K. PXRD data collection was performed at room temperature on a Bruker D2 PHASER diffractometer using CuK_α radiation within $2\theta = 5^\circ\text{--}75^\circ$.



type was assembled for EMF measurements in the 300–450 K temperature interval.

A glycerol solution of KCl with the addition of 0.1 % MnCl_2 was used as an electrolyte. Glycerol electrolytes are successfully used for the low-temperature thermodynamic analysis of chalcogenide systems [32, 33]. In order to avoid having moisture and oxygen in the electrolyte, the glycerol was thoroughly dried and degassed under vacuum at ~450 K and anhydrous chemically pure KCl and MnCl_2 salts were used.

In a cell of type (1), metal manganese was used as a negative electrode, while the positive electrode was an annealed alloy of the Mn-Te system. The phase compositions of all the

indicated alloys and correspondence to the phase diagram were confirmed by the PXRD method. As an example, Fig. 1 shows powder diffraction patterns of two selected alloys from these regions. Both electrodes were prepared by pressing the piece of manganese and powdered alloys of the Mn-Te system on a molybdenum wire in the form of pellets weighing 0.5 g.

The electrochemical cell was constructed similar to that in [32,33], which allows measuring the EMF values of several electrodes relative to a reference electrode.

EMF measurements were performed using a Keithley 2100 6 1/2 Digit Multimeter. The first EMF equilibrium values were recorded after keeping the cell at ~360 K for 20–40 h. Values were thereafter obtained every 3–4 h after establishing the desired temperature. The system

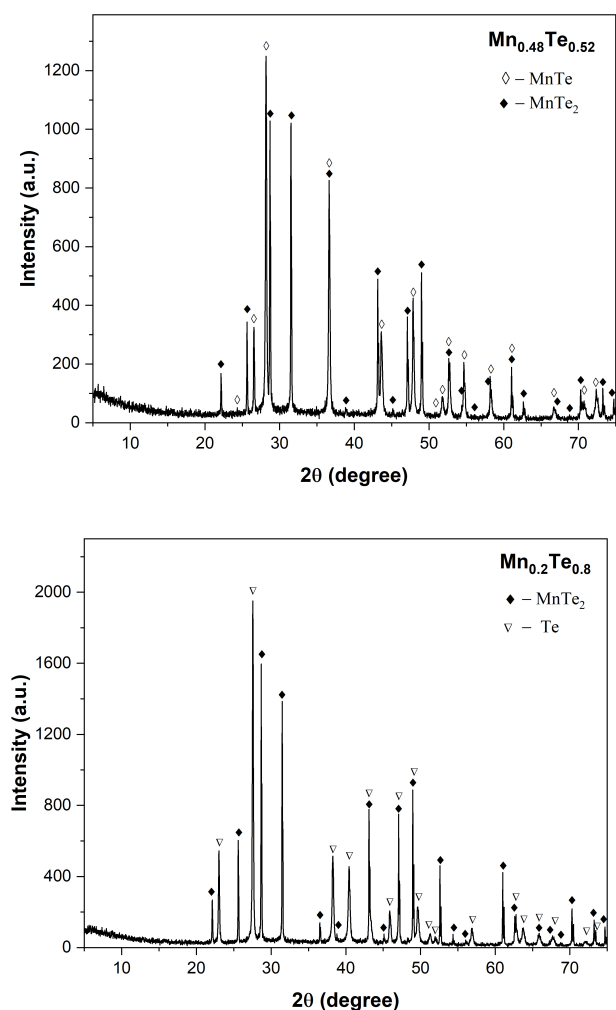


Fig. 1. PXRD patterns of the alloys from two-phase regions of the Mn-Te system

was considered to achieve an equilibrium state when the EMF values varied by less than 0.5 mV.

3. Results and discussion

The results of the EMF measurements of the concentration cell of type (1) confirms the existence of two-phase regions, namely MnTe+MnTe₂ and MnTe₂+Te in the Mn-Te system. The EMF isopleths at 400 K show that the EMF results in each two-phase region remain constant and change dramatically at the border (Fig. 2).

The temperature dependences of the EMF of type (1) cells for two-phase alloys are shown in Fig. 3. As can be seen, the EMF values increase linearly with increasing temperature. The linear relationship between EMF and temperature made it possible to consider the EMF measurement results using the least-squares method via computer software. Experimentally obtained data for temperature (T_i), EMF (E_i) and data associated with the calculation steps for both MnTe + MnTe₂ and MnTe₂ + Te phase regions of the Mn-Te system are listed in Tables 1 and 2.

We used the method of processing the results of the EMF measurements described in [34, 35]. The obtained linear equation of the type (2) are listed in Table 3 in the literature recommended form:

$$E = a + bT \pm t \left[\left(S_E^2 / n \right) + S_b^2 \cdot (T - \bar{T})^2 \right]^{1/2} \quad (2)$$

Here n is the number of pairs of E and T values; S_E and S_b – are dispersions of individual measurements of EMF and constant b ; \bar{T} – the average absolute temperature; t – the Student's t -test. At the confidence level of 95 %

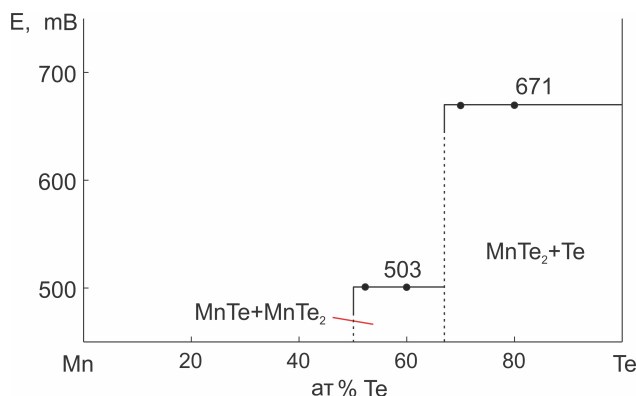


Fig. 2. The composition dependences of the EMF of type (1) cells at 400 K

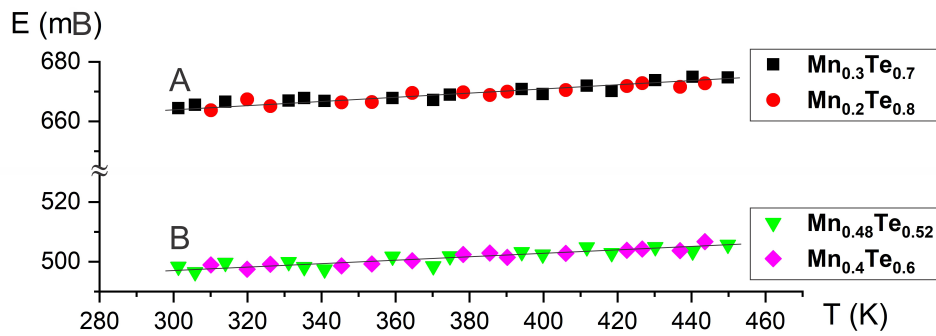


Fig. 3. The temperature dependences of EMF of the concentration cells type (1) for MnTe₂+Te (A) and MnTe+MnTe₂ (B) phase regions of the Mn-Te system

Table 1. Experimentally obtained data for the temperature (T_p), EMF (E_i) and data associated with the calculation steps for the MnTe₂+Te phase region of the Mn-Te system

T_p , K	E_i , mV	$T_i - \bar{T}$	$E_i(T_i - \bar{T})$	$(T_i - \bar{T})^2$	\bar{E}	$E_i - \bar{E}$	$(E_i - \bar{E})^2$
301.3	664.41	-74.90	-49766.52	5610.51	664.53	-0.12	0.01
305.8	665.53	-70.40	-46855.53	4956.63	664.80	0.73	0.53
310.1	663.72	-66.10	-43874.10	4369.65	665.07	-1.35	1.82
314	666.54	-62.20	-41461.01	3869.25	665.31	1.23	1.52
319.9	667.36	-56.30	-37574.59	3170.07	665.67	1.69	2.86
326.2	665.13	-50.00	-33258.72	2500.33	666.06	-0.93	0.86
331.1	666.91	-45.10	-30079.86	2034.31	666.36	0.55	0.31
335.3	667.81	-40.90	-27315.66	1673.08	666.62	1.19	1.43
340.8	666.82	-35.40	-23607.65	1253.40	666.95	-0.13	0.02
345.4	666.35	-30.80	-20525.80	948.85	667.24	-0.89	0.79
353.6	666.46	-22.60	-15064.22	510.91	667.74	-1.28	1.64
359.2	667.82	-17.00	-11355.17	289.11	668.08	-0.26	0.07
364.5	669.54	-11.70	-7835.85	136.97	668.41	1.13	1.28
370.2	667.13	-6.00	-4005.00	36.04	668.76	-1.63	2.66
374.7	668.91	-1.50	-1005.59	2.26	669.04	-0.13	0.02
378.3	669.74	2.10	1404.22	4.40	669.26	0.48	0.23
385.5	668.82	9.30	6217.80	86.43	669.70	-0.88	0.77
390.2	669.92	14.00	9376.65	195.91	669.99	-0.07	0.00
394.1	670.82	17.90	12005.44	320.29	670.23	0.59	0.35
399.8	669.16	23.60	15789.95	556.80	670.58	-1.42	2.01
406	670.51	29.80	19978.96	887.84	670.96	-0.45	0.20
411.7	671.92	35.50	23850.92	1260.01	671.31	0.61	0.37
418.4	670.14	42.20	28277.67	1780.56	671.72	-1.58	2.50
422.5	671.81	46.30	31102.56	2143.38	671.97	-0.16	0.03
426.7	672.82	50.50	33975.17	2549.91	672.23	0.59	0.35
430.2	673.83	54.00	36384.57	2915.64	672.45	1.38	1.91
436.9	671.54	60.70	40760.24	3684.09	672.86	-1.32	1.74
440.3	674.92	64.10	43260.12	4108.38	673.07	1.85	3.43
443.6	672.73	67.40	45339.76	4542.31	673.27	-0.54	0.29
449.8	674.75	73.60	49659.35	5416.47	673.65	1.10	1.21
$\bar{T} = 376.2$	$\bar{E} = 669.129$		$\Sigma = 3798.11$	$\Sigma = 61813.79$			$\Sigma = 31.2$

Table 2. Experimentally obtained data for the temperature (T_i), EMF (E_i) and data associated with the calculation steps for the MnTe+MnTe₂ phase region of the Mn–Te system

T_i , K	E_i , mV	$T_i - \bar{T}$	$E_i(T_i - \bar{T})$	$(T_i - \bar{T})^2$	\bar{E}	$E_i - \bar{E}$	$(E_i - \bar{E})^2$
301.3	498.36	-74.90	-37328.83	5610.51	497.29	1.07	1.14
305.8	496.52	-70.40	-34956.66	4956.63	497.54	-1.02	1.04
310.1	498.91	-66.10	-32979.61	4369.65	497.77	1.14	1.29
314	499.62	-62.20	-31078.03	3869.25	497.99	1.63	2.67
319.9	497.45	-56.30	-28008.09	3170.07	498.31	-0.86	0.74
326.2	499.16	-50.00	-24959.66	2500.33	498.65	0.51	0.26
331.1	499.91	-45.10	-22547.61	2034.31	498.92	0.99	0.98
335.3	498.23	-40.90	-20379.27	1673.08	499.15	-0.92	0.84
340.8	497.42	-35.40	-17610.33	1253.40	499.45	-2.03	4.11
345.4	498.61	-30.80	-15358.85	948.85	499.70	-1.09	1.19
353.6	499.24	-22.60	-11284.49	510.91	500.15	-0.91	0.82
359.2	501.72	-17.00	-8530.91	289.11	500.45	1.27	1.61
364.5	500.33	-11.70	-5855.53	136.97	500.74	-0.41	0.17
370.2	498.52	-6.00	-2992.78	36.04	501.05	-2.53	6.41
374.7	501.81	-1.50	-754.39	2.26	501.30	0.51	0.26
378.3	502.44	2.10	1053.45	4.40	501.49	0.95	0.90
385.5	502.91	9.30	4675.39	86.43	501.89	1.02	1.05
390.2	501.43	14.00	7018.35	195.91	502.14	-0.71	0.51
394.1	503.22	17.90	9005.96	320.29	502.35	0.87	0.75
399.8	502.43	23.60	11855.67	556.80	502.67	-0.24	0.06
406	502.81	29.80	14982.06	887.84	503.00	-0.19	0.04
411.7	504.82	35.50	17919.43	1260.01	503.31	1.51	2.27
418.4	502.91	42.20	21221.13	1780.56	503.68	-0.77	0.59
422.5	503.83	46.30	23325.65	2143.38	503.90	-0.07	0.01
426.7	504.24	50.50	25462.44	2549.91	504.13	0.11	0.01
430.2	504.91	54.00	27263.46	2915.64	504.32	0.59	0.34
436.9	503.73	60.70	30574.73	3684.09	504.69	-0.96	0.92
440.3	503.44	64.10	32268.83	4108.38	504.87	-1.43	2.06
443.6	506.72	67.40	34151.24	4542.31	505.05	1.67	2.77
449.8	505.71	73.60	37218.57	5416.47	505.39	0.32	0.10
$\bar{T} = 376.2$	$\bar{E} = 501.38$		$\sum = 3371.31$	$\sum = 61813.79$			$\sum = 35.89$

Table 3. Temperature dependences of the EMF for the cell of type (1) for alloys of the Mn–Te in the temperature range of 300–450 K

Phase area	$E, \text{mV} = a + bT + t \cdot \tilde{S}_E(T)$
MnTe ₂ +Te	$646.03 + 0.0614T \pm 2 \left[\frac{1.04}{30} + 1.7 \cdot 10^{-5} (T - 376.2)^2 \right]^{1/2}$
MnTe+MnTe ₂	$480.86 + 0.0546T \pm 2 \left[\frac{1.2}{30} + 1.9 \cdot 10^{-5} (T - 376.2)^2 \right]^{1/2}$

and $n = 30$, the Student's t-test ≤ 2 . Using the obtained equations of type (2) and the following thermodynamic expressions:

$$\Delta\bar{G}_{\text{Mn}} = -zFE \quad (3)$$

$$\Delta\bar{H}_{\text{Mn}} = -z \left[E - T \left(\frac{\partial E}{\partial T} \right)_P \right] = -zFa \quad (4)$$

$$\Delta\bar{S}_{\text{Mn}} = -zF \left(\frac{\partial E}{\partial T} \right)_P = zFb \quad (5)$$

the partial molar functions of manganese in the alloys at 298 K were calculated. The results are given in Table 4.

According to the phase diagram of the Mn-Te system, the values of the partial molar functions can be considered thermodynamic functions of the following virtual cell reactions (all substances are solid) [34, 35]:



According to the (6) and (7) reaction equations, the standard thermodynamic functions of formation for both MnTe and MnTe₂ compounds are calculated using the following expressions:

$$\Delta_f Z_{\text{MnTe}_2}^\circ = \Delta\bar{Z}_{\text{Mn}} \quad (8)$$

$$\Delta_f Z_{\text{MnTe}}^\circ = 0.5\Delta\bar{Z}_{\text{Mn}} + 0.5\Delta_f Z_{\text{MnTe}_2}^\circ \quad (9)$$

where $\Delta Z = \Delta G$ or ΔH . The standard entropy was calculated as:

$$S_{\text{MnTe}_2}^\circ = \Delta\bar{S}_{\text{Mn}} + S_{\text{Mn}}^\circ + 2S_{\text{Te}}^\circ \quad (10)$$

$$S_{\text{MnTe}}^\circ = 0.5\Delta\bar{S}_{\text{Mn}} + 0.5S_{\text{Mn}}^\circ + 0.5S_{\text{MnTe}_2}^\circ \quad (11)$$

In the calculations, the values of standard entropies of manganese (32.01 ± 0.13 J/(mol·K)) and tellurium (49.50 ± 0.21 J/(mol·K)) were taken from [25]. The errors were calculated by the error accumulation method. Available literature data and calculated values of the present work are summarized in Tables 5 and 6.

As can be seen from Tables 4 and 5, the values of standard Gibbs free energies of the formation of both MnTe and MnTe₂ compounds obtained by EMF measurements under standard conditions was determined with high accuracy. Our results show a good agreement with the results of high-temperature EMF (580–823 K) [21,22] studies and the combination of EMF with the DSC method [21]. These data are also well matched with the values of $\Delta_f G^\circ$ of both compounds given in the databases [23–26].

A comparison of our results for $\Delta_f H^\circ$ with all available literature data shows that the results calculated for the MnTe compound are in good agreement, except the old calorimetric data of Fabre [29]. For the MnTe₂ compound, our results are very close to the data obtained by a combination of EMF with DSC methods [21] and values recommended in databases [23–26]. At the same time, the values of the enthalpy of formation calculated by high-temperature EMF

Table 4. Relative partial thermodynamic functions of manganese in the alloys of the Mn-Te system (298 K)

Phase area	$-\Delta\bar{G}_{\text{Mn}}$	$-\Delta\bar{H}_{\text{Mn}}$	$-\Delta\bar{S}_{\text{Mn}}$, J/(mol·K)
	kJ/mol		
MnTe ₂ +Te	128.20±0.07	124.67±0.30	11.86±0.79
MnTe+MnTe ₂	95.95±0.08	92.79±0.32	10.54±0.85

Table 5. Standard thermodynamic functions of MnTe₂

$-\Delta_f G^\circ$	$-\Delta_f H^\circ$	$\Delta_f S^\circ$	S°	Ref., Methods
kJ/mol		J/(mol·K)		
128.2±0.1	124.7±0.3	11.9±0.8	142.9±1.4	This work, EMF, 300-450 K
127.6±0.6	131.2±1.2	-12.1±4.2		[21], EMF, 594-723 K
127.5±0.6	125.4±1.8	7.8±5.1		[21], EMF with DSC, 298-723 K
124.3±1.0	119.4±1.8	16.5±3.3		[22], EMF, 723-823 K
129.7	125.5±4.2		145	[23,24], recommend.
127.6	123.4±3.5		145.0±0.4	[25,26], recommend.
	120.5	10.7		[27], modeling
			145.0	[28], DSC

Table 6. Standard thermodynamic functions of MnTe

$-\Delta_f G^\circ$	$-\Delta_f H^\circ$	$\Delta_f S^\circ$	S°	Ref., Methods
kJ/mol		J/(mol·K)		
112.1±0.1	108.7±0.3	11.3±0.8	92.8±1.2	This work, EMF, 300–450 K
112.3±0.2	107.9±1.2	14.7±3.2		[21], EMF, 583–750 K
111.2±0.4	106.6±1.4	16.0±3.4		[21], EMF with DSC, 298–750 K
112.5±0.8	107.1±1.4	18.2±3.6		[22], EMF, 723–823 K
	94.2			[29], Calorimetry
	111.3±5.4			[30], Calorimetry
	109.6±8.0			[31], Vapor measur.
112.1	108.4±2.9		94.0±1.7	[25], recommend.
112.0	108.4		93.7	[23, 24], recommend.
	109.2±3.8		93.7±1.7	[26], recommend.
	107.0	15.1		[27], modeling

measurements are significantly different from each other and our results. These discrepancies are especially clearly reflected in the values of $\Delta_f S^\circ$ obtained in [21, 22, 27].

In summary, we note that our results on the standard entropies of both compounds are in good agreement with the literature data.

4. Conclusions

In the present paper, we report the results of a thermodynamic study of the Mn-Te system using the EMF method with a glycerol electrolyte in a temperature range from 300 to 450 K. According to the EMF measurements, the partial molar functions of manganese in two-phase regions, MnTe+MnTe₂ and MnTe₂+Te at 298 K, as well as the standard thermodynamic functions of the formation and standard entropies of MnTe and MnTe₂, were calculated. The new mutually consistent values of thermodynamic functions presented by us are the first experimental data obtained from EMF measurements under standard conditions. They supplement and clarify the previously obtained thermodynamic data for manganese tellurides.

Authors' Contributions

Orujlu E. N. – conducting experiments, processing data, writing text, final conclusions. Aliev Z. S. – X-ray diffraction analysis, discussion of results. Jafarov Y. I. – interpretation of the results. Ahmadov E. I. – review writing and text editing. Babanly M. B. – scientific supervision of research, concept of research, development of methodology.

Conflict of interests

The authors declare that they have no known competing financial interests or personal relationships that could have influenced the work reported in this paper.

References

- Kau A. B., Two-dimensional layered materials: structure, properties, and prospects for device applications. *Journal of Materials Research*. 2014;29(3): 348–361. <https://doi.org/10.1557/jmr.2014.6>
- Tedstone A. A., Lewis D. J., O'Brien P., Synthesis, properties, and applications of transition metal-doped layered transition metal dichalcogenides. *Chemistry of Materials*. 2016;28: 1965–1974. <https://doi.org/10.1021/acs.chemmater.6b00430>
- Ali Z., Zhang T., Asif M., Zhao L., Hou Y., Transition metal chalcogenide anodes for sodium storage. *Materials Today*. 2020;35: 131–167. <https://doi.org/10.1016/j.mattod.2019.11.008>
- Shang C., Fu L., Zhou S., Zhao J. Atomic Wires of transition metal chalcogenides: A family of 1D materials for flexible electronics and spintronics. *Journal of the American Chemical Society* AU. 2021;1(2): 147–155. <https://doi.org/10.1021/jacsau.0c00049>
- Xu Y., Li W., Wang C., Chen Z., Wu Y., Zhang X., Li J., Lin S., Chen Y., Pei Y. MnTe₂ as a novel promising thermoelectric material, *Journal of Materiomics*. 2018;4(3): 215–220. <https://doi.org/10.1016/j.jmat.2018.04.001>
- Sreeram P. R., Ganesan V., Thomas S., Anantharaman M. R. Enhanced thermoelectric performance of nanostructured manganese telluride via antimony doping. *Journal of Alloys and Compounds*. 2020;836: 155374. <https://doi.org/10.1016/j.jallcom.2020.155374>
- Basit A., Yang J., Jiang Q., Zhou Z., Xin J., Li X., Li S. Effect of Sn doping on thermoelectric properties

- of p-type manganese telluride. *Journal of Alloys and Compounds*. 2019;777: 968–973. <https://doi.org/10.1016/j.jallcom.2018.11.066>
8. Mong R. S. K., Moore J. E., Magnetic and topological order united in a crystal. *Nature*. 2019;576: 390–392. <https://doi.org/10.1038/d41586-019-03831-7>
9. Tokura Y., Yasuda K., Tsukazaki A. Magnetic topological insulators. *Nature Reviews Physics*. 2019;1: 126–143. <https://doi.org/10.1038/s42254-018-0011-5>
10. Wu J., Liu F., Sasase M., Ienaga K., Obata Y., Yukawa R., Horiba K. Natural van der Waals heterostructural single crystals with both magnetic and topological properties. *Science Advances*. 2019;5(11): eaax9989. <https://doi.org/10.1126/sciadv.aax9989>
11. Estyunin D. A., Klimovskikh I. I., Shikin A. M., Schwier E. F., Otrokov M. M., Kimura A., Kumar S., Filnov S. O., Aliev Z. S., Babanly M. B., Chulkov E. V. Signatures of temperature driven antiferromagnetic transition in the electronic structure of topological insulator MnBi_2Te_4 . *APL Materials*. 2020;8: 021105(1-7). <https://doi.org/10.1063/1.5142846>
12. Klimovskikh I. I., Otrokov M. M., Estyunin D., Ereemeev S. V., Filnov S. O., Koroleva A., Shevchenko E., Voroshnin V., Rybkin A. G., Rusinov I. P., Blanco-Rey M., Hoffmann M., Aliev Z. S., Babanly M. B., Amiraslanov I. R., Abdullayev N. A., Zverev V. N., Kimura A., Tereshchenko O. E., Kokh K. A., Petaccia L., Santo G. D., Ernst A., Echenique P. M., Mamedov N. T., Shikin A. M., Chulkov E. V. Tunable 3D/2D magnetism in the $(\text{MnBi}_2\text{Te}_4)(\text{Bi}_2\text{Te}_3)_m$ topological insulators family. *npj Quantum Materials*. 2020;5(1): 1–9. <https://doi.org/10.1038/s41535-020-00255-9>
13. Shikin A. M., Estyunin D. A., Klimovskikh I. I., Filnov S. O., Schwier E. F., Kumar S., Miyamoto K., Okuda T., Kimura A., Kuroda K., Yaji K., Shin S., Takeda Y., Saitoh Y., Aliev Z. S., Mamedov N. T., Amiraslanov I. R., Babanly M. B., Otrokov M. M., Ereemeev S. V., Chulkov E. V. Dirac gap modulation and surface magnetic interaction in axion antiferromagnetic topological insulator MnBi_2Te_4 . *Scientific Reports*. 2020;10: 13226. <https://doi.org/10.1038/s41598-020-70089-9>
14. Otrokov M. M., Klimovskikh I. I., Bentmann H., Estyunin D., Zeugner A., Aliev Z. S., Gafß S., Wolter A. U. B., Koroleva A. V., Shikin A. M., Blanco-Rey M., Hoffmann M., Rusinov I. P., Vyazovskaya A. Y., Ereemeev S. V., Koroteev Y. M., Kuznetsov V. M., Freyse F., Sánchez-Barriga J., Amiraslanov I. R., Babanly M. B., Mamedov N. T., Abdullayev N. A., Zverev V. N., Alfonsov A., Kataev V., Büchner B., Schwier E. F., Kumar S., Kimura A., Petaccia L., Di Santo G., Vidal R. C., Schatz S., Kießner K., Ünzelmann M., Min C. H., Moser S., Peixoto T. R. F., Reinert F., Ernst A., Echenique P. M., Isaeva A., Chulkov E. V. Prediction and observation of an antiferromagnetic topological insulator. *Nature*. 2019;576: 416–422. <https://doi.org/10.1038/s41586-019-1840-9>
15. Aliev Z. S., Amiraslanov I. R., Nasonova D. I., Shevelkov A. V., Abdullayev N. A., Jahangirli Z. A., Orujlu E. N., Otrokov M. M., Mamedov N. T., Babanly M. B., Chulkov E. V. Novel ternary layered manganese bismuth tellurides of the $\text{MnTe-Bi}_2\text{Te}_3$ system: Synthesis and crystal structure. *Journal of Alloys and Compounds*. 2019;789: 443–450. <https://doi.org/10.1016/j.jallcom.2019.03.030>
16. Babanly M. B., Chulkov E. V., Aliev Z. S., Shevelkov A. V., Amiraslanov I. R. Phase diagrams in materials science of topological insulators based on metal chalcogenides. *Russian Journal of Inorganic Chemistry*. 2017;62: 1703–1729. <https://doi.org/10.1134/S0036023617130034>
17. Babanly M. B., Mashadiyeva L. F., Babanly D. M., Imamaliyeva S. Z., Tagiev D. B., Yusibov Y. A. Some issues of complex studies of phase equilibria and thermodynamic properties in ternary chalcogenide systems involving Emf measurements (Review). *Russian Journal of Inorganic Chemistry*. 2019;64: 1649–1671. <https://doi.org/10.1134/S0036023619130035>
18. Abrikosov N. Kh., Dyul'dina K. A., Zhdanova V. V. Study of the Mn-Te System. *Izvestiya Akademii nauk SSSR, seriya Neorganicheskiye Materialy*. 1967;4: 1878–1884. (in Russ.)
19. Vanyarkho V. G., Zlomanov V. P., Novoselova A. V. Physicochemical study of manganese telluride. *Izvestiya Akademii nauk SSSR, seriya Neorganicheskiye Materialy*. 1969;6: 1257–1259. (in Russ.)
20. Schlesinger M. E. The Mn-Te (manganese-tellurium) system. *Journal of Phase Equilibria*. 1998;19(6): 591–596. <https://doi.org/10.1361/105497198770341806>
21. Vassilie V., Bykov M., Gambino M., Bros J. P. Thermodynamic investigation of the manganese-tellurium system. *Journal de Chimie Physique et de Physico-Chimie Biologique*. 1993;90(2): 463–476. <https://doi.org/10.1051/jcp/1993900463>
22. Loukachenko G., Polotskaya R. I., Dul'dina K. A., Abrikosov N. Kh. Thermodynamic properties of manganese-tellurium compounds. *Izvestiya Akademii nauk SSSR, seriya Neorganicheskiye Materialy*. 1971;7(5): 860–861. (In Russ.)
23. Barin I. *Thermochemical Data of Pure Substances*, Third Edition, VCH, 2008. 1936 p.
24. Mills K. C. *Thermodynamic data for inorganic sulphides, selenides and tellurides*, London, Butterworths; 1974. 845 p.
25. Iorish V. S., Yungman V. S. *Database of thermal constants of substances*. 2006. Available at: <http://www.chem.msu.ru/cgi-bin/tkv.pl>
26. Kubaschewski O., Alcock C. B., Spencer P. J. *Materials Thermochemistry*, Oxford: Pergamon Press Ltd; 1993. 363 p.

27. Chevalier P. Y., Fischer E., Marbeuf A. A thermodynamic evaluation of the Mn-Te binary system. *Thermochimica Acta*. 1993;223: 51–63. [https://doi.org/10.1016/0040-6031\(93\)80119-U](https://doi.org/10.1016/0040-6031(93)80119-U)

28. Westrum E. F., Gronvold F., Manganese disulfide (hauerite) and manganese ditelluride. Thermal properties from 5 to 350°K and antiferromagnetic transitions. *The Journal of Chemical Physics*. 1970;52: 3820–3826. <https://doi.org/10.1063/1.1673563>

29. Fabre C. Thermal studies on the selenides. *Annales de chimie et de physique*. 1887;10: 472–550. (in French)

30. Morozova M. P., Stolyarova T. A. Formation enthalpy of manganese selenides and tellurides. *Vestnik Leningradskogo Universiteta, Seriya Fiziki i Khimii*. 1964;19(16): 150–153. (in Russ.)

31. Wiedemeier H., Sadeek H. Knudsen measurements of the sublimation of manganese (II) telluride. *High Temperature Science*. 1970;2: 252–258.

32. Imamaliyeva S. Z., Musayeva S. S., Babanly D. M., Jafarov Y. I., Tagiyev D. B., Babanly M. B. Determination of the thermodynamic functions of bismuth chalcogenides by EMF method with morpholinium formate as electrolyte. *Thermochimica Acta*. 2019;679: 178319(1-7). <https://doi.org/10.1016/j.tca.2019.178319>

33. Mashadiyeva L. F., Mansimova S. G., Babanly K. N., Yusibov Y. A., Babanly M. B. Thermodynamic properties of solid solutions in the PbSe–AgSbSe₂ system. *Russian Chemical Bulletin*. 2020;69: 660–664. <https://doi.org/10.1007/s11172-020-2814-7>

34. Morachevsky A. G., Voronin G. F., Geyderich V. A., Kutsenok I. B. *Elektrokhimicheskie metody issledovaniya v termodinamike metallicheskih system*. [Electrochemical methods of investigation in thermodynamics of

metal systems]. Moscow: Akademkniga Publ.; 2003. 334 p. Available at: <https://elibrary.ru/item.asp?id=19603291> (In Russ.)

35. Babanly M. B., Yusibov Y. A. *Elektrokhimicheskie metody v termodinamike neorganicheskikh sistem* [Electrochemical methods in thermodynamics of inorganic systems]. Baku: BSU Publ.; 2011. 306 p.

Information about the authors

Elnur N. Orujlu, PhD student, Junior Researcher at the Institute of Catalysis and Inorganic Chemistry, Azerbaijan National Academy of Sciences, Baku, Azerbaijan; e-mail: elnur.oruclu@yahoo.com. ORCID iD: <https://orcid.org/0000-0001-8955-7910>.

Ziya S. Aliev, PhD in Chemistry, Assistance Professor, Azerbaijan State Oil and Industry University, Baku, Azerbaijan; e-mail: ziyasaliev@gmail.com. ORCID iD: <https://orcid.org/0000-0001-5724-4637>.

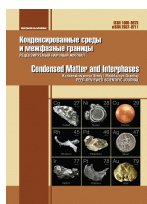
Yasin I. Jafarov, DSc in Chemistry, Associate Professor, Baku State University, Baku, Azerbaijan; e-mail: yasin.cafarov@hotmail.com. ORCID iD: <https://orcid.org/0000-0002-6597-2252>

Eldar I. Ahmadov, DSc in Chemistry, Professor, Baku State University, Baku, Azerbaijan; e-mail: eldar_akhmedov@mail.ru.

Mahammad B. Babanly, Corresponding Member of the Azerbaijan National Academy of Sciences, Deputy-director of the Institute of Catalysis and Inorganic Chemistry, Azerbaijan National Academy of Sciences, Baku State University, Baku, Azerbaijan; e-mail: babanlymb@gmail.com. ORCID iD: <https://orcid.org/0000-0001-5962-3710>.

Received 17 February 2021; Approved after reviewing 12 March 2021; Accepted 15 May 2021; Published online 25 June 2021

Edited and proofread by Simon Cox



Original articles

Research article

<https://doi.org/10.17308/kcmf.2021.23/3478>

Electrophilic-nucleophilic properties as a factor in the formation of antifriction and hydrophobic properties of surface-modified metals with ammonium and organosilicon compounds

A. G. Syrkov✉, V. R. Kabirov, A. P. Pomogaybin, Ngo Quoc Khanh

Saint Petersburg Mining University,
21st line V.O., 1, St. Petersburg 199106, Russian Federation

Abstract

Stabilisation of the functional properties of dispersed and compact metals, as well as the regulation of their reactivity, improvement of water-repellent, antifriction and anti-corrosion properties by creating the protective films on the surface is an urgent problem in relation to obtaining new materials. Previously, research conducted at REC “Nanotechnology” of the St. Petersburg Mining University proved that chemisorption of ethylhydridesiloxane vapours together with surfactants based on quaternary ammonium compounds has a beneficial effect on the water-repellent properties of metals. In order to obtain the physicochemical mechanism of the hydrophobisation of the surface of modified dispersed metals for the first time, the study of the electrophilic-nucleophilic properties of the active substances of the surface modifiers of metals was carried out using the methods of quantum-chemical modelling using HyperChem software package. The dipole moment, energy of the highest occupied and the lowest unoccupied molecular orbitals, electrophilic-nucleophilic properties were determined. The series of enhancement of nucleophilic/electrophilic properties and dipole moment for modifiers were obtained. The donor-acceptor properties, the differences in the characteristics of the molecules of alkamon, triamon, and hydrophobic silicone organic liquid were quantitatively and qualitatively established. The regularities of the formation of hydrophobic and antifriction properties in the composition of industrial oil I-20-surface-modified metal with various electrophilic-nucleophilic properties of the applied substances.

Keywords: Electrophilic-nucleophilic properties, Dispersed metals, Ethylhydridesiloxane oligomer, Quantum-chemical modelling, Hydrophobicity, Antifriction properties

For citation: Syrkov A. G., Kabirov V. R., Pomogaybin A. P., Ngo Kuok Khanh. Electrophilic-nucleophilic properties as a factor in the formation of antifriction and hydrophobic properties of surfaces-modified metals with ammonium and organosilicon compounds. *Kondensirovannye sredy i mezhfaznye granitsy = Condensed Matter and Interphases*. 2021;23(2): 282–290. <https://doi.org/10.17308/kcmf.2021.23/3478>

Для цитирования: Сырков А. Г., Каби́ров В. Р., Помога́йбин А. П., Нго Куок Кхань Электрофильно-нуклеофильные свойства как фактор формирования антифрикционных и гидрофобных свойств материалов, поверхностно-модифицированных аммониевыми и кремнийорганическими соединениями. *Конденсированные среды и межфазные границы*. 2021;23(2): 282–290. <https://doi.org/10.17308/kcmf.2021.23/3478>

✉ Andrey G. Syrkov e-mail: syrkovandrey@mail.ru
© Syrkov A.G., Kabirov V.R., Pomogaybin A.P., Ngo Quoc Khan, 2021



The content is available under Creative Commons Attribution 4.0 License.

1. Introduction

Stabilisation of the functional properties of metals, both dispersed and compact, as well as the regulation of their reactivity, improvement of water-repellent, antifriction and anticorrosion properties by creating the thinnest protective films on the surface is an urgent problem in relation to creating new materials. One of the promising approaches to obtaining these materials is the method developed at the Saint Petersburg Mining University for the layering of molecules of different sizes on metals (RF patent No. 2425910), implemented at a number of enterprises of the mineral resource complex of the Russian Federation and the Republic of Belarus. As part of the research at REC “Nanotechnology” of the St. Petersburg Mining University, it was proved that the chemisorption of the oligomer vapours of ethylhydridesiloxane together with surfactants based on quaternary ammonium compounds (QACs) increases the water-repellent properties of metals, such as, for example, aluminium and copper [1–3]. In this study, dispersed copper powder of the PMS-1 (Cu) grade – GOST 4960-75 was used as a metal-substrate. Interest in copper powder is explained by the potential of practical application as additives to lubricating compositions for various purposes and components of heating elements [4–7].

Modern developments in physical chemistry, chemical technology, dedicated to improving the properties of oils and lubricants, contribute to the solution of the designated problems [8–10]. At the same time, many known additives and fillers are quite expensive and do not always meet the environmental safety requirements. The latest developments of the Saint Petersburg Mining University in the modification of dispersed metal surfaces with organic preparations based on quaternary ammonium compounds allowed achieving a significant antifriction effect when adding appropriate additives to lubricating compositions [4]. The performed studies, including those presented here, allowed not only to substantiate the significant antifriction, anti-corrosion, and water-repellent effects when adding additives to organic matrices of oils, greases, and paints, but also describe the chemical principles of the synthesis of surface-modified metals, including the justification of the reagents

used in the synthesis, based on copper PMS-1. The corresponding technology is, in fact, an energy- and resource-saving synthesis technology, since the layering of ammonium compounds occurs at room temperature, and the amount of the applied modifier was not higher than 1 mass % of the sample. Monolayer application of the substance (5 mg/m²) provides significant savings in material resources [1].

When studying the hydrophobic and antifriction properties of the surface of modified samples based on copper powder PMS-1, interesting effects were revealed when applying organic modifiers (ammonium compounds and ethylhydridesiloxane) in various combinations on the surface of dispersed copper [1, 2]. It was found that Cu/T/A, Cu/A/HSL, Cu/(A+T) samples treated with ethylhydridesiloxane (HSL), triamon (T), and alkamon (A) - preparations based on ammonium quaternary compounds were characterised by a significant increase in the water-repellent properties [1,2]. At the same time, treatment with only one modifier did not enhance the hydrophobicity of the sample surface. It is important to note that according to the literature, the deposition of three or more layers does not lead to a significant hydrophobic and antifriction effect due to the weak interaction of the layers with a solid substrate [1,3].

The purpose of this study was the investigation of antifriction properties of additives based on dispersed copper in the composition of the industrial oil I-20, the analysis of the electrophilic-nucleophilic properties of modifier molecules used for the production of films on dispersed metals, using quantum-chemical modelling methods for further physicochemical substantiation of the antifriction effect in the composition of lubricants and the effect of hydrophobization of the surface of modified dispersed metals.

2. Experimental

Stabilized copper powder, grade PMS-1 (GOST 4960-2009), was used as the initial dispersed metal. A modern approach to the production of thin films on the surface of dispersed and compact metals is the method of layering different-sized molecules of quaternary ammonium compounds used in this study, which

has demonstrated to be a promising method for regulating various surface properties of dispersed metals such as copper, aluminium, nickel, etc. The surface modification of copper powders was carried out in alkamon (GOST 10106-75) and/or triamon (TU 6-14-1059-83) vapours based on QACs, as well as in vapours of a hydrophobic silicon-organic liquid HSL-94 based on ethylhydridesiloxane at room temperature, vapour pressure of 0.7–1.0 MPa [1–4]. The possibility of a synergistic enhancement of the water-repelling properties during the adsorption of QACs and ethylhydridesiloxane molecules on the surface is of particular interest [1]. The composition of triamon (T) - tris- (-oxyethyl) methyl-ammonium-methyl sulphate (TOMAM) – in pairs corresponds to the chemical formula $[(\text{HOC}_2\text{H}_4)_3\text{N}^+\text{CH}_3][\text{CH}_3\text{SO}_3^-]$ with low molecular weight radicals at the nitrogen atom. The composition of the cation of the used alkamon (A) contains a significant C_{17} hydrocarbon radical. The structural formula of the active substance of the used alkamon: $[\text{C}_n\text{H}_{2n+1}\text{OCH}_2\text{N}^+(\text{CH}_3)(\text{C}_2\text{H}_5)_2][\text{CH}_3\text{SO}_4^-]$, where $n = 16$. HSL-94 is hydrophobic silicon-organic liquid based on organohydridesiloxanes; it is an oligomer of polyethylhydridesiloxane [11]. HSL is used as a reagent for the enhancement of the water-repellent properties of textile, leather and paper products, as well as products made of concrete, brick, and other building materials. Usually it is applied from solutions [11]. It is widely used as an industrial surface water repellent in construction. The following samples were studied depending on the sequence and chemisorption mode of QACs and HSL preparation on the surface of the initial copper powder (Cu): Cu/(A+T), Cu/A, Cu/HSL, Cu/T/A, Cu/A/T, Cu/T/HSL, Cu/A/HSL, and Cu/T. A sample of Cu/(A+T) was obtained in a mixture of A and T vapours (1:1), Cu/T/A was obtained by sequential deposition of T and A.

Water-repelling properties (hydrophobicity) were evaluated by the adsorption of water vapour on the surface of the samples by the gravimetric method. The relative pressure of water vapour was about 0.98 ($P_{\text{H}_2\text{O}}/P_s \rightarrow 1$, where P_s is the saturated H_2O vapour pressure). The fact of water vapour adsorption by the samples was additionally monitored by the appearance in the XPS spectra and an increase in the intensity of the

peak with a binding energy of 532.5 ± 0.1 eV, which is characteristic for water adsorbed on the metal.

Quantum-chemical modelling was carried out using the HyperChem software package according to the semiempirical MNDO method. The application method and the fundamental principles of the calculation method are described in the literature [12–16]. Quantum-chemical calculations were based on the solution of the Schrödinger equation [17]. Direct calculation of multielectron atoms and polyatomic systems seems to be a non-trivial task due to the significant amount of required computational time. For this reason, semiempirical (approximate) methods for solving this equation are gaining importance in quantum chemistry [16–18]. According to the degree of approximation, all quantum chemical methods are divided into nonobservational (*ab initio*), semi-empirical, empirical (a group of methods of molecular mechanics) and methods of molecular dynamics [17, 19].

HyperChem is a software product providing opportunities for the quantum mechanical modelling of atomic and molecular structures. It includes programs, implementing the methods of molecular mechanics, quantum chemistry, and molecular dynamics. Force fields of molecular mechanics that can be used in HyperChem are MM+, Amber, OPLS, and BIO+ (based on CHARMM).

To determine the fundamental tribological characteristics: friction force (F_{fr}) and coefficient of friction (f) of tribosystems industrial oil I-20 (GOST 20799-88) with the addition of dispersed surface-modified metal ($M = \text{Cu}, \text{Al}$), a friction machine DM-29M was used. The friction pair of the DM-29M machine was slide bearing (Shaft – steel 45 (GOST 1050) – insert – bronze BrAZh 9-4 (GOST 18175), continuously lubricated with I-20 oil with adsorption-modified metal powders (Cu). The concentration of the additive in the composition of the oil did not exceed 1 wt. %. In addition, the integral index of friction D proportional to the friction force, was monitored by the acoustic emission method using a certified device ARP-11 (pressure $P = 47$ MPa) [3.5] (Table 1).

3. Results and discussion

In this study, the friction force (F_{fr}) and coefficient of friction (f) for tribosystems (copper

Table 1. Comparison of the adsorption of water vapor (a , g/g) on a surface-modified metal (Cu) with the value of the integral friction index D (pressure $P = 47$ MPa) [1]. D for I-20 oil is 1500

Type of powder	but _{H₂O} , g/g	Integral friction index D for industrial oil with powder
Cu/A	0.0299	1300
Cu/T	0.0268	1100
Cu/T/A	0.0260	270
Cu	0.0445	1450
Cu/(A+T)	0.0310	1480

powder-industrial oil I-20) were measured using a DM-29M friction machine for the first time. From the data shown in Fig. 1 and Table 2 it follows that the most significant decrease in the friction force and coefficient of friction in the slide bearing of the DM-29M friction machine lubricated with industrial oil I-20 was provided by copper powder (PMS-1) processed in the mixed mode (Cu/(A+T)) and sequential mode (Cu/T/A) with both modifiers (alkamon and triamon). It is interesting that the Cu/T/A and Cu/(A+T) samples were superior in terms of antifriction properties in the composition of lubricants when compared to the samples modified in A and T pairs and separately. This synergistic effect was manifested both by the assessment of antifriction properties based on the integral friction index D [1] and using the DM-29M friction machine (Table 1). According to data shown in Tables 1 and 2, there is a superiority in the ability to reduce friction of additives of the Cu/T/A type over additives treated with only one modifier, as well as over additives of a similar type Al/(A+T) and Al/T/A

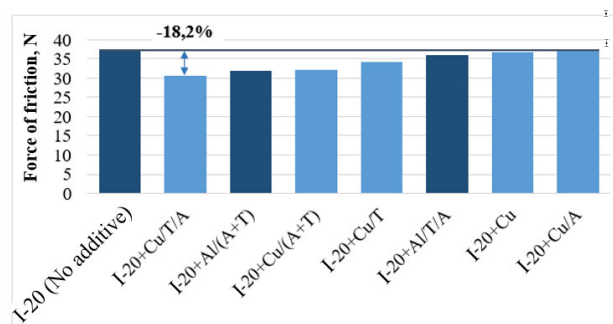


Fig. 1. The force friction in the tribosystem (load 5 kN) containing additives (1 wt%) based on dispersed copper, modified in various modes

based on the dispersed aluminium (PAP-2) that was investigated earlier [1].

According to the developed concepts [1,4], when approaching the “dry friction” mode (load pressure ≥ 40 MPa), the antifriction properties of the tribosystem were largely determined by the properties of the surface of the solid additive. Therefore, the reduction of friction in the system by several times (Table 1) at high pressures is quite understandable taking into account the difference in the surface of the additives in terms of hydrophobicity and adhesion of the applied surfactant film to the metal [3–5]. More modest indicators of the reduction of the friction force and coefficient of friction in the system with similar additives (Fig. 1, Tables 2, 3) were associated with the fact that the measurement of these characteristics using friction machine is technically possible at low pressures (not higher than 17 MPa). The enhancement of the antifriction effect is associated with an increase in the influence of the surface of the solid additive during the transition from the liquid-phase

Table 2. Characteristics of Cu-additives (1 wt%), including the relationship equation $F_{fr} = \mathcal{F}(N)$, change of F_{fr} (ΔF_{fr}) relative to the initial industrial oil the value of the coefficient of friction (f)

No.	Additive	Equation $F_{fr} = \mathcal{F}(N)$	R^2	$\Delta F_{fr}(av.)$, %	$\Delta F_{fr}(N = 5 \text{ kN})$, %	$f(N = 5 \text{ kN})$
1	Al/(A+T) [1]	$y = 0.0370x + 12.47$	0.991	-11.41	-15.92	0.0075
2	Al/T/A [1]	$y = 0.0480x + 10.81$	0.992	-7.75	-3.69	0.0079
3	I-20 (no additive) [1]	$y = 0.0500x + 12.29$	0.994	0	0	0.0089
4	Cu/T/A	$y = 0.0375x + 12.02$	0.995	-13.79	-18.22	0.0063
5	Cu/(A+T)	$y = 0.0393x + 12.43$	0.994	-10.29	-14.39	0.0066
6	Cu/T	$y = 0.0395x + 14.69$	0.997	-9.04	-1.86	0.0072
7	Cu	$y = 0.0412x + 15.09$	0.991	+2.65	-2.17	0.0083
8	Cu/A	$y = 0.0418x + 15.90$	0.985	+6.46	-1.40	0.0091

Table 3. Dependence of the value of the coefficient of friction (f) on the loading pressure in the range of 50-500 kgf on friction machines DM-29M

No.	Additive	f , 50 kgf	f , 100 kgf	f , 150 kgf	f , 250 kgf	f , 500 kgf
1	Al/(A+T)	0.0299	0.0173	0.0125	0.0086	0.0064
2	Al/T/A	0.0275	0.0164	0.0127	0.0091	0.0074
3	I-20	0.0308	0.0185	0.0134	0.0098	0.0077
4	Cu/T/A	0.0281	0.0167	0.0118	0.0084	0.0063
5	Cu/(A+T)	0.0291	0.0173	0.0125	0.0088	0.0066
6	Cu/T	0.0339	0.0193	0.0139	0.0098	0.0069
7	Cu	0.0339	0.0205	0.0146	0.0103	0.0075
8	Cu/A	0.0372	0.0209	0.0146	0.0105	0.0077

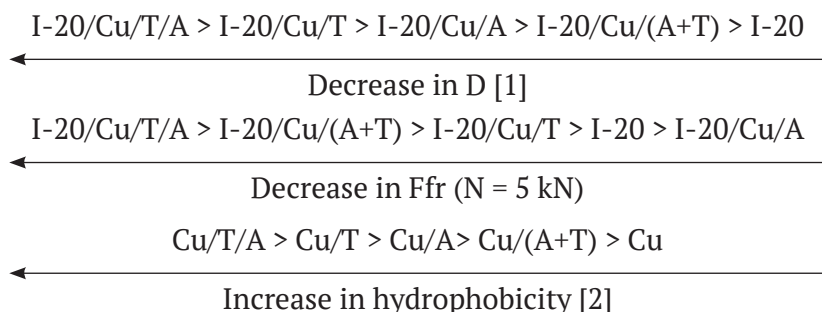
friction mode to the boundary one, and further to “dry friction”.

The need to study tribosystems in a wide range of loading pressures is explained by the widespread use of industrial petroleum oil in industry for lubricating a wide range of machine tool and mining equipment, characterized by uneven load on the actuating device.

The dependence between the friction force and the load for lubricating compositions with various Cu-additives based on I-20 industrial oil was approximated by a linear dependency with a confidence level R^2 in the range of 0.985 -

of Brunauer, Deming and Teller [19-20]. From the data provided in earlier studies, taking into account the testing of samples in saturated water vapour for hundreds of hours, it follows that the most hydrophobic of the studied samples is a sample of the Cu/A/HSL type with sequentially chemisorbed alkamon and ethylhydridesiloxane [2].

As a result of analysing the data presented in Fig. 1 and Tables 1 and 2, the series of enhancement of antifriction and water-repellent properties for copper-containing additives were obtained:



0.997. Cu-additives, which maximally reduce the friction force and coefficient of friction in the tribosystem (Cu/T/A, Cu/(A+T)), correspond to the equations with the minimum proportionality factor k (Table 2). The resulting equations $y = kx + b$ were similar to the formula for boundary friction ($F_{fr} = k(N + F_{af})$, where k is the coefficient of friction, N is the force of normal pressure (load), F_{af} is the additional force due to intermolecular attraction). F_{af} is minimal for Cu/T/A additive. Modification of copper allows adjusting the value of F_{af} (Table 2).

Water vapour adsorption isotherms for most copper-based samples correspond to type III isotherms [2] according to the classification

As can be seen from the comparison of the series, the antifriction effect of copper additives in tribosystems increased as the hydrophobicity of the latter increased. However, application of a hydrophobic substance (A or T) to dispersed copper powder (PMS-1) did not allow achieving a high antifriction effect. The best antifriction properties were revealed for copper samples containing triamon in the surface layer with small (C_1-C_2) organic radicals at the nitrogen atom. This obviously contributes to the fact that the T molecules relatively easily fill the “gaps” of the factory stearic stabilizing film. Also, due to the steric accessibility of nitrogen atoms in triamon, favourable conditions for the metal-nitrogen

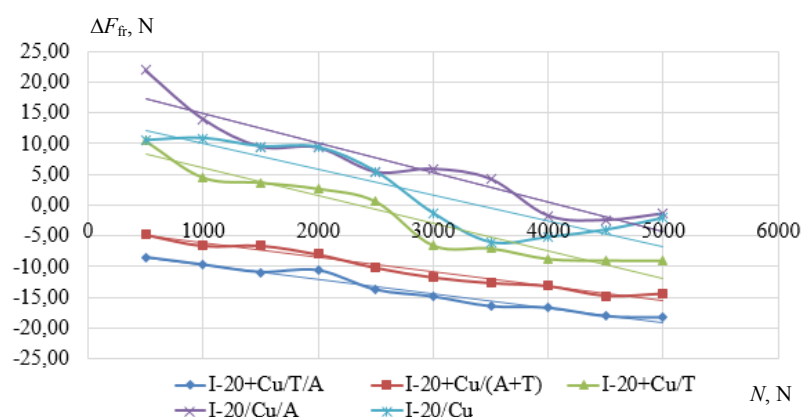


Fig. 2. Dependence of the antifriction effect in the tribosystem on the load for additives based on dispersed copper PMS-1, modified in different modes

interaction, enhancing the adhesion of the surfactant to the metal were created. The above is also evidenced by the tribological characteristics of the Cu/A sample treated with one alkamon, the addition of which to the oil composition did not lead to an increase in the antifriction properties in comparison with the addition of the initial PMS-1 copper powder (Table 2).

In this study, the quantum-chemical modelling using the HyperChem software package was applied for the determination of the structural-chemical and nucleophilic-electrophilic properties of molecules. The following molecular parameters

were determined: dipole moment, distribution of electrostatic potential, energy of the highest occupied molecular orbital (HOMO) and lowest unoccupied molecular orbital (LUMO). The value of the dipole moment of the adsorbed molecule is important for the estimation of the change in the interfacial potential and the energy of interaction of the adsorbate with a solid surface [17, 21–23].

The dipole moment of the ethylhydridesiloxane oligomer corresponds to 3.02 D (Table 4), and its direction is shown by the dotted line in Fig. 3. Oxygen atoms (0.66 eV) of organic radicals were the most reactive in the case of

Table 4. Results of quantum chemical modelling of active component of HSL-94 and ammonium compounds

	HSL-94	Alkamon	TOM
Dipole moment [D]	3.0	20.2	5.3
Energy HOMO [eV]	2.37	-13.10	-6.21
Energy LUMO [eV]	10.10	-1.95	0.38
Molecular Excitation Potential ΔE [eV]	7.23	11.15	6.59
Electrophilic-Nucleophilic properties (donor-acceptor) properties	Nucleophile	Electrophile	Nucleophile

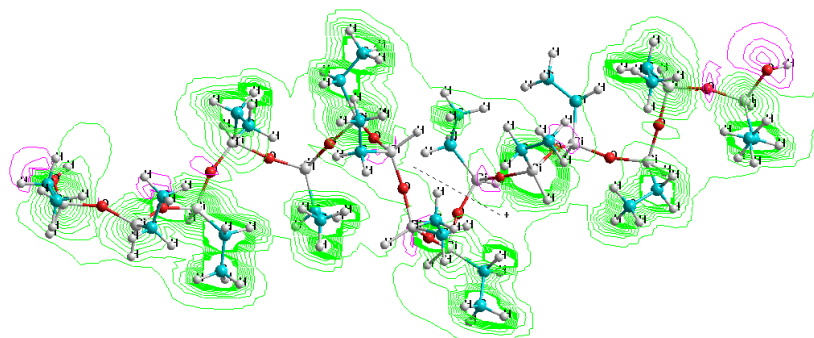


Fig. 3. Quantum chemical model of ethylhydridesiloxane oligomer ($n = 15$) with the distribution of electrostatic potential (silicon atoms – big grey balls)

electrostatic interaction (physical adsorption). For the determination of the nucleophilic and electrophilic (donor–acceptor) properties of the molecule, the energies of the lowest unoccupied and highest occupied molecular orbitals were determined, which were 2.374 and 10.097 eV, respectively (Fig. 4). Since the energy of LUMO is positive, the ethylhydridesiloxane oligomer molecule is a nucleophile. The excitation potential of the molecule was 7.233 eV. The results of a similar analysis of other molecules are shown in Table 4 for molecules of active substances in preparations based on quaternary ammonium compounds - triamon (TOMAM) and alkamon.

As can be seen from Table 5, samples containing combinations of modifiers with different nucleophilic-electrophilic properties (Cu/A/HSL), Cu/(A + T), Cu/T/A) in the surface layer possess the greatest hydrophobic and antifrictional effect, contributing to the chemical (electronic) interaction in the metal-deposited modifiers system, including interactions between deposited substances. Therefore, modification modes, including sequential treatment with hydrophobic compositions with different electrophilic properties, are most preferable for obtaining highly and superhydrophobic materials. It is interesting that modification with only one type of modifier (A, T, HSL) did not allow achieving a significant increase in the hydrophobicity of the surface in comparison with the original copper powder, probably due to the limited possibility of stabilizing the outer hydrophobic layer of the surface. The combination of electrophilic and nucleophilic modifiers allowing not only to block the hydrophilic centres of the surface, but also

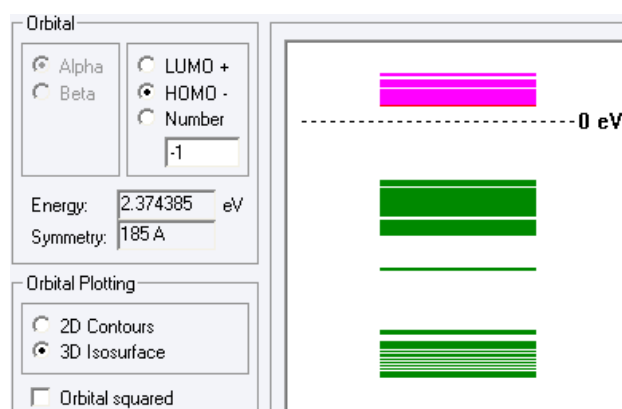


Fig. 4. The distribution of the molecular orbitals of ethylhydridesiloxane oligomer (HSL -94)

to increase the resistance of the metal-applied hydrophobic agents system to external influences.

According to A. A. Abramzon, an increase in the adhesion of a surfactant film to a solid surface is the key to its successful hydrophobization and antifriction effect [24]. The possibility of donor-acceptor interactions metal - QACs, metal - silicon hydrides has been repeatedly proven by IR and XPS spectroscopy [1,25,26].

Conclusions

For the first time, fundamental tribological characteristics (force and coefficient of friction) were measured for copper-based samples in the composition of I-20 oil and compared with the hydrophobicity of additives and antifriction properties of systems with high loading pressures. Quantum-chemical modelling of reagent molecules used in the process of layering of different-sized molecules of quaternary ammonium compounds on metals was performed using HyperChem software package.

Table 5. Comparison of average values of water vapour sorption ($P_{H_2O}/P_s = 0.98 \pm 0.02$) and friction force change for different samples in the time interval $24 \leq t \leq 216$ h with electrophilic-nucleophilic (donor-acceptor) properties of modifiers (A, T, HSL)

Sample	a_{av} , %	ΔF_{fr} ($N = 5$ kN), %	Electrophilic-nucleophilic characteristics of modifier (energy LUMO)
Cu/A/HSL	0.396	–	Electrophile (–1.95) + Nucleophile (10.10)
Cu/T/A	0.491	–18.2	Nucleophile (0.38) + Electrophile (–1.95)
Cu/(A+T)	0.507	–14.3	Nucleophile (0.38) + Electrophile (–1.95)
Cu/A	0.521	–1.4	Electrophile (–1.95)
Cu/HSL	0.532	–	Nucleophile (10.10)
Cu	0.534	–2.2	–
Cu/T	0.568	–1.4	Nucleophile (0.38)

In this study, the nucleophilic-electrophilic properties of active substance molecules of modifiers of metal surfaces were studied using quantum-chemical modelling methods. The properties of molecules were compared with the sorption characteristics of modified metals and antifriction properties in the composition of industrial oil. The donor-acceptor properties of molecules were compared with the adsorption characteristics of the surface of dispersed metals. Considering earlier studies of modification of dispersed metals and the data obtained in this study for antifriction properties in the composition of industrial oil I-20, a relationship between various modes of modification and the hydrophobicity of the surface of dispersed metals was established. The series of enhancement of nucleophilic/electrophilic properties and dipole moment for the used modifiers were obtained. Recommendations for the application of modifiers in practice were offered.

Author contributions

A. G. Syrkov – scientific guidance, editing (40 %). V. R. Kabirov – experimental work, preparation of materials (40 %). A. P. Pomogaybin – technical support for the study (10 %). Ngo Quoc Khanh – work with literary sources, technical support (10 %).

Conflict of interests

The authors declare that they have no known competing financial interests or personal relationships that could have influenced the work reported in this paper.

References

1. Syrkov A. G., Bazhin V. Yu., Mustafaev A. S. *Nanotekhnologiya i nanomaterialy. Fizicheskie i mineral'no-syr'evye aspekty* [Nanotechnology and nanomaterials. Physical and mineral aspects]. St. Petersburg: Politekh-Press Publ.; 2019. 244 p. (In Russ.)
2. Syrkov A. G., Pleskunov I. V., Kavun V. S., Taraban V. V., Kushchenko A. N. Changes in the sorption properties of dispersed copper containing ammonium compounds in the surface layer resulting from interaction with water vapours. *Kondensirovannye sredy i mezhfaznye granitsy = Condensed Matter and Interphases*. 2019;21(1): 146–154. <https://doi.org/10.17308/kcmf.2019.21/725> (In Russ., abstract in Eng.)
3. Silivanov M. O. *Adsorbtsionnye i kislotno-osnovnye svoystva metallov, soderzhashchikh na*

poverkhnosti organogidridsiloksan i ammonievye soedineniya i ikh vliyanie na antifriktsionnyi effekt [Adsorption and acid-base properties of metals containing organohydridesiloxane and ammonium compounds on the surface and their influence on the antifriction effect]. Diss. Cand. Chem. Sciences / Saint Petersburg: Saint-Petersburg State Institute of Technology; 2018. 108 p. Available at: <https://search.rsl.ru/ru/record/01008716048> (In Russ.)

4. Syrkov A. G., Silivanov M. O., Sychev M. M., Rozhkova N. N. Alteration of the acid-base properties of the oxidized surface of disperse aluminum during the adsorption of ammonium compounds and the antifriction effect. *Glass Physics and Chemistry*. 2018;44(5): 474–479. <https://doi.org/10.1134/s1087659618050206>

5. Remzova E. V. *Nelineinost' khimiko-organicheskikh svoistv poverkhnostno-modifitsirovannykh metallov i geterogennykh sistem na ikh osnove* [Nonlinearity of chemical-organic properties of surface-modified metals and heterogeneous systems based on the]. Diss. Cand. Chem. Sciences / Voronezh: Voronezh State University; 2013. 140 p. Available at: <https://search.rsl.ru/ru/record/01005058782>

6. Slobodov A. A., Syrkov A. G., Yachmenova L. A., Prokopchuk N. R., Kavun V. S. Effect of temperature on solid-state hydride metal synthesis according to thermodynamic modeling. *Journal of Mining Institute*. 2019;239(5): 550–555. <https://doi.org/10.31897/pmi.2019.5.550>

7. Pleskunov I. V., Prokopchuk N. R., Syrkov A. G., Kabirov V. R. Water-repellent properties of copper powder modified by ammonium compounds during long-term treatment with saturated water vapor. *Proceedings of BSTU Series 2: Chemical technologies. Biotechnology. Geoecology*. 2019;2: 98–105. Available at: <https://elibrary.ru/item.asp?id=40802132> (In Russ., abstract in Eng.)

8. Korobochkin V. V., Potgieter J. H., Usoltseva N. V., Dolinina A. S., An V. V. Thermal preparation and characterization of nanodispersed copper-containing powders produced by non-equilibrium electrochemical oxidation of metals. *Solid State Sciences*, 2020;108: 106434. <https://doi.org/10.1016/j.solid-statesciences.2020.106434>

9. Inamdar A. I., Pathak A., Usman M., Chiou K. R., Tsai P. H., Mendiratta S., Lu K. L. Highly hydrophobic metal-organic framework for self-protecting gate dielectrics. *Journal of Materials Chemistry A*. 2020;8(24): 11958–11965. <https://doi.org/10.1039/d0ta00605j>

10. Berezhnoi Y. M., Lipkin V. M., Likhota A. D. The influence of polyelectrolytes on the properties of ultramicro and nanosized powders of copper. *Materials Science Forum*. 2018;945: 505–508. <https://doi.org/10.4028/www.scientific.net/MSF.945.505>

11. Khananashvili L. M., Andrianov K. A. *Tekhnologiya elementoorganicheskikh monomerov i oligomerov* [Technology of organoelement monomers and oligomers]. Moscow: Khimiya Publ.; 1983. 380 p. (In Russ.)
12. Ignat'ev V. M., Emel'yanova N. S., Sanina N. A. Quantum chemical modeling in the system polyvinylpyrrolidone – cation of the dinitrosyl iron complex. *Russian Chemical Bulletin*. 2020;69(12): 2265–2269. <https://doi.org/10.1007/s11172-020-3045-7>
13. Gribanov E. N., Markov O. I., Khripunov Yu. V. Quantum chemical modeling bismuth-based clusters. *Materials Physics and Mechanics*. 2020;43(1): 72–83. https://doi.org/10.18720/MPM.4312020_9 (In Russ., abstract in Eng.)
14. St. John P. C., Guan Y., Kim Y., Etz B. D., Kim S., Paton R. S. Quantum chemical calculations for over 200,000 organic radical species and 40,000 associated closed-shell molecules. *Scientific Data*. 2020;7(1): 244. <https://doi.org/10.1038/s41597-020-00588-x>
15. Grambow C. A., Li Y. P., Green W. H. Accurate thermochemistry with small data sets: A bond additivity correction and transfer learning approach. *The Journal of Physical Chemistry A*. 2019;123(27): 5826–5835. <https://doi.org/10.1021/acs.jpca.9b04195>
16. Kumer A, Sarker M, Paul S. The theoretical investigation of HOMO, LUMO, thermophysical properties and QSAR study of some aromatic carboxylic acids using HyperChem programming. *International Journal of Chemistry and Technology*. 2019;3(1): 26–37. <https://doi.org/10.32571/ijct.478179>
17. Clark T. *A handbook of computational chemistry: A practical guide to chem. structure a. energy calculations*. New York: Wiley; 1985. 332 p.
18. Nechaev I. V., Vvedenskii A. V. Quantum chemical modeling of the interaction in MeN(H₂O)M (Me = Cu, Ag, Au; N = 1–3; M = 1, 2) system. *Kondensirovannye sredy i mezhfaznye granitsy = Condensed Matter and Interphases*. 2019;21(1): 105–115. <https://doi.org/10.17308/kcmf.2019.21/722> (In Russ., abstract in Eng.)
19. Kim A. M. *Organicheskaya khimiya* [Organic chemistry]. Novosibirsk: Izdatel'stvo Novosibirskogo un-ta Publ.; 2002. 844 p. (In Russ.)
20. Lowell S., Shields J. E. Adsorption isotherms. In: *B. S. Powder Surface Area and Porosity*. Dordrecht: Springer; 1984. 320 p. https://doi.org/10.1007/978-94-009-5562-2_3
21. Roberts M. W., McKee C. S. *Chemistry of the metal-gas interface*. Toronto: Clarendon Press; New York: Oxford University Press; 1978. 594 p.
22. Salem R. R. *Fizicheskaya khimiya: Nachala teoreticheskoi elektrokhemii* [Physical Chemistry: Beginnings of Theoretical Electrochemistry]. Moscow: Lenand Publ.; 2021. 320 p. (In Russ.)
23. Pozhidaeva S. V., Ageeva L. S., Ivanov A. M. Comparative analysis of zinc and tin oxidation with acids at room temperatures. *Journal of Mining Institute*. 2018;235(1): 38–46. <https://doi.org/10.31897/pmi.2019.1.38>
24. Abramzon A. A. *Poverkhnostnoaktivnye veshchestva. Sintez, analiz, svoistva, primeneniye* [Surfactants. Synthesis, analysis, properties, application]. Leningrad: Khimiya Publ.; 1988. 200 p. (In Russ.)
25. Hussein O. A., Khudhair D. M., Aljbar A. A. A. IR spectroscopic study of triiodosilane (SiI₃) by using semi-empirical quantum program. *Journal of Physics: Conference Series*. 2021;1818 (1): 012014. <https://doi.org/10.1088/1742-6596/1818/1/012014>
26. Pleskunov I. V., Syrkov A. G., Kabirov V. R. Quantum-chemical modeling of quaternary ammonium compounds for modification of metal surface (Book Chapter). In: *New Materials: preparation, properties and applications in the aspect of nanotechnology*. New York: Nova Science Publishers, Inc; 2020. p. 75–84.

Information about the authors

Andrey G. Syrkov, DSc in Engineering, Professor, Department of General and Technical Physics, Saint Petersburg Mining University, Saint Petersburg, Russian Federation; e-mail: Syrkov_AG@pers.spmi.ru. ORCID iD: <https://orcid.org/0000-0001-6152-6012>.

Vadim R. Kabirov, PhD student, Department of Physical Chemistry, Saint-Petersburg Mining University, Saint-Petersburg, Russian Federation; e-mail: vkabirov1@gmail.com, ORCID iD: <https://orcid.org/0000-0003-1842-3733>.

Alexander P. Pomogaibin, Master student, Mineral Processing Department, Saint Petersburg Mining University, Saint Petersburg, Russian Federation; e-mail: Pomogaibin.sasha@yandex.ru. ORCID iD: <https://orcid.org/0000-0001-7325-0682>.

Ngo Kuok Kkhan, PhD student, Department of Chemical Technologies and Energy Processing, Saint Petersburg Mining University, Saint Petersburg, Russian Federation; e-mail: ngoquockhanh292@mail.ru. ORCID iD: <https://orcid.org/0000-0001-6742-317X>.

Received 29 April 2021; Approved after reviewing 20 May 2021; Accepted for publication 15 June 2021; Published online 25 June 2021.

Translated by Valentina Mittova
Edited and proofread by Simon Cox